Technische Universität München
TUM School of Engineering and Design

Structure-Integrated Antennas for Solar Sailing Spacecraft

Nicolas Michael Etienne Appel

Vollständiger Abdruck der von der TUM School of Engineering and Design der Technischen Universität München zur Erlangung des akademischen Grades eines

Doktors der Ingenieurwissenschaften (Dr.-Ing.)

genehmigten Dissertation.

Vorsitz: Prof. Dr. Sophie Armanini

Prüfende der Dissertation:

1. Prof. Dr. Ulrich Walter
2. Prof. Dr.-Ing. Enrico Stoll

Die Dissertation wurde am 28.11.2023 bei der Technischen Universität München eingereicht und durch die TUM School of Engineering and Design am 25.03.2024 angenommen.

Acknowledgement

Diese Arbeit wäre ohne die Unterstützung vieler Personen nicht möglich gewesen, denen ich zu Dank verpflichtet bin.

Zuallererst möchte ich meinen Prüfern Prof. Walter und Prof. Stoll, die diese Arbeit erst ermöglicht haben, meinen Dank aussprechen. Darüber hinaus gilt Prof. Walter großer Dank, da ohne dessen Ermutigung, Unterstützung und Vertrauen es mir nicht möglich gewesen wäre, so frei an diesem Thema zu forschen. Ich danke ebenfalls für die großartige Zeit und Freiheit, die ich als Student und anschließend als Mitarbeiter am LRT hatte. Nirgendwo anders hätte ich mich so gut entwickeln können, wie hier.

Prof. Erwin Bibl vom Lehrstuhl für Höchstfrequenztechnik danke ich für die Hilfsbereitschaft und den Zugang zu seinen Einrichtungen. Mein herzlicher Dank geht an die Mitarbeiter des HOT, allen voran Michael Hani für seine unschätzbare Unterstützung, die lustigen Zeiten und die großartige Freundschaft über all die Jahre.

Ich möchte Prof. Thomas Eibert vom Lehrstuhl für Hochfrequenztechnik dafür danken, dass er sich die Zeit genommen hat, meine Forschung zu diskutieren und fachkundige Einblicke zu geben, Messungen meiner Antenne durchzuführen und seine Einrichtungen zur Verfügung zu stellen. Außerdem danke ich Thomas Mittereder für seine Unterstützung bei der Herstellung von Leiterplattenprototypen.

Ich danke Prof. Klaus Drechsler vom Lehrstuhl für Carbon Composites der mir großzügig Zugang zu seinen Fertigungsanlagen gewährt und so die Forschung an den CTM Antennen erst ermöglicht hat. Ein besonderer Dank geht an Leo Heidemann und Maximilian Steinhardt für ihre engagierte Unterstützung meiner Studenten und die vielen interessanten Gespräche.

Meine Wertschätzung gilt überdies Rene Fust und Frederic Groth von der AERO-Coating GmbH für großartige Hilfe bei der Fertigung der IVD Prototypen.

Großen Dank bin ich Markus Becherer vom Lehrstuhl für Nano- und Quantensensoren und Anika Kwiatkowski schuldig. Eure Unterstützung bei den Aufdampftests waren von unschätzbarem Wert. Danke für eure offene und herzliche Art, die mir den Arbeitsalltag verschönert hat.

I am grateful to Willem Jordaan of Stellenbosch University for his profound insights and fruitful discussions about my work in particular and the field of solar sailing in general.

Mein tiefster Dank gilt Martin Rott, der mittels arkaner Künste immer irgendwie Budget gefunden hat, um meine Forschung zu unterstützen. Ohne Martin wäre der LRT nicht denkbar gewesen und ich bin dankbar, dass ich die Gelegenheit hatte, mit ihm zu arbeiten. Wir hatten großartige Zeiten als wir zusammen Singapur erkundet und unsicher gemacht haben. Ebenfalls möchte ich bei Uta Fellermair danken, die immer ein offenes Ohr für meine Anliegen hatte und mir so viele Interaktionen mit der Verwaltung erspart hat. Danke für deine Unterstützung bei so vielen Festen und die vielen lustigen Gespräche. Durch dich hat der LRT neuen Schwung erhalten.

Meinen Kollegen am LRT danke ich für die wunderbaren Zeiten, die wir zusammen von unseren

Tagen als Studenten bis zur Promotion hatten. Danke für die unzähligen Kaffeepausen, Mittagessen, Grillabende und Feste.

Ganz besonderer Dank gilt meinen beiden Freunden und Kollegen Sebastian Rückerl und Thomas Lausenhammer, die meine Arbeit Korrektur gelesen haben. Sebastian, unsere tägliche Kaffeerunde, anregenden Gespräche, Diskussionen und deine Unterstützung waren von unschätzbarem Wert. Thomas, danke für die unzähligen Ovo-Runden, Diskussionen, Festivals und Konzerte. Mögen noch viele davon folgen.

Ich danke meinen Freunden Bernhard, Jonas, Phil, Jan, Aileen, Philipp, Katharina, Sebastian und Dennis, eure unerschütterliche Unterstützung war eine konstante Quelle der Stärke und Freude auf dieser Reise. Ich bin jedem von euch für eure Unterstützung, Freundschaft und Beiträge zu dieser Arbeit dankbar. Euer Einfluss auf mein akademisches und persönliches Leben ist unermesslich, und ich bin glücklich, euch auf meinem Weg zu haben.

Ich möchte mich ebenso bei meiner Familie für ihre unerschütterliche Unterstützung und Ermutigung über meinen ganzen Lebensweg hinweg bedanken. Danke, dass ihr immer für mich da seid.

Mein vorzüglichster Dank gilt meiner Partnerin Carina. Deine Liebe, Geduld und dein Verständnis waren mir während dieses Unterfangens ein Fels in der Brandung. Danke für all dies, für die gemeinsame Zeit und Zukunft.

Garching, November 12, 2023 *Nicolas Michael Etienne Appel*

Abstract

Solar sails are among the most promising technologies for future space missions. Solar sails provide propellantless propulsion using the momentum of photons from the Sun to accelerate a spacecraft. The miniscule force of the photons is contrasted by the large mass of spacecraft and the velocity changes required for space travel. Hence, one of the main challenges of solar sailing is increasing the specific acceleration, as this directly affects possible missions and mission duration. Developing lighter spacecraft components is essential in order to achieve this goal. Solar sail structures are large, thin, metalized membranes that are often deployed and stabilized by carbon fiber reinforced polymer booms.

Previous work on solar sail antennas has investigated Fresnel reflectors embedded into surface of the solar sail membrane. While this principle is capable of providing high gain, it requires a large separation between radiating element and reflector and so imposes strict requirements on the overall system. Active antennas, on the other hand, can be integrated into the solar sail structures and provide a more compact solution, and have pricipally less impact on the system design. This thesis investigates antennas integrated into the solar sail membrane and the sail boom. The goal of this research is to analyse the feasibility of such designs, their performance, limits and impact on the sail system.

In the case of the membrane antenna, we first analyze suitable sate-of-the-art transmission line technologies. We find that the single-conductor spoof surface plasmon polariton (SSPP) technology is the only viable solution for this kind of solar sail antenna, as it allows low-loss transmission of electromagnetic waves and purely planar power divider and antenna designs. For further research, prototypes of antennas and power dividers are manufactured and measured, and combined larger structures simulated using full-wave solvers. Given the performance data of the prototypes, an analysis is carried out to estimate the performance of very large arrays. The analysis revealed a potential peak gain of 31 dBi at 8.5 GHz and an aperture areal density of less than $0.2\,\mathrm{kg\,m^{-2}}$. Such an antenna would improve the state of the art with regard to the aperture areal density by two orders of magnitude, with the caveat of increased manufacturing complexity compared to conventional antennas.

Moreover, we develop the concept of a slotted waveguide antenna integrated into collapsible tubular mast (CTM) structures. This deployable structure can act as waveguide due to the conductivity of the carbon fiber material and turned into a travelling waveguide antenna by adding slots. The investigation involves analysis of the propagating electromagnetic modes, slot placement and radiation patterns using numerical full-wave simulations. Afterwards, we perform electromagnetic and structural tests on manufactured prototypes made from carbon fiber reinforced plastic that show the feasibility, but also the limitations of the concept. We find that the most suitable mode for a travelling wave antenna, the TM_{11} mode, exhibits attenuation typical for this waveguide material. The structural analysis expectedly showed reduced load-bearing capacity. This type of waveguide antenna is therefore more suitable for less demanding missions.

Zusammenfassung

Sonnensegel gehören zu den vielversprechendsten Technologien für zukünftige Raumfahrtmissionen. Sonnensegel ermöglichen einen treibstofflosen Antrieb, indem sie den Impuls von Photonen der Sonne nutzen, um ein Raumschiff zu beschleunigen. Die winzige Kraft der Photonen steht im Gegensatz zur großen Masse des Raumfahrzeugs und den für Raumfahrtmissionen erforderlichen Geschwindigkeitsänderungen. Daher ist eine der Hauptherausforderungen des Sonnensegelns die Erhöhung der spezifischen Beschleunigung, da dies direkte Auswirkungen auf mögliche Missionen und die Missionsdauer hat. Die Entwicklung leichterer Raumfahrzeugkomponenten ist entscheidend, um dieses Ziel zu erreichen. Sonnensegelstrukturen bestehen aus großen, dünnen, metallisierten Membranen, die oft von Bäumen aus kohlefaserverstärkten Kunststoff entfaltet und stabilisiert werden.

In vorherigen Arbeiten zu Sonnensegelantennen wurden Fresnel-Reflektoren untersucht, die in die Oberfläche der Sonnensegelmembran eingebettet sind. Obwohl dieses Prinzip einen hohen Gewinn bieten kann, erfordert es einen großen Abstand zwischen dem strahlenden Element und dem Reflektor und stellt daher strikte Anforderungen an das Gesamtsystem. Aktive Antennen hingegen können in die Sonnensegelstrukturen integriert werden und bieten eine kompaktere Lösung, die grundsätzlich weniger Auswirkungen auf das Systemdesign hat. In dieser Arbeit werden Antennen untersucht, die in die Sonnensegelmembran und die Segelstreben integriert sind. Das Ziel dieser Forschung ist die Analyse der Machbarkeit solcher Designs, ihrer Leistung, Grenzen und Auswirkungen auf das Segelsystem.

Im Fall der Membran-Antenne analysieren wir zunächst geeignete Übertragungsleitungstechnologien auf dem neuesten Stand der Technik. Wir stellen fest, dass die Einzelleiter auf spoof surface plasmon polariton (SSPP)-Technologie die einzige praktikable Lösung für diese Art von Sonnensegelantennen darstellt, da sie den verlustarmen Übertrag von elektromagnetischen Wellen und rein planare Leistungsteiler- und Antennendesigns ermöglicht. Für weitere Forschungszwecke werden Prototypen von Antennen und Leistungsteilern hergestellt und vermessen, und größere kombinierte Strukturen werden unter Verwendung von Vollwellenlösungsverfahren simuliert. Basierend auf den Leistungsdaten der Prototypen wird eine Analyse durchgeführt, um die Leistung sehr großer Arrays abzuschätzen. Die Analyse ergab eine potenzielle Spitzenverstärkung von 31 dBi bei 8.5 GHz und eine Aperturflächendichte von weniger als $0.2\,\mathrm{kg\,m^{-2}}$. Eine solche Antenne würde den Stand der Technik bezüglich der Aperturflächendichte um zwei Größenordnungen verbessern, jedoch mit der Einschränkung begrenztem Gewinns und komplexerer Herstellung im Vergleich zu konventionellen Antennen.

Ferner entwickeln wir das Konzept einer geschlitzten Hohlleitungsantenne, die in collapsible tubular mast (CTM)-Strukturen integriert ist. Diese ausfaltbare Struktur kann aufgrund der Leitfähigkeit des Kohlefaser-Materials als Hohlleiter dienen und durch das Hinzufügen von Schlitzen in eine Wanderfeldhohlleiterantenne umgewandelt werden. Die Untersuchung beinhaltet die Analyse der sich ausbreitenden elektromagnetischen Moden, die Platzierung der Schlitze und die Abstrahlungsmuster unter Verwendung numerischer Vollwellen-Simulationen. Anschließend führen wir elektromagnetische und strukturelle Tests an hergestellten Prototypen aus kohlefaserverstärkten Kunststoff durch, die die Machbarkeit, aber auch die Grenzen des Konzepts zeigen. Wir stellen fest, dass die am besten geeignete Mode für eine Wanderfeldantenne, die TM_{11}-Mode, eine materialtypische Dämpfung aufweist. Die strukturelle Analyse ergibt eine erwartungsgemäß niedrigere Traglast. Daher ist diese Art von Hohlleiterantenne für Missionen mit geringeren strukturellen Anforderungen eher geeignet.

Contents

Acronyms

ACS3	Advanced Composite Solar Sail 3
AM0	Air Mass Zero
AR	Axial Ratio
CFRP	Carbon Fiber Reinforced Plastic
COTS	Commercial Off-the-shelf
CP	Circular Polarization
CPS	Coplanar Strips
CPW	Coplanar Waveguide
CTM	Collapsible Tubular Mast
DFP	Dry Fiber Placement
DL	Downlink
DLR	German Aerospace Center
DSN	Deep Space Network
ENIG	Electroless Nickel Immersion Gold
ESA	European Space Agency
ESTRACK	European Space Tracking
GBL	γ-Butyrolactone
GCPW	Grounded Coplanar Waveguide
GEO	Geostationary Orbit
IKAROS	Interplanetary Kite-Craft Accelerated By Radiation Of The Sun
IR	Infrared Light
ITU	International Telecommmunications Union
IVD	Ion Vapor Deposition
JAXA	Japan Aerospace Exploration Agency
JPL	Jet Propulsion Laboratory
LCM	Liquid Composite Molding
LEO	Low-earth Orbit
LHCP	Left Hand Circular Polarization
LLT	Linear Laminate Theory
MarCO	Mars Cube One
NASA	National Aeronautics And Space Administration

NEA Scout Near Earth Asteriod Scout
NMP N-methyl-2-pyrrolidone

PCB Printed Circuit Board
PEC Perfect Electrical Conductor
PEN Polyethylenenaphtalate
PET Polyethylene Terephthalate
PGL Planar Goubau Line
PLA Polylactic Acid
PMC Perfect Magnetic Conductor
PVD Physical Vapor Deposition
PW Plain Weave

RF Radio Frequency
RHCP Right Hand Circular Polarization
RO4003C Rogers Corporation Laminate 4003C
RO4350B Rogers Corporation Laminate 4350B
RTM Resin Transfer Molding

SAR Synthetic Aperture Radar
SIW Substrate-integrated Waveguide
SLL Sidelobe Level
SMA Subminiature Version A
SPP Surface Plasmon Polariton
SSPP Spoof Surface Plasmon Polariton
SWA Slotted Waveguide Antenna

TE Transversal Electric
TEM Transversal Eletromagnetic
TL Transmission Line
TM Transversal Magnetic
TM/TC Telemetry And Telecommand
TRAC Triangular Rollable And Collapsible
TWA Traveling Wave Antenna

UL Uplink
UV Ultraviolet Light

VARI Vacuum-assisted Resin Infusion Process
VNA Vector Network Analyzer

Chapter 1

Introduction

> Given ships or sails adapted to the breezes of heaven, there will be those who will not shrink from even that vast expanse. Therefore, for the sake of those who, as it were, will presently be on hand to attempt this voyage, let us establish the astronomy, Galileo, you of Jupiter, and me of the moon.
>
> *Johannes Kepler*

1.1 Motivation

Exploring and understanding our environment is a desire deeply rooted in humanity. Our ancestors traveled across the sea into the unkown to find places to settle and new resources to exploit. They developed instruments to study and predict nature. Once mankind learned to predict, they were able to shape the future. They discovered new continents and resources, created new technology and medicine which prevented hunger and disease. From these discoveries, we have all benefited greatly and readily, and we must continue this task for generations to come. The explorers, scientists and engineers of the past are the Leviathan on whose shoulders we stand today, who elevate us to allow us to explore what is sometimes called *the last frontier:* outer space.

The exploration, investigation and eventually conquest of outer space is crucial for the future of mankind. Outer space contains virtually everything there is, and its exploration is not only a logical progression, but also provident. On the one hand, discoveries on new worlds deepen our understanding of nature and its phenomena and inspire new research. On the other hand, mankind will be able to use space faring technology for planetary defense and satisfy its hunger for ever more resources by mining asteroids. Achieving these goals is a matter of accessibility which is limited by economical and technological feasibility.

Space missions have always been associated with a technological level at the limit of feasibility and also came at a very high cost. While there are many exploration targets deemed interesting, budgetary limitations constrict our reach into space to very few select high profile targets. The total cost of a typical exploration mission consists mainly of the development of the spacecraft, launch and operations. Hidden within those three items is another limitation of space exploration missions: propulsion. Virtually all exploration missions of the past were launched by rockets and maneuvered in space using rocket engines. The Tsiolkovsky rocket equation describes the amount of velocity change, Δv, that can be effected by a rocket. It states that the initial mass of a rocket grows exponentially with required Δv. Because of this, the practical limit to carrier rocket size also limits our reach into space. A way to circumvent the rocket equation are gravity asssist slingshot maneuvers. This technique has allowed missions like New Horizons to reach the outermost planets and even leave the solar system with Voyager. Despite all efforts, many goals, such as interstellar travel, have been out of reach. Moreover in order to scale up the numbers of our space missions a more economical way of space travel is needed.

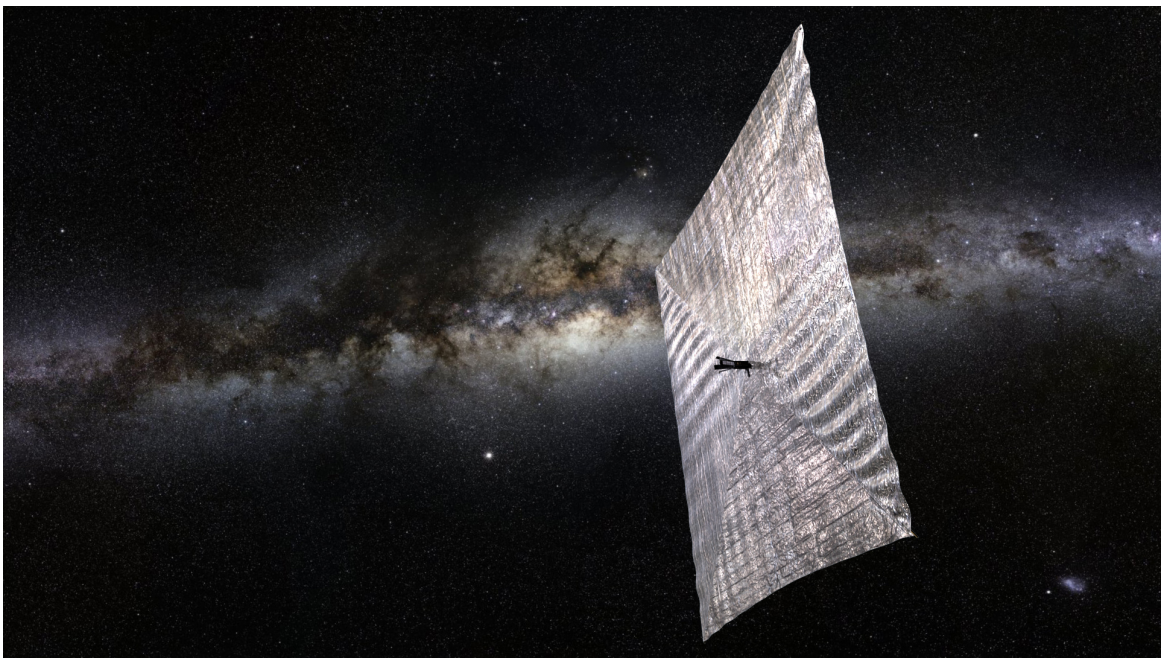

Figure 1.1: Rendering of a solar sailing spacecraft. Image Credit: NASA

1.2 Problem Statement

A promising technology for inexpensive exploration missions are small solar sailing probes. Solar sails are large optical mirrors, made of very thin metalized foils (see Fig. 1.1). Solar sails produce very small but continuous amounts of thrust by the reflection of the sun's light. This way of propulsion is not based on the expulsion of mass and the rocket equation does not apply. Solar sailing could allow spacecraft to reach the outer planets[1], orbit the sun's poles[2], mine asteroids[3, 4] and even fly interstellar[5]. Solar sailing has the theoretical capability to provide a spacecraft with virtually unlimited Δv, with the caveats that the velocity change is limited by the spacecraft's life time and that the acceleration depends on the spacecraft's total mass. For that reason, mass reduction in solar sailing is an active and worthwile field of research.

One approach to reduce a solar sailing spacecraft's mass and also volume is reusing existing structures to implement other required functionalities. The Interplanetary Kite-Craft Accelerated by Radiation Of the Sun (IKAROS) mission has demonstrated that the large area of a solar sail can act as surface for thin solar cells, as part of the attitude control system by adjusting the reflective surface, and also host scientific experiments[6, 7].

Solar sailing spacecraft face some special challenges in regards of communication. Antennas are among the largest structures in deep space missions. The further a spacecraft travels away from earth, the larger its antennas need to be in order to maintain contact. This is because the free-space path losses of the transmitted signal increase with the square of the distance. Larger antennas come with larger stowage volume and also mass, both factors detrimental to the performance of a solar sail. Furthermore, large antennas occlude part of the sail, reducing the sailcrafts performance even further.

To remedy this issue, Khayatian et al. performed theoretical research of planar Fresnel reflectors on solar sail membranes[8, 9]. Several issues arise with this concept, the primary being the required focal length, which is incomaptible with current solar sail designs (cf. Chapter 2). A viable solution had yet to emerge. However, this research showed the way to active antennas, which do not suffer from this disadvantage. Hence, the goal of this thesis can be summarized as follows:

To develop and investigate concepts for the integration of
microwave antenna arrays into the structures of a solar sailing spacecraft.

1.3 Approach and Structure of this Thesis

Chapter 2 provides an introduction to the fundamentals solar sailing theory and the state-of-the-art of solar sailing and microwave technology. Based on these findings, the research gaps are identified in Section 3.1. The requirements for this work are discussed in Section 3.2. Subsequently the thesis objectives are presented in Section 3.3.

Next, Chapter 4 presents the research on a high-gain membrane antenna array design. The topic is approached in Section 4.1, where the fundamental design choices of a planar array are discussed and the unknown factors that require further research are introduced. To this end, a technological study assesses the applicability of current microwave technology (Section 4.2) in terms of manufacturability and low attenuation. Afterwards, we refine the study of the membrane array through simulation and manufacturing of array components (Section 4.3 and 4.4) using printed circuit board technology. By combining the components, an outlook on the performance and issues of larger arrays on membrane material is derived using simulations (Section 4.5). An account of manufacturing trials of microwave structures on membrane material using electroplating and ion vapor deposition processes is given in Section 4.6. Using this knowledge, a theoretical assessment of the membrane array in terms of maximum gain, size and mass is presented in Section 4.7. Future work on this topic is discussed in Section 4.8. Finally, a concluding discussion of the membrane antenna array is given in Section 4.9.

A secondary concept of a medium-gain slotted waveguide antenna integrated into the solar sail booms is discussed in Chapter 5. First in Section 5.1, we further expand on the intricacies of the collapsible tubular mast geometry and booms, before we introduce the properties waveguides and waveguide antennas. This information is then used to synthesize and discuss possible waveguide configurations (Section 5.2). It follows an analysis of the microwave properties of collapsible tubular mast waveguides (Section 5.3) using simulations. Afterwards, a study of the slot antenna is carried out using simulations in order to determine behavior and optimal properties (Section 5.4). Subsequently, given the optimal properties of the slot antenna, a sample array design is simulated and parametric variations and the influence of the solar sail are studied. For the following experiments, several boom prototypes were manufactured using the process described in Section 5.5. Section 5.6 presents the measurements of the attenuation of the propagating modes inside the collapsible tubular mast waveguides. Next, the stability properties of slotted booms are compared to non-slotted booms for static load cases in Section 5.7. Finally, an outlook on future work (Section 5.8) together with a concluding discussion of the boom slotted waveguide antenna is given(Section 5.9).

In the end, a summary and conclusion of this work is given in Chapter 6, together with a outlook of future work and final thoughts.

Chapter 2

Fundamentals and State of the Art

This chapter discusses the fundamentals needed for this thesis. First we will provide a brief introduction to solar sailing in section 2.1. In this context we will elaborate on the physical principle of solar sailing, the current state of the art of structures and materials involved. Section 2.2 afterwards discusses recent missions and advanced mission concepts. Next, relevant light-weight antenna concepts of the recent past are reviewed in section 2.3. Finally, we briefly elaborate on deep space communications in section 2.4.

2.1 Solar Sailing

In this section, we will briefly discuss the fundamental physics of solar sailing and the derived key figures of merit. Afterwards, we will review the most commonly examined solar sailing configurations and their properties. Next, we review solar sailing structures. Finally, we take a closer look at geometric imperfections of the sail, i.e. creases and wrinkles.

2.1.1 Introduction

In his 1620 publication "De Cometis Libelli Tres" astronomer Johannes Kepler observed a comet's train to be always directed away from the sun[10], as if it were *blown away* by what he later described as *'breezes of heaven'*[11]. Scientific discoveries of the 19th century lead to the formulation of the unified theory of electromagnetism by James Clerk Maxwell. Maxwell predicted that electromagnetic waves carry momentum and can exert a force on matter: radiation pressure[12].

According to McInnes, radiation pressure can be explained in two ways[12]: With Maxwell's equations, the momentum transfer from an incident electromagnetic wave on a reflective surface can be explained as a result of the Lorentz force. An incident field $\mathbf{E}$ induces a current $\mathbf{j}$, which with the magnetic field component $\mathbf{B}$ generates the Lorentz force $\mathbf{F} = \mathbf{j} \times \mathbf{B}$. The alternative model for radiation pressure comes from quantum mechanics. Photons carry energy that is inversely proportional to their wavelength λ. Based on the relationship of relativistic energy, the momentum of a single photon is:

$$p = \frac{h}{\lambda} = \frac{E}{c} \tag{2.1}$$

where h is the Planck's constant and c is the vacuum speed of light. Assuming a photon flux perpendicular to a surface A, the radiation pressure is given as[12]:

$$P_0 = \frac{F}{A} = \frac{1}{A}\frac{\mathrm{d}p}{\mathrm{d}t} = \frac{1}{Ac}\frac{\mathrm{d}E}{\mathrm{d}t} = \frac{S_0}{c} \tag{2.2}$$

where F is the force acting on A, S_0 is the power flux density.

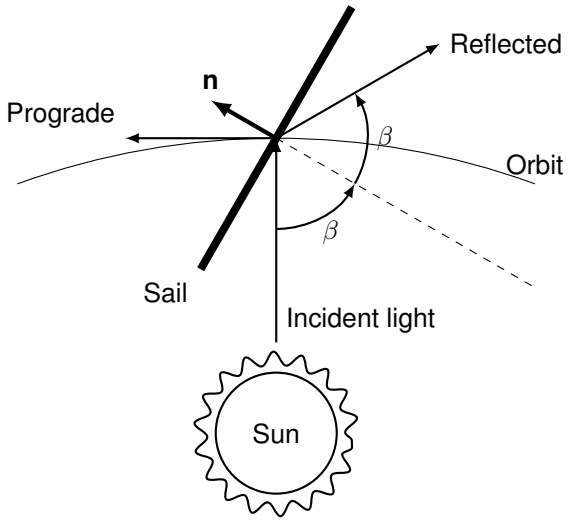

Figure 2.1: Diagram of the solar sailing principle.

The total average power flux density, or irradiance, received at Earth in the optical spectrum can be calculated from the air mass zero (AM0) spectrum[13] (see Fig. 1) and is $1367.58\,\mathrm{W\,m^{-2}}$. Using Equation (2.2) we can determine the total radiation pressure $P_0 = 4.561\,76 \times 10^{-6}\,\mathrm{N\,m^{-2}}$ at 1 AU. The power flux density adheres to the inverse square law and so, at distance r to the sun, the radiation pressure is given by:

$$P = P_0 \left(\frac{R}{r}\right)^2 \tag{2.3}$$

where $R = 1\,\mathrm{AU}$.

In the case of a perfectly reflective surface, the photons are reflected and ideally, the total momentum transfered to the surface is twice as high. This effect is used by solar sailing spacecraft, as is shown in the diagram in Figure. 2.1. The solar sail points into the direction of its sail normal vector **n**. Light impinges on the sail at an angle β to the sail normal, and gets reflected at the same angle. Hence, the thrust vector is parallel to the sail normal. The radiation pressure in this case is given as[1]:

$$\mathbf{P_r} = 2\eta P \cos^2\beta\,\mathbf{n} \tag{2.4}$$

where the sail efficiency $\eta < 1$ accounts for an imperfect reflector. The β angle is mission specific, as it affects other critical parameters, such as mission duration and sail temperature[1] as well as drag, when close to Earth.

The performance of a solar sail is typically reduced to the lightness of the sail. The sail loading factor is a key figure of merit and calculated as follows[14]:

$$\sigma_s = \frac{m_s}{A} \tag{2.5}$$

where m_s is the total mass of all components involved in the sail assembly. Analog to σ_s, there is a total loading factor, that also includes the payload's mass:

$$\sigma = \sigma_s + \frac{m_p}{A} \tag{2.6}$$

where in this case, the payload is defined as the entire remaining spacecraft assembly. Another key figure is the characteristic acceleration of a solar sailing spacecraft[14]. This property is the acceleration experienced by a solar sail, pointed at the sun, at 1 AU distance:

$$a_c = \frac{2\eta P_0 \cdot A}{m} = \frac{2\eta P_0}{\sigma} \tag{2.7}$$

Lastly, the lightness number is a constant, calculated from the ratio of characteristic acceleration divided by the sun's gravitational acceleration at 1 AU:

$$\lambda = \frac{a_c}{\mu_S} \tag{2.8}$$

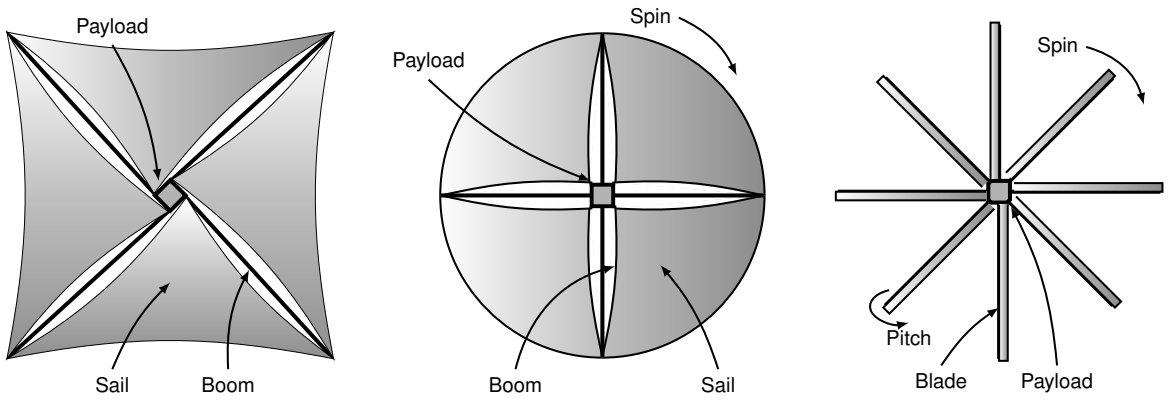

Figure 2.2: Solar sail configurations from left to right: Square, spinning disc and heligyro.

2.1.2 Sail Satellite Types

Solar sails can be built in three main fashions, that are square sail, spinning disc and heligyro[12] which are depicted in Figure 2.2.

The square sail is the most popular sail configuration and the only one flown so far. The sail can either consist of a continuous square membrane or four triangular petals. The payload or satellite bus is located in the center of the sail and acts as connecting hub. The sail is deployed either by centrifugal force[15] or using four sail booms, of which two are connected to the outer corners of a given petal. If the sail is designed as a spinner, it can be connected to the satellite bus via tethers. The sail booms keep the petals stiff in absence of a rotation and transfer the momentum to the bus. Using booms provides more stability at the expense of higher overall mass[14].

Similar to the square sail, the spinning disc sail consists either of a continuous circular membrane, attached to the central payload, or several petals that are deployed by booms. The continuous membrane is simple to deploy and the spinning motion provides stiffness without additional booms or stiffeners. However, changing the attitude of the satellite is a slow process[16].

The final concept is the Heligyro. It consists of multiple long blades located around the central hub. The entire configuration is stabilized by a slow spin and can be rotated by pitching the blades accordingly. The Heligyro does not require booms to deploy and stabilize the sail, but requires larger structures to provide a similar sail area compared to the square and disc sail configurations.

2.1.3 Sail Structure and Deployment

The solar sail is a compound structure consisting of a plastics membrane with different metal coatings (cf. Fig. 2.3). The reflection layer provides the reflective properties of the solar sail, while the optional emission layer improves thermal control. A large membrane section consists of smaller patches or lengths connected together using adhesives. The metallization surfaces are connected with conductive straps in order to prevent different electrostatic charge. Thicker strips of polyimide or similar material can be placed on the membrane surface to prevent tears from propagate through the entire sail. These strips are referred to as “ripstops”.

Sail Membrane

The solar sail membrane provides structural stability for the metal layers. Among others, the membrane material needs to be flexible, yet robust and impervious to solar wind, atomic oxygen and ultraviolet light (UV) radiation. A high operational temperature is benefical to more advanced mission concepts[1].

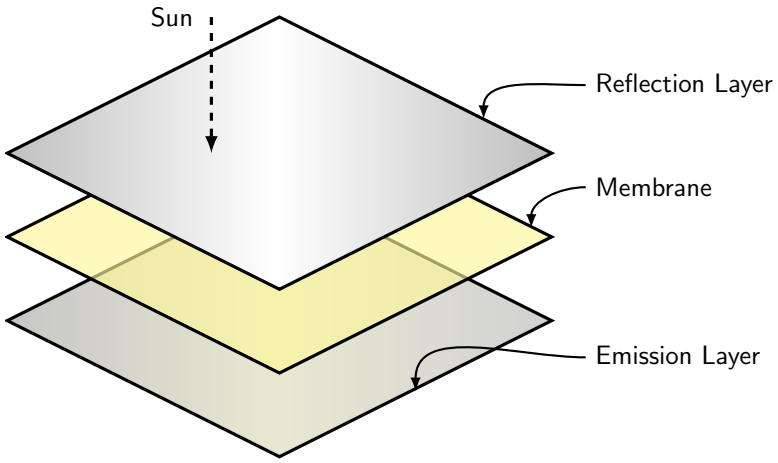

Figure 2.3: Typical buildup of a solar sail membrane.

Several high performance plastics have been tested and utilized for solar sailing and are presented in Table 2.1. The materials in the polyimide group, such as Kapton EN or CP1 are generally very resistant against UV radiation. CP1 is reportedly even rated for ten years in geostationary orbit (GEO)[17]. Polyimides have high dimensional stability and are reported to have a long-term operational temperature between 520 K to 570 K[18]. Kapton EN is available at a thickness of $3\,\mu$m[1], whereas CP1 can be manufactured as thin as $2.54\,\mu$m. polyethylene terephthalate (PET) and polyethylenenaphtalate (PEN) polymers have lower density compared to polyimides. However, they are susceptible to UV radiation and should not be exposed[18].

Table 2.1: Overview of the material properties of commercially available membrane polymers.

Material	Type	UV properties	Thickness [μm]	Density [$\mathrm{g\,m^{-3}}$]	Availability
Kapton EN[19, 20]	Polyimide	resistant	5	1.46	COTS
CP1[17]	Polyimide	resistant	2.5	1.54	COTS
Mylar[18, 21]	PET	susceptible	2.54	1.39	COTS
Teonex[18, 22]	PEN	susceptible	3.56	1.36	COTS

Membrane Coating

The reflective surface of the solar sail is made of a thin layer of metal. The metal is deposited onto the membrane via a physical vapor deposition (PVD) process. Fig. 2.4 compares the reflectance R of aluminium, copper, silver, gold[23] and lithium[24] in the optical spectrum. It can be seen that aluminium retains a high reflectance of more than 90 % well into the far ultraviolet range. Other metals experience a sharper drop in reflectance in the visible spectrum. Lithium, as the metal with the lowest density, is regarded by some as a future coating option[12, 25]. However, this would require additional coating, as well as handling and storage either in vacuum or an inert atmosphere because of lithium's strong reaction with oxygen. In all missions flown so far, the reflective coating was made of aluminium.

The thickness of the metal coating strongly affects the overall areal density of the solar sail and must therefore be as thin as possible. Kezerashvili investigated the minimum required thickness of metal coatings depending on the skin depth[26]. The method calculates the skin depth based on an approximation for a temperature and frequency dependent conductivity. Fig. 2.5 presents the skin depth of aluminium for wavelengths between $0.2\,\mu$m to $3\,\mu$m and temperatures in the range of 300 K to 600 K.

[1] At the time of writing, Kapton 12EN ($3\,\mu$m) is in pre-production. Samples of Kapton 12EN were made available to the author by DuPont de Nemours.

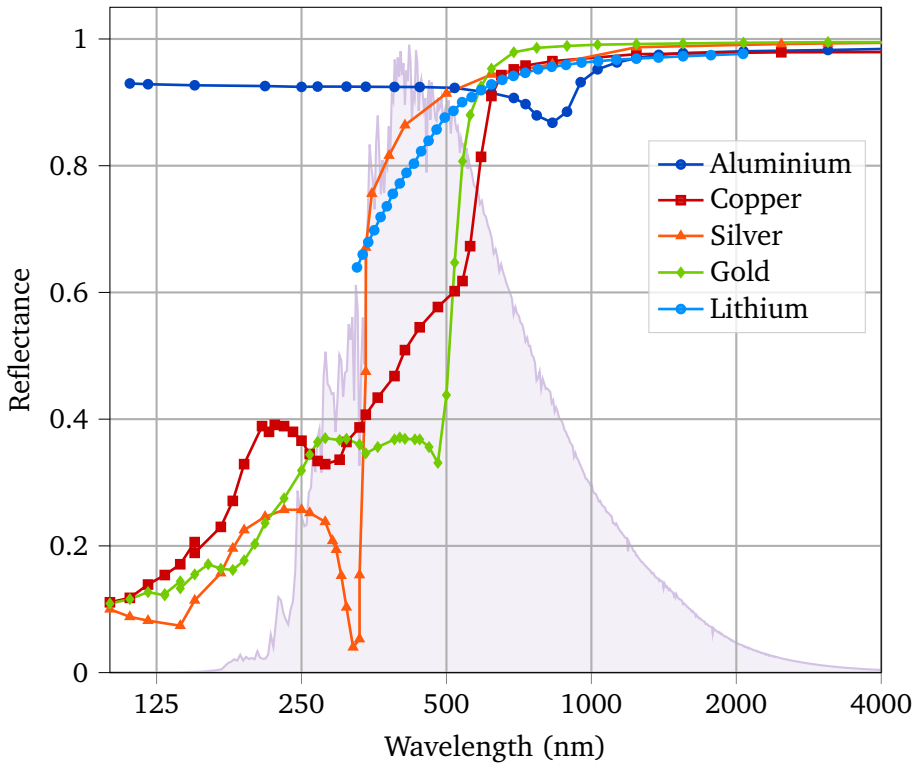

Figure 2.4: Spectral reflectance of aluminium, copper, silver, gold at perpendicular incidence. The AM0 spectrum is displayed qualitatively in the background.

The figure reveals only little frequency dependency of the skin depth for the visible and infrared light (IR) spectrum. In the UV spectrum, we can observe a dramatic increase of the skin depth with temperature and frequency. In the relevant temperature range (cf. 2.1.3) up until 600 K, this leads to a maximum skin depth of 42 nm at a wavelength of 200 nm and 600 K. Because the skin depth only denotes the distance after which the current decreased by $1/e$, the actual sheet thickness should be higher than the skin depth in order to provide maximum reflection. In fact, the typical thickness of the aluminum coating falls between 80 nm[15] and 100 nm[27].

Seefeldt researched potential coatings for solar sails[28]. He argues that while aluminium is able to resist atomic oxygen, it does not provide sufficient shielding against other types of radiation, namely UV and protons from solar wind. Seefeldt notes that for the aluminium to shield UV radiation with a wavelength of 30 nm, a sheet thickness of 1.5 μm would be required. This statement is in stark contrast to the calculations given by Kezerashvili, who merely focused on propulsion. Seefeldt also reports that a layered coating made from aluminium, silicon oxide, and titanium oxide can provide effective radiation shielding while retaining a reflectance of 87.5 %.

Many solar sail mission concepts involve close flybys to the sun, resulting in a high thermal load on the structure. A thin chromium layer on the backside of the sail can improve the infrared emissivity and help disspiate heat more effectively. Typically, this layer has a thickness between 15 nm to 30 nm[27]. However, missions such as Near Earth Asteriod Scout (NEA Scout), LightSail or IKAROS did not feature a chromium layer (cf. Section 2.2).

Deployables

Booms are used to deploy the solar sail when deployment via rotation is not desired or additional stiffness is required. A wide range of deployable structural elements have been developed in the past. A good overview of the technology is provided by Puig[29]. In solar sailing, the deployables and their mechanisms must be light-weight, as are the structures deployed by them. Therefore, shape memory or inflatable booms are the primary choice for this task. Shape memory booms are typically made from

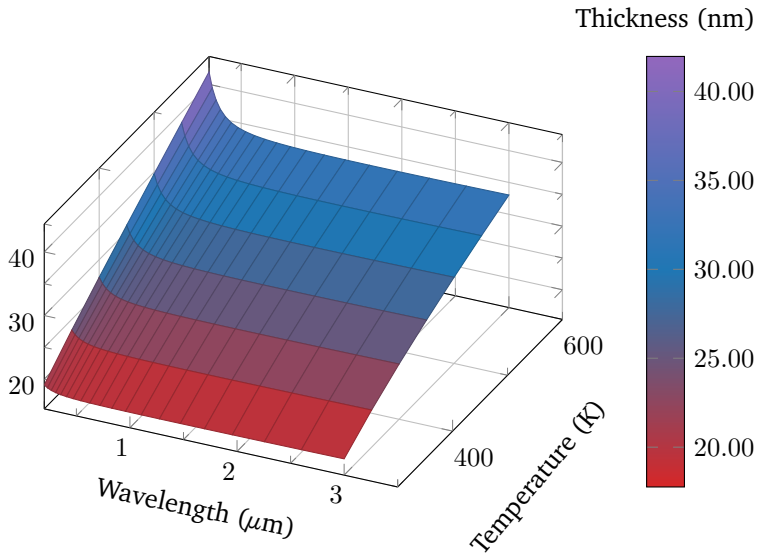

Figure 2.5: Frequency and temperature dependence of the aluminium thickness on wavelength and temperature. Recreated according to [26].

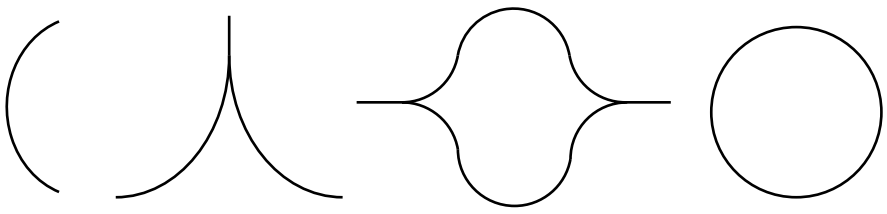

Figure 2.6: Boom types (left to right): C-Shape, TRAC, CTM, circular

either elgiloy or carbon fiber reinforced plastic (CFRP). Inflatable structures consist of thermoplastic laminates that are inflated and subsequently cured by the space environment[30]. In practice, only shape memory booms have been used on solar sailing missions.

We can reduce the boom structures to their lateral cross-sections, which define their potential load-bearing properties. The booms of the solar sail are available in several designs (cf. Fig. 2.6). C-shaped booms are the simplemost structure and were used on the InflateSail mission[31]. Composite booms with circular cross-section were tested by a group of L'Garde, National Aeronautics and Space Administration (NASA) Langley and Jet Propulsion Laboratory (JPL). These booms had a conical shape and were inflated during deployment[32].

triangular rollable and collapsible (TRAC) booms consist of two C-shaped profiles attached together at one edge. The resulting structure can be rolled up and stored on a drum. The profile has better stiffness and load-bearing capability than the C-shape and is easier to deploy than the circular shape. TRAC booms were used on the NanoSail-D and LightSail missions[14, 25], and were part of the defunct NEA Scout mission[14]. Hence, TRAC are the only boom type flown on actual solar sailing missions.

The remaining boom type is the collapsible tubular mast (CTM) boom. The CTM boom consists of two omega-shaped half-shells. This kind of boom can be flattened and coiled up on a drum. Through the spring force inherent to its shape, it automatically returns to the lenticular cross-section. Although CTM was the designated boom technology of DLR's Gossamer mission[33] and was also considered for NEA Scout[34], no CTM booms were flown so far.

2.1.4 Sail Deformations

Solar sails are subject to a number of deformations, resulting in a non-planar surface. We distinct three different kinds. Creases are plastic deformations of the membrane, created during the folding process. Wrinkles are elastic deformations of the membrane, caused e.g. by tensions on the membrane. Billowing is also an elastic deformation type and is a result of solar pressure.

The requirement for low mass and thus small packaging volumes of all deployables inevitably results in plastic deformations of the sail. Papa et al.[35] analytically studied the creases created by the Miura-ori folding pattern[36]. They found the crease amplitude in polyimide between 1.3 mm to 11.9 mm for a panel size of 100 mm and a tensioning force up 0.2 N. Note that the amplitude is subject to change depending on material properties, panel size and tensioning force.

Zou et al. studied the wrinkling behavior of triangular sail petals under increasing tensioning force. A simulation result of their analysis is shown in Figure 2.7[37]. The figure illustrates the non-planarity of the sail,depending on the tensioning force. Note that billowing and creases were not considered here. We can observe wrinkles spreading torwards the center of the sail and fading along the way. In the center of the sail, the effect has mostly died down, with wrinkles in the sub-millimeter range.

Billowing as an effect of solar radiation pressure was analyzed by Jordaan[16] in the case of a rotating circular sail. Figure 2.8 shows the sail's surface offset, depending on location and angular velocity. As expected, the rotation effects a tensioning of the sail and so, reduced billowing. The angular rates shown in this graphic are comparatively large and may be lower (down to non-rotating sails), with higher billowing. However, we can observe a plateau in the center of the sail, where the gradient is minimal.

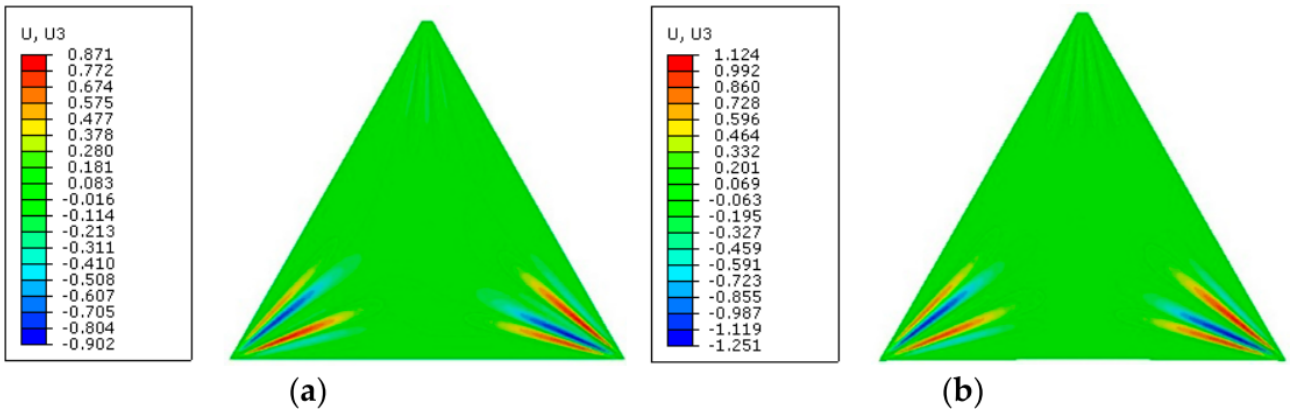

Figure 2.7: Simulation results of wrinkles on a triangular shaped petal with tensioning force 5 N (a) and 10 N (b). The force is applied to the lower left and right corners. The wrinkle amplitudes are given in mm. Reproduced from [37] under the terms of the CC BY license.

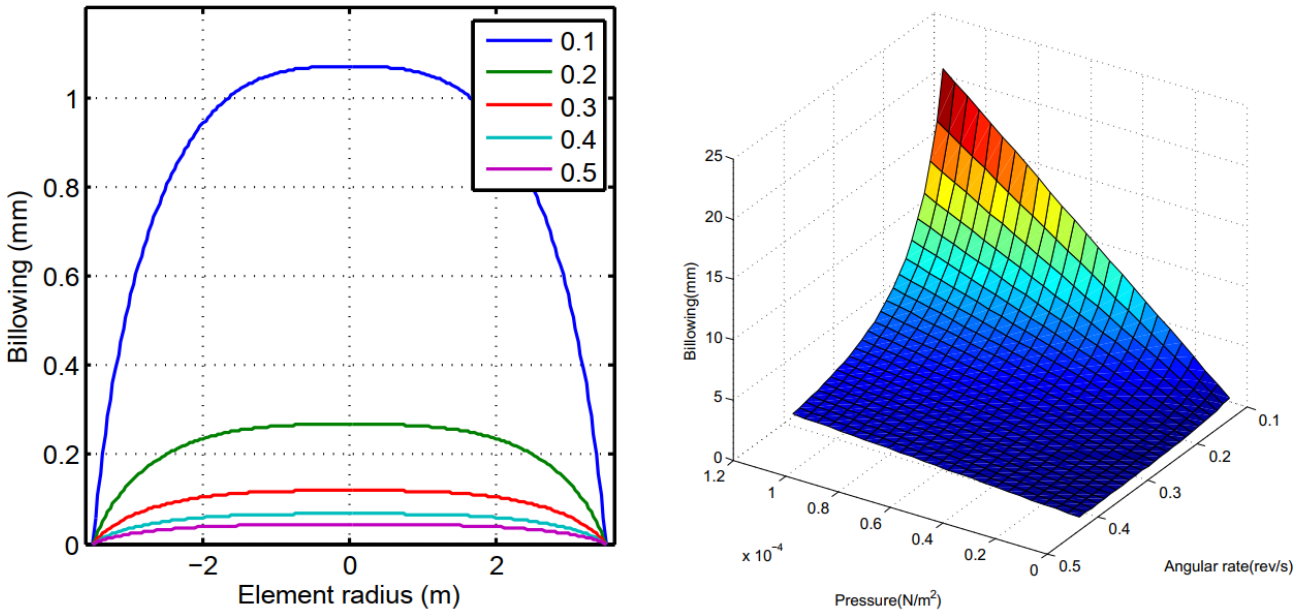

(a) 2-D cross section of the sail at different angular rates (rev/s)

(b) Maximum billowing of sail with increasing pressure and angular rate

Figure 2.8: Illustration of sail billowing[16]. Reproduced with permission.

2.2 Solar Sailing Missions and Campaigns

This section reviews recent and previous solar sailing missions with regard to their mission goals, sail design and deployment. Table 2.2 provides an overview of the missions discussed in this section.

Table 2.2: Summary of solar sailing small satellite missions.

Source	Organization	Name	Mission Goal	Launch Date
[38, 39]	NanoSail-D2	NASA	Demonstration	2010
[6, 7]	IKAROS	JAXA	Demonstration	2010
	The Planetary Society	Light Sail 1	Demonstration	2016
[40]	Surrey Space Centre	InflateSail	Demonstration	2017
[41]	The Planetary Society	Light Sail 2	Demonstration	2018
[42]	NASA	CubeSail	Demonstration	2018
[43]	NASA	NEA Scout	Demonstration	2022
[44]	NASA	ACS3	Demonstration	>2023

2.2.1 Sunjammer

Sunjammer was a NASA solar sailing mission in cooperation with L'Garde, with the goal to demonstrate solar sailing and to measure space weather closer to the sun[45]. The membrane intended for the solar sail would have had a total area of $1200\,\mathrm{m}^2$ and a total mass of $8.5\,\mathrm{kg}$. In 2005, a demonstration and deployment testing prototype with a sail area of $318\,\mathrm{m}^2$ was made from aluminized $5\,\mu\mathrm{m}$ Kapton. The solar sail demonstrator was the largest tested so far. The deployment of the solar sail was done using inflatiable conical composite booms[32, 45]. The project was cancelled by NASA at the end of 2014.

2.2.2 Gossamer-1

Gossamer-1 was a solar sailing demonstration mission by European Space Agency (ESA) and German Aerospace Center (DLR)[33]. The quadratic solar sail consisted of four foil triangular segments made of aluminized polyimide. The total area of the sail was $25\,\mathrm{m}^2$ and the thickness of the foil was $7.5\,\mu\mathrm{m}$. The sail was deployed by four CTM booms made of CFRP. The satellite bus had an estimated mass of $30\,\mathrm{kg}$. The sail featured an experimental thin film solar array. The official roadmap aimed to develop Gossamer-2 with a $25\,\mathrm{m}\times25\,\mathrm{m}$ sail and Gossamer-3 with a $50\,\mathrm{m}\times50\,\mathrm{m}$ sail. However due to budgetary reasons, the Gossamer-1 spacecraft was never launched to space.

2.2.3 NanoSail-D/2

NanoSail-D was a solar sailing mission by NASA[38]. The goals of the NanoSail-D mission was to demonstrate depolyment of the sail and to successfully de-orbit the spacecraft. The spacecraft was a 3U Cubesat, where 2U were occupied by the sail and deployment mechanism and 1U by the bus. The sail had a size of $10\,\mathrm{m}^2$. The membrane was made of Aluminium coated CP-1 polyimide with a thickness of $2\,\mu\mathrm{m}$[14]. The sail was deployed by TRAC elgiloy booms[14].

NanoSail-D was destroyed in 2008 when the SpaceX Falcon-1 rocket launch failed. Its sister satellite NanoSail-D2 was launched in November 2010. The satellite successfully deployed its sail and lost power shortly after[39].

2.2.4 IKAROS

IKAROS was a solar sailing mission by Japan Aerospace Exploration Agency (JAXA) and the first solar sailing mission in general. IKAROS was launched in May 2010 along with the JAXA Venus Climate Orbiter[15]. In December 2010, IKAROS made its closed approach to Venus at a reported distance of 80 800 km[7]. The mission ended in 2013.

The IKAROS spacecraft was a small satellite with a mass of 307 kg. The spacecraft had a quadratic sail with a diagonal of 20 m, resulting in a total area of 200 m^2. Of these 200 m^2, 173.6 m^2 were covered by the sail membrane[15]. The membrane was made of two polyimides, both with a thickness of 7.5 μm and covered with 80 nm of aluminium. The total mass of the sail assembly was 16 kg[14] of which the membrane accounts for 1.849 kg[15].

The spacecraft was designed as a spinner, which sets it apart from previous solar sailing designs. The spacecraft also used centrifugal force to deploy the sail. To maintain the sails shape, the petals are connected with stiffeners ("bridges"). The sail is connected to the spacecraft bus via 16 tethers and four wire harnesses.

Another unique characteristic of the IKAROS mission is the multifunctionality of the sail. The sail hosts thin film solar cells, dust counters and experimental reflection control surfaces. The solar cells covered 5% of the sail area, with a maximum power of almost 300 W[15]. The reflection control surfaces are liquid crystal sheets which can alter their optical properties from specular to diffuse reflection.

The communication antennas on the spacecraft were two low gain antennas with opening angles of approximately 120°. There are reports of signal strenght being an issue during operations around Venus[46].

The results of the IKAROS mission are described by Tsuda et al. in [7]. One of the mission's goals was to measure the orbital acceleration by the solar radiation pressure. The authors report a thrust of 1.12 mN at 1 AU measured using orbit determination. The total Δv gained over the course of 6 months was reported to be 100 m s^{-1}.

2.2.5 InflateSail

InflateSail was a mission by the Surrey Space Centre with the goal to demonstrate a drag sail deorbiting system[40]. While it was not a solar sailing mission, it is based on the same technological foundation. The InflateSail spacecraft was a 3U cubesat, with 2U allocated to the sail and deployment mechanism. The square sail had a size of 10 m^2 and was made of 12 μm thick PEN[40]. The sail was deployed by four C-shaped CFRP booms. The spacecraft was launched in a 380 km × 700 km orbit. The total duration of the mission was 72 days, after which it successfully deorbited[31].

2.2.6 Lightsail 2

LightSail 2 was the second solar sailing mission of the Planetary Society[41]. The spacecraft was launched in 2019 into a 720 km orbit. The mission aimed to demonstrate controlled solar sailing with a CubeSat. The spacecraft had a form factor of 3U, with 2U allocated to the sail and 1U for avionics. The square sail had a size of 5.6 m×5.6 m, 32 m^2 in total. The sail membrane was made of aluminized Mylar with a thickness of 4.6 μm. The sail was deployed using four TRAC elgiloy booms[25]. The mission demonstrated the solar propulsion principle with a variety of slew maneuvers, that successfully altered the spacecraft's orbit[25]. One TRAC boom has not deployed correctly[25].

2.2.7 Near Earth Asteriod Scout

The NEA Scout mission is the latest solar sailing mission of NASA[43]. The goal of this mission is to demonstrate the merit of small solar sailing probes in exploration. The small 6U Cubesat was launched

Figure 2.9: Deployed sail of Near Earth Asteriod Scout. Image source: NASA

on a lunar transfer orbit with Artemis-1 on November 16th 2022. The destination of NEA Scout was the Asteroid 199VG. However, communication with the probe was not successful and deployment of the sail could not be confirmed at the time of writing this thesis[47].

The technology of NEA Scout is based on the previous experience and technolgies of NanoSail-D and the Lightsail missions[48]. The NEA Scout spacecraft uses a 86 m^2 square solar sail made of aluminized CP-1 polyimide with a thickness of 2.5 μm. The sail is deployed by four TRAC elgiloy steel booms with a length of 6.8 m each. The total mass of the spacecraft is projected to be 12 kg, giving rise to an expected aerial density of 145 $g\,m^{-2}$[14]. This renders the NEA Scout spacecraft the lightest solar sailing spacecraft to date. NEA Scout communicates with an X-band 64-element patch antenna array with an approximate gain of 25 dBi[49]. Additionally, two low gain antennas are available as well.

2.2.8 ACS3

The Advanced Composite Solar Sail 3 (ACS3) spacecraft is the most recent solar sailing mission of NASA[44]. The goal of this mission is to “(...) demonstrate NASA deployable composite boom technology in a solar sailing application in the LEO space environment”[44]. To this end, the ACS3 spacecraft will be delivered to a low-earth orbit (LEO) orbit between 700 km to 900 km. After deployment, the spacecraft will spend a total of 60 days raising and lowering its orbit. The expected raising rate is 2 $km\,d^{-1}$ and the lowering rate will be 7 $km\,d^{-1}$.

This will be achieved by the square solar sail, which has a total size of 9.9 m × 9.9 m, and a total sail area of 80 m^2. The sail membrane consists of 2.0 μm PEN with a reflective 100 nm aluminium layer and 15 nm chromium on the backside. Wilkie states that this choice was made because of the availability of wide and thin PEN swaths, as well as the low mission duration[44]. The metalized PEN swaths with a width of 0.75 m are bonded together using a "polyester melt-adhesive technique"[44], forming a sail petal (cf. Fig 2.10). The bonding process provides additional strength, replacing along this axis. Additional strength is given by a Kevlar lining in each seam.

The solar sail consists of four petals, deployed by four CFRP CTM booms. This choice was made as NASA found TRAC booms to provide insufficient torsional stiffness at larger boom lengths[44]. The booms will be deployed by "tape-puller" concept, developed by DLR. For deployment, this mechanism pulls on a metal tape that was rolled up together with the boom. Each boom has a length of 7 m and a mass of 164 g[50].

Wilkie notes that “the ACS3 solar sail system is an approximately 40 % sub-scale version of a future composite solar sail system sized for near-term CubeSat class deep space solar sail missions”[44].

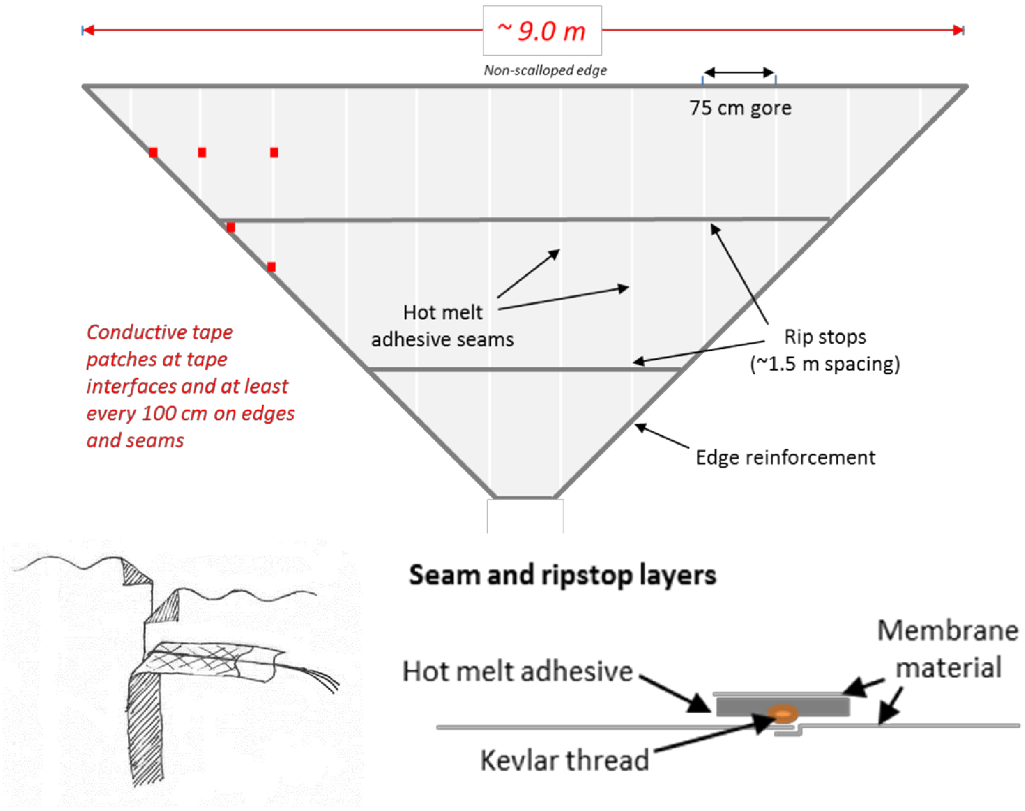

Figure 2.10: ACS3 solar sail design and seam configuration[44].

2.2.9 Mission Concepts and Trajectories

The strength of solar sails is the lack of propellant, allowing for missions beyond what is feasible with rocketry. Several advanced concepts that exploit the strength of solar sailing have been proposed in the past.

Mewaldt and Liewer proposed an interstellar probe that travel beyond the heliopause (200 AU) in 15 years[5]. The spacecraft projected for this mission had a mass of 150 kg and the hexagonal sail a projected area of about $1 \times 10^5\,\mathrm{m}^2$. This gives the spacecraft a theoretical $\sigma = 1.5\,\mathrm{g\,m}^{-2}$ and allows it to accelerate a exit velocity of 15 AU/a. An interesting aspect of this mission concept was the 2.7 m dish antenna in the center of the sail, which served as primary structural element.

In their 2006 paper, MacDonald and Hughes studied a potential solar polar orbiter[2]. In the mission concept, a 153 m × 153 m sail allows the probe to increase the inclination to 90° while lowering to a circular 0.48 AU orbit. The authors planned with a wet mass, including a generous margin, of 533 kg.

Dachwald performed a theoretical analysis of minimum flight times required to reach the outer planets via solar sail[1]. The investigated trajectories included several flybys of the sun at low distance. Given the low distance, Dachwald included a thermal limit of 240 °C. Given this limit, he found that a neptune flyby would be possible with a mission duration of less than 10 years, given a characteristic acceleration of better than $0.5\,\mathrm{mm\,s}^{-2}$. Enduring hotter surface temperatures can have a significant effect on the mission duration required and so, can justify heavier sail materials.

2.3 Light-weight Antennas

We now turn to several existing concepts and proven designs for small satellite antennas either with the goal of large apertures or light-weight design. First, we discuss reflector antennas. Subsequently antenna concepts and designs including sails or membranes are discussed.

Table 2.3: Summary of performance parameters of solar sailing campaigns. The calculated parameters are taken from [14] unless indicated otherwise by an asterisk (*).

Mission	σ_s ($\mathrm{g\,m^{-2}}$)	σ ($\mathrm{g\,m^{-2}}$)	a_c ($\mathrm{mm\,s^{-2}}$)	λ
IKAROS	77	1566	5.8×10^{-3}	9.8×10^{-4}
NanoSail-D2	135	400	2.3×10^{-2}	3.8×10^{-3}
LightSail 1	15	154	5.9×10^{-2}	9.9×10^{-3}
LightSail 2	15	156	5.8×10^{-2}	9.8×10^{-3}
InflateSail	140	320	2.9×10^{-2}	4.8×10^{-3}
NEA Scout	43	145	6.3×10^{-2}	1.1×10^{-2}
ACS3*	45	188	4.9×10^{-2}	8.3×10^{-3}
Interstellar probe[5]*	-	1.5	6.1	1.0
Solar Polar Orbiter[2]*	8.5	22.7	0.40	6.8×10^{-2}
Asteroid Miner[4]*	-	15	0.6	0.1

2.3.1 Reflector-Based Antennas

Research on high-gain CubeSat antennas currently focusses on three types of reflector: inflatable, parabolic and reflectarrays. These antennas always provide their own structure and are therefore only interesting as object of comparison.

Fresnel Zone Antennas Fresnel zone antennas are aperture antennas, where the aperture is divided into individual zones of reflecting or non-reflecting surfaces[51]. The individual zones are constructed such that when incident radiation is observed from a feed point, its phase falls within a $\pm\pi/2$ range and interferes constructively[51]. Generally, these antennas can be made in any shape, but most often, they are designed as planar surfaces with circular zones (see Figure 2.11). The idea for using Fresnel zone antennas dates back to the 19th century[52], whereas their application to spacecraft communications was introduced by Malliot in 1994[53].

Research by Khayatian et al. from 2001 to 2004 led to a number of simulated Fresnel zone antennas for solar sails[8, 54, 55]. The published designs were X-band Fresnel antennas for the deep space X-band at 8.4 GHz. The authors showed simulation results for reflectors of 4 m and 10 m size. Both concepts included a reflector separated by $\lambda/4$ from the sail surface to increase efficiency. The simulated aperture efficiency ranged from approximately 40% to 44%[8]. The authors later published X-band dual-band antenna designs, with similar performance as the previous designs[8, 55].

There are some downsides to Fresnel zone antennas and aperture antennas in general in this application. Aperture antennas require an additional feed at a certain focal distance. This distance depends on the antenna's diameter, meaning that the antenna choice strongly influences the spacecraft and mission design. Only single-layered phase-correcting Fresnel zone antennas are viable with solar sails. However, their theoretical efficiency is restricted to 40.5 %[51].

Parabolic Reflector Deployable parabolic reflectors for CubeSats are developed by a group at JPL [56–58]. The most recent antenna can be stored in a volume of 1.5U and unfolds to a 0.5 m Cassegrain reflector dish. The antenna is designed for Ka-band and is by principle of operation very broad band, as the bandwidth mostly depends on the feed. The antenna reaches a gain of approximately 42.6 dBi at 35.75 GHz, which corresponds to an aperture efficiency of 52%. The antenna has a mass of 2.1 kg.

The antenna is used on the RainCube mission, which demostrates the use of radar on a CubeSat to profile the precipitation on earth[58]. A rendering of the RainCube satellite with deployed dish antenna is found in Figure 2.12.

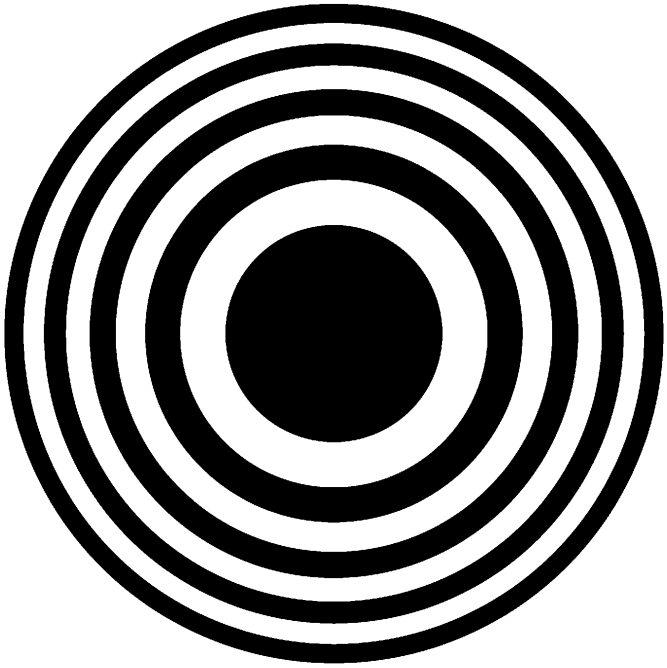

Figure 2.11: Illustration of a circular Fresnel zone plate.

Inflatable Reflector Inflatable antennas were developed by Babuscia et al.[59–61]. A schematic of such a reflector is illustrated in Figure 2.13. The inflatable reflector is a gas filled balloon made of Mylar. Half of the balloon is transparent to microwave radiation, and the other half is covered with a reflective metallization layer. The most recent prototype of the antenna reached a directivity of 24.2 dBi and gain of 19.4 dBi in X-band[61], which corresponds to an aperture efficiency of 4%. The antenna concept reportedly suffers from deflation issues due to leakage and micrometeorite impacts.

MarCO Reflectarray The reflectarray for the Mars Cube One (MarCO) mission was developed by NASA's JPL[62]. Figure 2.14 shows a picture of a MarCO satellite with deployed reflectarray. Additional to the large gain needed to cover a link over the distance of more than 1 AU, the technical challenges of the development were reducing stowage volume, cost and mass. Traditional antenna designs like parabolic reflector antennas or microstrip patch arrays were not able to handle the unique requirements of the mission profile. The mission required the spacecraft to have a 23 degree angle between earth and the pointing angle of the antenna.

The resulting design is a folded-panel reflectarray antenna. This antenna type consists of a two components. A 4x2 microstrip patch antenna array operates as feed. The second component is a surface consisting of microstrip patches that shift the phase incident wave front to create a planar wave front in the desired direction. This reflectarray has an effective aperture of 857 cm^2 and reaches a gain of 29 dBi in X-band. The mass of the antenna is reported as less than 1 kg.

2.3.2 Membrane Antennas

The development of large antenna structures with low mass was mainly driven by synthetic aperture radar (SAR) applications. Starting in the 1990's, different groups worked on subproblems of large membrane antennas for SAR purposes. Research by DLR and Kaiser Threde on deploying large membrane structures showed how to deploy such membrane sails[63].

Starting out in 1998, researchers from the California Insititue of Technology worked on integrating antennas on membrane structures for L-band and X-band. Different designs were evaluated, the first

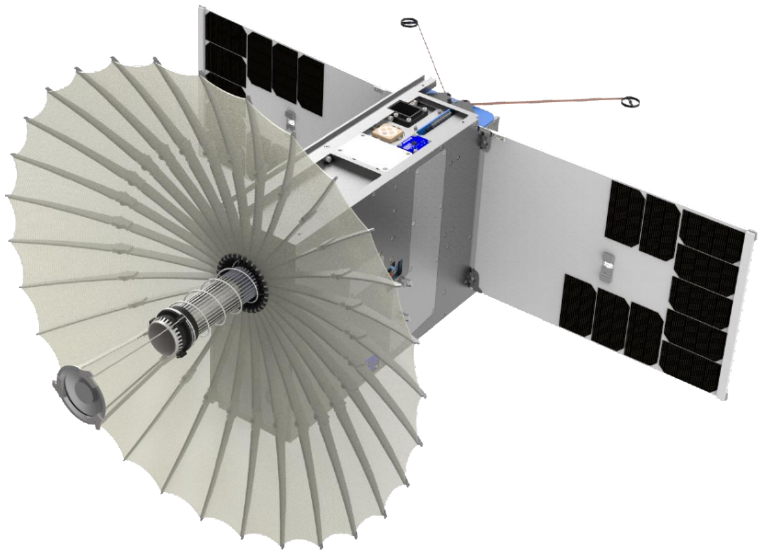

Figure 2.12: RainCube satellite with deployed 0.5m dish antenna. Image Credit: NASA/JPL-Caltech

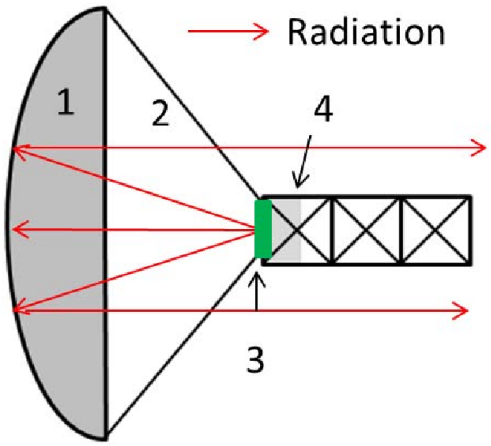

Figure 2.13: Schematic of the inflatable reflector antenna[61]. The numbers indicate the reflector (1), the transparent side (2), the patch antenna feed (3), and the volume occupied in the CubeSat (4). ©2016 IEEE

one being a 3x10 L-band microstrip patch array. Huang et al. report a very good aperture efficiency of 52 % and a bandwidth of 80 MHz[64]. The antenna was build on a 0.254 μm thick Kevlar membrane, and the prototype had a total mass of 9 kg. The researchers prospect a final average mass of 1.7 kg m^{-2}.

Huang et. al also evaluated a 1-m X-band reflectarray on 0.05 mm Kapton[65]. The produced prototype had a 37 % aperture efficiency, which the authors argue to be due to manufacturing inexperience. The authors noted an expected aperture efficiency of 50 % with proper manufacturing. Other designs by Huang et al. for SAR applications are aperture-coupled microstrip patches[66–69]. The reported antennas were manufactured on 50 μm Kapton substrate. The reported bandwidth of these antennas is 100 MHz. These antennas could theoretically be used for large aperture sizes but are very three-dimensional and require additional structures.

Lichodziejewski et. al published a 2.2 m × 1.1 m slotted waveguide antenna for L-band[70, 71]. The antenna was manufactured with 0.01 mm thick Kapton membranes. The antenna consisted of eight waveguides with 13 slots each. The waveguides were fed by a microstrip divider network that was separated from the membrane via a foam substrate. The achieved gain was about 23 dBi and the total mass was reported as 56.7 kg. Compared to simulations, the gain was about 6.1 dB lower, which the authors attribute to conductive losses due to the low metallization of less than one skin depth[72].

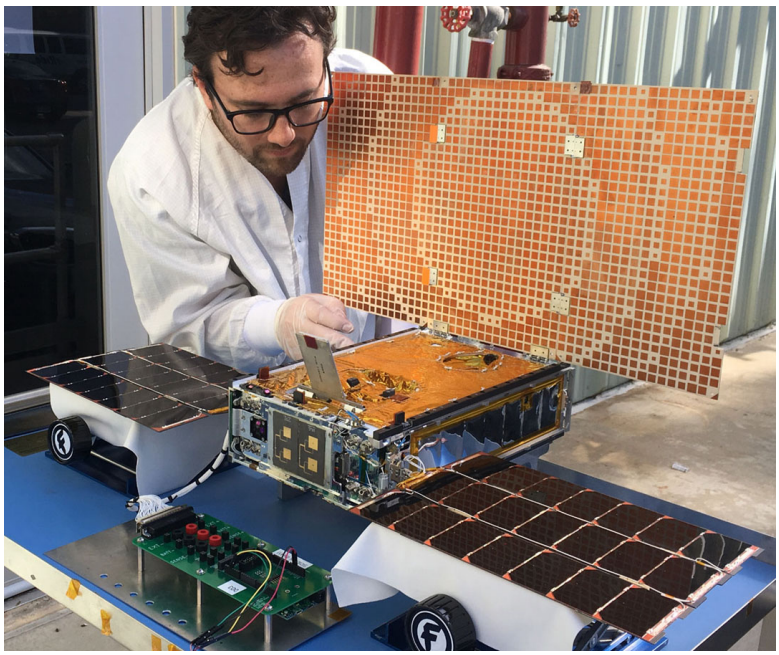

Figure 2.14: MarCO satellite with deployed reflectarray. Image Credit: NASA/JPL-Caltech.

Table 2.4: Allocated frequency bands for deep space communications[73].

Designation	Deep Space Bands (>2 Mm from Earth)		Near Earth Bands (≤2 Mm from Earth)	
	Uplink (MHz)	Downlink (MHz)	Uplink (MHz)	Downlink (MHz)
S-band	2110 – 2120*	2290–2300	2025–2110	2200–2290
X-band	7145–7190	8400–8450	7190–7235	8450–8500
K-band			22500-27000	
Ka-band	34200–34700	31800–32300		

2.4 Deep-Space Communications

For the requirements derivation we briefly review allocated frequency bands, bandwidths and ground station options.

2.4.1 Deep-Space Frequency Bands

Deep space communication takes place in the frequency bands allocated by the International Telecommunications Union (ITU) (cf. Tab. 2.4). For the purpose of this analysis, the frequency bands for space stations more than 2 Mm from Earth are of interest. In this category, the allocations are as follows[73]: In S-band, a bandwidth of 10 MHz is available for each uplink (UL) and downlink (DL), with a channel spacing of 341.049 kHz/370.370 kHz (UL/DL). In X-band, 45 MHz are allocated for uplink and 50 MHz for downlink, with a channel spacing of 1.156 MHz/1.358 MHz. In Ka-band, 500 MHz are allocated both for UL and DL, with a channel spacing of 5.554 MHz/5.18 MHz. The low bandwidth available reflects the power restricted nature of deep space radio links.

S-band is used for telemetry and telecommand (TM/TC) because of legacy reasons, its low susceptibility to tropospheric effects. X-band is the legacy high data rate band, but in the future, the Ka-band may take over this task.

Figure 2.15: Malargüe Station Deep Space Communications Antenna. (© ESA/D. Pazos - CC BY-SA IGO 3.0)

2.4.2 Ground Station Networks

In this scope, it is sufficient to study the European Space Tracking (ESTRACK) (ESA) and Deep Space Network (DSN) (NASA) networks.

Both networks comprise earth stations in America, Europe and Australia. The locations for these stations are chosen such that ideally, their longitudinal separation is about 120°. The antennas in DSN or ESTRACK are large dish antennas (see Fig. 2.15), with 34 m to 70 m diameter. The smaller 34 m and 35 m antennas at one locataion can be arrayed together, giving them similar performance as one 70 m dish. The feeds of the dish antennas are circular polarized. An overview of the performance characteristics of DSN and ESTRACK antennas can be found in Table 2.

Chapter 3

Gap Analysis

Having discussed the fundamentals and state of the art of solar sailing technology, we now turn to the analysis of the research gaps that will be subject of this thesis. First we will identify the research gaps in Section 3.1. The following Section 3.2 presents the requirements for the researched antenna concepts. Afterwards, Section 3.3 will discuss the objectives of this research.

3.1 Gap Identification

In the previous chapter presented the fact that improved lightness is crucial to the success of solar sailing as a technology. In order to achieve even the most daring mission designs, the characteristic acceleration of solar sailing spacecraft must increase by one to two orders of magnitude (cf. Tab 2.3). In the future, this will lead to larger and lighter membrane assemblies, in order to offset the invariably massive payloads.

Lightness is also an important topic in antenna engineering, as regular satellite missions are typically mass- and volume-constrained as well. In Section 2.3, examples of light-weight antennas were presented. Some of which were designed to be relatively light-weight, but with the large aperture requirements of SAR in mind and sturdy structure. Other antennas, like the RainCube dish antenna, were designed to be small in volume, so that they could fit inside a CubeSat but could also provide a substantial aperture. The ideal antenna for solar sailing combines the properties of both types and is light-weight, foldable but provides a comparatively large gain.

For a comparison of the previously presented antennas, their key parameters are listed in Table 3.1. The table lists volume, mass, effective aperture size and aperture efficiency A_e, and aperture areal density ϱ_a. The ϱ_a figure is based on the definition of σ_s and used in this work to obtain a combined figure for antenna performance and lightness. It is given as:

$$\varrho_a = \frac{m}{A_e} = m\frac{4\pi}{G\lambda^2} \tag{3.1}$$

Table 3.1: Comparison of lightweight satellite antenna properties. Projected values are marked with an asterisk (*)

Source	Year	V (cm³)	M (kg)	A_e (m²)	ϱ_a(kg/m²)
[64]	1998	–	15	1.5	9.9
[65]	1999	–	1.2	0.24	4.9
[8]	2002	–	* 0.48	6.2	* 0.078
[61]	2016	500	0.5	0.009	56.6
[57]	2016	1500	2.1	0.10	20.6
[62]	2017	833	1	0.08	13.2

where m is the antenna mass, A_e is the antenna effective aperture. The effective aperture is a non-physical property of aperture antennas, such as reflector antennas, horns or slots and does not necessarily correspond to the antenna's physical expansion. It is derived from the antenna gain G and the free-space wavelength λ, resulting in figure that is, within a limits of physical implementation, not dependent on frequency. Therefore, this is the ideal figure of merit for comparing the antennas in this work.

The table reveals that the reflectarray antennas from [64] and [65] are among the most efficient in terms of ϱ_a. The membrane-integrated Fresnel zone antenna from [8] is a special item in this table, as no real prototype was ever built. However, this was the only antenna concept designed for solar sailing and has the best ϱ_A value[1]. Integrating antennas within the solar sailing architecture offers notable advantages. However, the Fresnel zone reflector presents a challenge due to its requisite focal length, comparable to the antenna's diameter. Employing the Fresnel zone reflector necessitates either relocating the feedpoint away from the sail, leading to considerable occlusion and added mass, or shifting the entire spacecraft bus, which is not ideal given that current solar sailing missions position the spacecraft bus proximate to the sail's center. Thus, the antenna subsystem would have profound implications on the system's overall design, encompassing both deployment and attitude control.

The presented research leaves two paths untouched, which constitute two research gaps:

Research Gap 1 *Antenna array integrated into the solar sail's membrane*

An antenna array integrated into the solar sail's membrane has not yet been researched. As the radiating elements of the antenna are part of the reflective layer, this concept requires no focal distance and is compatible with the designs of recent solar sailing systems. At the same time, it reuses the existing membrane and metal coating for structural integrity and signal conduction. Therefore, this concept is expected to offer mass reduction with comparatively moderate impact on the overall system's complexity and component coupling.

Research Gap 2 *Antenna array integrated into the solar sail deployables*

Beyond the membrane, the solar sail design can incorporate deployable structures. When considering circular and CTM booms, these deployables exhibit a closed surface. Such conductive, closed surfaces have the capability to propagate electromagnetic waves. Introducing radiation-emitting slots into this conductive surface transforms the waveguide into an antenna. As CTM booms are typically manufactured from carbon fiber composites, the surface will be conductive. This innovative perspective, particularly in the context of CTM booms, remains untouched in current research.

3.2 Requirements and Design Goals

For the antenna designs to be viable within the framework of solar sailing, they must meet the criteria outlined below.

Requirement 1 (Integration) *The antenna shall integrate into the existing solar sailing structure so that the original function is preserved.*

Rationale: This integration requirement ensures that the introduction of the antenna does not compromise or alter the original functions of the solar sail structure, which would void the original purpose of the antenna integration. However, this requirement deliberately omits consideration of the antenna's impact on system performance, as such considerations are too specific to implementation and thus beyond the scope of this thesis.

[1]The mass and aperture areal density estimate of the Fresnel zone reflector assumes a 3.5 μm Kapton membrane with 2.7 μm aluminium on the reflective sections, with a aperture coverage of 50 %. Additional assembly not included.

Requirement 2 (Modifications) *The modifications required to create the antenna shall not affect the procedures of the solar sail assembly, such as stowage, folding and deployment.*

Rationale: Introducing the modifications inevitably results in altered characteristics of the system. This requirement aims to constrain the wide range of potential modifications, so that they are kept to a minimum. By reducing the required modifications and deviations from standard solar sail designs and procedures, the practicality of the integrated antenna and it's real-world adoption potential are increased. The modifications may however result in different structural parameters.

Requirement 3 (Frequency Band) *The antennas shall operate in the deep-space X-band frequency bands.*

Rationale: In the future, the role of higher frequency bands will play a even more prominent role in deep-space communications. With this in mind, the X-band is a reasonable target frequency because it offers higher gain at smaller apertures than the S-band. At the same time, compared to Ka-band, the band is more accessible and more lenient tolerance requirements.

Requirement 4 (Polarization) *The antenna should be circularly polarized.*

Rationale: Circular polarization introduces a degree of attitude invariance, and allows continuous communication even if the spacecraft is rotating. This polarization is used by DSN and ESTRACK antennas, therefore using circular polarization minimizes the polarization loss.

Design Goal 1 (Aperture Areal Density) *The aperture areal density of the antenna shall be lower than* $0.5\,\mathrm{kg\,m^{-2}}$.

Rationale: The structure-integrated antenna are accompanied by a certain degree of cohesion between initially decoupled subsystems and therefore increased overall system complexity. To offset this detriment, an improvement of the aperture areal density by at least one order of magnitude is reasonable.

Design Goal 2 (Effective Aperture) *The effective aperture should be at least* $0.1\,\mathrm{m^2}$ *(equivalent to a gain of* $\geq$30 dBi *at* 8.4 GHz*).*

Rationale: The antenna will be designed to operate in a deep-space context, with vast separation between potentially involving vast distances to the communication link partners. In order to provide a viable alternative to more conventional antenna designs, the performance should be equivalent to state-of-the-art CubeSat antennas.

3.3 Objectives

This section introduces the objectives of this thesis based on the previously presented overall goal (Section 1.2) and the previous gap identification (Section 3.1).

The following key challenges arise at this point:

Objective 1 *Assess microwave technology with regard to their applicability to membrane antennas.*

Objective 2 *Design and build the microwave structures required for a membrane antenna array.*

Objective 3 *Investigate manufacturing processes for the membrane antenna.*

Objective 4 *Analyze the performance limits of the membrane antenna array.*

For the membrane antenna array, the focus is on the exploration and development of microwave technology suited to this structure. First, we will evaluate various microwave technologies to discern their suitability for integration with membrane antennas. This will be followed by the actual design and construction of the necessary microwave structures tailored for a membrane antenna array. Parallel to this, an in-depth study will be carried out to identify a manufacturing process for the membrane antenna. The culmination of this segment will involve a analysis of the performance capabilities and limits of the finalized membrane antenna array.

Objective 5 *Investigate the properties of CTM booms as slotted waveguide arrays.*

Objective 6 *Analyze the mechanical effects of the slotted CTM waveguide antenna.*

Objective 7 *Demonstrate feeding mechanism of CFRP CTM waveguides.*

With regard to the use as waveguide, let alone as slotted waveguide antenna, CTM structures are a blank page. Objective 5 will therefore be comprehensive study to explore the inherent properties of CTM booms when they are conceptualized as waveguides and ultimately as slotted waveguide arrays. Understanding the waveguide propagation modes and radiation characteristics of the slotted boom are cruicial to deciding on the suitability of this technology. Subsequent to this, the research will transition into a detailed analysis of the mechanical implications posed by the slotted CTM waveguide antenna. Objective 6 is essential to investigating how these slots, while required for microwave radiation, might influence the structural integrity of the CTM boom. In the final phase of this segment, the measurement of a pure CFRP waveguide will demonstrate the feasibility feeding a CTM waveguide via mode adapters and allow to determine the waveguide attenuation.

Chapter 4

Membrane Antenna

This chapter will discuss the concept of a planar antenna array integrated into the reflective metal layer on the sail membrane. The investigation of this concept begins with an analysis of suitable antenna types and their placement on the membrane in Section 4.1. Afterwards in 4.2, we evaluate suitable transmission line technologies, for the antenna array. Subsequently, Section 4.3 discusses the design of the array elements. Next, a power divider is presented in Section 4.4. Two advanced design that utilize multiple antennas or power dividers are discussed in Section 4.5. In the following Section 4.6, we discuss the results of different manufacturing trials on membrane material. Section 4.7 presents a theoretical evaluation of the potential mass and size of the membrane antenna array. Section 4.8 gives and outlook on future additions and modifications to the antenna array. Finally, this chapter is concluded in Section 4.9.

4.1 Introduction

The design of an array begins with the radiating elements, as many significant properties (e.g. polarization, beam width, beam direction) are inherited by the array. The beam direction is a good starting point for the analysis, since the antennas may not radiate into the sail and so, it affects element placing. In terms of beam direction, we can loosely distinguish between two groups: broadside and end-fire radiating antennas[74].

The group of broadside radiating antennas have their maximum of radiation perpendicular to the antenna plane. Broadside radiating antennas are, in case no reflector is present, bidirectional. Broadside antennas can also be circularly polarized, especially if the elements radiate circular polarization (CP) to begin with. This type of antenna can be placed virtually anywhere on the sail's surface, as long as the surface is not significantly creased.

End-fire antennas have their maximum of radiation parallel to the plane of the array. In general, end-fire antennas are unidirectional and the elements tendentially have higher gain than broadside radiating elements. CP is possible with end-fire antennas, however this is only true for non-planar designs. This type of antenna can only be placed on the outer edge of the sail. Compared to broadside radiating arrays, the directivity of end-fire arrays is twice as high[74].

We can see that choosing end-fire or broadside strongly impacts significant array properties. The lack of CP in planar end-fire antennas is a grave disadvantage, but this concept also allows for antenna elements with higher gain, which may make up for this drawback in some situations. Nevertheless, another serious disadvantage reveals itself when considering rotating sailcraft. A solar sail in the same ecliptic as earth will produce severe signal fading as the sail can never be oriented towards earth for long. Hence, we consider end-fire antennas not a viable option for this concept.

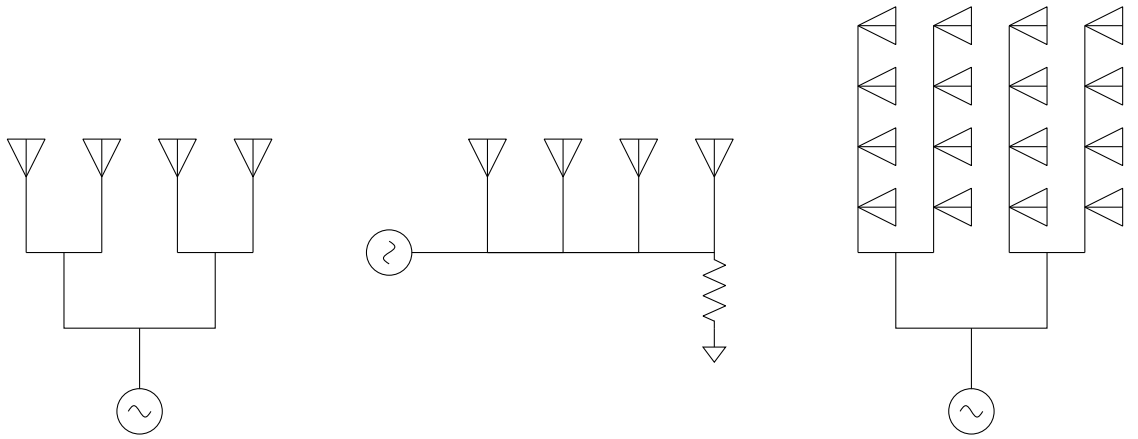

Figure 4.1: Illustration of the corporate feed (left), series feed (middle) and series-corporate feed (right).

4.1.1 Feeding an Array

Continuing with the broadside array, we now turn to the feed network of such an antenna. The elements of broadside antennas are excited with the same phase or a phase difference of integer multiples of 2π. If the elements are also excited with the same magnitude, we speak of a uniform array.

The basic building blocks for an array are displayed in Fig. 4.1. A corporate feed realizes same-phase excitation whereas a series feed works with progressive phase that depends on βd. A combination of both is the series-corporate feed.

The corporate feed can produce any geometry of planar 2D array, with the limitations being purely of geometric nature, i.e., the feed line width and element spacing (we can see this issue in Fig. 4.2). If the separation between the radiating elements is too small to fit a feedline, an arrangement where the feed sits on the side of the elements is possible. The vertically stacked elements will produce a fan-like shape in the radiation pattern. Since all elements are excited with the same phase, the feedline length to each element is the same and grows proportional to the number of elements in the array.

The series feed is a chain of elements connected to eachother by a strip of transmission line of constant length, resulting in a constant phase offset. The phase offset can be used to angle the main lobe and influence the side-lobe magnitude. For broadside radiation, the elements are spaced by $\beta d = 2\pi = \lambda_g$. Uniform excitation is achieved by adjusting the coupling of each element, e.g. by varying their shape. The series feed produces a linear array, which naturally leads to a fan-like shape of the radiation pattern. The series feed is difficult to design for larger numbers of elements and examples with more than ten elements are rare.

The synthesis of both types, the series-corporate feed combines the advantages. It allows for a two-dimensional, arrangementof the radiating elements, even if the array is one-layered and no space for feedlines is available between the elements.

In conclusion, both corporate-feed and series-corporate feed can produce significant gain in two planes. For larger arrays, the growing line lengths of corporate feeds can accrue substantial losses. To a certain degree, the series-corporate feed can add additional gain without this issue. In order to make an informed statement the losses and achievable maximum gain, a careful choice of transmission line (TL) and antenna elements is required.

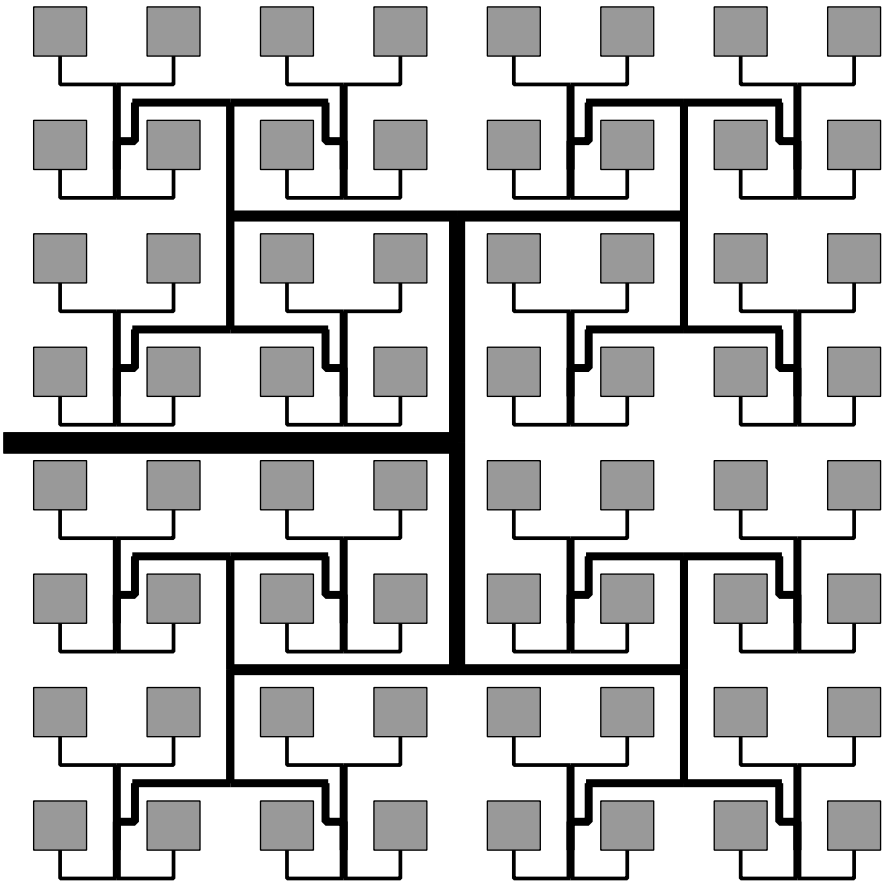

Figure 4.2: Illustration of a parallel, uniform antenna array in the form of the very common microstrip patch array. The shown array features 64 patches, which are drawn as gray rectangles, connected by the feedlines drawn in black. The required ground plane is not shown. This design is a popular choice, as it appeals through simplicity, ease of manufacturing and high gain.

4.2 Transmission Line Analysis

In the following analysis we will derive suitable technologies for the membrane antenna array. The thin membrane imposes a unusual constraint on the microwave circuits and antennas. These constraints require a closer inspection of all available microwave technologies and their applicability to this problem.

The selection of appropriate TL is the key element of the design of the antenna. On the one hand, that is because the structure of the sail, the thicknesses of metal layer and membrane directly influence the electrical properties of the TL. On the other hand, the theoretical size of the antenna array, in terms of geometric expansion and also number of elements, is limited by the losses involved with signal conduction and division. The power transfered in a TL decreases exponentially along the direction of travel due to attenuation by resistance, dielectric losses and radiation leakage.

An ideal TL candidate offers low losses, while also minimizing the required modifications to the sail structure. Such being the case, we limit the search space for a suitable technology to the area of planar TL. Figure 4.3 presents an ontology of planar TL that adhere to the three-layered structure of solar sail membranes. The planar TL are be divided into four groups, based on their physical structure.

The first group uses coplanar metal strips and planes on one metal layer. This group is attractive because only one metal layer means a lower impact on the mass budget and generally a comparatively low manufacturing complexity. Representatives of this group are coplanar lines and waveguides, and slotlines.

The second group uses an additional ground plane on the opposite side of the dielectric. This group comprises microstrip lines and grounded coplanar lines. While microstrips only use one ground plane, grounded coplanar waveguides use two metal layers. This severely impacts the mass of this type, but brings the additional problem of disconnected potentials. Typically, this is solved with vertical interconnect access (vias).

The third group is the substrate-integrated waveguide (SIW), which utilizes two metal planes. This type of waveguide requires no surface modification except via connections, which can be seen as an advantage for manufacturing complexity.

The last group is formed by the single conductor waveguides, which, like the first group, use only one metal layer. The difference is that only one metal line is required. This type extends the advantages of coplanar lines with the advantage that only one potential needs to be maintained.

In the following, we will discuss the geometry, characteristics and losses of the various TL in more detail. A preliminary analysis of the coplanar waveguide (CPW) and spoof surface plasmon polariton (SSPP) was published in [75].

4.2.1 Classical Transmission Lines

Coplanar Waveguide and Strips

CPW, coplanar strips (CPS) are two of the main constituents of the group of coplanar transmission lines, the third being the slotline. Their geometries are presented in Fig 4.4. The CPW consist of two disjunct ground planes and the main line in the middle. The metal structure is mechanically supported by a dielectric layer. We can observe that CPS are complementary to CPW in the sense that the metal and gaps are exchanged.

The CPW supports two propagating modes, the even mode and the odd mode. The even mode is the main mode that propagates a quasi-transversal eletromagnetic (TEM) wave. The odd mode, also called slotline mode, is excited when the two ground planes have a difference in potential and is generally considered parasitic. The potentials between both ground planes may diverge for various reasons (e.g. manufacturing inaccuracies, bends, discontinuities,...). A usual technique to remedy

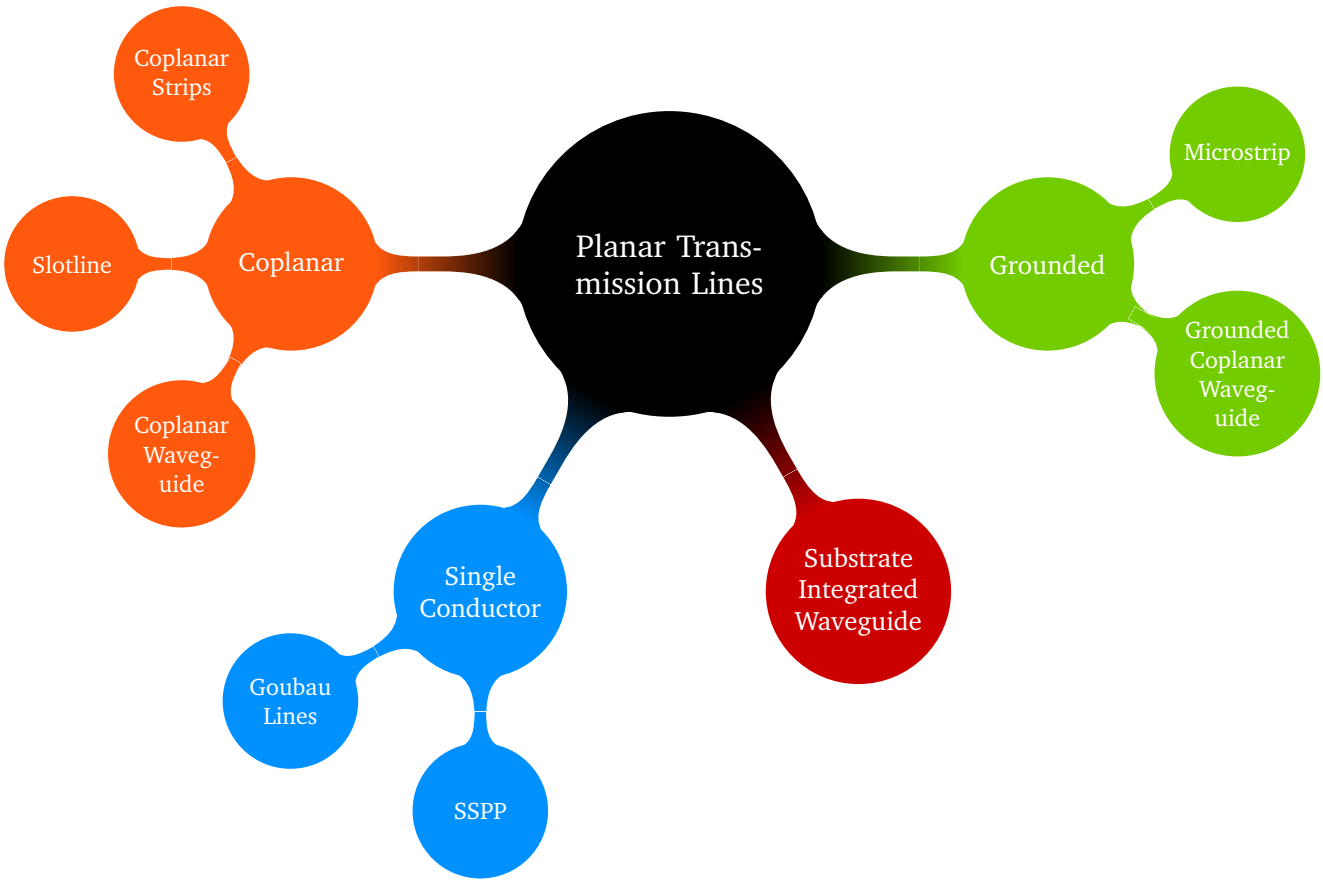

Figure 4.3: Ontology of planar transmission lines.

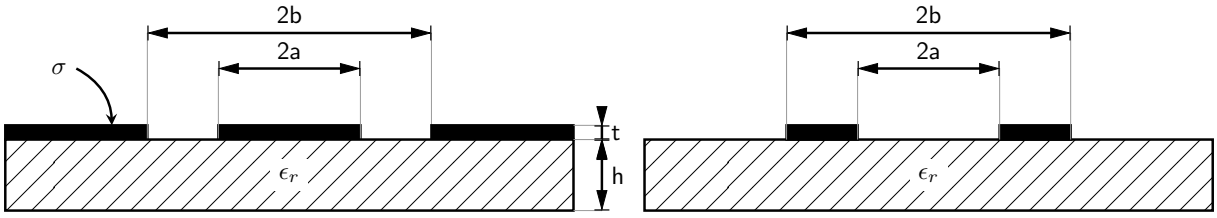

Figure 4.4: Cross-section of a CPW (left) and CPS (right).

this are air bridges, which short the parasitic modes and ensure equal potential[76] or another ground plane on the opposite side of the dielectric, connected with periodic via holes (see grounded coplanar waveguide (GCPW)). This however, makes the TL non-planar and renders the design more complicated.

We now turn to the loss analysis of CPW. A preliminary version of this analysis was published in [75]. Holloway et al. have derived a quasi-closed form expression to calculate conductor losses[77]:

$$\alpha_c^{cpw} = \frac{8.86 R_{sm} b^2}{16 Z_0^2 K(k_1)^2 (b^2 - a^2)} \left\{ \frac{1}{a} \ln\left[\left(\frac{2a}{\Delta}\right)\left(\frac{b-a}{b+a}\right)\right] + \frac{1}{b} \ln\left[\left(\frac{2b}{\Delta} - 1\right)\left(\frac{b-a}{b+a}\right)\right]\right\} \quad \text{dB/unit length} \tag{4.1}$$

where

$$R_{sm} = \omega_0 \mu_0 t \, \mathrm{Im}\left(\frac{\cot(k_c t) + \csc(k_c t)}{k_c t} \right),$$
$$k_c = \omega_0 \sqrt{\mu_0 (\epsilon_0 - j\sigma/\omega_0)},$$
$$k_1 = a/b,$$

and Δ is the numerically determined stopping distance calculated from the ratio of strip thickness to skin depth $t/2\delta$. $K(k)$ is the elliptic integral of the first kind, σ is the conductivity. Z_0 is the characteristic impedance, calculated as:

$$Z_0^{cpw} = 30\pi \cdot \frac{K'(k_1)/K(k_1)}{\sqrt{(\epsilon_{re})}} \tag{4.2}$$

The dieletric losses are calculated according to [76]:

$$\alpha_d^{cpw} = 27.3 \frac{\epsilon_r}{\sqrt{\epsilon_{re}}} \frac{\epsilon_{re}}{\epsilon_r - 1} \frac{\tan\delta}{\lambda_0} \qquad \text{dB/unit length} \tag{4.3}$$

where

$$\epsilon_{re} = 1 + \frac{(e_r - 1)K(k_2)K'(k_1)}{2K'(k_2)K(k_1)},$$
$$k_2 = \frac{\sinh((\pi a)/(2h))}{\sinh((\pi b)/(2h))},$$
$$K'(k) = K(\sqrt{1-k^2})$$

and $\tan\delta$ is the dielectric loss tangent. The radiation losses are given by the equation by Frankel et al.[78]:

$$\alpha_r^{cpw} = 8.86 \left(\frac{\pi}{2}\right)^5 2 \frac{(1-\epsilon_{re}/\epsilon_r)^2}{\sqrt{\epsilon_{re}/\epsilon_r}} \cdot \frac{(2b)^2}{K(k)K'(k)} \frac{1}{\lambda_d^3} \qquad \text{dB/unit length} \tag{4.4}$$

where $\lambda_d = \lambda_0/\sqrt{e_r}$.

We calculated the losses for a CPW waveguide on 7.5 μm polyimide ($\varepsilon_r = 3.3$, $\tan\delta = 0.003$). The chosen aluminium thicknesses t are 1 and 3 skin depths. Chosen conductor widths $2a$ are 0.15 mm, 0.3 mm and 0.5 mm.

Figure 4.5 shows an exemplary loss calculation for CPW with varying center conductor widths over impedance. We can see a strong dependence of the line attenuation on the conductor width and characteristic impedance. On the lower end of the impedance scale, the losses are dominated by conduction, where the conductor gap is small and little radiation occurs. The conductive losses taper off with increasing gap width. However, this leads to quickly increasing radiation losses, which we can observe for wider a. Dielectric losses are negligible because the effective dielectric constant $\epsilon_{re} \approx 1$. We can observe a minimum loss of 6 dB/m for $2a = 0.3$ mm and $t = 3\delta$.

The CPS are complementary to CPW, giving them a form of symmetry in the calculation of their properties. The factor $K'(k_1)/K(k_1)$ in the formula for the characteristic impedance of CPW turns into $K(k_1)/K'(k_1)$ in the expression for CPS[76]. Otherwise, the same formulas apply. The impedance of CPS is calculated with:

$$Z_0^{cps} = \frac{120\pi}{\sqrt{\epsilon_{re}}} \frac{K(k_1)}{K'(k_1)} \tag{4.5}$$

where

$$\epsilon_{re} = 1 + \frac{e_r - 1}{2} \frac{K'(k_2)}{K(k_2)} \frac{K(k_1)}{K'(k_1)},$$
$$k_2 = \frac{\tanh((\pi a)/(2h))}{\tanh((\pi b)/(2h))}$$

Frankel et al. give the radiation losses for CPS with[78]:

$$\alpha_r^{cps} = 8.86\pi^5 \frac{3-\sqrt{8}}{2} \sqrt{\epsilon_{re}/\epsilon_r} \cdot (1-\epsilon_{re}/\epsilon_r)^2 \frac{(2b)^2}{K'(k_1)K(k_1)} \frac{1}{\lambda_d^3} \qquad \text{dB/unit length} \tag{4.6}$$

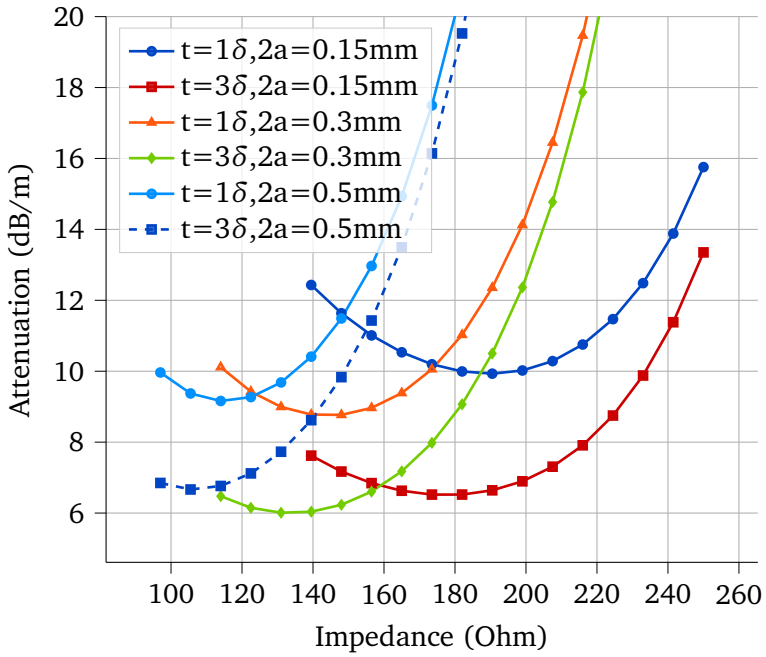

Figure 4.5: CPW attenuation over impedance, for different conductor thicknesses t and center conductor widths s. Calculated at frequency $f = 8.45\,\text{GHz}$, $e_r = 3.3$, $\tan\delta = 1 \times 10^{-3}$, substrate thickness $h = 7.5\,\mu\text{m}$. Configurations having $2b > \lambda_0/4$ and $b - a < 100\,\mu\text{m}$ were excluded from the results.

Analog to the previous calculation, Figure 4.6 shows an exemplary loss calculation for CPS. The loss characteristic is also complementary to that of CPW. For low values of Z_0, the CPS requires a larger separation of conductors, resulting in dominating radiation losses. Higher values of Z_0 result in unviable geometries.

Slotline

Moving on now to consider the characteristcs of the slotline based on the analysis by Cohn[79]. A slotline consists of two adjacent metal sheets on a dielectric substrate, separated by a gap of width $2a$ (see Fig. 4.7). The slotline can act as transmission line, if the dielectric constant of the substrate is large, and the guided wavelength λ_s is smaller compared to λ_0. A small guided wavelength results in closely confined fields around the slotline and thus, low radiation loss. Contrary to the previously discussed lines, which propagate a quasi-TEM, the slotline propagates a transversal electric (TE) mode.

Cohn analyzed the slotline radiation based on an approximation for the far-field components of electromagnetic field at radius r around the slot (cf. Fig. 4.8). For sufficiently large r The far-field components H_r, H_x and E_ϕ may be written as:

$$H_z = AH_0^{(1)}(k_c r) \tag{4.7}$$

$$H_r = -\frac{\gamma_z}{k_c^2}\frac{\partial H_z}{\partial r} = \frac{A}{\sqrt{1-(\lambda_s/\lambda_0)^2}}H_1^{(0)}(k_c r) \tag{4.8}$$

$$E_\phi = \frac{j\omega\pi}{k_c^2}\frac{\partial H_z}{\partial r} = -\eta H_r \lambda_s/\lambda_0 \tag{4.9}$$

where A is some arbitrary amplitude coefficient, H_0 and H_1 are the Hankel functions of first kind, order n. k_c is the complex wavenumber, $\gamma_x = j2\pi/\lambda_s$ is the propagation constant in z-direction, λ_s is the guided wavelength and η is the impedance of free space. For large r the Hankel functions may also be written as[76]:

$$H_n^{(1)}(j|r|) = \frac{2}{\sqrt{j\pi|r|}}\exp(-|r| - j\frac{n\pi}{2} - j\frac{\pi}{4}) \tag{4.10}$$

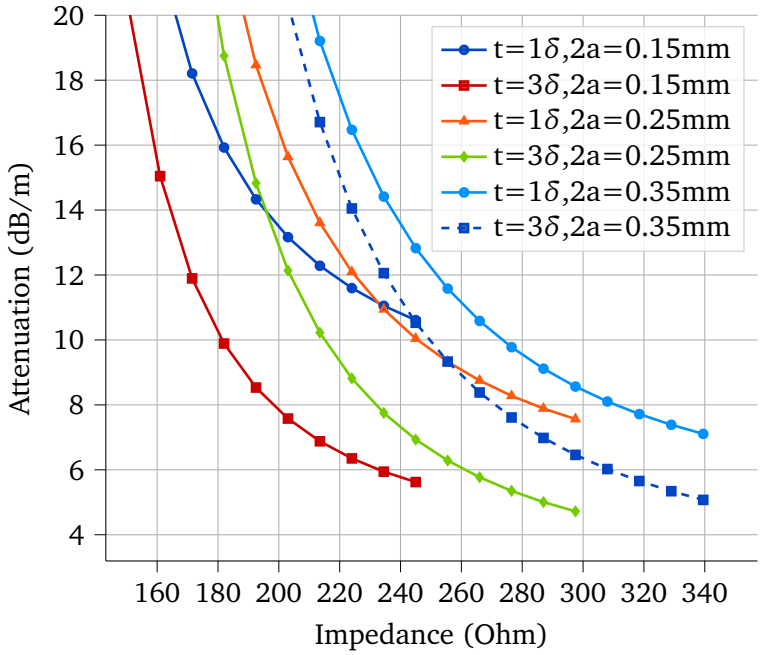

Figure 4.6: Total CPS attenuation over impedance, for different conductor thicknesses t and center conductor widths s. Calculated at frequency $f = 8.45\,\text{GHz}$, $e_r = 3.3$, $\tan\delta = 3 \times 10^{-3}$, substrate thickness $h = 7.5\,\mu\text{m}$. Configurations having $2b > \lambda_0/4$ and $b - a < 100\,\mu\text{m}$ were excluded from the results.

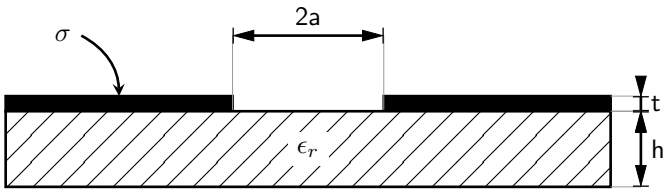

Figure 4.7: Cross-section of slotline.

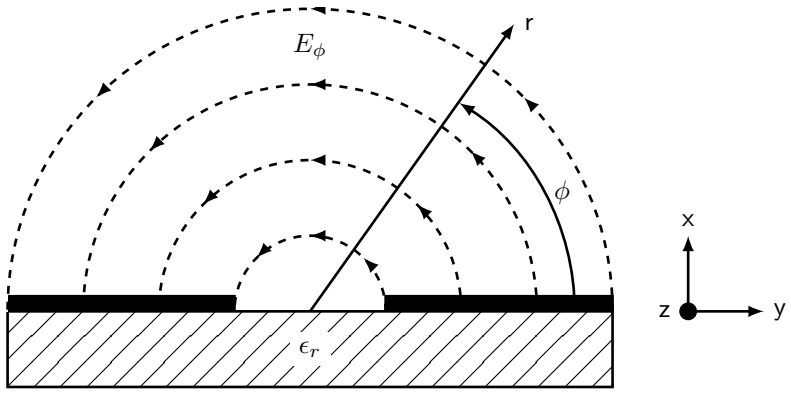

Figure 4.8: Cyclindrical coordinates for the analysis of the slotline. Recreated from [76].

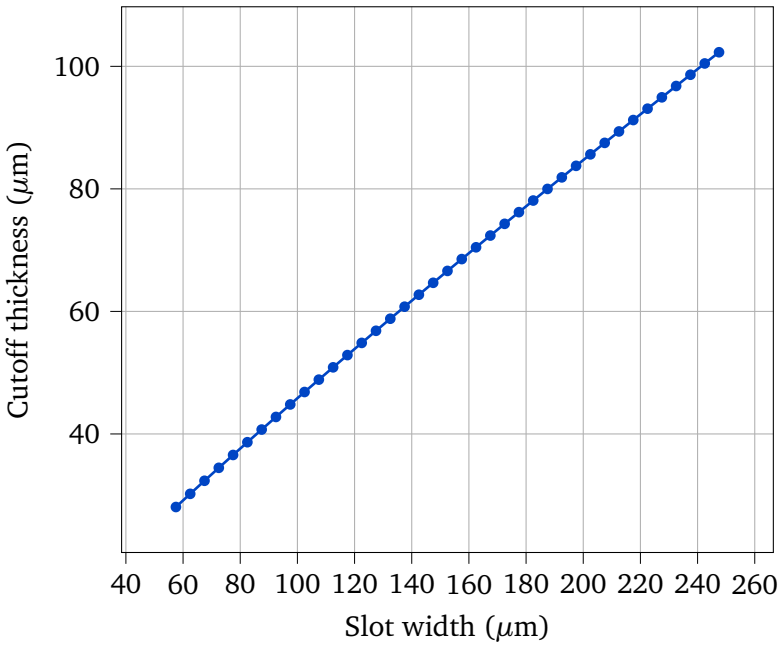

Figure 4.9: Cutoff thickness versus slot width for a slotline on dielectric with permittivity $e_r = 3.3$ at 8.45 GHz.

An approximation of the slotline's guided wavelength for $0.0015 \leq 2a/\lambda_0 \leq 0.075$ and $2.22 \leq \epsilon_r \leq 3.8$ is given by[80]:

$$\lambda_s/\lambda_0 = 1.045 - 0.365\ln(\epsilon_r) + \frac{6.3(2a/h)\epsilon_r^{0.945}}{238.64 + 1002a/h} \tag{4.11}$$

$$-[0.148 - \frac{8.81(\epsilon_r + 0.95)}{100\epsilon_r}] \cdot \ln(h/\lambda_0) \tag{4.12}$$

The coefficient k_c is

$$k_c = j\frac{2\pi}{\lambda_0}\sqrt{\frac{\lambda_0}{\lambda_s}^2 - 1} \tag{4.13}$$

To ensure low radiation, we require the radial component of the field to decay with distance. This is the case if $k_c r$ is imaginary which is true for $\lambda_s/\lambda_c < 1$.

For low permittivity dielectrics we can approximate the ratio λ_s/λ_0 from equation (4.12). Using the formula, we can numerically determine a cutoff-frequency, at which radiation occurs. The results for $f_0 = 8.45$ GHz and $e_r = 3.3$ are shown in Figure 4.9. The graph shows the cutoff thickness decreasing with slot width. Hence, it is clear that the required slot width for micrometer thick polyimide membranes will be impossible to manufacture.

Microstrip Line

Microstrip lines are among the most widely used planar TL. The geometry of a microstrip line is presented in Fig. 4.10. The microstrip line consist of a conductor of width W and thickness t separated by a dielectric of height h from a ground plane. The electric field of the microstrip line is not entirely contained in the dielectric, rendering the propagating mode a quasi-TEM wave with frequency dependent properties[81].

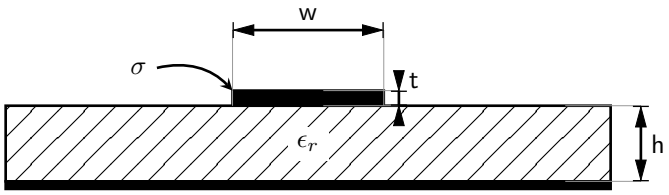

Figure 4.10: Cross-section of the microstrip line.

Pozar gives an empiric formula for the calculation of microstrip characteristic impedance[81]:

$$Z_0 = \begin{cases} 60/\sqrt{\epsilon_e} \cdot \ln(8h/W + W/4h) & \text{for } W/h \leq 1 \\ 120\pi/\sqrt{\epsilon_e} \cdot [W/h + 1.393 + 0.667\ln(W/h + 1.444)]^{-1} & \text{for } W/h > 1 \end{cases} \tag{4.14}$$

where ϵ_e is the effective dielectric constant:

$$\epsilon_e = \frac{e_r + 1}{2} + \frac{e_r - 1}{2} \frac{1}{\sqrt{1 + 12h/W}} \tag{4.15}$$

Moreover, the conductor loss of a microstrip line can be calculated with [76]:

$$\alpha_c^{MS} = 8.69 \frac{R_s}{Z_0 W} \qquad \text{dB/unit length} \tag{4.16}$$

where $R_s = \sqrt{\omega\mu_0/(2\sigma)}$ is the surface resistivity of a conductor with conductivity σ.

As we can see from (4.14), dielectric thickness has a strong impact on the conductor width. For ultra thin dielectrics, the W/d ratio is critial for two reasons. First, practical limits of manufacturing methods and physical stability limit the upper bound of feasable impedances. This has an impact on all circuit elements, such as dividers, tapers and filters. Additionally, a thinner conductor also results in higher conductive losses according to (4.16).

Dielectric losses are negligible for thin dielectrics, as most of the field will be outside of the dielectric. The formula is given in B. Figure 4.11 shows the calculated conductive losses of a microstrip line over impedance Z_0 and the corresponding conductor width. The calculation was performed for a relatively thick dielectric of 7.5 μm and a realistic sail thickness of 2.5 μm. The figure reveals the diametrically opposed behavior of the two quantities. While this is generally desirable, for an impedance of 30 Ω, the conductive losses of a line on a 7.5 μm dielectric remain excessive with more than 0.15 dB/mm. The microstripline is therefore no viable candidate.

Grounded Coplanar Waveguide

The GCPW or conductor-backed CPW can be regarded as a combination of the microstrip line and the CPW. The geometry of this waveguide is illustrated in Figure 4.12. Additional to the two coplanar ground planes of the CPW, the GCPW uses a ground plane on the opposite side of the dielectric. The ground planes are connected with via holes. Because of this, the GCPW does not require air bridges to suppress parasitic modes.

The characteristic impedance of the GCPW is calculated as[82]:

$$Z_0^{gcpw} = \frac{60\pi}{\sqrt{\epsilon_{re}}} \frac{1}{K(k)/K'(k) + K(k_1)/K'(k_1)} \tag{4.17}$$

where $k = a/b$ and k_1 and ϵ_{re}[76]:

$$k_1 = \frac{\tanh((\pi a)/(2h))}{\tanh((\pi b)/(2h))} \tag{4.18}$$

$$\epsilon_{re} = 1 + \frac{K(k_1)/K'(k_1)}{K(k)/K'(k) + K(k_1)/K'(k_1)}(\epsilon_r - 1) \tag{4.19}$$

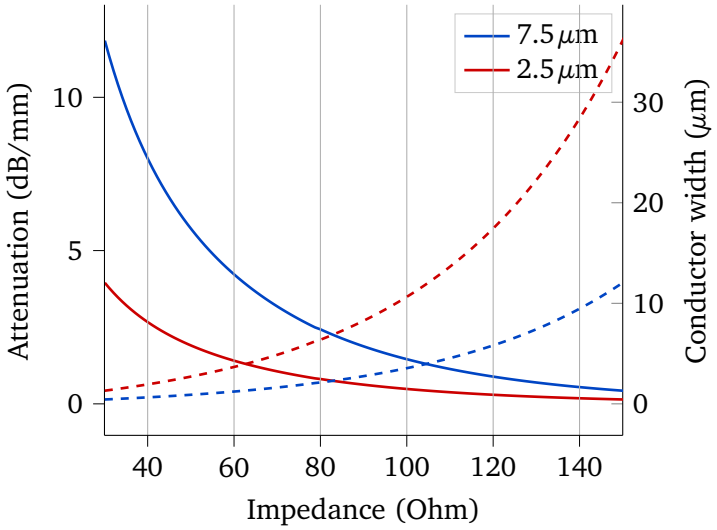

Figure 4.11: Conductor width and conductor loss (dashed) of an aluminium microstrip line with $h = 7.5\,\mu$m and $2.5\,\mu$m, $\epsilon_r = 3.3$ at 8.45 GHz versus line impedance.

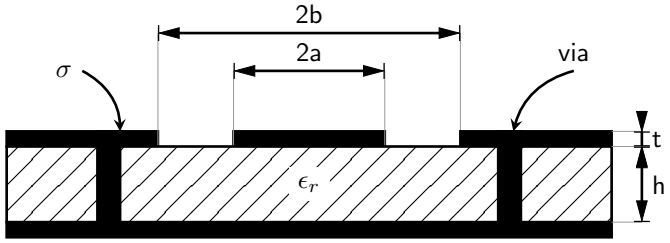

Figure 4.12: Geometry of the GCPW.

We calculated the losses for a GCPW waveguide using (4.1) and (4.3) on a $7.5\,\mu$m thick polyimide ($\varepsilon_r = 3.3$, $\tan\delta = 0.003$). The aluminium thickness is $t = 3\delta$. Similar to the microstrip line, the conductors of the GCPW become exceedingly thin and were chosen as $0.3\,\mu$m, $5\,\mu$m, $10\,\mu$m and $15\,\mu$m. The results for this analysis are given in Fig. 4.13. The figure shows a very high attenuation, regardless of strip width or impedance. Moreover, the figure reveals that the impedance and attainable impedance range decrease with strip width. Lower impedances are omitted because of the gap width limit, which has been exceptionally relaxed to $2\,\mu$m to have presentable solutions to begin with. It becomes clear that this type of waveguide need not be considered for further analysis.

Substrate Integrated Waveguides

SIW are the last type of the classical planar waveguides. The SIW can be regarded as the planar version of a dielectric-filled rectangular waveguide. The SIW is a sandwich structure of two conductive sheets separated by a dielectric layer. The conductive sheets are connected with via holes of diameter d, which are laterally separated by w and longitudinally spaced by s. The via diameter is typically smaller than $w/8$[76]. To prevent radiation leakage, s should be small compared to the guided wavelength and is typically chosen as $2d$[76]. The SIW can be analyzed analog to the rectangular waveguide. Therefore, the effective width of the equivalent rectangular waveguide can be approximated as[76]:

$$w_{eff} = w - 1.08\frac{d^2}{s} + 0.1\frac{d^2}{s} \tag{4.20}$$

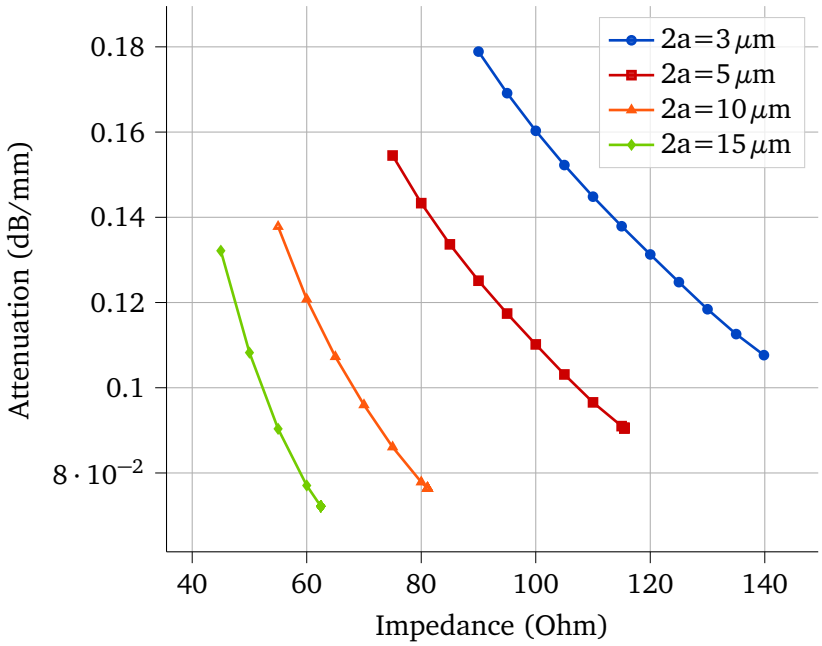

Figure 4.13: Total GCPW attenuation over impedance, for different conductor thicknesses t and center conductor widths s. Calculated at frequency $f = 8.45\,\text{GHz}$, $e_r = 3.3$, $\tan\delta = 1 \times 10^{-3}$, substrate thickness $h = 7.5\,\mu\text{m}$. Configurations having $2b > \lambda_0/4$ and $b - a < 2\,\mu\text{m}$ were excluded from the results.

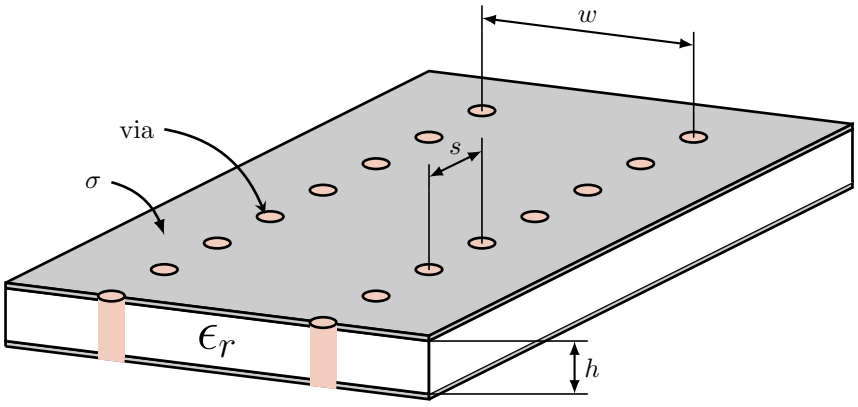

Figure 4.14: Geometry of a SIW.

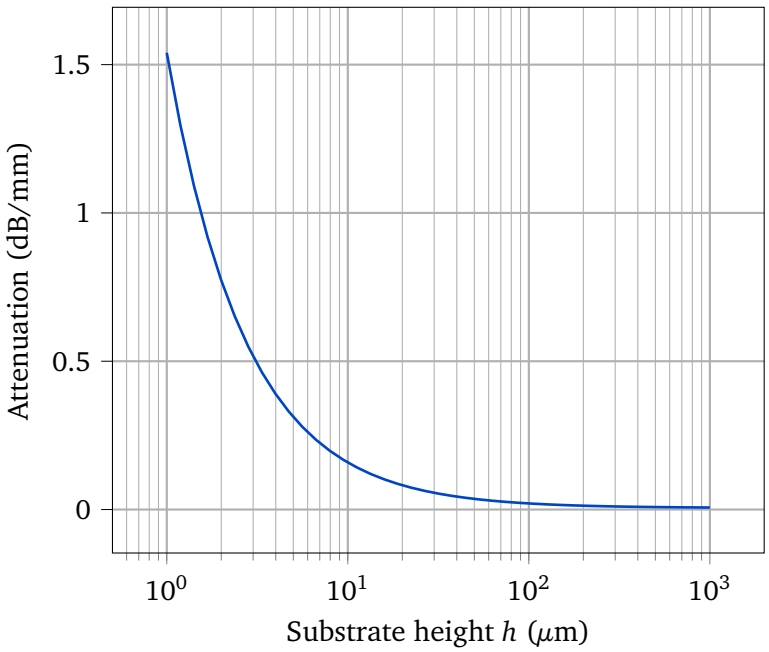

Figure 4.15: Attenuation due to conductor and dielectric loss of the SIW.

The conductive and dielectric losses for are given as[76]:

$$\alpha_C = \frac{\sqrt{\pi f \epsilon_0 \epsilon_r}}{h\sqrt{\sigma_c}} \frac{1 + 2(f_c/f)^2 h/w_{eff}}{\sqrt{1-(f_c/f)}} \quad \text{dB/unit length} \tag{4.21}$$

$$\alpha_D = \frac{\pi f \sqrt{\epsilon_r}}{c\sqrt{1-(f_c/f)^2}} \tan\delta \quad \text{dB/unit length} \tag{4.22}$$

The cutoff-frequency of the TE_{10} mode of the rectangular waveguide is[81]:

$$f_c = \frac{1}{2w_{eff}\sqrt{\mu\epsilon}} \tag{4.23}$$

We can see that the charateristics of the waveguide are mostly defined by its width. The sum of equations (4.21) and (4.22) has a loss minimum depending on the cutoff frequency. We determine the minimum for $f_0 = 8.45\,\text{GHz}$ and a SIW with $\epsilon_r = 3.3$, $\tan\delta = 0.003$, $\sigma_c = 3.77 \times 10^7$, $h = 7.5\,\mu\text{m}$. The resulting cutoff frequency is $f_c = 4.91\,\text{GHz}$ and corresponding effective width $w_{eff} = 16.8\,\text{mm}$. Fig. 4.15 shows the corresponding attenuation of the waveguide for different substrate thicknesses. The graph shows that the attenuation begins with 1.54 dB/mm at 1 μm and quickly declines to about 0.02 dB/mm at 0.1 mm and continues to slowly decrease to 6.75 dB/m at 1 mm.

4.2.2 Single Conductor Transmission Lines

As discussed before, a critical disadvantage of classical TL is the geometric necessity for three-dimensional structures in power dividers. Parallel to classical planar transmission lines which require least two conductors, there are also single-conductor transmission lines. Single-conductor lines are promising because they allow for purely planar and one-layered designs. As we will investigate in the following, they also promise very low attenuation.

Single conductor waveguides go back to investigations by Sommerfeld[83]. Sommerfeld investigated the propagation of surface waves on a smooth cylindrical conductor. Surface waves propagate parallel to the interface between two materials, but decay vertically to it[84]. Georg Goubau extended this research to conductors with dielectric cover or corrugated surface (Goubau lines)[85]. The Goubau line supports the propagation of a surface wave with high bandwidth and low cutoff frequency. The

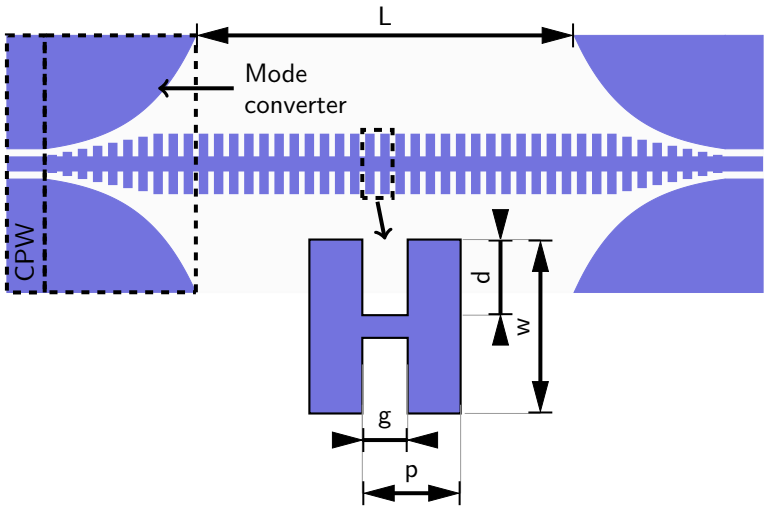

Figure 4.16: Configuration and parameters of a SSPP waveguide with CPW feed mode converter (top) and SSPP unit cell (bottom).

Goubau line has been revisited by Xu et al. in regard to mm-Wave and THz transmission, with the result of planar goubau line (PGL) for integrated circuits[86]. The properties of classical Goubau lines have been further analyzed by Vaughn et al., who reported the conductor losses to be about a magnitude lower than of a coaxial line with equivalent thickness[87]. They also reported phase and group velocity to be approximately at the speed of light. This line, however, tends to radiate strongly when the dielectric becomes very thin.

The concept of a planar corrugated Goubau line was revisited with the goal to produce spoof (or designer) surface plasmon polariton (SPP). SPP are surface waves in the optical spectrum, where they can propagate along the dielectric/metal interface, because of the non-PEC behavior of metals[88]. SPP are slow waves with tight confinement of the field around the conductor surface. SSPP in the microwave spectrum are realized as transversal magnetic (TM) surface waves using metamaterial, with periodic sub-wavelength structures, like slits, grooves and holes in a conductor. Cui et al. developed planar SSPP on flexible ultrathin films, showing their resilience to twists and 90° angled bends[89]. Since then, various microwave circuits based on SSPP, such as power dividers[90–96], couplers[96], antennas[97–99] and amplifiers[100] have been demonstrated.

Characteristics

A SSPP TL itself is a repetition of unit cells. Unit cells can take many forms, most commonly as H or U shapes. The geometry of the unit cell defines the dispersion, cutoff frequency and field confinement of the SSPP mode. The geometry of U- and H-unit cells is defined by their period p, width w, groove depth d and groove width g and metal thickness t (cf. Fig. 4.16).

The wavenumber k_z of the U-shaped unit cell with infinite thickness $t \to \infty$, for propagation in the z-direction can be calculated analytically[101]:

$$k_z = k_0 \sqrt{1 + \frac{g^2}{p^2} \tan^2(k_0 d)} \tag{4.24}$$

where $k_0 = \omega/c_0$ is the wavenumber in free space. We can observe from the formula, that while the ratio g/p plays a role, k_z is mainly defined by d. The corresponding dispersion diagram for a unit cell with $p = 4\,\text{mm}$, $w = 7\,\text{mm}$ is given in Fig. 4.17. We can observe that the wavenumber increases as d increases. At the same time, the cutoff frequency is decreased. Within one period of a unit cell, the phase change $\Delta\phi$ of the SSPP wave is at most $\Delta\phi = \pi$ and the corresponding frequency is the cutoff frequency[102]. In this application, a very thin conductor is required. The effect of a finite t

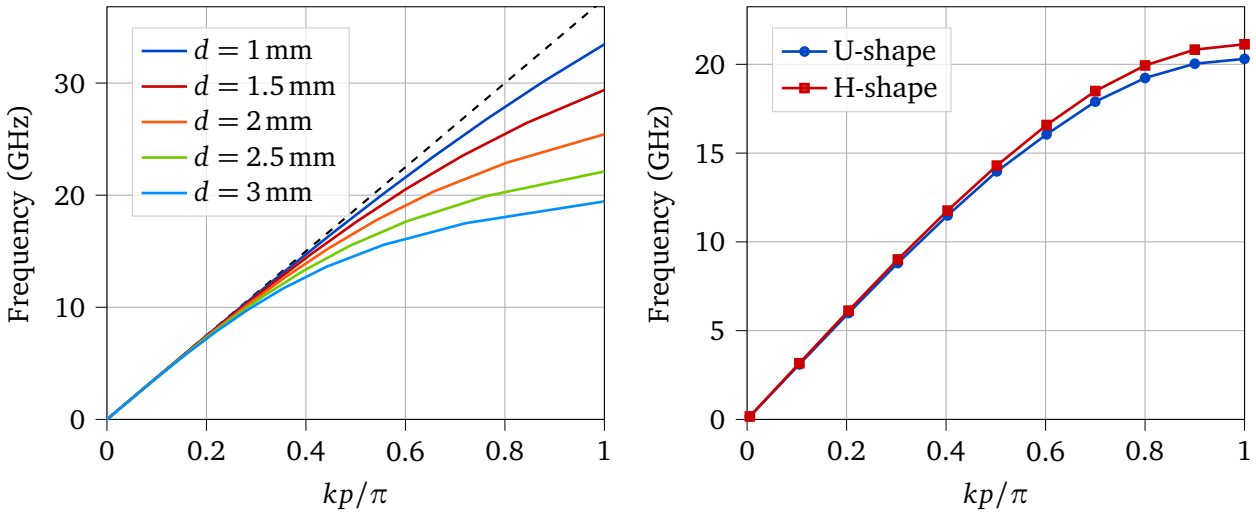

Figure 4.17: Left: Dispersion curve of the U-shaped SSPP unit cell with infinite thickness t, $p = 4\,\mathrm{mm}$, $g = 0.6p$, $w = 3.5\,\mathrm{mm}$ and different d. Right: Dispersion diagram of the same unit cell and dimensions, but with finite thickness $t = 2.7\,\mu\mathrm{m}$ and $d = 2.1\,\mathrm{mm}$. The H-shape is the mirrored U-Shape, i.e., $w_H = 2w_U$. The dashed line represents the propagation of light (light line).

was studied by Shen et al., who report an increase of k_z with decreasing t until a threshold of about $t < 0.002p$[103].

We approximate the dispersion curves for thin U- and H-shaped unit cells through an Eigenmode analysis in CST Microwave Studio. The unit cells are simulated with a periodic boundary in the x-direction and perfect magnetic conductor (PMC)/perfect electrical conductor (PEC) boundaries in the z- and y- direction, respectively (see Fig. 4.18). The modes are determined by the eigenmode solver through a phase sweep in the propagation direction. The resulting dispersion curves are presented in Fig. 4.17. The simulation reveals similar results for both shapes. This comes at no surprise, since the H-shape is the symmetric version of the U-shape.

To study the effect of a varying dielectric thickness, we simulate H-shape unit cell on dielectric with $\epsilon_r = 3.3$ and thickness h_d =1 mm, 0.25 mm, 0.025 mm and 0.0025 mm. The unit cells have the parameters $p = 4\,\mathrm{mm}$, $g = 0.6p$, $t = 2.7\,\mu\mathrm{m}$, $d = 0.3w$ and $w = 7\,\mathrm{mm}$. The results are shown in Fig. 4.19. Until about 8 GHz, there is only a miniscule difference between the individual graphs and little influence of the dielectric. Above, we can observe a momentum increase with higher dielectric thickness and at the same time, a reduction in the cutoff frequency. Conversely, we can also observe a small difference between $e_r = 1$ and $e_r = 3.3$ at low thicknesses. Moreover, we study the effect of a strongly varying dielectric constant. As we can see in the right graph, the effect is negligible as long as the dielectric remains thin.

Because the surface wave decays exponentially vertically to the interface, the fields are tightly confined around the SSPP waveguide. The decay constant of the field perpendicular to the propagating direction is given as[84]:

$$\alpha = \sqrt{k_z^2 - k_0^2} \tag{4.25}$$

We can see that a higher momentum also corresponds to tigher field confinement around the conductor. Figure 4.20 shows the simulated magnitude of the electrical field of the SSPP TL. As we can see in Fig. 4.21, along the y-axis, the electrical field exhibits a maximum at the edge of the conductor, and afterwards sharply drops by about −20 dB at a distance of 10 mm to the center. The maximum is connected to d, where a larger d results in a higher field strength at the conductor tip, however this effect diminishes with distance. A tighter confinement can be realized by increasing d, which is desirable, as it decreases the used surface area and, as we will see later, is also linked to lower radiation losses. A wider center line is however associated with lower conductor loss.

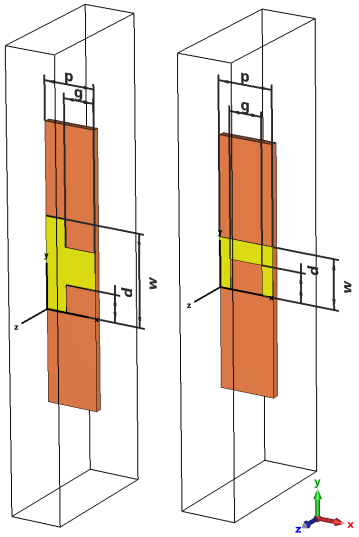

Figure 4.18: Simulation models of the U- and H-shaped unit cells with boundary conditions. The boundary conditions applied are PEC in $\pm y$ and PMC in $\pm z$ and periodic in $\pm x$.

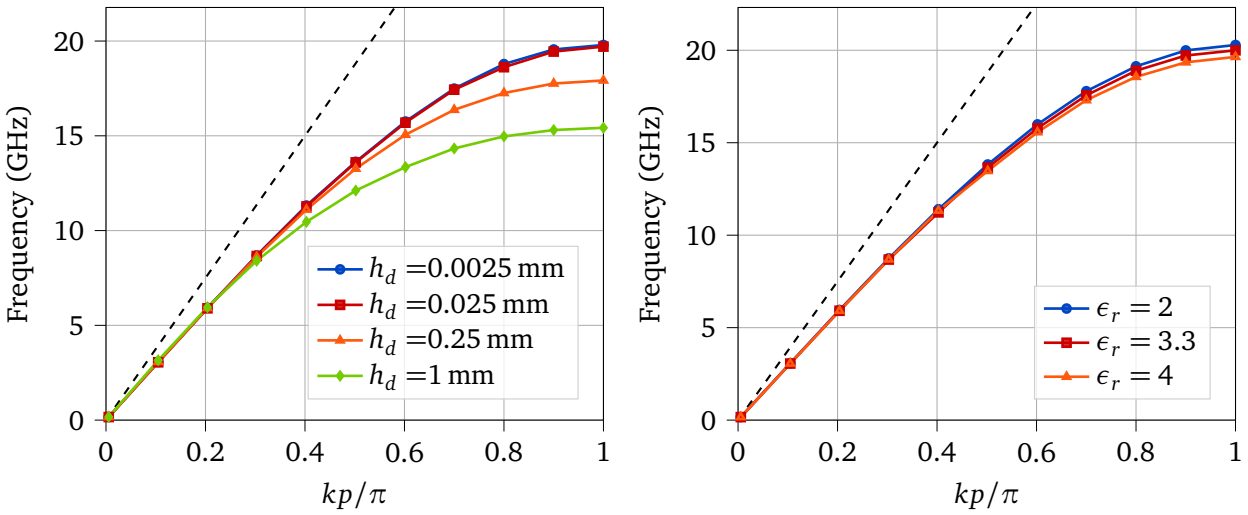

Figure 4.19: Influence of dielectric on the mode frequencies of H-shape unit cell with $p = 4\,\text{mm}$, $g = 0.6p$ and $d = 0.3w$ and $w = 7\,\text{mm}$. Variation of thickness (left) and variation of e_r with $h_d = 5\,\mu\text{m}$ (right). The dashed line represents the propagation of light (light line).

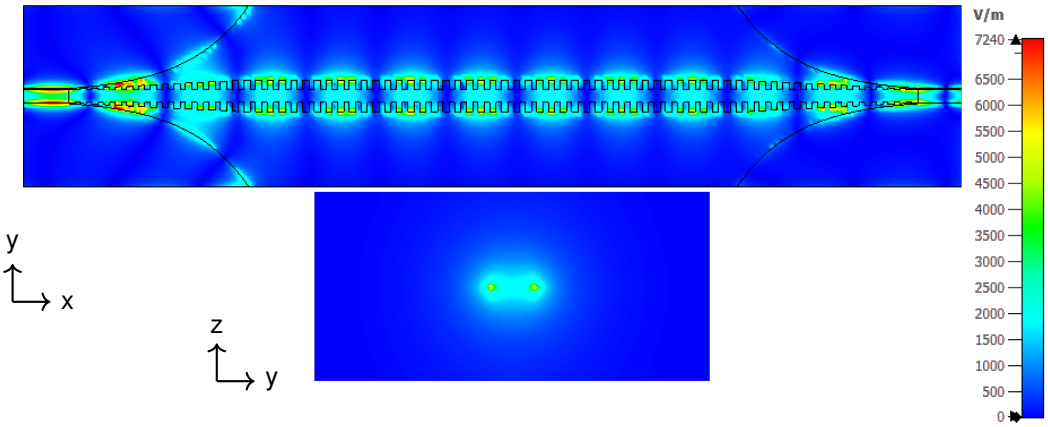

Figure 4.20: Absolute value of the electric field of the H-shaped SSPP TL evaluated at 8.45 GHz along the x-y plane (top) and y-z plane (bottom).

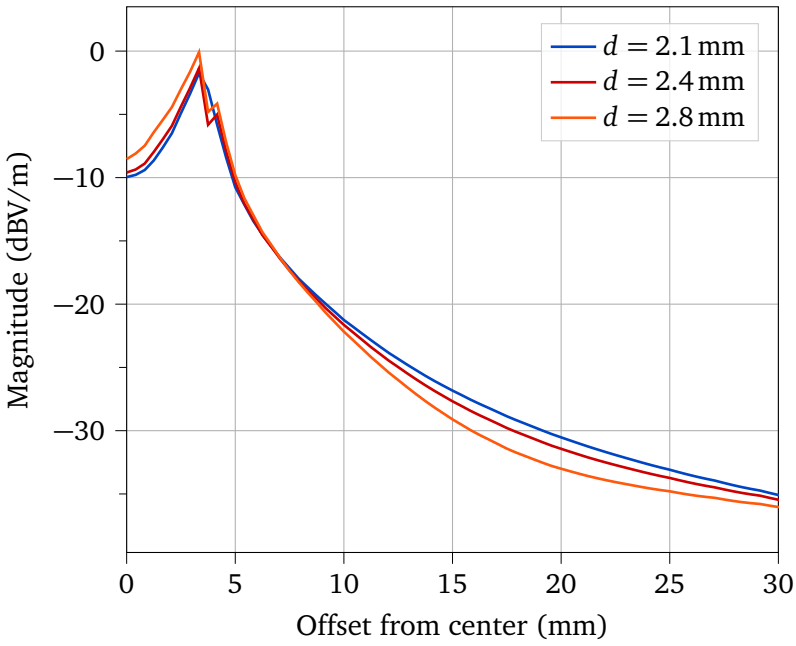

Figure 4.21: Influence of the gap width d on the magnitude of the E-field in y-direction around the H-unit cell.

Table 4.1: Unit cell and mode converter parameters of the simulation model

p	g	w	w_c	g_c	w_1	a	r
3.0 mm	$0.3p$	7.0 mm	1.70 mm	0.150 mm	$w_c/4.44$	1.140	0.350
Δl	l_1	l_2	l_3	g_1	g_2	g_3	
0.78 mm	$p-2\Delta l$	$p-\Delta l$	2.72 mm	1.15 mm	1.32 mm	1.49 mm	

Loss analysis

Used in a waveguide, SSPP have comparatively low loss. Kaianinejad et al. have published experimental results of SSPP TL on 0.5 mm FR-4 showing signifcantly lower losses for SSPP TL than for CPW[102]. A newer analysis by Zheng et al. showed lower loss of U-shaped SSPP lines compared to microstrip lines on a 0.5 mm FR-4 substrate for frequencies between 1 GHz to 10.5 GHz[104]. The reported attenuation consisted mainly of dielectric losses and was below 1 Np/m at 8.5 GHz.

In the following, we will study the losses of the SSPP TL in more detail with a simulation model in CST Microwave Studio (cf. Fig. 4.22). The model consists of a polyimide dielectric ($h_d = 3.5\,\mu$m, $\epsilon_r = 3.3$) and a metal sheet with a thickness of 2.7 μm. The unit cell has the parameters $p = 3$ mm, $g = 0.3p$, $w = 7$ mm. The thin dielectric is supported by an additional RO4350B substrate ($\epsilon_r = 3.6$) with a thickness 0.5 mm in the area of the CPW and mode converter. This is to reduce the dimensions of the CPW, allow 50 Ω matching, and so improve manufacturability of a later model. The mode converter is modeled according to [105]. The parameters of the unit cell and mode converter are given in Tab. 4.1.

CST allows us to separate the losses into the individual components, i.e., radiation, conduction and dielectric. Expectedly, the dielectric losses are negligible due to the low dielectric thickness and range below −30 dB of the total stimulated power.

Radiation Losses The radiation losses in this TL are of particular interest and have been investigated by Kaianinejad[102] and Xu et al. [106]. According to Kianinejad, the radiation losses predominately come from mode conversion, whereas only a small fraction can be attributed to leaky loss, which is proportional to the length of the TL[102].

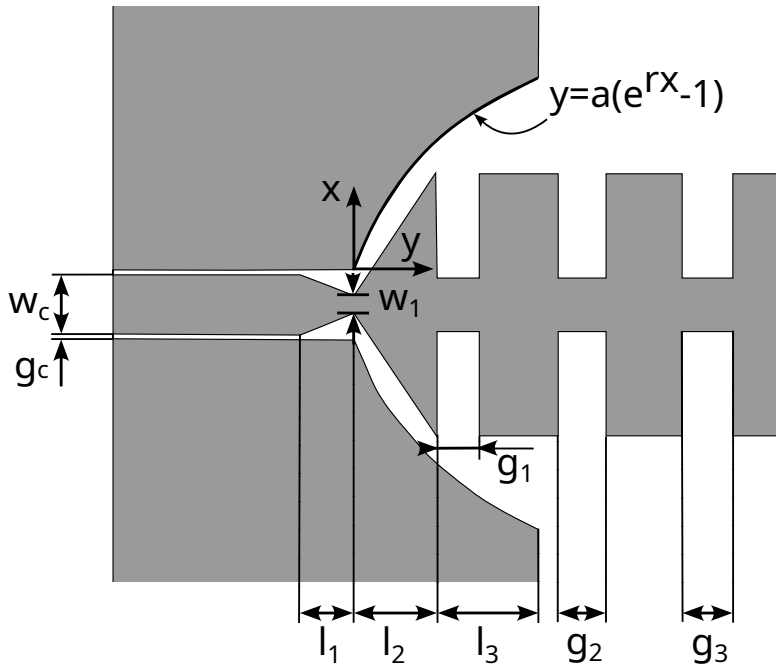

Figure 4.22: Short SSPP mode converter design according to Kianinejad[105].

Contrary to Kianinejad, Xu et al. report that this leaky loss is not proportional to the waveguide length and instead exhibits a periodic variation. They reason that the opposing currents in the direction of propagation are separated sufficiently to give rise to radiation. The instantaneous current on the waveguide (cf. Fig. 4.23) is given by:

$$J_z = J_0 \times e^{-j\beta_z z} \tag{4.26}$$

where β_z is the phase constant in the direction of propagation. Xu et al. argue, that the slow-wave radiation mechanism of leaky traveling-wave antennas as studied by co-author Li et al.[107] applies. Li et al. modeled the leaky wave antenna as uniform current flowing over the length of the waveguide (see Fig. 4.24).

For a given angle θ, there exists a pair of elements of length S, for which the radiation will cancel in the far-field due to interference. The length S is given by:

$$S = \frac{\pi}{|k_0 \sin\theta - \beta_z|} \tag{4.27}$$

Not taking conductor losses into account, the effective radiation in the far-field is created by the effective radiation sections L_e on both ends of the waveguide, for which no such counterpart exists. L_e is given as:

$$L_e(\theta) = \begin{cases} L_{e0}(\theta), & \text{if } L_{e0} \leq \frac{S(\theta)}{2} \\ S(\theta) - L_{e0}(\theta), & \text{else} \end{cases} \tag{4.28}$$

The section L_{e0} is given as:

$$\forall L_{e0} \leq \frac{L}{2}: \quad L_{e0}(\theta) = \frac{L - 2N(\theta)S(\theta)}{2} \tag{4.29}$$

where N is the angle-dependent number of S-sections pairs in L. In Fig. 4.25, we illustrate the results of these equations for a waveguide with length $L = 300\,\text{mm}$ at $f = 8.45\,\text{GHz}$. Expectedly, the maxima are to find around $\theta = 90°$. We can observe a reduction of S with increasing β_z, which also corresponds with a reduction in L_e. As a corollary, we want to note that for small enough S, we can assume

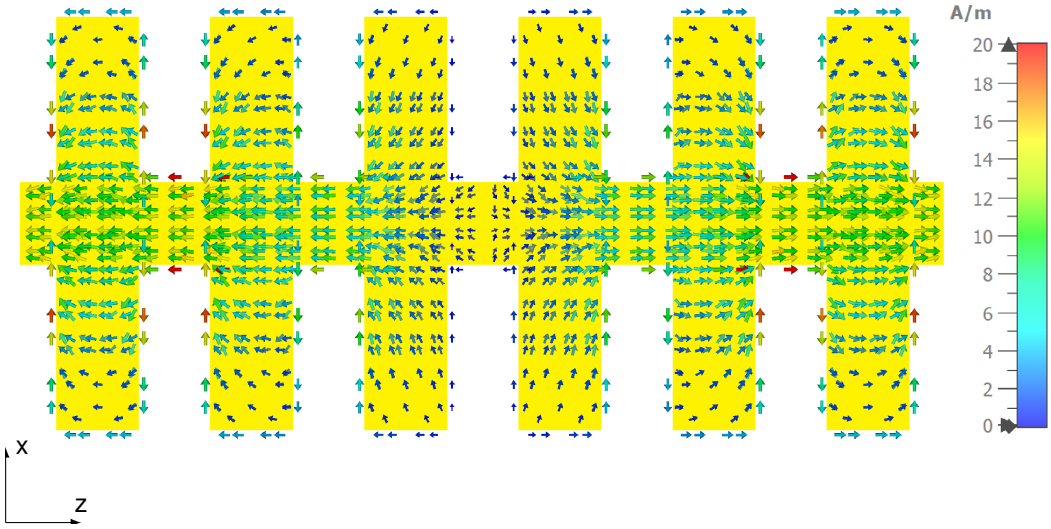

Figure 4.23: Current distribution on the SSPP unit cell.

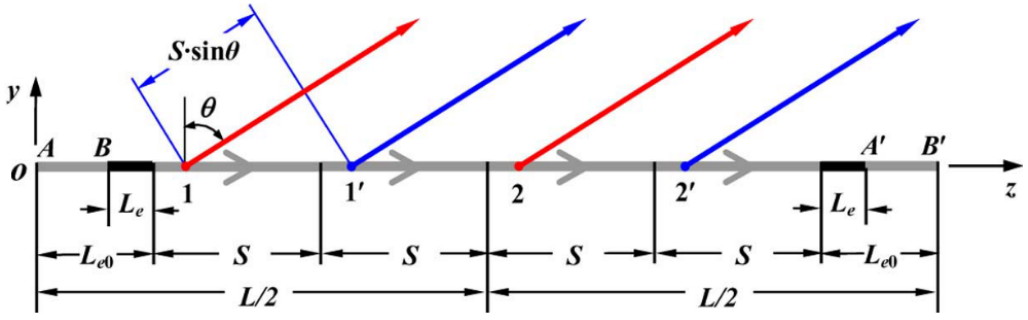

Figure 4.24: Line-source model of traveling-wave current [107]. ©2013 IEEE

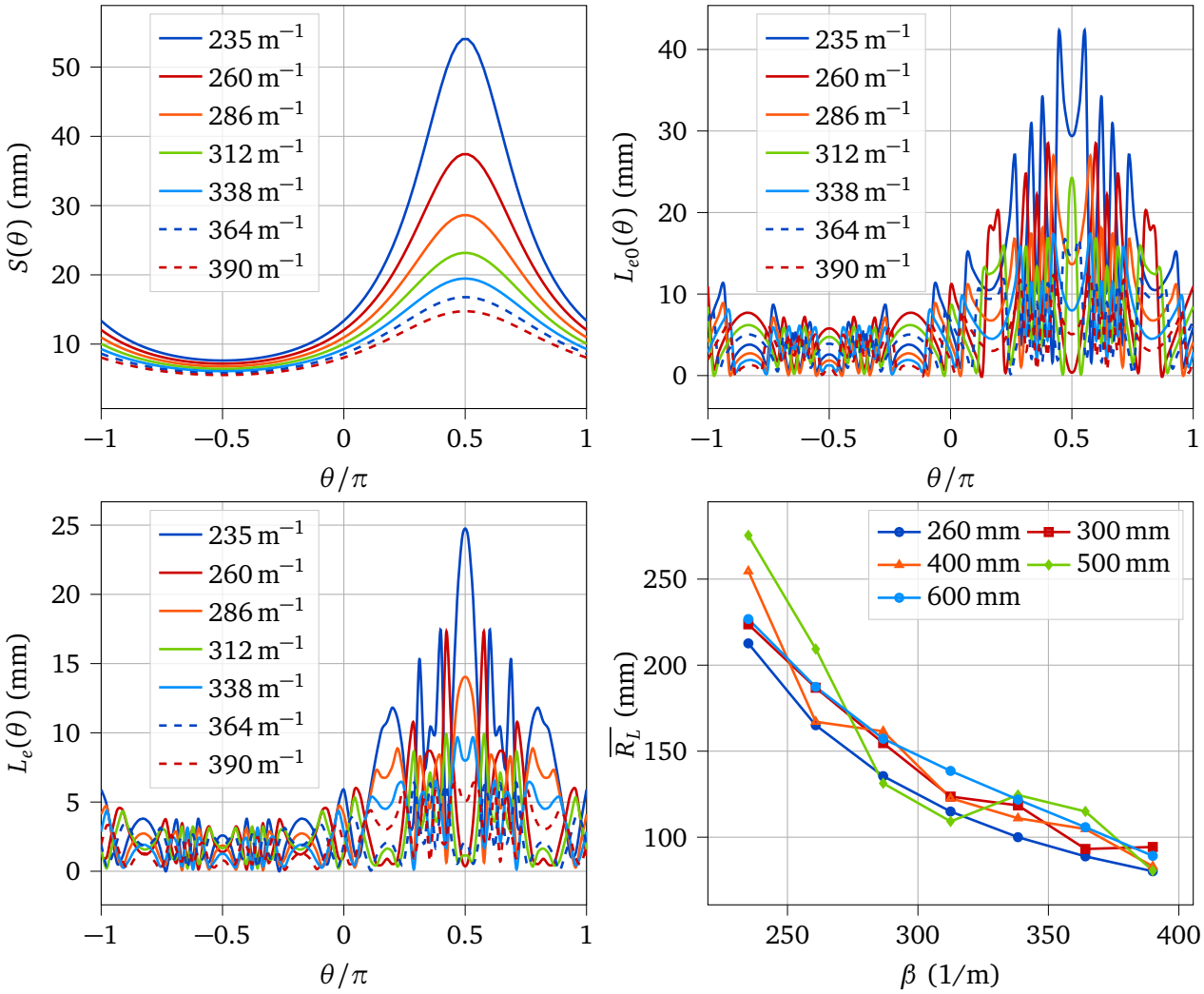

Figure 4.25: Graphs of S, L_{e0}, L_e and $\overline{R_L}$ for different values of β_z.

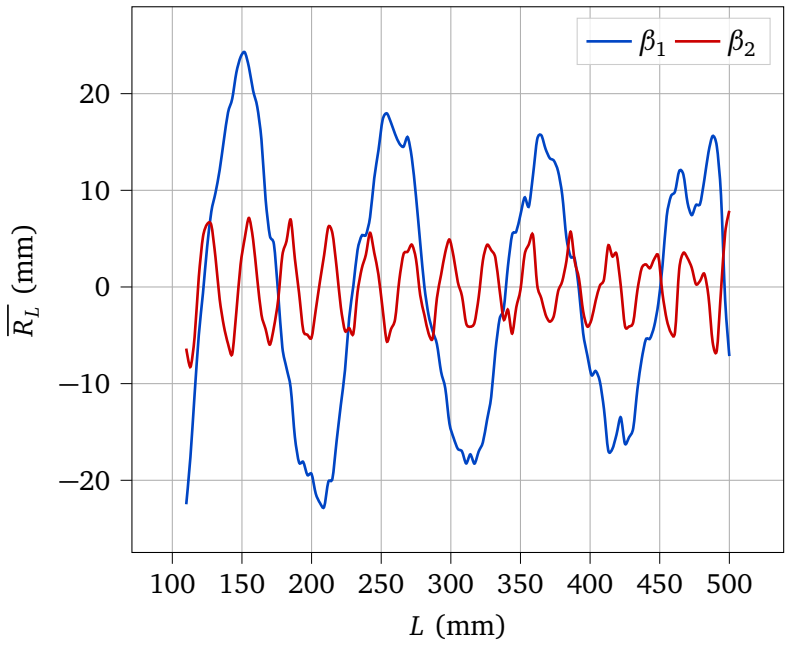

Figure 4.26: $\overline{R_L}$ vs length, β_1 =235 m^{-1} and β_2 = 390 m^{-1}.

the current constant between two S-pairs. Therefore, the influence of conductor losses as source of radiation fades with decreasing S.

Based on the work of Li, Xu et al. derive a *average radiation length* (ARL), denoted here as $\overline{R_L}$, which they argue is proportional to the radiation loss:

$$\overline{R_L} = ARL = \frac{1}{\pi}\int_0^{\pi} L_e(\theta)\, d\theta \tag{4.30}$$

$\overline{R_L}$ is illustrated on the bottom right of Fig. 4.25. The Figure depicts the graphs of different line lengths L. We can observe a decrease of $\overline{R_L}$ for larger β, and therefore, we expect the radiation loss to decrease with increasing d, as this also increases β. Depending on the line length, the characteristic of the graphs alternates between a strictly monotonically decreasing and decreasing with seemlingy periodic spikes. When comparing the smooth, strictly monotonically decreasing graphs of L_1 =260 mm and L_2 =600 mm, the $\overline{R_L}$ for 260 mm is lower by a margin of 22 mm to 9 mm.

The spiky behavior is striking and needs more investigation. Figure 4.26 shows the centered $\overline{R_L}$ versus TL length in steps of 1 mm for β_1 =235 m^{-1} and β_2 = 390 m^{-1}. We can observe the periodicity of $\overline{R_L}$, with longer periods and higher amplitudes for the smaller β. The periods are approximately 110 mm and 28 mm, which corresponds to the respective $2S(\pi/2)$.

The report by Xu et al. does not give the means for the quantification of radiation loss. Therefore, we study the effect of radiation with the aforementioned SSPP TL simulation model in CST Microwave Studio.

The total loss ratio of this structure is shown in Figure 4.27. The figure shows the percentage of the total power lost due to radiation versus the total length of the SSPP transmission line for different values of d. The graphs clearly exhibit a periodicity, where the amplitude grows with increasing d. A linear relationship between length and radiation loss is not visible. There appears to be a constant loss connected to d, which could be attributed to the mode converter.

What is striking in this figure is the higher fluctuation of the radiation losses with line length for lower values of d. Moreover, from the previous theory we expect longer and different periods, whereas the fluctuations appear to be more or less in phase with each other. Because of the short period of about $\lambda/2$, we suspect that this variation is rather the result of a standing wave, caused by mismatch in

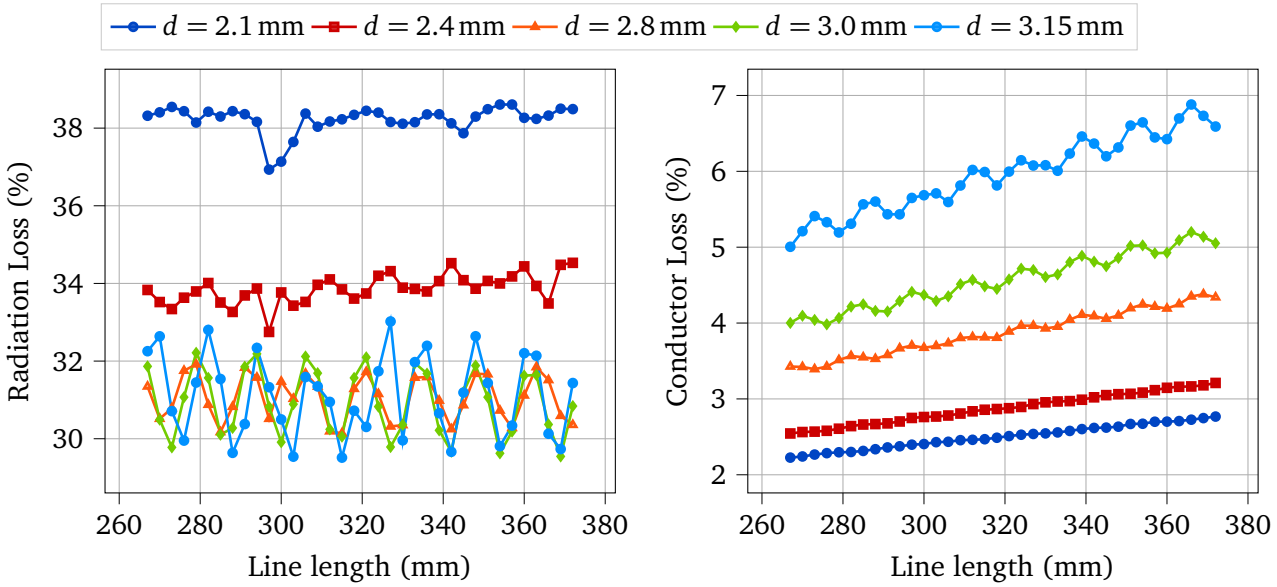

Figure 4.27: Radiation loss (left) and conductor loss (right) in percent of the total excited power versus total length of the SSPP line (excluding mode converter).

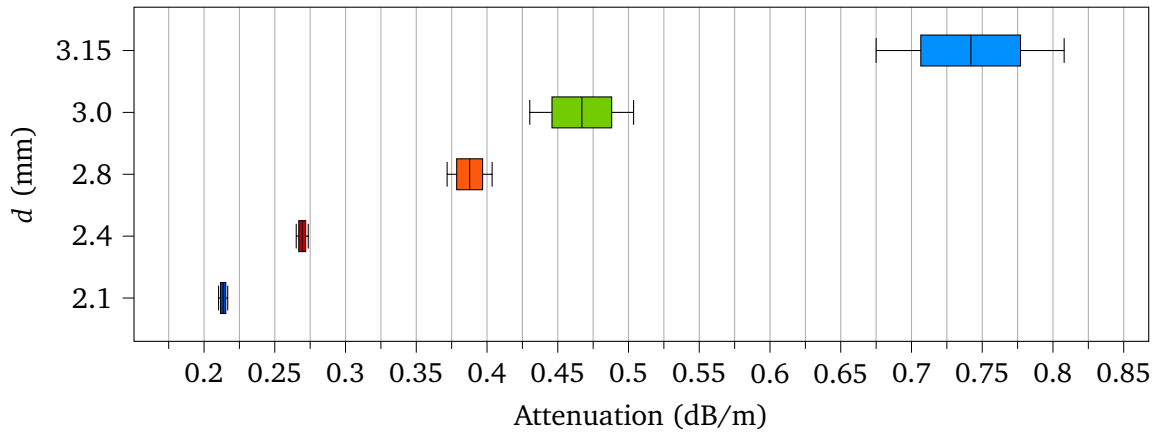

Figure 4.28: Conductor loss obtained by the regression analysis.

the mode converter, rather than that of radiation. Xu et al. did not address the resonant behavior of their structure, which had an input return loss of $S_{11} \approx -15\,\mathrm{dB}$. The mismatch at the converter results in a standing wave on the waveguide and therefore a current distribution that differs from the pure travelling wave. For this reason, we believe that the findings from Xu must be approached with caution.

Conductor Losses The simulated conductor losses are presented in Fig. 4.27. We can observe a very linear relationship between conductor length and loss. A higher value of d is clearly associated with higher conductor losses, which we attribute to a smaller center conductor. The loss curves also begin to exhibit a ripple for $d > 2.4\,\mathrm{mm}$, which fits to the ripple observed in the radiation loss diagram.

From these results, we can extract the conductor attenuation constant, α_c, via the slope of the lines. We determine the slope with a linear regression analysis in Matlab. The results of this analysis are shown in Figure. 4.28. The results clearly indicate an increase in conductor loss with decreasing center conductor width $w-2d$. At the lower end of the spectrum, the attenuation is as low as $0.21\,\mathrm{dB\,m^{-1}}$ for $d = 2.1\,\mathrm{mm}$. At the higher end, the 95th percentile for $d = 3.15\,\mathrm{mm}$ reaches $0.81\,\mathrm{dB\,m^{-1}}$.

Attenuation Constant

The studied waveguide with converters has non-negligible reflections, therefore the attenuation constant cannot be determined via power ratios, as this would include the reflected loss as well[81]. Instead, a viable method is to extract the attenuation constant via the multiline calibration method[108] as was done by[104].

The multiline method allows us to analyse a symmetric two port network by dividing the network into a cascade of three T-parameter components, represented by the relation:

$$M = XT\bar{X} \tag{4.31}$$

$$MX = XT \tag{4.32}$$

where T, X and $\bar{X}$ represents the device under test and the converters and connectors, respectively.

$\bar{X}$ is calculated from X as:

$$\bar{X} = \begin{bmatrix} 0 & 1 \\ 1 & 0 \end{bmatrix} X^{-1} \begin{bmatrix} 0 & 1 \\ 1 & 0 \end{bmatrix} \tag{4.33}$$

Since we will apply this theory to a simulation, we can assume an ideal TL and T is given as:

$$T = \begin{bmatrix} e^{-\gamma l_i} & 0 \\ 0 & e^{+\gamma l_i} \end{bmatrix} \tag{4.34}$$

where γ is the complex propagation constant and l_i is the line length. Using two iterations with different l_i and l_j, we can obtain:

$$M^{ij}X = XT^{ij} \tag{4.35}$$

$$M^{ij} = M^j(M^i)^{-1} \tag{4.36}$$

$$T^{ij} = T^j(T^i)^{-1} = \begin{bmatrix} \lambda_1^{ij} & 0 \\ 0 & \lambda_2^{ij} \end{bmatrix} = \begin{bmatrix} e^{-\gamma(l_j-l_i)} & 0 \\ 0 & e^{+\gamma(l_j-l_i)} \end{bmatrix} \tag{4.37}$$

$\lambda_{1,2}^{ij}$ are the Eigenvalues of M and T and are calculated as:

$$\lambda_{1,2}^{ij} = \frac{1}{2}\left[(T_{11}^{ij} + T_{22}^{ij}) \pm \sqrt{(T_{11}^{ij} - T_{22}^{ij})^2 + 4T_{12}^{ij}T_{21}^{ij}}\right] \tag{4.38}$$

We obtain α as the real part from complex γ:

$$\alpha = \Re(\gamma) = -\Re\left[\frac{1}{l_j - l_i} \ln\left(\frac{\lambda_1^{ij} + \frac{1}{\lambda_2^{ij}}}{2}\right)\right] \text{ dB/unit length} \tag{4.39}$$

We study the losses of the waveguide shown in Fig. 4.22 using the previous simulation results. For each combination (d, l_i), we calculate the attenuation constant using a shorter reference with length $l_0 = 99\,\text{mm}$. In order to improve the quality of the results and generate a reliable distribution, we resample the data set via bootstrapping of the mean value distribution.

The results are presented in Fig. 4.29. From this data, we can observe that attenuation for $d \geq 2.8\,\text{mm}$ is only slightly (yet significantly) higher than what was predicted by the conductor loss analysis. A surprising result to emerge from the data are the losses for $d = 2.1\,\text{mm}$ and $d = 2.4\,\text{mm}$ however, which are much higher than predicted. At the same time, they also exhibit a wider spread than what we would expect from the results until now. The causative factors for this have yet to be determined. Because of this, the lowest attenuation is found at $d = 2.8\,\text{mm}$, with a value of approximately $0.45\,\text{dB}\,\text{m}^{-1}$.

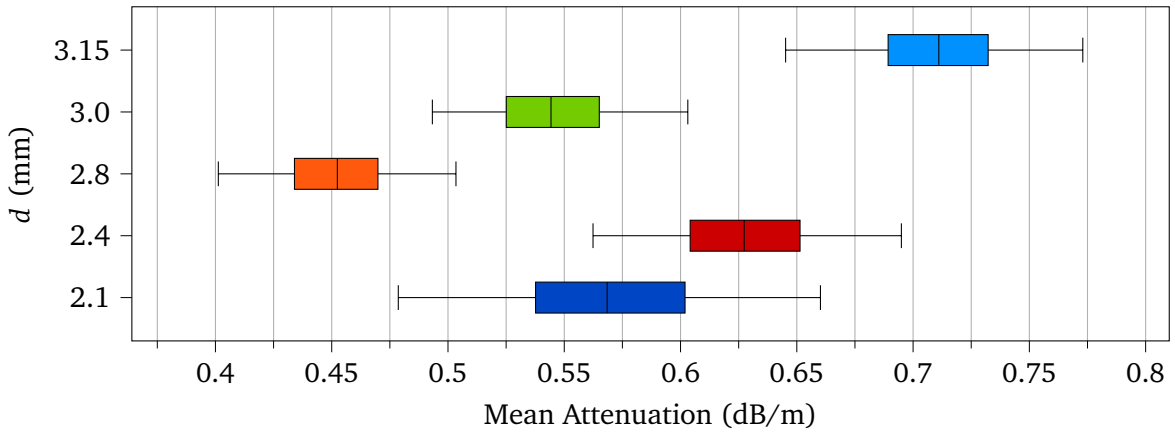

Figure 4.29: Distribution of the mean total attenuation of the SSPP line.

4.2.3 Discussion

In this section, we provided an analysis of the most prominent representatives of classical planar transmission lines with regard to their use on thin solar sailing membranes. Using either the design formulas or the theoretical analysis of attenuation, we could exclude any of the presented consituents as potential candidates for a membrane antenna array.

In the case of CPW and CPS, this was due to high radiation losses. The slotline mode, too, is radiative for any meaningful geometric parameters. Note that in addition to these issues, these TL are purely planar, hence for purely geometric reasons, power division excites parasitic modes. Solutions to this issue either use a third dimension, such as air bridges[76] or defected ground structures[109], or use slotline transitions[110] which again, do radiate.

Microstrip line and GCPW both suffer from the close separation to a potential ground plane and exhibit high conductive losses. Additionally the GCPW suffers from severe geometric limitations, so that they appear impossible to manufacture. The SIW concept was also taken into consideration. While an unlikely option to begin with, the results from design formulas demotivate any further investigation in this direction.

Having exhausted all classical TL, we turned to single conductor lines. A class of single conductor metamaterial known as spoof surface plasmon polariton promises a purely planar design without the aforementioned isses in power division. Using simulations in CST Microwave Studio, we investigated the SSPP unit cells. We found that the properties of the unit cell become insensitive to changes in the dielectric properties as long as the thickness is less than about 25 μm. In conclusion, a design manufactured on thicker commercial off-the-shelf (COTS) polyimide can be expected to behave very similar to an antenna manufactured on thin solar sailing foil under the caveat that metal thickness may still make a difference. The expansion of the electric field around the conductor depends strongly on the groove depth, with a higher depth causing the field to decay faster, which will be an advantage since less of metal area around the conductor must be cleared.

On a solar sail membrane, the dielectric losses of an SSPP line will be negligible compared to conductor and radiation losses. Radiation losses in SSPP come from leaky losses appearing at discontinuities, e.g. the beginning and end of a waveguide. Based on the research by Xu et al.[106], we investigated the radiation losses of a particular parameter set. We found that a larger groove depth generally results in lower radiation losses. As predicted by Xu, the losses do not increase with line length, but tend to fluctuate in a cyclic fashion with increasing groove depth. These fluctuations may partially be attributed to converter losses and more research in this direction is required. The conductor losses however, exhibit a very linear relationship with conductor length. A lower groove depth results in lower losses, due to the wider center conductor where the largest portion of the current is concentrated. Since the radiation loss does not grow linearly with length but exhibits a rather cyclic behavior, the total losses of the SSPP line were calculated over a range of lengths and the losses are given as a

range as well. Both loss mechanisms work opposite to each other, so that an optimal groove depth exists at about $0.4w$ resulting in a low total attenuation between $0.42\,\mathrm{dB\,m^{-1}}$ to $0.48\,\mathrm{dB\,m^{-1}}$. Therefore, the SSPP line can be regarded as a suitable TL for the membrane antenna.

4.3 Leaky Wave Antenna Prototype

We now turn to the types of antenna possible with the SSPP technology. As discussed above, the SSPP line does not radiate, with the exception being discontinuities. This can be used to build two kinds of leaky-wave antennas by introducing discontinuities in a targeted manner.

The first way to do build an SSPP based antenna is to modulate the geometry of the unit cell. An effective geometric parameter to create radiation is the width of the unit cell, and a first demonstration of this method was by Xu et al.[97]. They developed a linear polarized antenna, operating at 14 GHz. Kong et al. published an antenna based on modulations of the groove depth[111], which is shown in Fig. 4.30. The approach was adopted by Hao, who connected four leaky-wave antennas via a corporate feed[112]. The antenna array had a reported maximum gain of 12.5 dBi at 6.6 GHz.

The second option is to couple the SSPP waveguide with adjacent patches that will then radiate. Sanchez-Escuderos demonstrated this concept first with PGL and perpendicular patches[113], and later with inclined patches for circular polarization[114]. The two-layered designs reached maximum gains of 13 dBi at 41 GHz in the linear polarized case and 15.6 dBi at 40 GHz in the circular polarized case. The antennas had a reported size of $4.97 \times 0.94 \times 0.66\lambda^3$. Zhang et al. later adopted the "herringbone" design for a one-layered SSPP antenna with CP. The authors report a gain of 10.5 dBic at 6 GHz with a radiation efficiency of 87 %. The reported axial ration was 1.5 dB over a bandwidth of 15 %.

Both options have advantages. In case CP is not required in a different design, we consider the modulated waveguide a more suitable option due to its simplicity and reduced footprint. We proceed with the leaky wave based on radiating patches, as this allows for CP.

4.3.1 Design

We designed a prototype 2x7 leaky-wave array antenna based on the design of Zhang etal.[99]. The antenna consists of three components (cf. Fig 4.31). The first section is a CPW line to connect a subminiature version a (SMA) coaxial connector. The CPW has a total width of 3.4 mm and a conductor width of 3 mm. The following mode converter comprises an exponentially flaring ground and eight SSPP unit cells that gradually increase in width through a linear taper. Finally follows the SSPP waveguide with two rows of slanted patches, which are horizontally shifted in order to generate circular polarization. The antenna is designed to be manufactured on Rogers corporation laminate 4350B (RO4350B) substrate ($\epsilon_r = 3.66$, $\tan\delta = 0.0037$) with a thickness of 0.254 mm and a copper layer thickness of 18 μm. The total dimensions of the antenna are 264.21 mm × 58.6 mm.

Special attention was paid to the design of the unit cells. The unit cells have an impact on several parts of the design. First of all, the simulation has shown that the reflection of the converter improves if the width difference between w_{cpw} and SSPP center line width decreases. A greater width of the unit cell also results in a wider separation of the rows of radiating patches, which is detrimental to the achievable CP beamwidth. In Fig. 4.32 we can see the simulated dispersion diagram of the unit cell. The phase velocity v_p of this unit cell is comparatively fast with about $0.85/c_0$ at 8.5 GHz or a $\lambda_g = 30.2\,\mathrm{mm}$.

The guided wavelength is an important property, as this design uses a series feed and all radiating elements are excited with a progressive phase. In order to achieve broadside radiation, the patches of one row must be separated so that the phase between them is an integer multiple of 2π. The separation between the rows must be $\pi/2$, so that the orthogonal polarizations form circular polarization. A higher phase velocity results in a wider spacing of the radiating patches. Reducing the difference

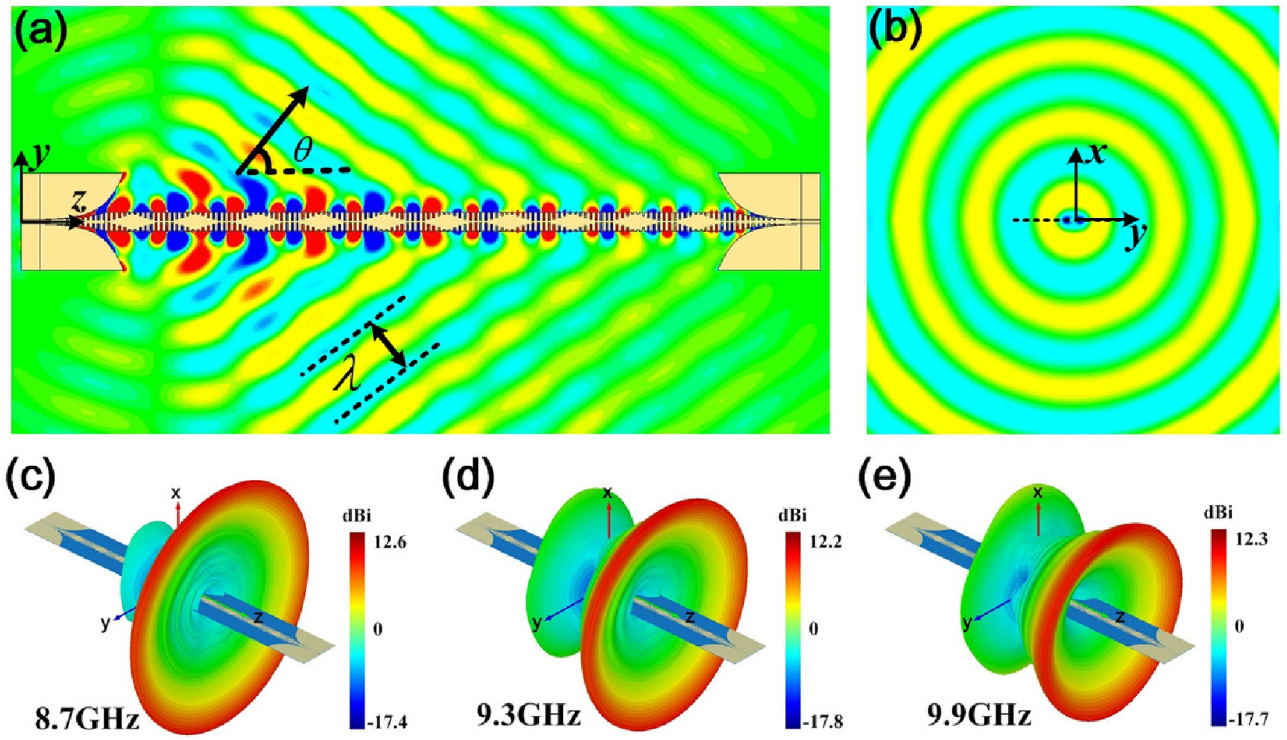

Figure 4.30: SSPP leaky-wave antenna produced by Kong et al.[111]. The figure shows the electric field distribution near the antenna in the y-z plane (a) and x-y plane (b). The far-field patterns at 8.7 GHz, 9.3 GHz and 9.9 GHz are shown in (c-e). Reproduced under the terms of the CC-BY license.

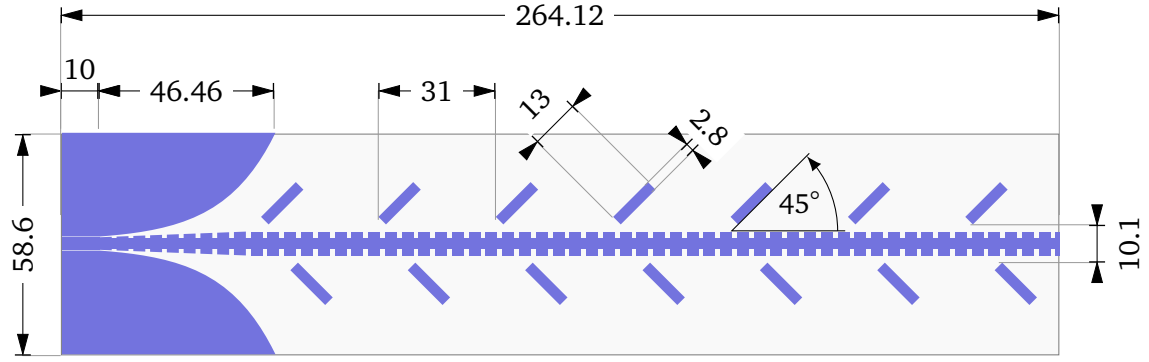

Figure 4.31: Mask of the leaky wave antenna. Components in the antenna from left to right: CPW line for coaxial adapter, flaring ground, waveguide with radiating elements.

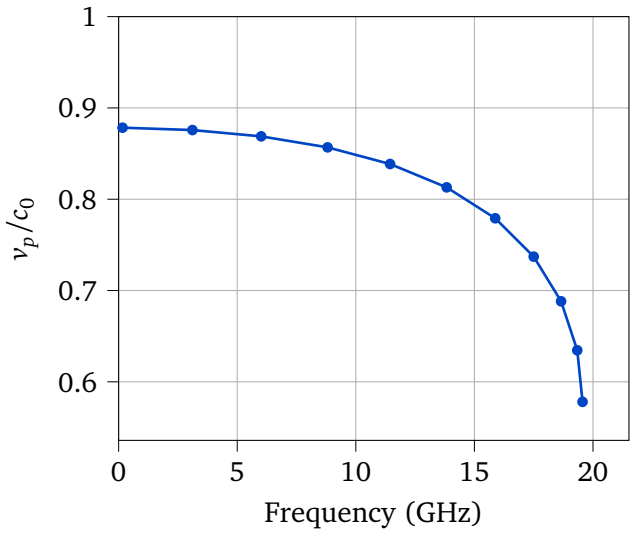

Figure 4.32: Dispersion diagram of the waveguide unit cell.

between λ_g (and thus, the patch separation) and the free-space wavelength λ also improves the antenna gain and so is preferred.

The patches themselves act as dipoles and are excited via capacitive coupling. The coupling can be manipulated by moving the patches closer or further away from the waveguide. This however, was not done to reduce the degrees of freedom in this design, resulting in non-uniform excitation. A future design should also consider this option as it potentially decreases sidelobes. The length of the ideal dipole would be $\lambda/2$, with the actual length being reduced by the velocity factor of the patch. A shorter patch has advantages, as it reduces the footprint of the assembly. This however, comes at the cost of reduced radiation efficiency and gain, the more the patch length deviates from $\lambda/2$.

The antenna in this design is not a travelling wave antenna, in contrast to the antenna shown in Fig. 4.30. The matched termination used in that design is not feasible without additional circuit elements like resistors. While Zu et al. have shown, that bendable carbon resistors can be integrated on thin foil SSPP circuits[96], the consequences of such an implementation with regard to thermal and environmental aspects require more study. The design shown here instead uses an imperfect open termination. The termination is imperfect in the sense that it is not well-defined and will result in leaky radiation. However, this problem can be minimized by radiating enough power before the termination so that its impact becomes small. Since this design uses a non-uniform excitation, this also means that the last radiating element couple will have a smaller impact on the gain. Therefore, there is a trade-off to be made between element number and termination quality, in order to reduce the antenna's footprint. In this design however, we used 7 element couples as a good tradeoff that also factored in manufacturing cost.

In order to find a good balance between these aspects and parameters that ensure high gain, high CP quality and a broadside beam, we optimized the initial design using CST's built-in genetic algorithm optimizer. The optimization was performed in 60 iterations with a population size of 64. The optimization goals were:

Goal	Target	Range
S_{11}	$< -20\,\mathrm{dB}$	8.4 GHz to 8.5 GHz
S_{11}	move min	8.45 GHz
Gain	move max	$(\varphi = 0, \theta = 0)$
AR	move min	$(\varphi = 0, \theta = 0)$

The parameters obtained from the optimization are given in Tab. 4.2. The simulation result shows very good performance in terms of radiation efficiency of 93 % and a gain of 10.4 dBi. Both values are

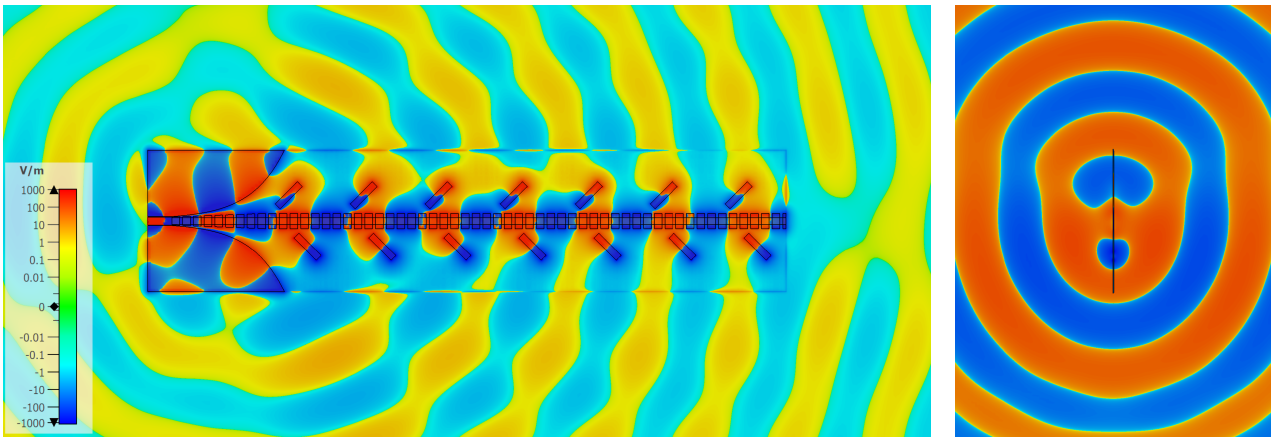

(a) x-y plane (b) y-z plane

Figure 4.33: Normal components of the instantaneous E-field at frequency 8.45 GHz on a common scale. The radiated power in the lateral direction is significantly lower. The radiating elements are all in phase with only little variation in the upper element row.

Table 4.2: Parameters of the leaky wave antenna. Values are given in mm.

Parameter	p	w	h	g	L0	W0	L1	L2	L3
Value	4.43	6.32	1.74	1.27	264	58.6	31	13	10.1

very similar to those given in [99].

The resulting antenna 3D left hand circular polarization (LHCP) directivity pattern is shown in Fig. 4.34. We can observe a fan-like pattern, with the main lobe pointing broadside. There are two larger side-lobes pointing backwards in the $\pm y$-direction which result from the lack of backplane.

4.3.2 Measurement

The antenna was produced on RO4350B substrate with a 18 μm copper layer and electroless nickel immersion gold (ENIG) surface finish. The prototype is shown in Fig. 4.35. The reflection parameter of the antenna was measured using a Rohde&Schwarz ZNB20 vector network analyzer (VNA). The simulated and measured results are presented in Fig. 4.36. The results appear in good agreement, with a minor shift of the resonance frequency and slightly higher reflections. This may be caused at least in parts by an imperfect connection at the coaxial adapters.

To further verify the simulation results, the far-field radiation pattern was measured in an anechoic chamber (see Fig. 4.37). Due to the thin substrate, the antenna is not stiff enough to be mounted on its own. Hence, the antenna was stabilized in a 3D-printed mounting bracket made from PET. The model of the mounted antenna is shown in Fig. 5. The simulation results presented in the following include the bracket.

4.3.3 Results and Discussion

The E-plane far-field patterns of the antenna are presented in Fig. 4.38. The results show good agreement between simulation and measured result. We can see that there is no angular difference between the three frequency samples, owing to the flat dispersion curve in the band. The amplitude deviation between the frequencies is very consistent and low. However, in the $\varphi = 0°$, we can see back-lobe that is not present in the simulation, which is caused by a poor axial ratio (AR) in this direction.

We further inspect the AR in Fig. 4.39. Here, the AR is displayed for cuts in θ. We can see that the AR

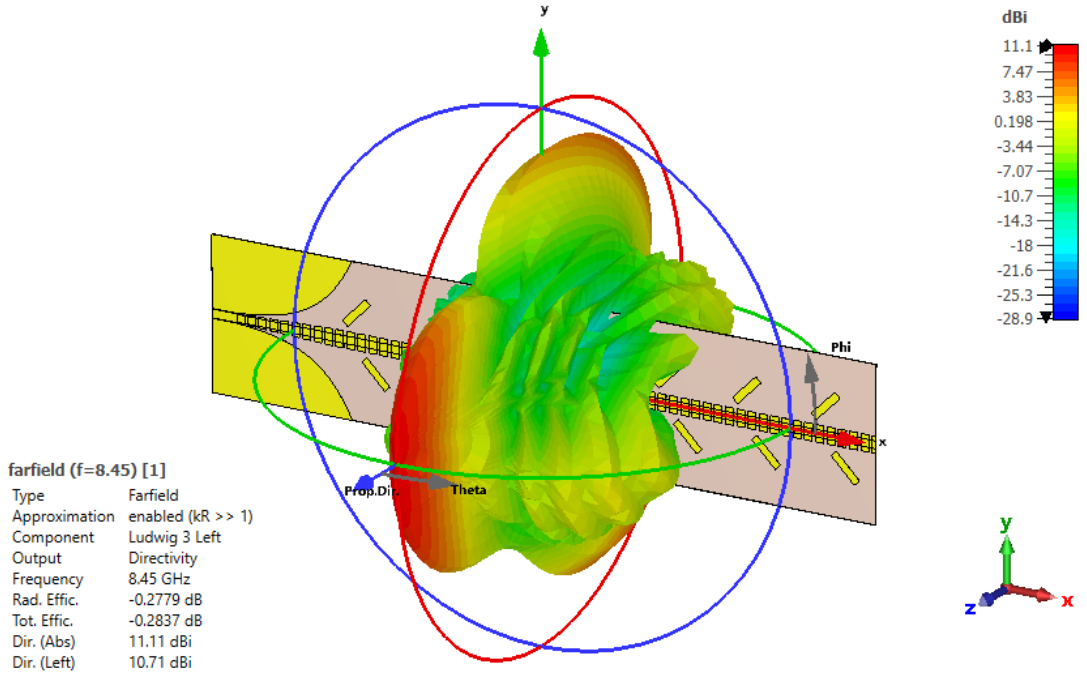

Figure 4.34: LHCP far field directivity of the leaky wave antenna, simulated in CST MWS.

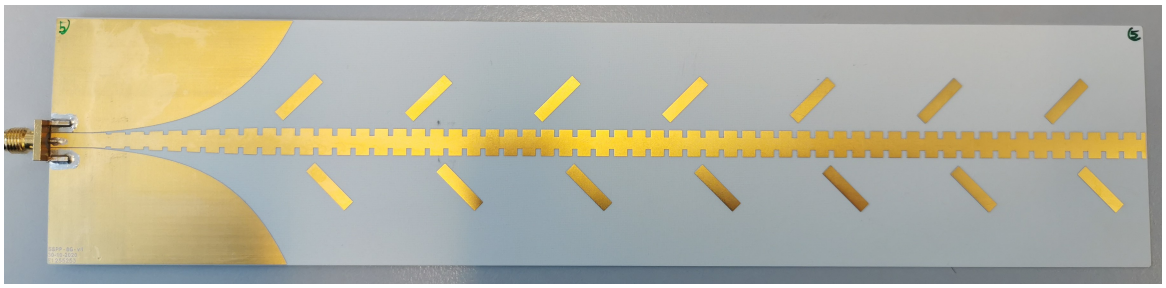

Figure 4.35: Manufactured prototype of the circular polarized leaky wave antenna.

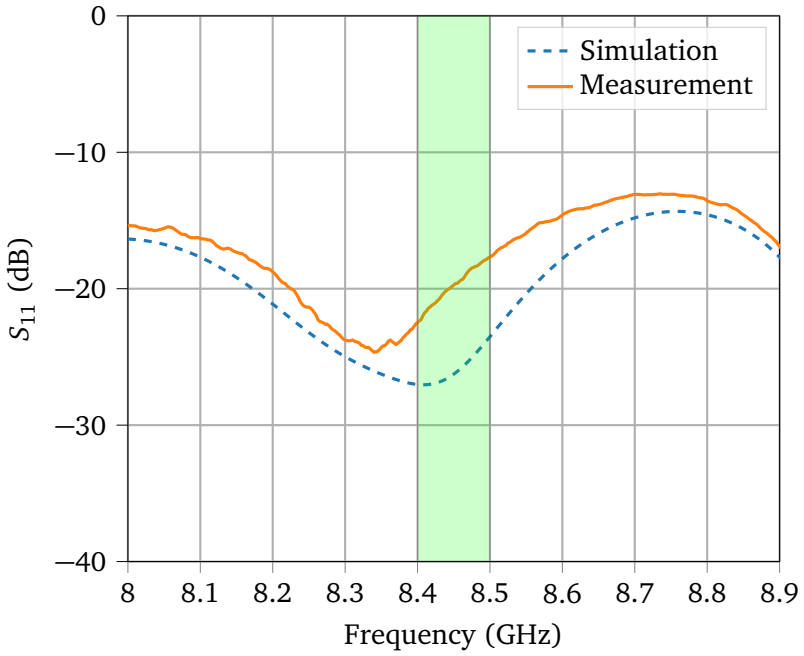

Figure 4.36: S-Parameters of the leaky wave antenna. The desired frequency band of 8.4 GHz to 8.5 GHz

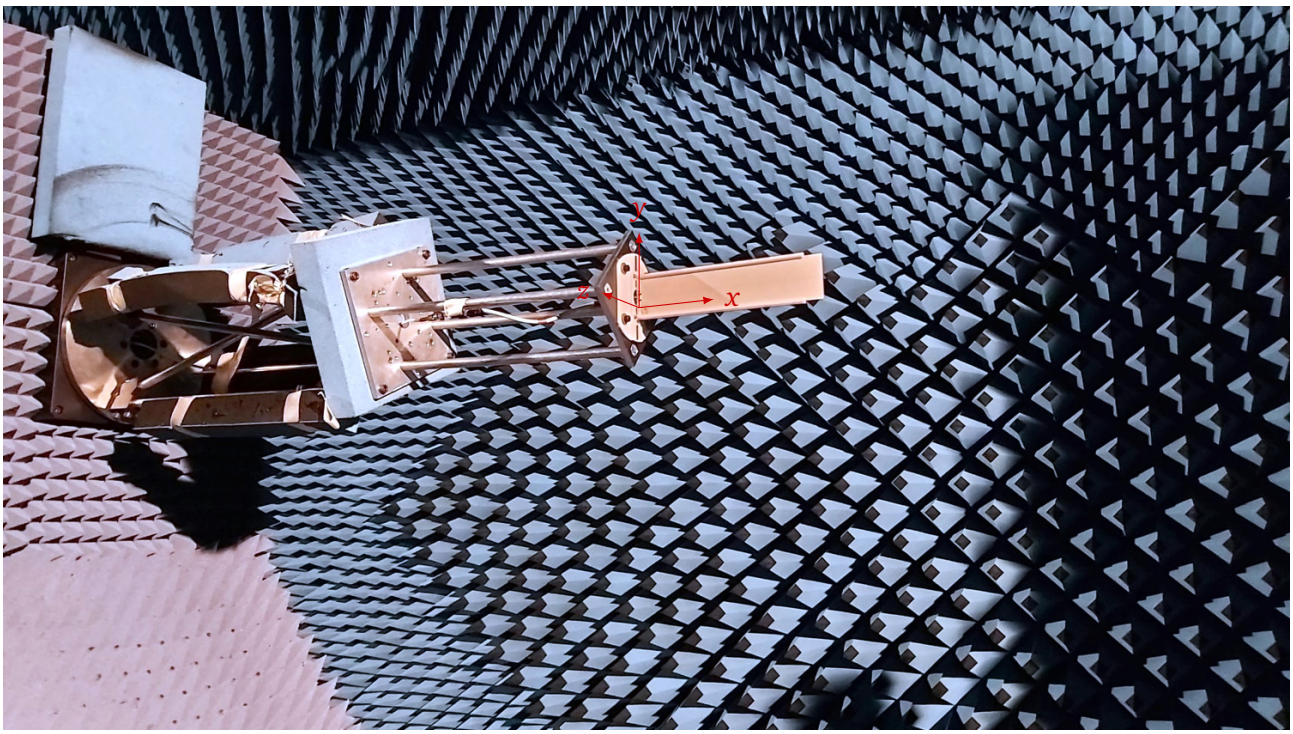

Figure 4.37: Antenna measurement in the anechoic chamber of the Chair of High-Frequency Engineering at TUM. Image Credit: T. Eibert (TUM).

is significantly higher in the main beam direction $\varphi = 0$ with a separation of 6.5 dB in the measurement vs. 1.3 dB in the simulation. Additionally, the lowest point is shifted by about 15°. Some degradation of this property is expected, e.g. due to manufacturing inaccuracies and the holding bracket. Additional sources of unknowns are the coaxial adapter as the antenna proved to be sensitive regarding the solder connection with the coaxial connector adapter. Another important unknown is the ENIG surface finish, which consists of a 3 μm to 6 μm nickel layer that separates the copper from the top gold layer with a thickness of about 0.1 μm. Earlier publications focused on the resonant properties of nickel at about 2 GHz to 3 GHz, and reported only minor effects beyond higher attenuation in microstrip lines beyond that frequency range[115, 116]. Seiler et al. investigated the effect of ENIG on microstrip lines and reported higher attenuation and dispersion due to the nickel content for frequencies lower than 20 GHz[117]. The effect of the surface finish is less pronounced in microstrip lines, as most of the current flows on the substrate side. For this reason, we can expect the dampening and dispersive effect of nickel to be more noticeable in SSPP where the current flows over the nickel covered surface.

In the simulation, as well as in the measurement, the antenna showed great potential towards a utiliziation in a solar sail antenna array and at the same time, affords ample opportunity for further enhancement. A major improvement to the antenna would be the implementation of additional radiating elements for higher gain. This would best be combined with the implementation of an improved excitation scheme, in order to improve power distribution to the farther elements, but also further reduce the side-lobe level.

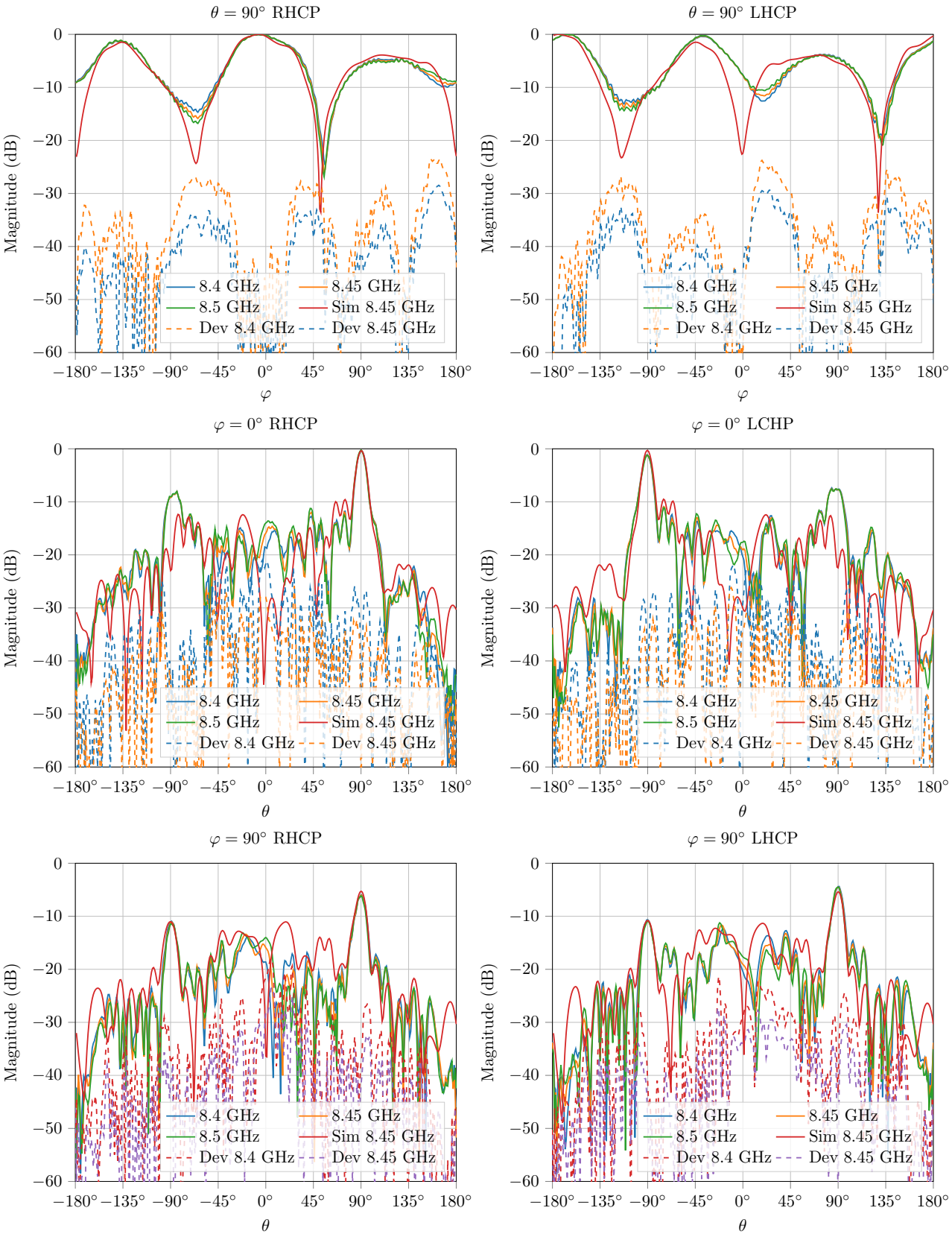

Figure 4.38: Measured RHCP and LHCP E-field magnitude of the leaky wave antenna. The patterns were normalized to the respective maximum. The dashed lines show the deviation at the respective frequency from the 8.5 GHz reference value. The patterns show good agreement with the simulation. The $\varphi = 0°$ cut reveals a front-to-back ratio that is higher than expected.

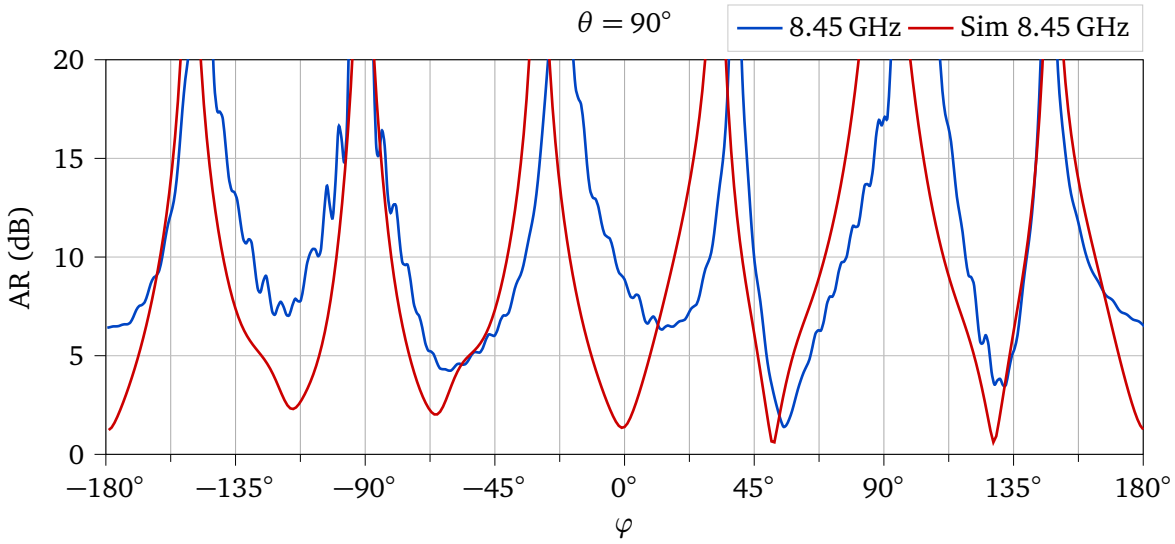

Figure 4.39: Simulated and measured AR for $\varphi = 0°$.

4.4 Power Divider

The power divider is a crucial element of the corporate feed of the array antenna. Several power dividers based on the SSPP TL have been published in the past:

Gao investigated an equal Y-splitter based on a transition from a "composite H-structure" to a common H-shape unit cell[90] (see Fig. 4.40(a)). Around the center frequency of 9 GHz, the divider achieved an excess insertion loss[1] of more than 1 dB and no information regarding phase imbalance and isolation were given. A three-way power divider also based on a composite structure was presented by Farokhipour with 3.5 dB excess insertion loss, 9 dB isolation and 4° phase imbalance at a center frequency of 5.25 GHz[118]. Wu presented several equal and unequal power dividers based on bowtie-shaped unit cells (see Fig. 4.40(b))[92]. The excess insertion loss was measured lower than 3 dB in the 3 GHz to 8 GHz band. Zhou developed a divider with >4.5 dB excess insertion loss[94] and four-way splitter with >3 dB excess insertion loss[95]. Li et al. presented a Y-splitter using bowtie unit cells operating around a center frequency of 3.3 GHz with an excess insertion loss of 2.3 dB[93]. Zu developed a flexible "Wilkinson" divider with 3 dB excess insertion loss at 9.5 GHz[96] (see Fig. 4.40(c)). The design was built on a flexible PCB with a graphene flake as resistor, that improves the isolation of ports two and three to about −17 dB. Interesting about this design is also the transition from H-shaped to u-shaped unit cell.

4.4.1 Design

When designing SSPP power dividers, careful consideration must be given to how the individual unit cells will seamlessly interconnect when multiple dividers are chained together in series. Unfortunately, existing power divider designs suffer from a lack of continuity in their unit cell structures. For instance, these designs often commence with an H-shaped cell but conclude with a u-shaped cell, resulting in an ill-defined transition from H to u.

This discontinuity in the unit cell structure gives rise to significant losses when chaining multiple power dividers together. The impedance mismatch at the junction between cells leads to undesirable reflections, consequently diminishing the overall performance of the power divider. This concern becomes even more pertinent when contemplating corporate feeds involving numerous interconnected power dividers.

[1] We define excess insertion loss as the ratio between the theoretical insertion loss caused by splitting and the measured insertion loss.

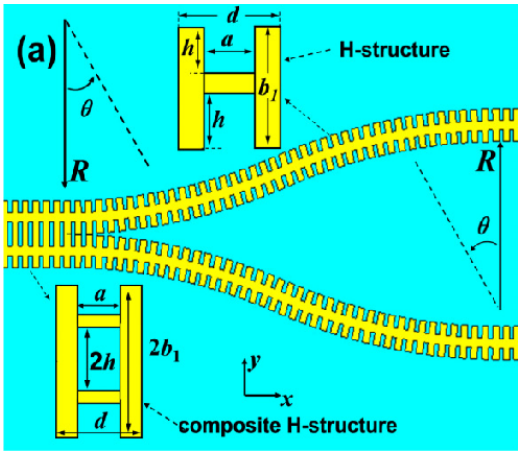

(a) Power Divider by Gao[90]. ©2015 Optica Publishing Group.

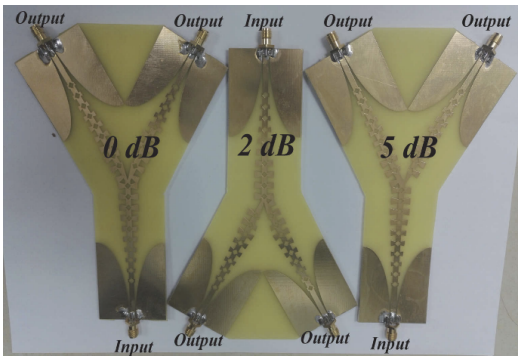

(b) Power Divider by Wu[92]. Reproduced under the terms of the CC-BY license.

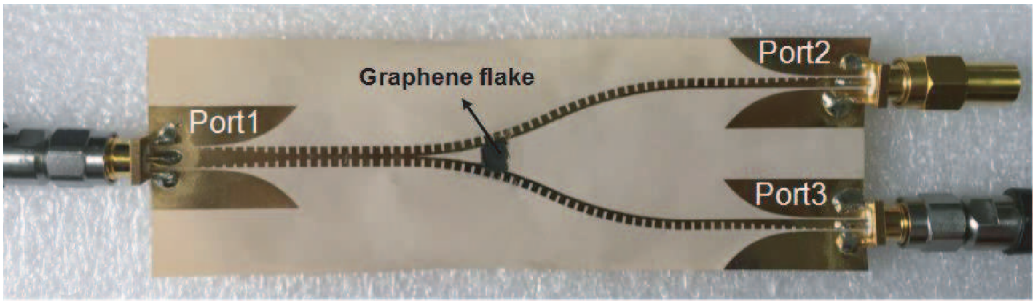

(c) Power Divider by Zu[96], ©2019 IEEE

Figure 4.40: Images of related equal and unequal power dividers.

To overcome this challenge, our focus lies in the development of a structure that maintains a continuous and coherent transition throughout the divider. While envisioning a seamless transition from the "composite H-structure" proposed by Gao to the conventional H-structure presents difficulties, direct splitting of the structure, as employed with bowtie unit cells, is unappealing due to the reported high losses documented in the literature[92].

However, the H-to-u transition introduced by Zu[96] provides a promising foundation for constructing a splitter with an intermediate u-shaped line that subsequently reverts back to the H-shape. In the subsequent sections, we present a design that employs a linear transition from the u-shaped unit cell to the H-shaped unit cell, ensuring continuity within a cascaded divider configuration.

A sample divider design, exemplifying the implementation of this complete transition, is illustrated in Fig 4.41. By incorporating this seamless transition, we aim to mitigate the challenges posed by the discontinuity and enhance the overall performance and efficiency of the power divider system.

The design uses a unit cell with $p = 3mm$, $w = 7mm$, $g = 0.6p$ and $d = 0.4w$. The divider is designed for 0.5 mm Rogers corporation laminate 4003C (RO4003C) with a 35 μm copper layer. The divider consists of six different regions. Starting at port 1, first comes a CPW for the attachment of the coaxial adapter. Afterwards, the CPW mode is converted to SSPP with an exponential tapered ground. These converter steps are the same for all ports.

It follows the divider with a H-unit cell to u-unit cell bent transition which divides the path into two. To realize the bend, the five u-unit cells are inclined evenly for a total angle of 21°. The unit cells in this section are wider with $w = 7.12$ mm and $d = 0.41w$ to account for the smaller separation at the tip due to the angle. As we can see in Fig. 4.42 the properties of u-cell and H-cell agree well. Determining the optimal angle for the bend involves careful consideration of various factors, including space requirements, TL length, and overall footprint area. A shallower angle effectively mitigates discontinuities and reflections within this section. Conversely, a steeper angle leads to greater devia-

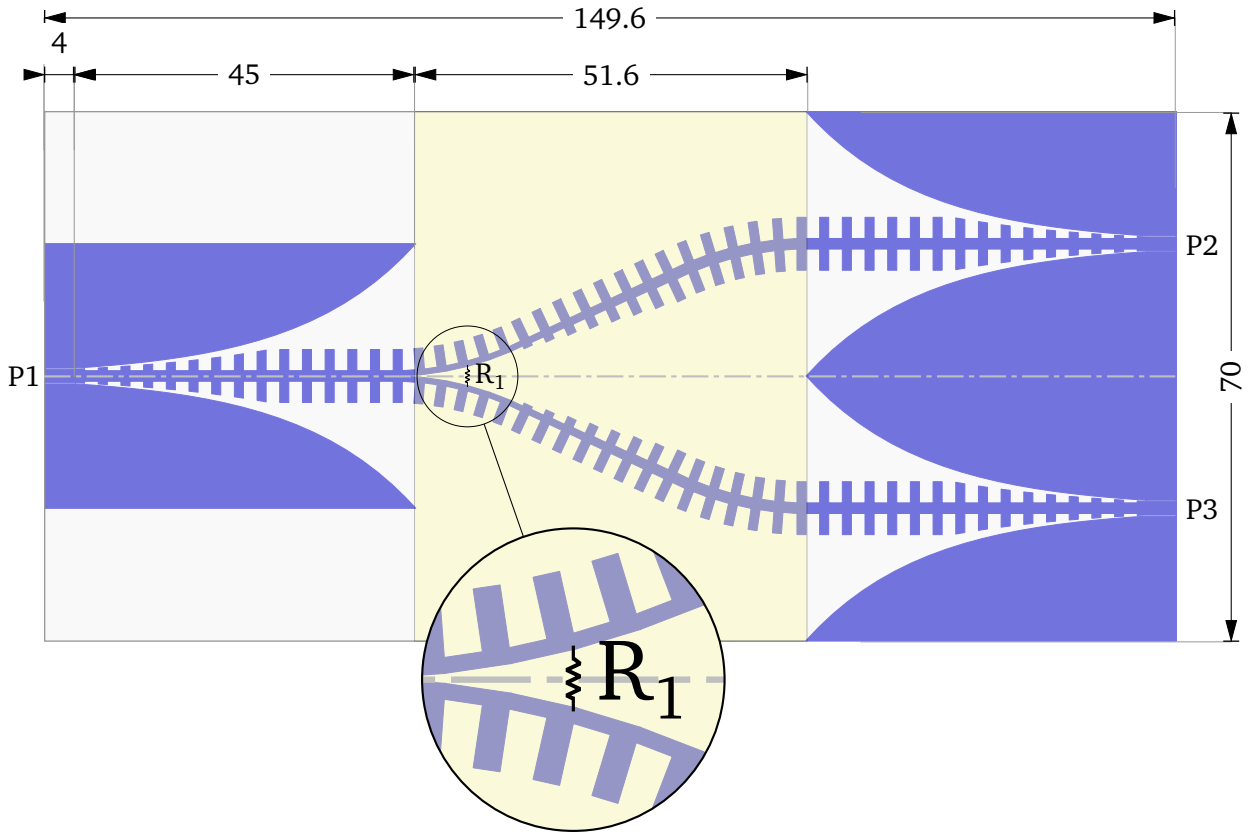

Figure 4.41: Surface profile and dimensions of the SSPP divider.

tions in unit cell behavior from the anticipated simulated properties. It is noteworthy that due to the non-periodic nature of the bent unit cell, accurately modeling the dispersion within the bend poses inherent challenges.

Subsequently, a linear section follows, transforming the u-unit cells into H-unit cells through a progression of seven steps. Lastly, just prior to reentering the converter, the H-unit cell's transmission line undergoes another bend, ensuring its alignment with the initial orientation. It is worth noting that this particular adjustment is not necessary for all power dividers within the corporate feed, but solely for the last one preceding the antenna.

However, it is important to consider that due to limitations in CST's time domain solver, the alignment of waveguide ports with the mesh becomes necessary. Consequently, as the entire bend constitutes a discontinuity, there may be some additional losses through radiation, although this is not a prevalent issue in most cases.

The power divider was subjected to simulation using two distinct dielectric materials, namely RO4350B and RO4003C, characterized by respective relative permittivity values of $\epsilon_r = 3.38$ and a loss tangent of $\tan\delta = 0.0027$. This approach was adopted to account for the influence of different manufacturing processes, which will be elaborated upon in subsequent discussions.

Figure 4.43 showcases the reflection and transmission parameters obtained from the simulation results. Notably, both versions of the power divider exhibit a predominantly similar characteristic. It is worth observing a slight resonance shift in the S_{11} plot due to the variation in ϵ_r between the two dielectric materials.

Both versions exhibit favorable performance, characterized by a good S_{11} reflection coefficient below -20 dB and S_{21} transmission coefficient ranging between -4.0 dB and -3.85 dB. Comparatively, the S_{21} transmission coefficient is marginally superior in the case of the RO4003C material. This is partially due to the lower loss tangent of the RO4003C material.

Considering the minimal reflection at the input port, we infer that the insertion loss is not predom-

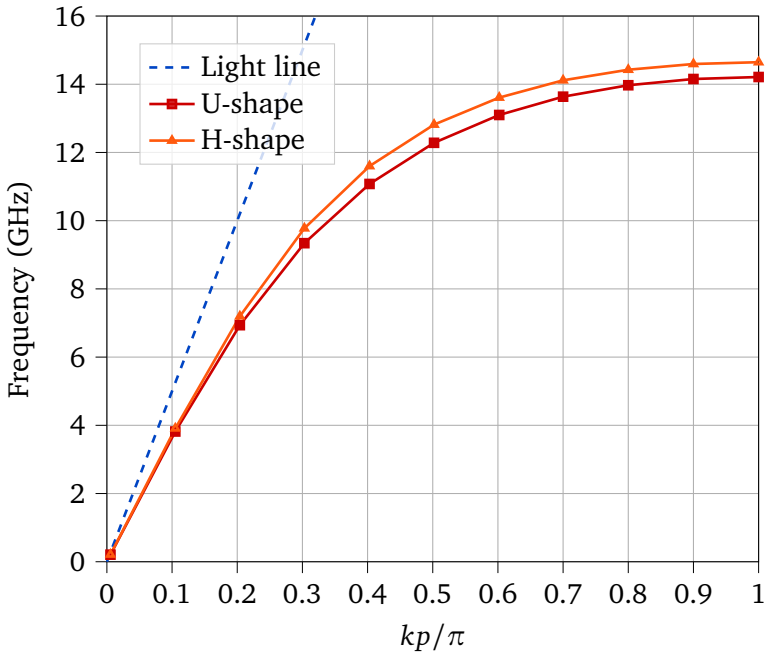

Figure 4.42: Simulated dispersion diagram of the unit cells used in the divider design. The dashed line represents the propagation of light (light line).

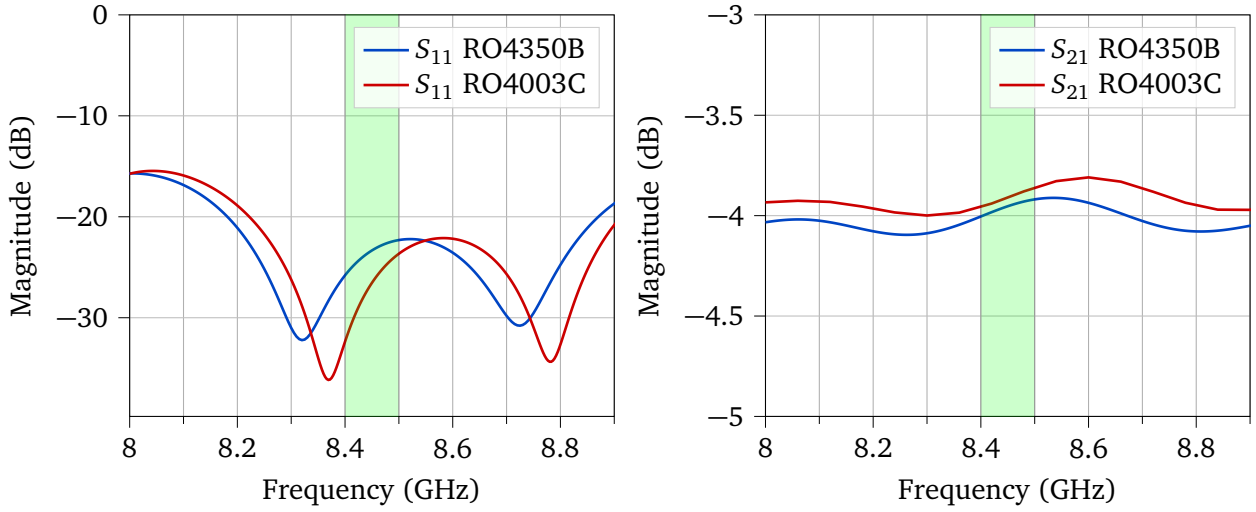

Figure 4.43: Simulated S-parameters of the power divider using RO4350B and RO4003C substrate.

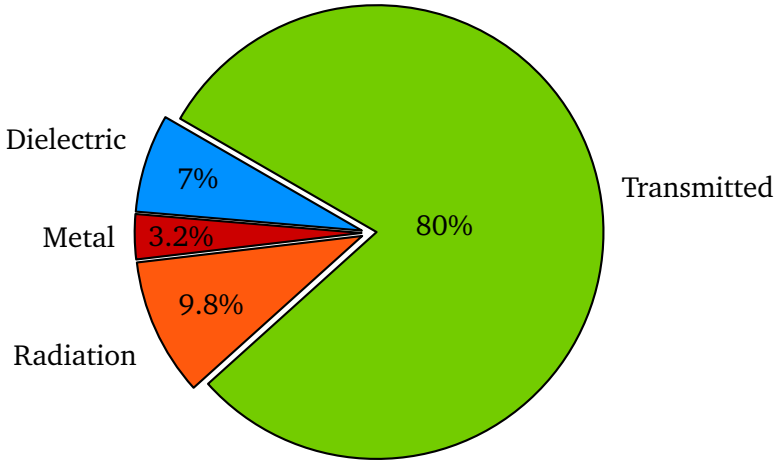

Figure 4.44: Power lost in the power divider relative to the total excited power.

inantly attributed to reflection. To further analyze the losses, we refer to the built-in loss analysis feature of CST Microwave Studio (cf. Fig. 4.44). As we can see, a large portion of the loss is due to the dielectric substrate, and will not apply when used on the membrane. The radiation loss percentage aligns with the expected behavior for the utilized mode converter, as observed previously in Section 4.2.2.

Port Isolation Let us now shift our focus to the crucial aspect of port isolation. As a passive device, the power divider inherently possesses reciprocity and is not inherently lossy. However, it is important to address the issue of port isolation. According to network theory, due to the symmetric nature of ports 2 and 3, both ports must exhibit equal levels of mismatch, resulting in a lack of isolation [81].

The absence of port isolation can potentially present challenges within a larger system, as reflections from one port can adversely affect the other. In an extreme scenario, such as when a part of the membrane is damaged by an impacting micrometeorite, the reflection could have a detrimental impact on the other port, potentially leading to the complete malfunctioning of the entire antenna. In a more probable scenario, the presence of isolated ports helps mitigate the effects of minor reflections arising from manufacturing imperfections.

To overcome this challenge, the design principle of the Wilkinson divider introduces a resistor between the two ports, thereby introducing a controlled level of loss [81]. This principle was first demonstrated with SSPP by Zhou et al.[94]. Later, Zu et al. demonstrated that a graphene flake placed between the two arms of the divider can serve as the desired resistor while maintaining flexibility [96]. The resistor is positioned at a distance of approximately $\lambda/4$ from the split, as illustrated in Figure 4.41, and its dimensions are optimized to ensure that the voltage from a reflection is effectively canceled out by its shifted image on the other arm.

To explore the impact of different resistance values, we conducted a simulation sweep with the resistor placed 8 mm from the split. The results of this sweep are depicted in Figure 4.45, providing valuable insights into the performance of the power divider with varying resistance values of 150 Ω and 200 Ω.

Both resistance values demonstrate excellent matching characteristics at the output port, with a return loss of −20 dB, while effectively reducing the isolation to below −25 dB. It is worth noting that higher resistance values are preferred to minimize losses. The figure clearly indicates an optimal resistance range between 150 Ω to 200 Ω, as higher resistance values tend to shift the S_{23} parameter towards higher frequencies.

Additionally, the transmission parameter S13 remains relatively constant across the different resistance values. However, it is important to highlight that lower resistance values would lead to a degradation in the performance of S13.

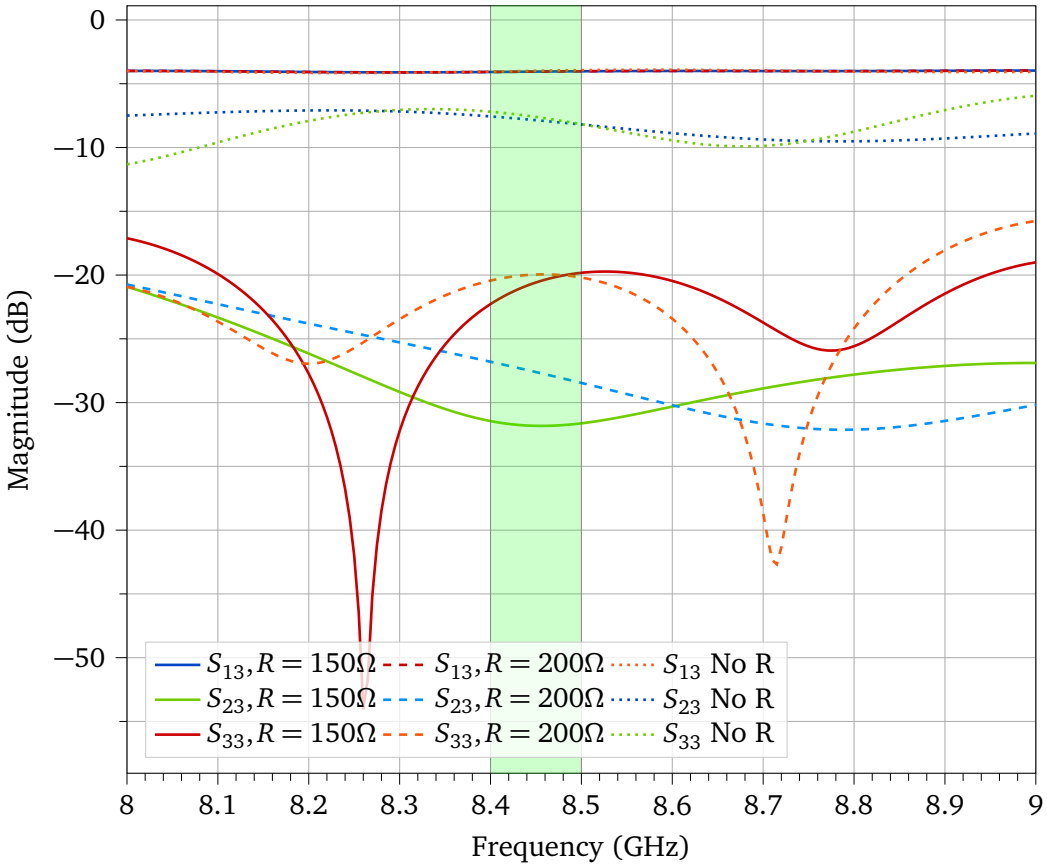

Figure 4.45: Improved port matching and isolation with a resistor placed between the ports.

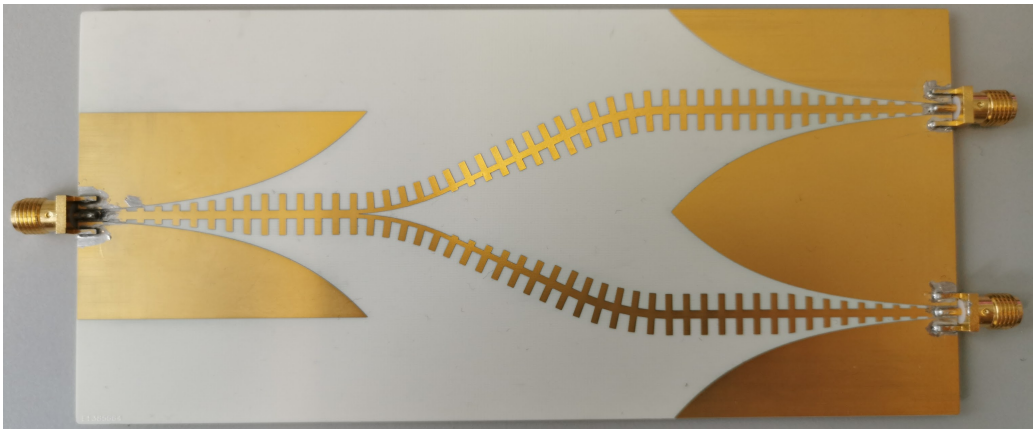

Figure 4.46: Picture of the power divider on RO4350B with ENIG finish.

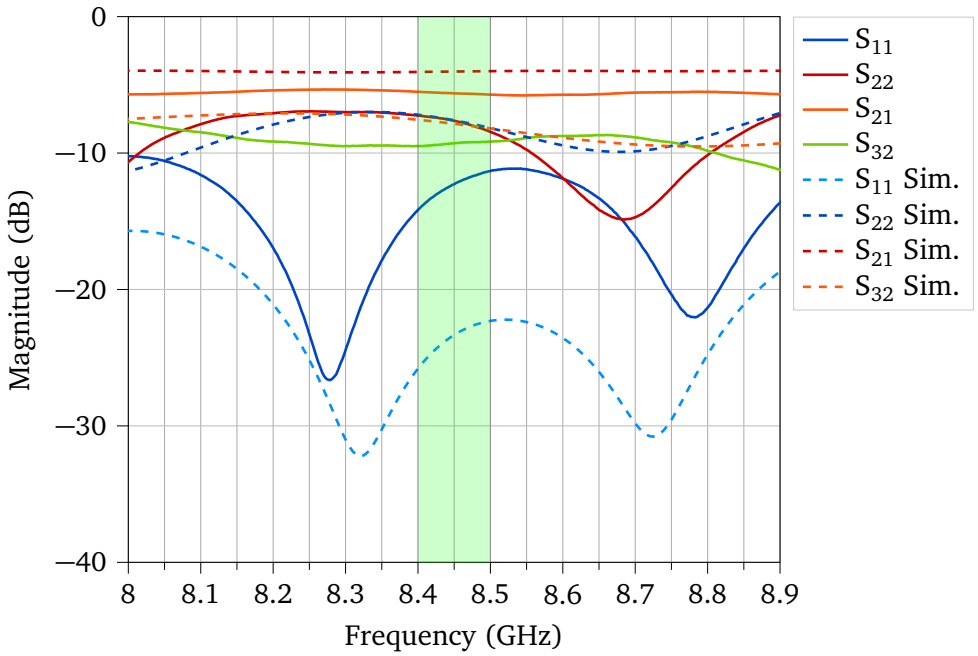

Figure 4.47: Simulated and measured S-parameters of the ENIG power divider without isolating resistor between port 2 and 3.

4.4.2 Measurement

The power divider was manufactured on 0.5 mm RO4350B with 18 μm copper weight and ENIG surface finish. The divider was measured in a 3-port measurement using a Rohde&Schwarz ZNB20 vector network analyzer. Figure 4.47 displays the subset of port 1 reflection and transmission parameters. The measurement reveals a surprisingly high S_{11} magnitude with a wide margin of more than 10 dB to the simulation. This is accompanied by a decrease of the transmission parameter by −1.4 dB to −1.8 dB.

To rule out any effects from the surface finish, a second divider model made on RO4003C substrate and bare copper surface was manufactured. In Figure 4.48 we can see the difference in reflection and transmission between the two models. The measured S_{11} parameters of both models are in close agreement. The difference of the measured S_{21} of both models is within the predicted range, given some additional leeway for manufacturing tolerances. Both models differ vastly from the simulation. Further investigation into this issue were conducted with improved coaxial adapter transition with $S_{11} < -20dB$ below 10 GHz and $S_{21} < -1.1dB$ below 8.5 GHz. The measurements of this improved transition are presented in Appendix C. This test proves that a large portion of the discrepancy is caused by the coaxial adapters.

The measured matching and isolation of port 2 and 3 matches the prediction with a magnitude of −9.1 dB to −9.4 dB. As previously discussed, the port matching and isolation can be improved through a resistor. Figure 4.49 shows the measured result of the power divider with a 150 Ω resistor inserted between the divider arms. We can see a drastic improvement of the output return loss to −15 dB and the port isolation improving to −22 dB.

We now turn to the amplitude and phase balance of the divider, which are important properties, especially when considering a larger array with many elements, as phase and amplitude errors accumulate and deteriorate array performance. Fig. 4.50 depicts the magnitude imbalance of the transmission parameters of the divider with and without the matching resistor. The low-frequency ripple of 0.4 dB magnitude is a product of connector mismatch. We can see that the resistor reduces the amount of ripple and imbalance between the ports, while simultaneously improving the transmission by 0.2 dB. Without the resistor, the amplitude imbalance is 0.1 dB and reduces to 0.05 dB with resistor.

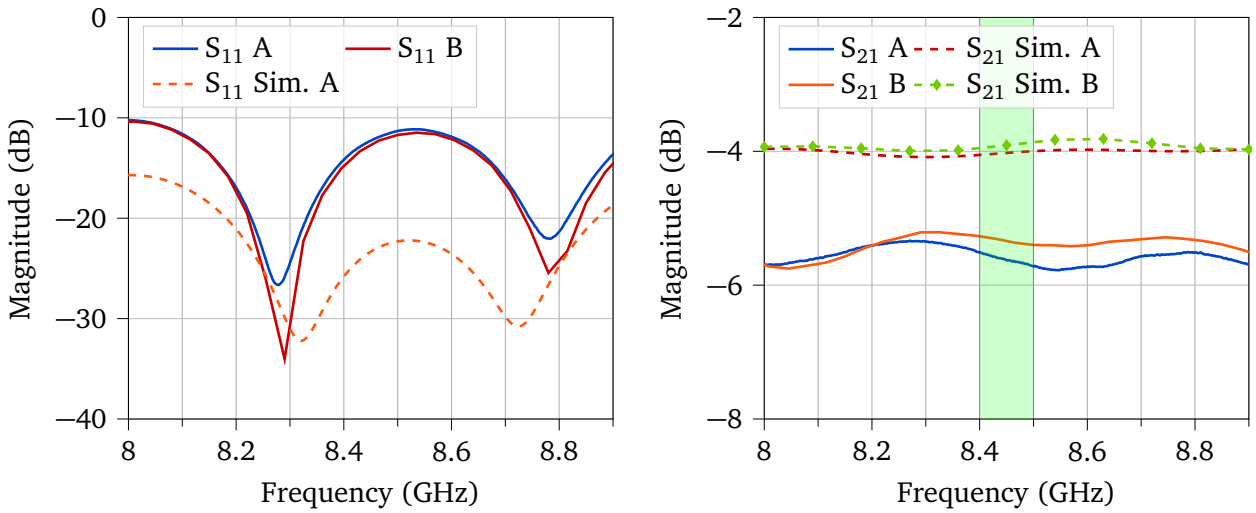

Figure 4.48: Comparison of the power divider models built on RO4350B (A) and RO4003C (B) substrate.

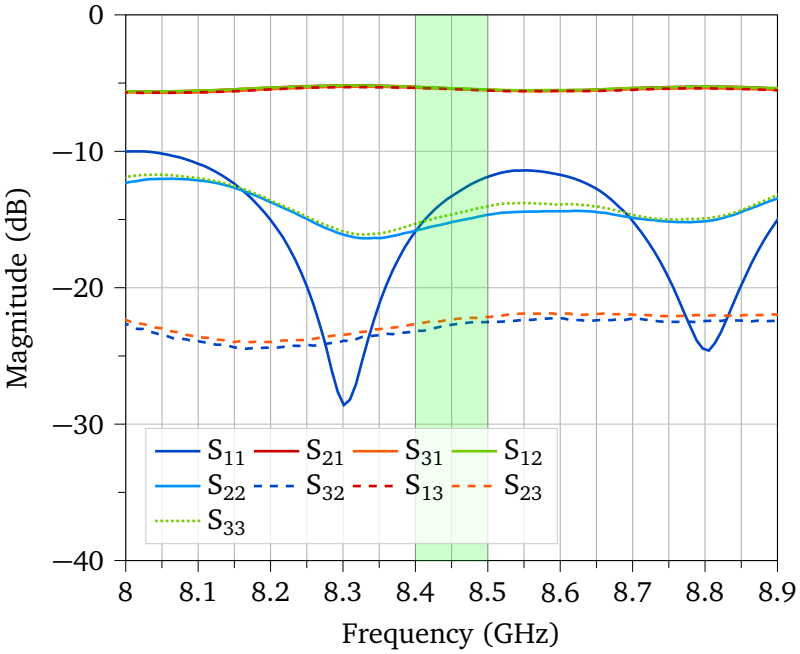

Figure 4.49: S-Parameters of the divider with 150 Ω resistor.

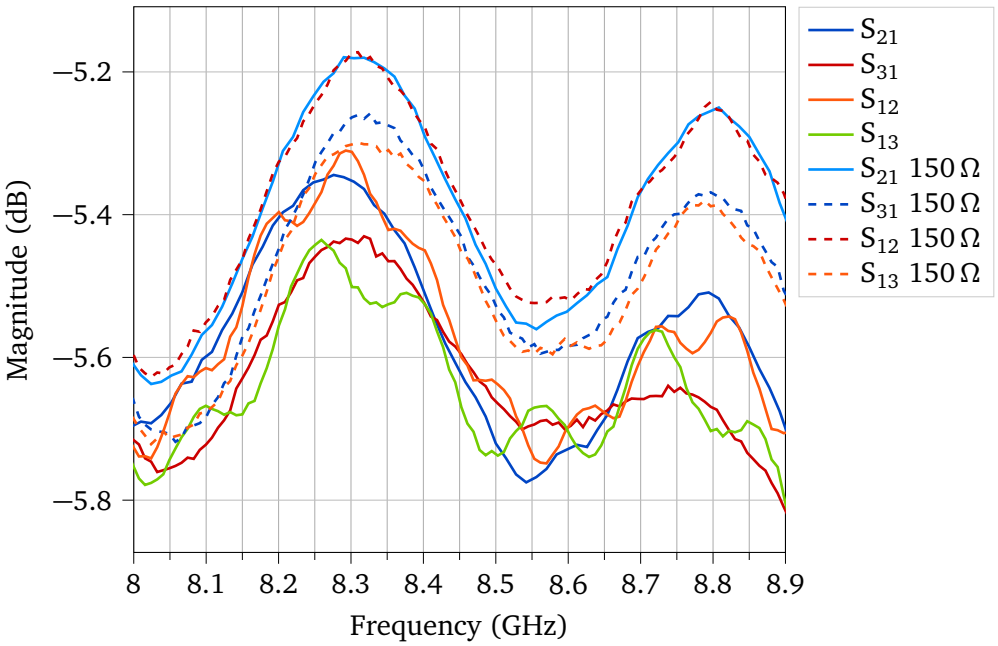

Figure 4.50: Magnitude imbalance of power divider with and without matching resistor.

The measured phase difference between the ports has an excellent value of 1.7° to 2.0° between 8.4 GHz to 8.5 GHz.

4.4.3 Discussion

In this section we presented a power divider based on SSPP TL. The key objective was to develop a divider design that can further be used as a component in the membrane array. A major issue in this regard is the geometric division of the SSPP line into two, while maintaining low reflection. A solution was found in the literature with a curved transition from a symmectric H-shaped unit cell to a u-shaped unit cell. The power divider is supposed to be cascaded in the corporate feed of the membrane antenna and therefore, an additional transition to the H-shaped unit cell is required. This transition was designed as asymmetric linearly tapered H-cell. Low insertion loss is an desireable property in the divider, especially for larger arrays. Hence, the parameters of the prototype were fine-tuned so that finally, the simulated excess insertion loss was only 1 dB.

We produced a prototype divider on 0.5 mm RO4350B and measured it using a VNA. The measured performance was significantly lower than anticipated, which we could trace back to poor coaxial connectors. The measured excess insertion loss was between 2.3 dB to 2.8 dB in the range of 8 GHz to 9 GHz. Nevertheless, the prototype provided valuable insight into the design. The prototype was measured with an additional resistor between the arms, as to form a sort of Wilkinson divider. The measurement verified that this can significantly improve the isolation between the ports to −22 dB. This modification also improved the return loss of port 2 and 3 to −15 dB and decreased the insertion loss by 0.2 dB and reduced ripple. Despite the connector issues, the measured phase difference between the ports has an excellent value of 1.7° to 2.0°.

The power divider design showcased in this work exhibits satisfactory characteristics in terms of insertion loss, return loss, and transmission efficiency. These results align with similar power divider designs reported in previous literature (cf. Tab. 4.3). However, it is crucial to acknowledge that the connector mismatch, which affects the impedance matching at the ports, prevents the power divider from achieving its optimal performance.

If the connector mismatch issue were resolved, it is reasonable to expect an improvement in the performance of the power divider. This could potentially result in reduced insertion loss, enhanced

Table 4.3: Comparison of SSPP power dividers

Source	Frequency	Excess IL	Isolation	Phase Imbalance
[90]	9 GHz	1 dB	N/A	N/A
[118]	5.25 GHz	3.5 dB	9 dB	4°
[92]	3 GHz	3 dB	N/A	N/A
[94]	6 GHz	1.5 dB	N/A	N/A
[93]	3.3 GHz	2.3 dB	11.7 dB	1.9 dB
[95]	7 GHz	1.8 dB	N/A	N/A
[96]	9.5 GHz	3 dB	15 dB	N/A
This Work	8.5 GHz	2.1 dB	22 dB	1.7°

return loss, and improved transmission efficiency. Therefore, the presented power divider design has the potential to surpass the performance of similar designs reported in the literature.

It is worth noting that the connector mismatch is a common challenge in practical implementations and may not be easily overcome. Nevertheless, the results obtained in this work provide a valuable benchmark for future research. Addressing the connector mismatch issue and refining the converter design could lead to an even more advanced and efficient power divider in the future.

4.5 Advanced Designs

The section below describes advanced designs for an array antenna and power divider that build on the previous sections. First, we will present a four-way power divider that extends the design from the previous section. Afterwards, we will discuss a leaky wave antenna with corporate feed. The goal of this section is to investigate the properties and challenges that arise when scaling the combining the individual components to a larger array.

Moreover, the performance figures obtained in this section lay the foundation for the performance estimation of larger arrays. By characterizing the power divider's key parameters, such as insertion loss, amplitude and phase balance, we gain valuable insights into its behavior and can make informed predictions about its performance when integrated into larger antenna arrays.

Similarly, by studying the behavior and performance of a small array, we can make valuable predictions and extrapolate insights for larger arrays. Small arrays serve as a representative sample that allows us to understand the fundamental characteristics and interactions between individual elements, paving the way for estimating the performance of larger-scale arrays.

Analyzing a small array provides us with essential information about key parameters such as radiation pattern, beamwidth, sidelobe levels, and overall array performance. By carefully observing the behavior of the small array, we can identify patterns, trends, and potential challenges that may arise when scaling up to a larger array configuration.

4.5.1 Four-Way Divider

The design of the previously discussed two port divider was extended to a four port divider through a basic cascade (cf. Fig. 4.51). In order to retain the same parameters of the previous model, an additional straight section with a length of 42 mm was inserted after the first division. This model allows us to study the effects of such a cascade and potential issues arising in a larger array.

Upon closer inspection, it becomes apparent that the geometry of the SSPP line leading to the individual ports is not symmetric. The curvature of the line, especially the number of bends into a certain direction is the same for port two and five, as well as three and four. The bending affects the unit cell properties, i.e., results in a different propagation velocity between each side of the unit cell. This

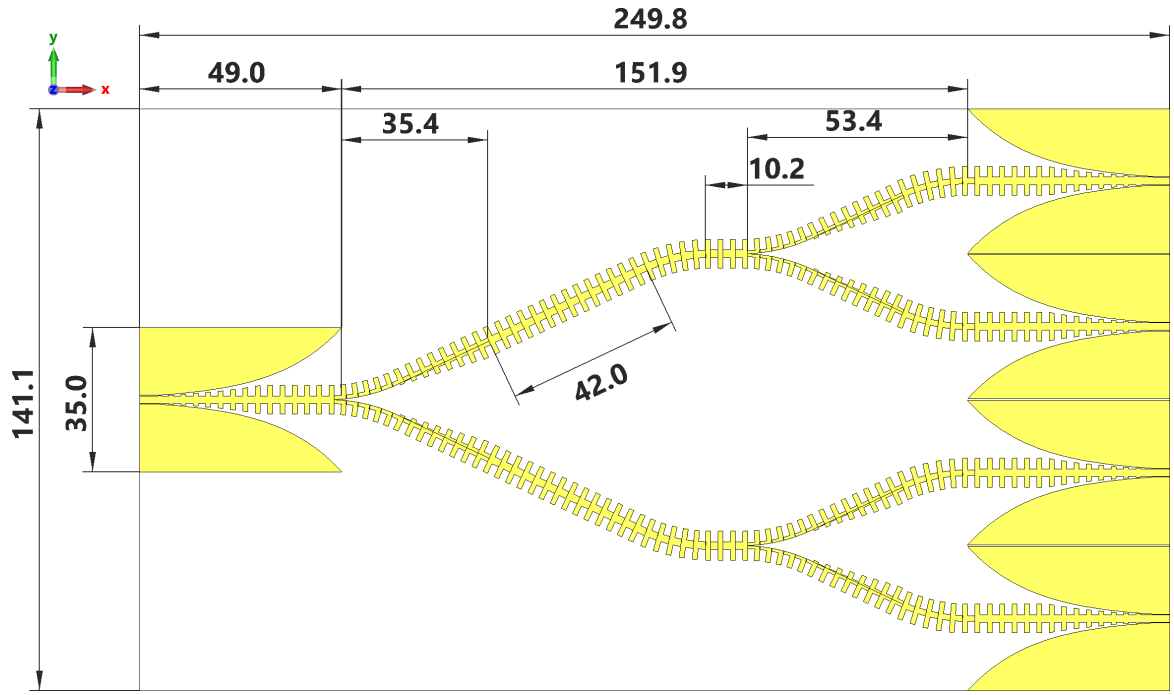

Figure 4.51: Dimensions of the 4-way SSPP divider

problem is also known with classical transmission lines[76]. Since the unit cells are almost $\lambda/4$ wide, this is expected to cause imbalance. We study the structure using simulation.

The model was simulated using CST Microwave Studio, the results of which are presented in Fig. 4.52. First of all, we can see a distinct amplitude difference between the ports 2 and 3 (the graphs of port 4 and 5 have been omitted but are the same) with an excess insertion loss of 1.5 dB and 2.3 dB, respectively. The larger loss is unsurprising, given the larger network and cascaded division steps. Figure 4.53 displays a breakdown of the losses in the divider. Compared to the two port divider, dielectric losses have only increased by less than 34 %, radiation loss has increased by 140 %. We suspect that this is also caused by the asymmetric bends and is also the cause for the decreased transmission, compared to the two port model. Not shown in the figure are the phases of the transmission parameters. The phase difference between S_{21} and S_{31} is 2.2°. This strongly indicates that more sophisticated bends are stringently required to compensate for the asymmetry of the bent unit cell.

Moreover we adress the issue of isolation in this design. Only one resistor was used at port 1, whereas the other ports have remained bare. This results in a considerable mismatch at the output ports and very low isolation between the asymmetric port pairs(S_{32}). The isolated ports give better results with an isolation of more than 16 dB. However, there appears also to be a trend towards decreased isolation, when comparing this to the values obtained in the two-port model.

In conclusion, the presented cascaded power divider design demonstrates issues in phase and amplitude balance. There may arise some issues with regard to isolation in larger designs and bare designs without resistors. However, these problems are not unsurmountable and leave room for further research.

4.5.2 Array Antenna

We now move on to a design of an array antenna with corporate feed. This design is the synthesis of the leaky wave antenna presented in Section 4.3 and the two-port power divider from the previous Section 4.4. The array and its dimensions are illustrated in Fig. 4.54. The antenna presented in the picture features two rows with seven radiating elements, which are evenly distanced from the waveguide. Thus, a non-uniform array excitation results. Later we will discuss the effects of a higher

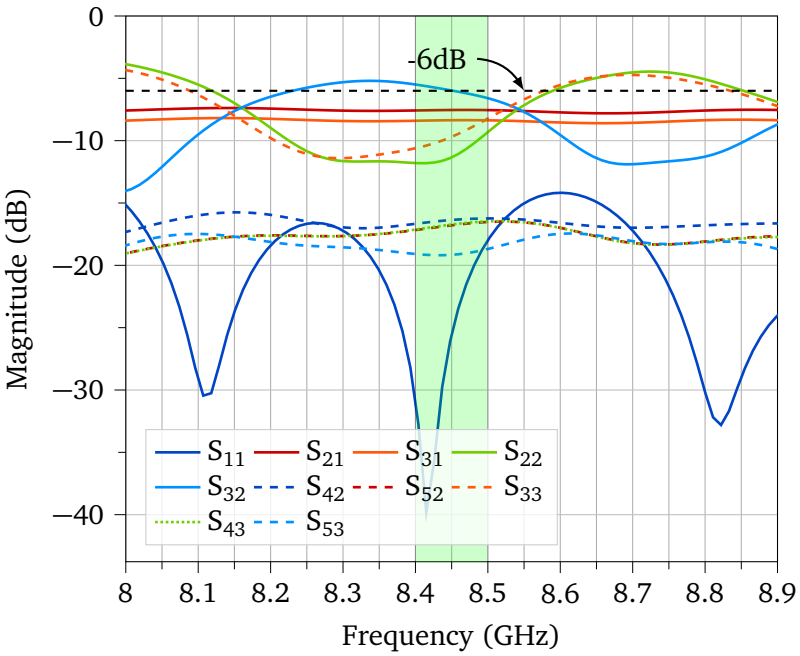

Figure 4.52: Simulated S-Parameters of the four-way divider. The S-matrix is symmetric and some parameters are omitted for better visualization.

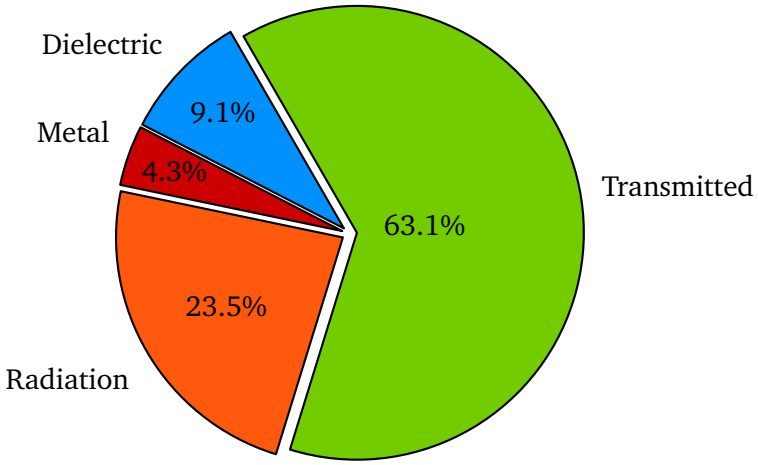

Figure 4.53: Power lost in the four-way power divider relative to the total excited power.

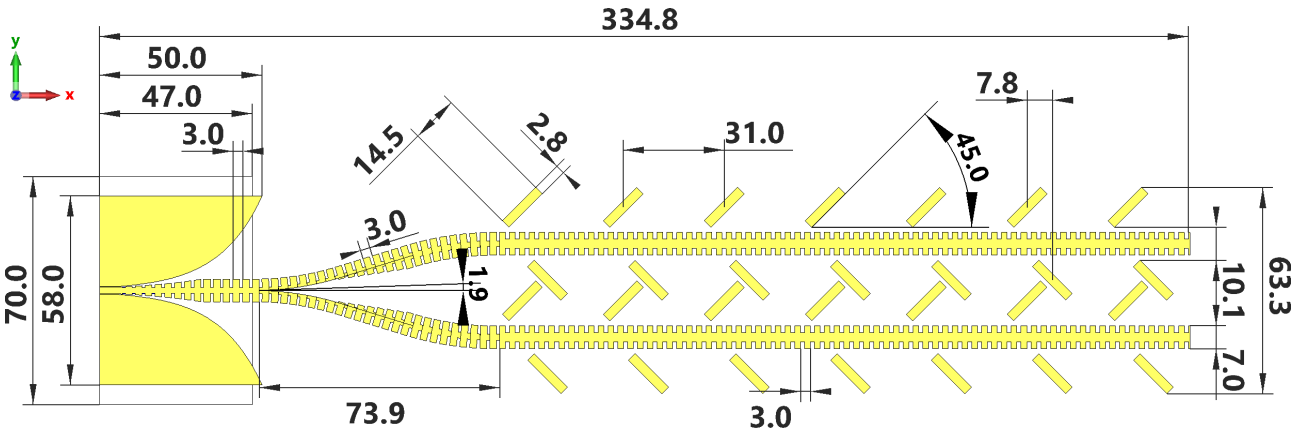

Figure 4.54: Dimensions of the antenna simulation model.

Table 4.4: Parameters of the unit cells used in the array design.

Unit cell	p (mm)	w (mm)	d	g
H-cell Antenna	3	7	0.30w	0.42p
H-cell Converter	3	7	0.38w	0.30p
U-cell	3	7	0.37w	0.31p

number of elements and different spacing.

In contrast to the precursor prototypes, this design was directly developed for a thin film Kapton substrate. Thin dielectrics have an unfavorable effect on the geometry of the CPW port. Hence, a short dielectric slab of 0.625 mm thickness and a length of 47 mm was added under the converter section.

The most prominent change is with regard to the unit cells. The unit cell properties were adjusted with regard to their function in the array. The parameters of the unit cells are given in Tab. 4.4. In contrast to the leaky wave antenna, the approach followed here is towards a faster propagation velocity in the antenna section, based on the $p = 3$ mm unit cell. This affects the preceding power divider and converter that have been adapted to reduce mismatch. The dispersion diagrams of all unit cells are shown in Fig 4.55.

In addition, the radiating element length was increased to 14.5 mm. This has positive effects on the total gain of the array. The separation between the rows is controlled via the bending angle of the divider section and is a useful parameter to tune the axial ratio. As we can see from Fig. 4.56(a), there appears to be some minor disturbance of the E-field of the transmission line.

In the prototype design of the leaky wave antenna from Section 4.5.2, there were a total of 14 elements, due to limitations of the manufacturing. However, increasing the number of elements in the array significantly benefits the antenna gain, as we can see from Fig. 4.57. Due to the non-uniform excitation and waveguide loss, the gain of each additional element pair added to the array subsides (cf. Fig 7 that illustrates this effect on a 40-element array). Compared to an array of uniformly excited dipoles with perfect excitation, the gap between the ideal array and our simulation model shrinks to 1.2 dB at 8 elements, and grows to 1.5 dB as the array increases further. Clearly, a larger array would be sensible with a more uniform excitation and some additional improvements can bring the array closer to the theoretical maximum. Albeit from a system perspective, the number of elements is not only limited by waveguide losses, but also by the area occupied by the array and the resulting mass.

We continue with the discussion of the array's farfield pattern. The 3D farfield gain pattern of the antenna is depicted in Fig. 4.58. Figure 4.59 displays farfield θ-cuts having φ of 0° and 90°. The figure shows a 3 dB beamdwidth of about 10° to 7° in the x-z plane, shrinking with an increasing number of elements. Interestingly, in the y-z plane, the beam widens with number of elements with a

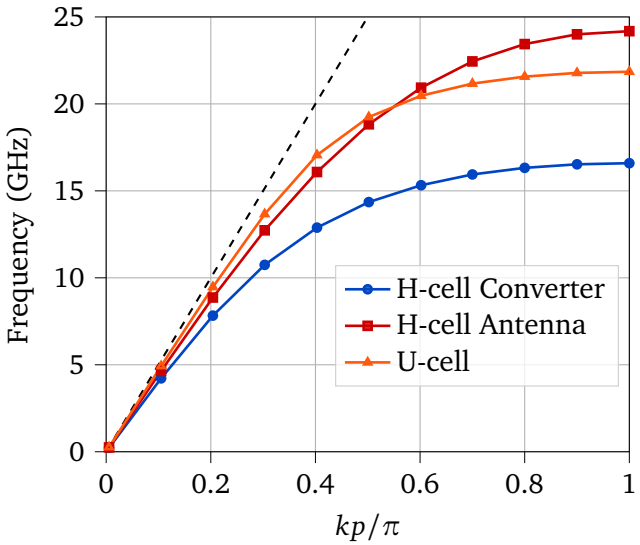

Figure 4.55: Dispersion diagrams of the unit cells used in the array design.

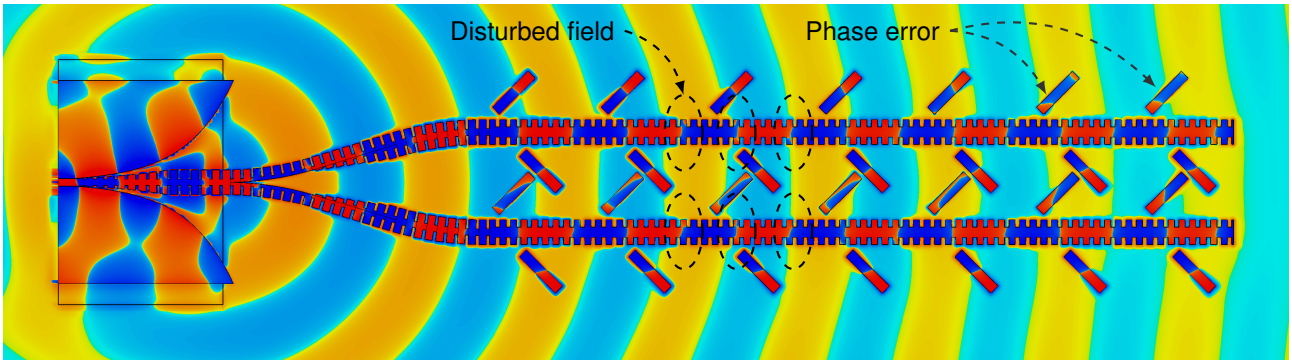

(a) x-y plane

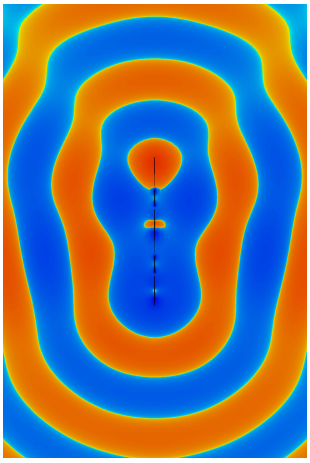

(b) y-z plane

Figure 4.56: Normal components of the instantaneous E-field at frequency 8.45 GHz on a common scale. Some phase instability is visible on in the first and third row from the top. Moreover, we can see a slightly uneven field distribution on the transmission line.

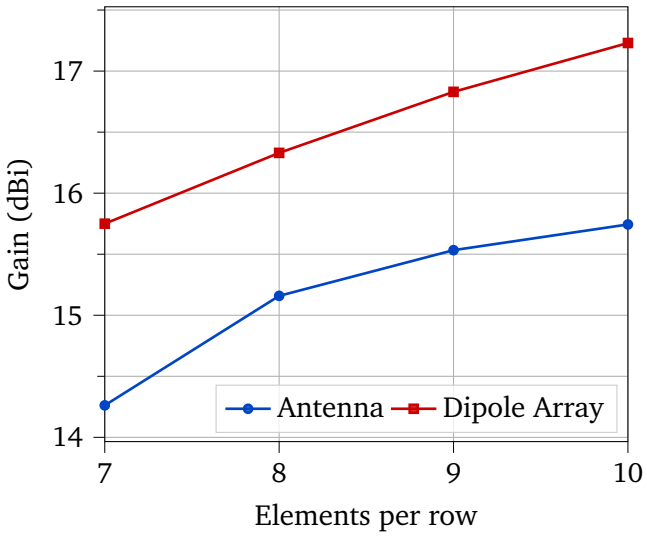

Figure 4.57: Simulated maximum gain of the antenna array and the theoretical maximum gain of a uniform dipole array with the same number of elements.

range between 32° to 36°. The figure also reveals a sidelobe level (SLL) with of less than −11 dB for $\phi = 0°$ and a backlobe of −6 dB.

The axial ratio of the array is presented in Fig. 4.60. Here we can see the array having good axial ratio of less than 3 dB over a wide angle, with the minimum being skewed depending on the number of elements. The reason for this lies in the termination. For each of the presented results, the termination was adjusted by the length of a full unit cell, which is the smallest unit of change feasible.

Element offset

The radiating elements of the antenna are evenly separated from the transmission line, resulting in non-uniform excitation. This reduces the efficiency of the downstream elements and overall gain. We want to swiftly study the effect of reduced coupling of the first elements without delving deeper into array design (i.e., Dolph-Chebychev weighting). Instead we modify the 40-element antenna with an additional y-offset δ_y of the first five elements per row. In addition, the divider angle was increased to 3° per unit cell, to accommodate the larger offset. Fig. 4.61 shows a sweep over δ_y. The graph begins with a lower gain, due to the initially unfavorable angle, but steadily increases to 16.24 dBi. A closer inspection of the antenna pattern shows slightly improved SLL for $\delta_y = 1.5$ mm with −13.4 dB (cf. Fig. 4.62). Likewise, the angle change initially degraded the AR but that property reverts to its initial low value of 1.1 dB.

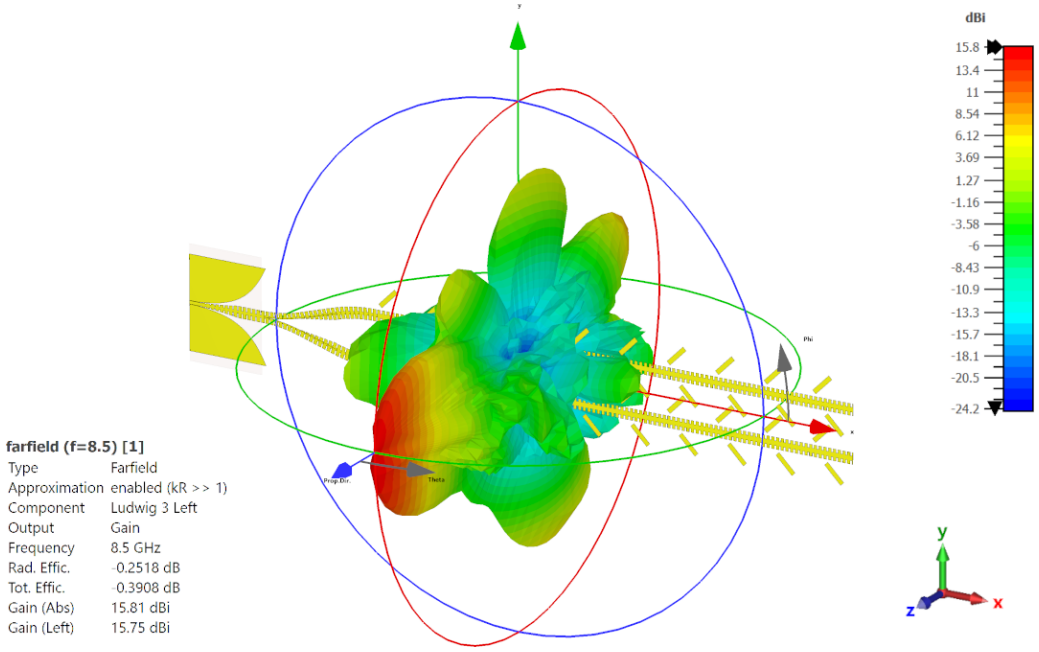

Figure 4.58: Simulated LHCP farfield gain pattern of the 40-element array.

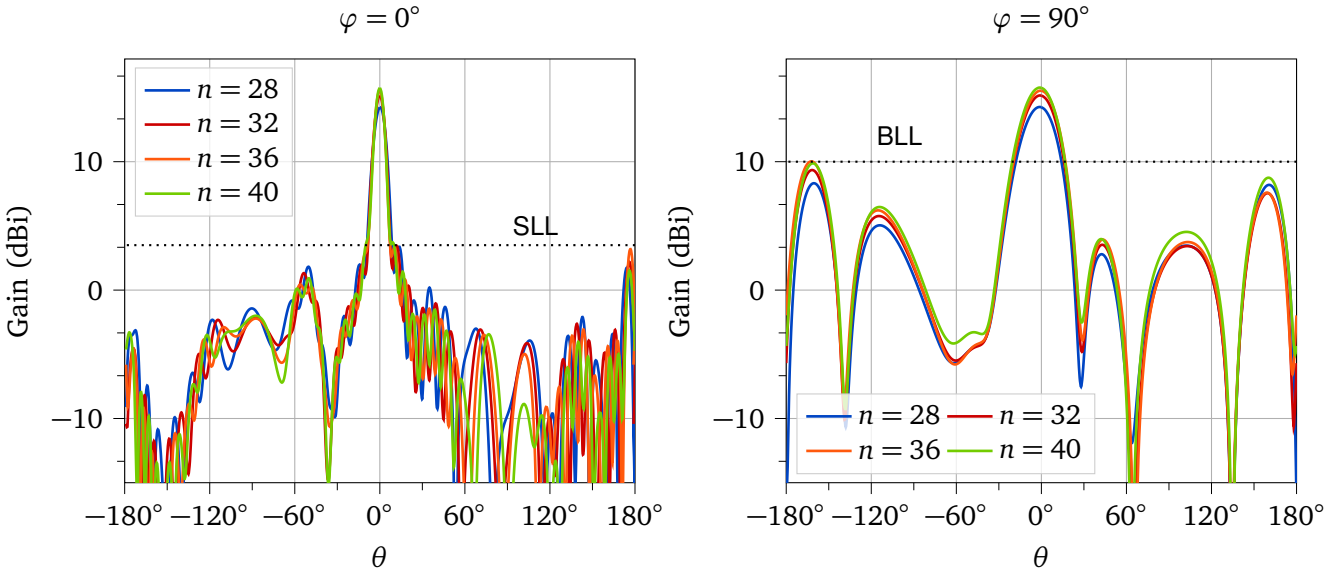

Figure 4.59: Farfield gain (LHCP) of the array with n elements at 8.45 GHz.

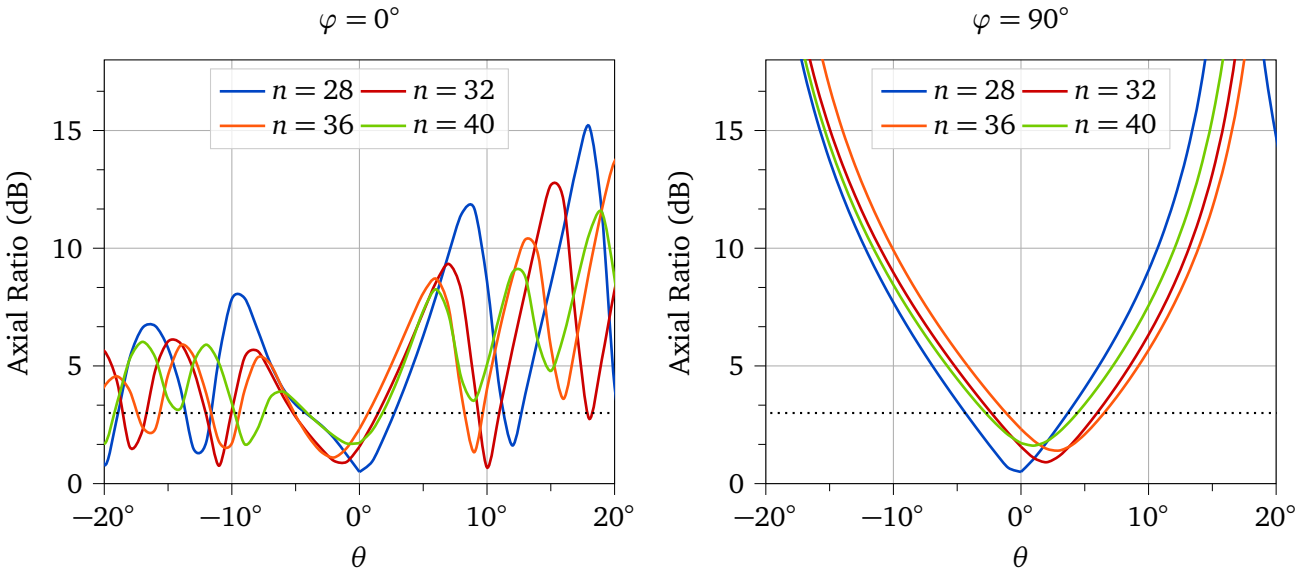

Figure 4.60: Axial ratio of the array with n elements at 8.45 GHz. The 3 dB limit is indicated with a dashed line.

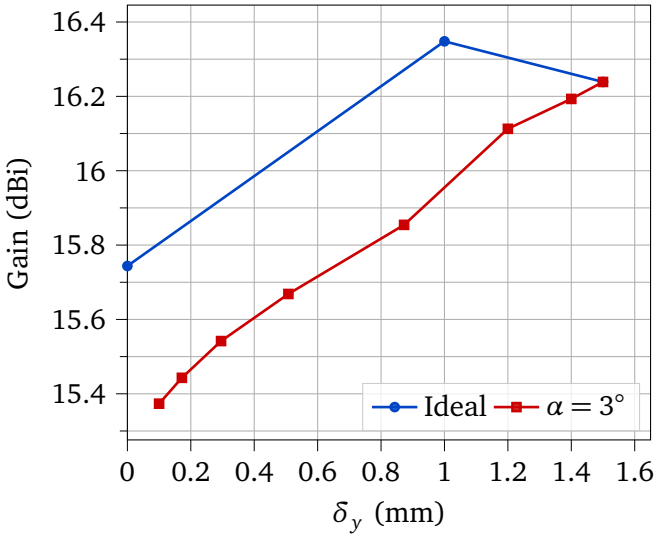

Figure 4.61: Simulated maximum gain (LHCP) of the antenna array with 40 elements, depending on δ_y of the first five elements of each row. Configurations with the same element spacing in the center rows are marked as *ideal*.

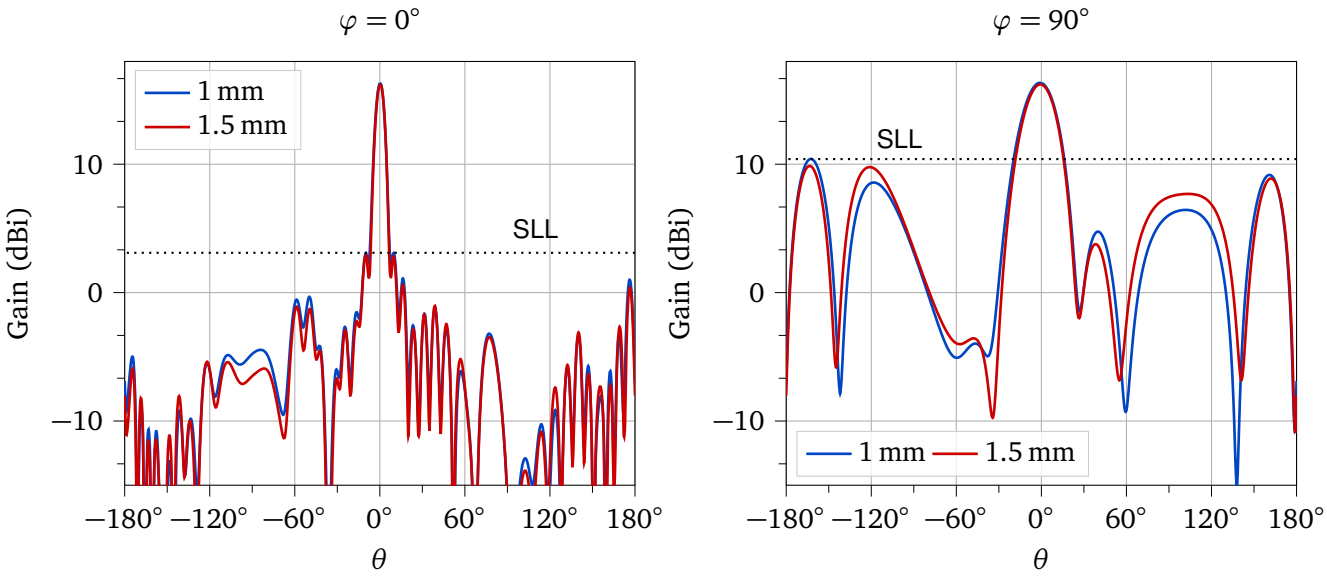

Figure 4.62: Farfield gain (LHCP) of the 40 element array with variable δ_y of the first five elements of each row.

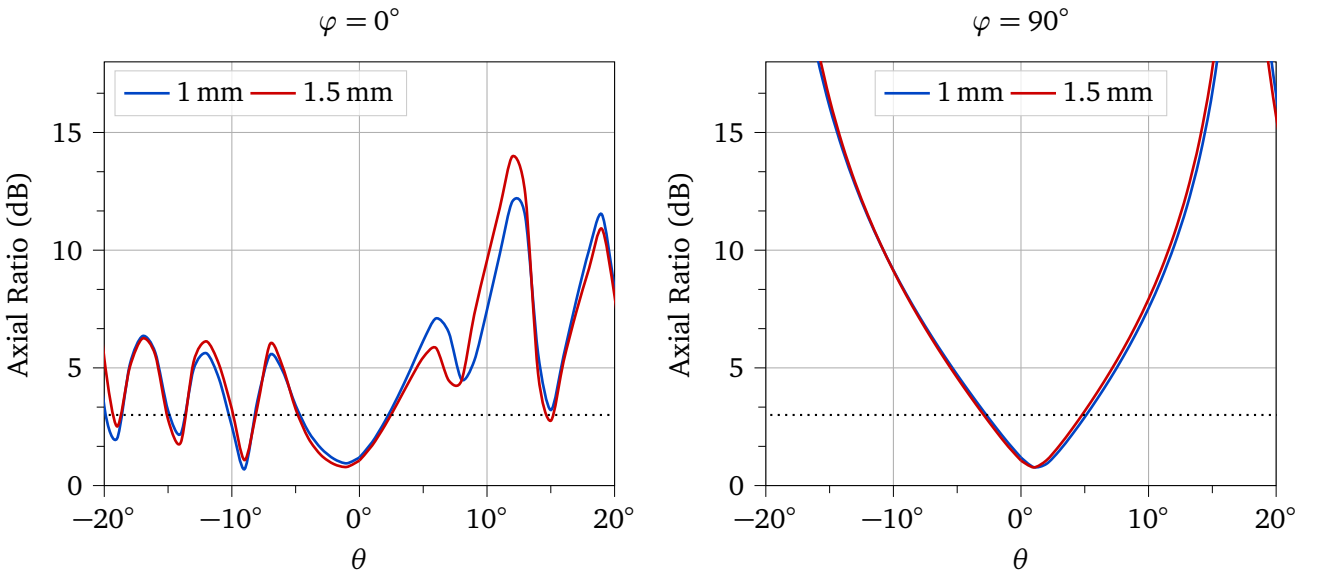

Figure 4.63: Axial ratio of the 40 element array with variable δ_y of the first five elements of each row.

4.6 Manufacturing

Manufacturing is a central problem of the membrane antenna that must be solved to lift this concept existence. We can break down this problem into several different manufacturing processes each increasing the quality of the prototypes and the technology in general.

In the preceding section, we successfully developed microwave prototypes of the radio frequency (RF) components based on COTS printed circuit boards. This expedited manufacturing process, known for its reliability and repeatability, facilitated testing through conventional methods, with the only uncertainty being the design. However, crucial properties, such as material thicknesses and types, were decidingly different from the intended design.

In the subsequent phase, a distinct manufacturing process is required to transfer these designs onto a thin metal layer on a foil, possessing similar characteristics to a solar sail. Ideally, this process is of similar complexity as manual printed circuit board (PCB) manufacturing and yield comparable quality. Through this approach, it is possible to validate simulations, refine designs, and identify potential design and handling issues. It is important to note that this particular process does not address the manufacturing of larger antennas and can be based on a simpler principle.

Afterwards, we will use the knowledge gained to make another stride towards a prototyping process with the potential for later array production and space-grade surface quality. An obvious candidate is PVD, which is used to metalize actual solar sail membranes[12] and therefore should be considered the primary approach.

Proceeding further along this path towards large-scale antennas entails many issues in integration, sail manufacturing itself and on the system level. Each of these problems are very interesting objects of research but regrettably out of scope for this thesis.

4.6.1 Related Work

We proceed on potential solutions to our manufacturing by gaining a wider view on our problem and reviewing related work. In general, we can divide manufacturing into subtractive and additive processes.

Regular PCB manufacturing is a subtractive process, called photolithography. The blank PCB is covered with a photoresist that is subsequently exposed to UV radiation through a development mask. Excess photoresist is stripped with a solvent. The intended copper areas are protected by the photoresist layer, the excess copper is removed with acid. Afterwards, the remaining photoresist is removed and the process is finished.

This commercially available process also allows manufacturing of printed circuits on polyimide foil with thickness down to $25\,\mu$m and copper thicknesses as low as $18\,\mu$m. Yang et al. demonstrated 60 GHz microstrip patch antennas and slot-dipole antennas on polyimide films with a non-commercial process[119]. While the prototypes showed good results, especially considering the high frequency, the authors hint at difficulties with handling the Kapton substrate. Yang utilized a silicon wafer as host carrier with a spin-coated polymer layer to fixate the Kapton foil. Flex PCB in itself are a significant improvement over the thicker RO4350B dielectrics used in rigid PCB. However, the regular layer buildup of flexible PCB consists of multiple copper, adhesive and coverlay layers that alter the high-frequency properties of the circuit. The desired buildup would merely consist of copper clad polyimide, which is a non-standard configuration. At the time of writing this thesis, this was not a cost-effective possibility and therefore will not considered further.

The advantage of photolithography is low non-recurring cost for the development mask, very precise tolerances and high repeatability. The downsides are the handling of hazardous chemicals which requires a significant initial investment in laboratory equipment, machinery and safety. Moreover, establishing a repeatable process requires some additional time investment. Lastly and most importantly, to the author's best knowledge, there are no COTS thin-film laminates available, which would

essentially mean to establish and refine an additional process beforehand.

Apart from this subtractive process, several additive options have been evaluated in the past in the context of wearable systems. This typically involved either inkjet or screen printing methods. Chauraya et al. have demonstrated an inkjet printing process for wearable antennas in the 2 GHz band[120]. They used a Dimatix DMP-2831 materials printer to print silver ink onto Kapton and various fabrics. Goliya et al. have printed transparent antennas from silver nanowire with a screen printing process[121]. The printed antennas were simple bowties and dipoles, designed for the 2.4 GHz frequency band. While transparency is not a desired property of the antennas discussed in this thesis, it could be interesting for solar sails with different optical properties. As part of the Gossamer mission, Spietz et al. have developed ink-jet printed thermistors on thin polyimide foil[122]. The thermistors were made from platinum, however a different material choice appears possible for printed antennas.

4.6.2 Thin-Film Deposition Process

We now turn to discuss the methods used to deposit thin metal films on a substrate. An important parameter of the manufacturing process is metalization thickness, as this affects the mass impact of the antenna (cf. Section 4.7.4), and also its ability to conduct microwaves.

In this work, we studied two methods for thin-film deposition, the ion vapor deposition (IVD) and copper electroplating.

Copper Electroplating

Electrodeposition of copper is the ideal process to quickly manufacture prototypes without the need for large and cost-intensive facilities. Electroplating can achieve layers of suitable thickness, which would allow us to study the effects of thin metal layers of variable thickness on thin solar sailing foil. An electroplating process for Kapton foil was investigated by Jona Hoppe as part of his bachelor's thesis[123]. The work will be summarized in the following.

The electroplating process consists of two elemental steps. The first step is depositing a layer of copper varnish onto the Kapton through a shadow mask that projects the microwave circuit's geometry. In the next step, this fundamental layer is grown via electrodeposition to the desired thickness.

A central part of the work with the copper varnish was improving surface adhesion and ensuring an even distribution of the varnish on the foil (wetting). Both properties strongly depend on the surface free energy γ_s of the polyimide, with a higher surface free energy improving the wetting envelope and adhesive bond. The research was carried out on Kapton 20EN polyimide with a thickness of 5 μm.

To this end, several wet chemical surface treatment options, as well as plasma activation were evaluated with respect to the change in the free surface energy. The used chemical combinations were:

- None
- Unimolar NaOH solution
- NaOH and ethane acid buffer solution
- Paraffin
- n-methyl-2-pyrrolidone (NMP)
- γ-butyrolactone (GBL)

These combinations allowed testing the effects of both acidic and basic conditions. The so treated Kapton 20EN samples were left to settle for a 24 h period. The change of the surface free energy was then determined using contact angle measurement device DSA25. The fluids used in the measurement

Table 4.5: Surface free energy measurement results of Kapton 20EN samples after chemical treatment and different settling periods.

Treatment	γ_s [mJ m^{-2}] (24h)	γ_s [mJ m^{-2}] (15d)
None	47.05 ± 1.47	47.05 ± 1.47
GBL	42.99 ± 1.55	49.40 ± 1.87
NMP	48.07 ± 1.23	51.30 ± 0.66
Parrafin	53.54 ± 1.65	44.99 ± 1.73
Buffer	54.91 ± 1.12	44.52 ± 2.46
Plasma	64.96 ± 3.35	N/A
NaOH	71.64 ± 2.44	64.96 ± 3.35

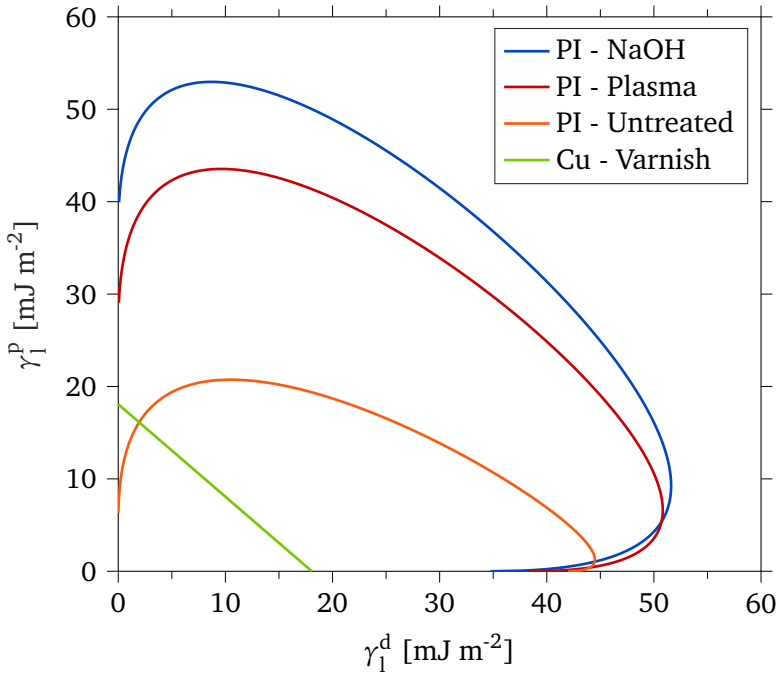

Figure 4.64: Wetting envelope of untreated Kapton and Kapton samples treated with NaOH and plasma and surface tension of the copper varnish.

were Diiodomethane (CH_2I_2) and H_2O. Another measurement was done after a 15 d period. In addition, the physical treatment with atmospheric pressure plasma was tested. The plasma generator was a Plasmatreat FG5001 operated at 21 kHz, 280 V and continuuous discharge. More details on the surface treatment parameters can be found in the work by Hoppe. The results are summarized in Tab. 4.5.

The samples treated with NMP and GBL did not exhibit in a significant increase of γ_s, and even showed a reduced value after the 15 d settling period. However, the NaOH treatment resulted in an immediate increase by 52 % and also showed good long-term stability. The plasma treatment also exhibited promising results.

The surface adhesion can further be predicted by the wetting envelope. The wetting envelope is displayed as the graph of the polar (γ_l^p) versus the dispersive (γ_l^d) components of the surface free energy. If the surface tension of the varnish is inside the wetting envelope of the Kapton sample, this equals a contact angle of 0° and complete wetting of the sample. The wetting envelope of (un-)treated Kapton and varnish is shown in Fig. 4.64. For either treatment option the wetting is complete and good adhesion can be expected.

In order to qualitatively test the surface adhesion, a peel test was performed on six varnished and electroplated samples. A 15 mm × 10 mm piece of Tesa 4657 adhesive tape was manually pressed on

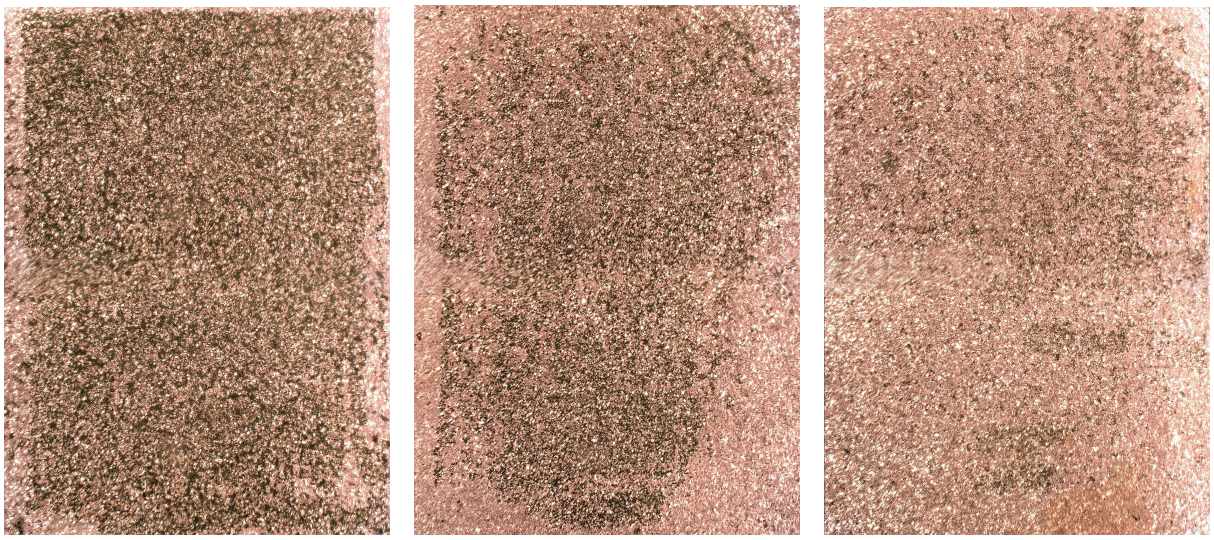

(a) Untreated (b) Plasma (c) NaOH

Figure 4.65: Results of the peeling test with varnished and electroplated samples. Areas of low adhesion have a visible darker tone.

the samples for 60 s and then quickly peeled off at an angle of about 45°. Microscopy images of the samples after the peel test are shown in Fig. 4.65. The adhesion of the copper varnish on the untreated sample was weak, and resulting in large-scale detachment of the copper surface after the peel test. The plasma-treated probe showed better results, despite significant detachments on the entire surface. The sample treated with NaOH displays the best results, with only little peel-off visible.

In addition to the peel test, the surface roughness and conductivity of electroplated samples were determined. The surface roughness was measured on an electroplated sample with an average copper thickness of 0.6 μm and 2 μm varnish. The copper thickess was determined by weighing and averaging over the surface area. The measurement was performed using the depth from defocus process, which created a 3D-surface of the measured profiles. Five profiles were evaluated according to DIN EN ISO 4287, and smoothed using a Gauss filter. The results gave an inhomogenous picture, with R_z between 0.61 μm to 10 μm and R_q between 0.13 μm to 1.0 μm. The large roughness may be caused by contaminants and the roughness properties of most profiles was on the lower end of these ranges.

The conductivity was measured using a four-point-probe method, which allows to determine the sheet resistance. This was performed on several samples with varying sheet thickness. Just as with the surface roughness, the conductivity varied heavily between the samples but a sharp decline from 80 % of σ_{Cu} below 20 μm was observed. Due to this, a much thicker sheet thickness is required compared to pure copper.

After these tests, several microwave prototypes were manufactured. The different circuit geometries were structured using a shadow masks. An issue encountered here was evenly and properly attaching the shadow mask to the foil. The most basic approach was fixing the two together using spring clips, which resulted in geometric unsharpness. Strong attachment provided by neodymium magnets however resulted in satisfactory results with sharp edges (cf. Fig 4.66). Here too, attention is required as stronger magnetic fields affect the copper ions and can yield a distorted result.

Several limitations of the electroplating process were revealed during this investigation. Structure widths below 0.15 mm were impossible to manufacture because they were disturbed by the magnetic fields. Moreover, that the practical limit to the foil area was around 15 cm × 10 cm, as was shown in tests. Sizes above that limit were too difficult for manual handling and even wetting with the copper varnish could not be established. Finally, solder and scratch tests were performed on an electroplated waveguide prototype (cf. Fig 4.67). These tests showed insufficient adhesion and hardness of the copper film, which could be removed with a hot solder iron simply by touch. At room temperature, the film was more resilient, but attachment to a measurement fixture could not be achieved without

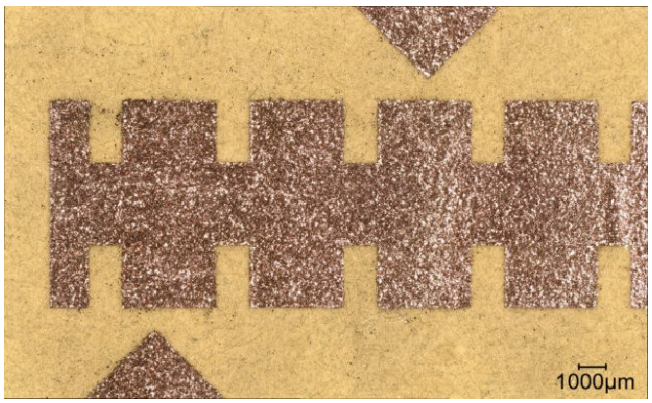

Figure 4.66: Detailed image of a varnished sample SSPP structure. The shadow mask was attached using magnets resulting in very good geometric sharpness.

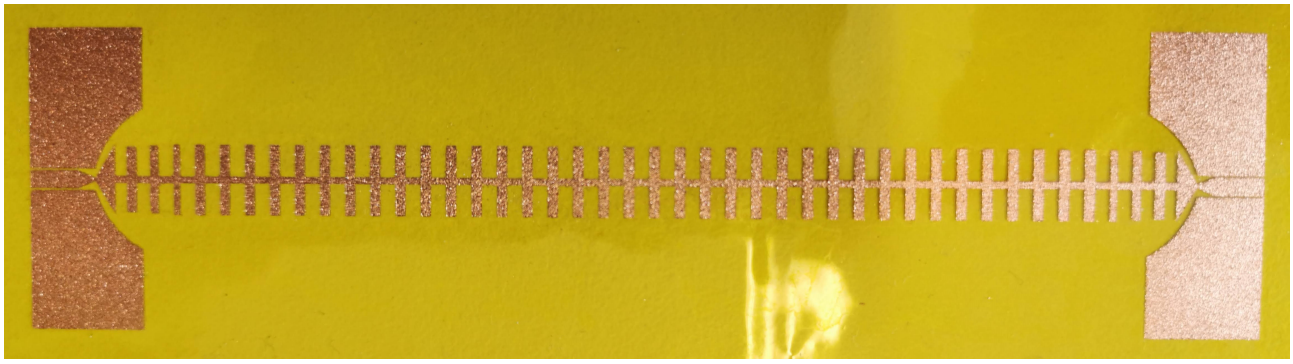

Figure 4.67: Electroplated prototype SSPP waveguide showing very good geometric sharpness.

visible damage.

Ion Vapor Deposition

A typical process to deposit thin metal layers on a metal surface is PVD, where a metal is evaporated in a vacuum and subsequently condensed on the target substrate. There are many processes in this family, which differ in how the gaseous phase is created and transported to the target. Among the most common processes in this family are evaporation deposition, IVD and sputter deposition ("sputtering"). In general, PVD can support a wide range of layer thicknesses, which in the end depend on the particular facility used.

The sputtering and evaporation deposition facilities available for this research were not able to produce layer thicknesses thick enough ($> 1\delta$) for further consideration and also did not support materials that would allow further layer growth through a different process, such as electroplating. IVD is uses aluminium for anticorrosive coatings, so that higher layer thicknesses are the default.

The IVD is a common process used in the aerospace industry to produce a pure aluminium, anticorrosive coating for a vast variety of parts. The process takes place inside a vacuum chamber. Prior to the coating, ionized argon gas is introduced into the chamber. The argon plasma cleans the substrate by means of glow discharge. Afterwards, the source is heated in a ceramic crucible, turning it into a vapor. The argon plasma ionizes the vapor, which then travels towards the grounded substrate and condenses there. The coatings produced by the aluminium IVD have a dull gray appearance, as is visible later (cf. Fig. 4.69). Therefore, in a final step, the surfaces are blasted with glass beads.

Typical thicknesses reached by aluminium IVD systems can produce thicknesses from $3\,\mu$m to more than $25\,\mu$m. Because this, the method is able to produce all sheet thicknesses required. Additionally, typical IVD chambers are able to house very large components, such as wing structures. As a result

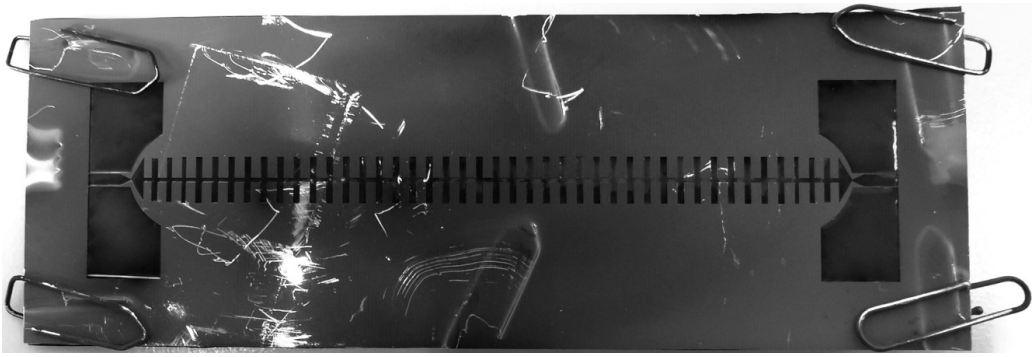

Figure 4.68: Shadow mask and foil after the deposition test. Note the black surface coming from pollutants.

we consider the IVD the ideal solution for later manufacturing of membrane antennas.

Preparation A first IVD manufacturing trial was carried out in cooperation with AERO-COATING GmbH. The trial consisted of two separate manufacturing runs of the previously mentioned SSPP waveguide. The membrane samples used for this trial were two strips of 12.5 μm Kapton HN. For better handling and to prevent wrinkling, the Kapton foil was placed on silicone paper. A shadow mask of 0.1 mm laser cut stainless steel provided the SSPP waveguide geometry. Membrane and shadow mask were laid together and fixated on a 1 mm aluminium plate using simple paperclips, as magnets would divert the ions and distort the result.

Results Approximately 5 μm of aluminium were deposited on each specimen. Figure 4.68 depicts the prototype and shadow mask in the assembly as received after the IVD process. The exposed surfaces are covered with a dark gray layer that comes from pollutants. As we can see, the layer is sensitive to scratching and can simply be polished or scratched off, exposing the pure aluminium layer underneath.

The usual method to remove the surface impurities on the aluminium is glass peening. However, we were uncertain about the effects this additional process might have on the integrity of the membrane and quality of the deposited aluminum film. Consequently, we chose to retain the samples in their original state after the IVD process, without subjecting them to glass bead peening. Further exploration and refinement of the deposition parameters may be necessary to mitigate the issue of sample dirtiness and improve the overall quality of the deposited films.

Fig. 4.69 presents the two prototypes after being removed from the shadow mask assembly. We can see that both prototypes differ from the intended geometry and shape. Sample A exhibits strong underflow of condensed aluminium around the center edges. This effect is more dominant on the lower section of the bottom side of the waveguide. It appears the shadow mask has shielded the surface from the pollutants in some regions.

The second attempt with sample B proved more promising with only little deposition of aluminium under the shadow mask. More detailed microscope images of sample B are presented in Fig. 4.70. The structure and color of the background surrounding the aluminium comes from the silicone paper used to carry the foil. The different surface color is an effect of direction of the light source. Note that the impurities on the surface are not a product of the IVD process but come from linting cleaning wipes.

In the left image, we can see a small section of the waveguide that illustrates the different quality of the deposition. While there is excess aluminium and other impurities on the left side, the right side exhibits good sharpness of the edges and very little distortion. The right image shows a CPW with a gap of 0.1 mm width. As we can see, the shadow mask was mostly able to project this gap, with only little underflow.

The surface adhesion of the aluminium surface was difficult to assess, as the Kapton foil does not

(a) Sample A

(b) Sample B

Figure 4.69: Ion vapor deposited Aluminium on Kapton foil.

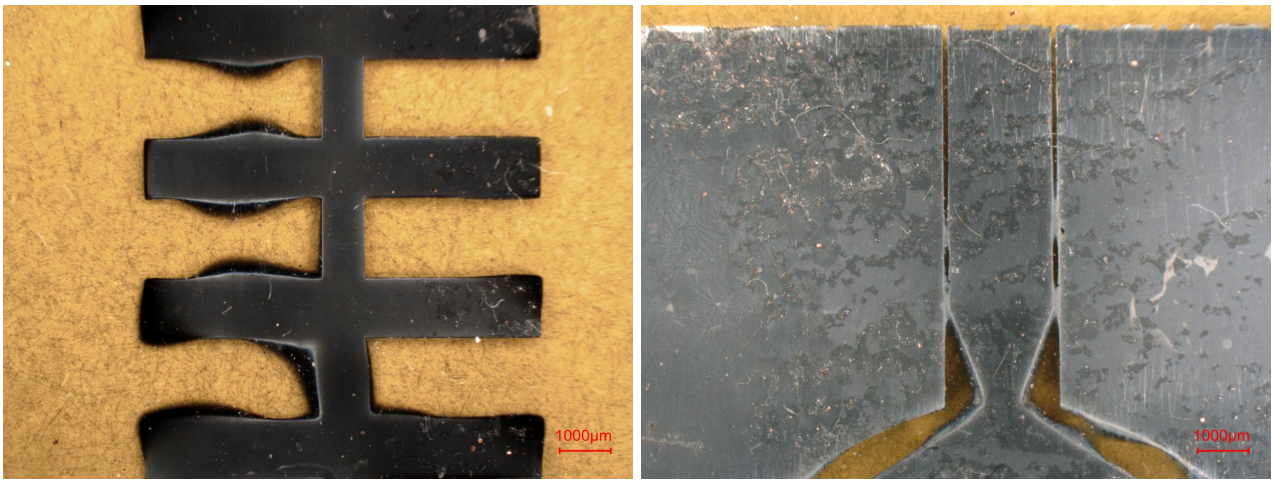

Figure 4.70: Detailed microscope imagery of IVD sample B.

tolerate much force and must be handled carefully. The surface of sample B was scratched with a scalpel several times at two locations, which removed the gray residue but left the aluminium intact. Moreover, the aluminium surface appeared insensitive to any bending or folding it incurred during storage, handling or testing.

4.6.3 Discussion

The electrodeposion process presented in this section showed good results in terms of geometric sharpness, down to structure widths of 0.15 mm. Using copper varnish as fundamental layer for the electrodepsition process resulted in a rough surface, especially at lower thicknesses. This in return resulted in low conductivity so that prototypes with low sheet thicknesses provide no value. Moreover, surface adhesion sufficient for testing microwave properties of the prototypes could not be established. Hence, this process does not meet the requirements for a quick method to develop and test thin-film microwave circuits.

The IVD is the most promising technology for manufacturing large membrane antennas, as it is able to treat large surfaces with thick aluminium layers. The surface obtained directly after the vapor deposition step exhibts a dark gray color, stemming from pollutants that set down. The residue must be cleaned off the surface, could be done by glass peening but a less aggressive method may be preferred to prevent tearing of the foil.

While the geometry was correctly projected by the shadow mask, there are sufficient distortions in both samples to render them useless from a microwave point of view, either because of short circuits or significant distortions of the SSPP structure. We suspect the underflow coming from the shadow mask not being properly pressed on the surface of the Kapton foil. Since the mask is electrically charged, ions are also attracted to the backside of the mask and creep into small gaps. Both CPW sections and CPW-to-SSPP transitions exhibit short circuits. However given the results obtained with the basic paperclip fixture, we are optimistic that this problem can be solved. Applying sufficient and even pressure to the shadow mask however, may prove challenging with larger structures. An alternative non-conductive shadow mask material, such as PEEK or thicker Kapton could also prevent the underflow.

The surface adhesion of the aluminium appeared strong. The deposited film could not be destroyed or detached without risking tearing of the foil. The IVD can produce aluminium films of sufficient adhesion and strength for microwave testing. Additionally, we assume that it is also appropriate for space. However, we cannot substantiate this claim and more environmental tests are required.

4.7 Evaluation

So far we have established the fundamental feasibility of the membrane antenna concept. We now turn to an analysis of the limits of the membrane antenna. An actual implementation of a membrane antenna is limited by the area available on sail, but also by its mass and losses. While the latter do not pose physical limitations, they put an upper bound to the actual usefulness of the membrane antenna, regardless of other factors.

The mass of the membrane antenna is one of the most fundamental arguments for its use. As mentioned in the beginning in Chapter 3, the aperture areal density figure enables comparison with other antenna technologies, as it combines mass and gain, regardless of frequency. The losses in the array's feeding network accumulate and rise with increasing number of elements. Hence, there exists a maximum gain that can be achieved with any given technology. After reaching this peak, increasing the number of elements actually degrades its performance.

As we can see, the derivation of the limits of the membrane antenna must begin with an analysis of the size of the feed network. By obtaining the required TL lengths, we can calculate the attenuation

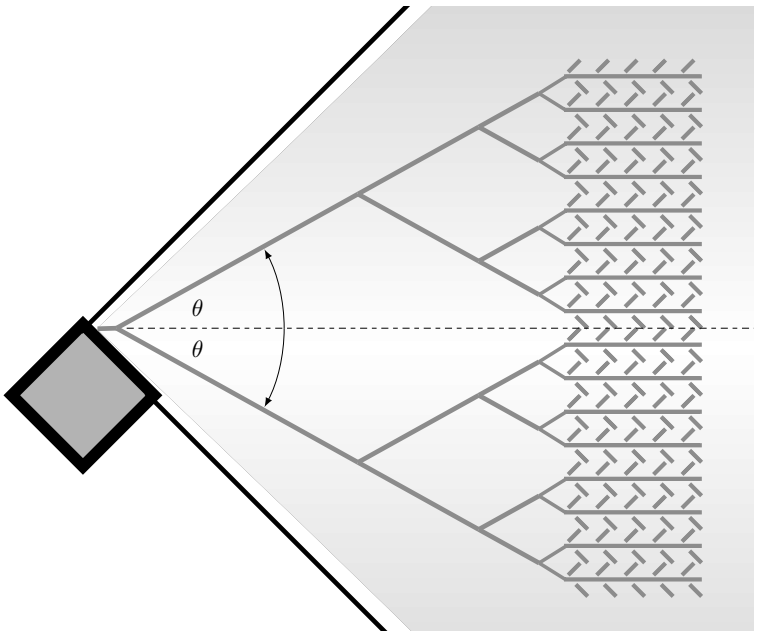

Figure 4.71: Exemplary illustration of the sail array.

and area occupied. Afterwards, the total area of the array and gain can be determined and finally, the aperture areal density. A preliminary version of this analysis was also published in [75].

4.7.1 Modelling

Given the technology discussed in this chapter, we are able to construct a model array with uniform excitation of vertically stacked antennas. The feed network forms a binary tree, where each division represents a Y-divider. This creates a linear, broadside and uniform array, as is shown in Figure 4.71. As a result of this configuration, the array has 2^n vertically stacked antennas, where n is the number of divisions.

In order to estimate the directivity of an array of arbitrary number of elements, we utilize the directivity of the antenna in Section 4.5.2. From the directivity, we can derive aperture and efficiency values:

$$D = A_e \frac{4\pi}{\lambda^2} = A\eta_a \frac{4\pi}{\lambda^2} \tag{4.40}$$

where A_e is the effective aperture, A is the area occupied by the array and η_a is the aperture efficiency. In the following, we will assume η_a to be constant, while A varies with the number of elements. This assumption is valid, as we have seen an increase in gain of about 3 dB between the 2x7 SSPP antenna and the 4x7 antenna array. Hence, the antenna directivity is simply given by the formula:

$$D_n = 2^n D \tag{4.41}$$

So far, we have assumed the solar sail to be a perfectly flat aluminium surface on a dielectric membrane. For the following analysis, we will introduce the sail deformations introduced previously in Section 2.1.4 in the form of a random surface error. Random surface error can be modeled as phase error between the individual elements. Using Ruze's equation, we can calculate the power loss associated with a normal distributed phase error with variance σ^2[124]:

$$L_s^{-1} = \frac{1 - e^{-\sigma^2}}{N} + e^{-\sigma^2} \tag{4.42}$$

where N is the total number of radiating elements in the array. The loss due to random surface error σ_s is shown in Fig. 4.72, where $\sigma = 2\pi\sigma_s/\lambda$. The graphs show a steep decline and eventual plateau of

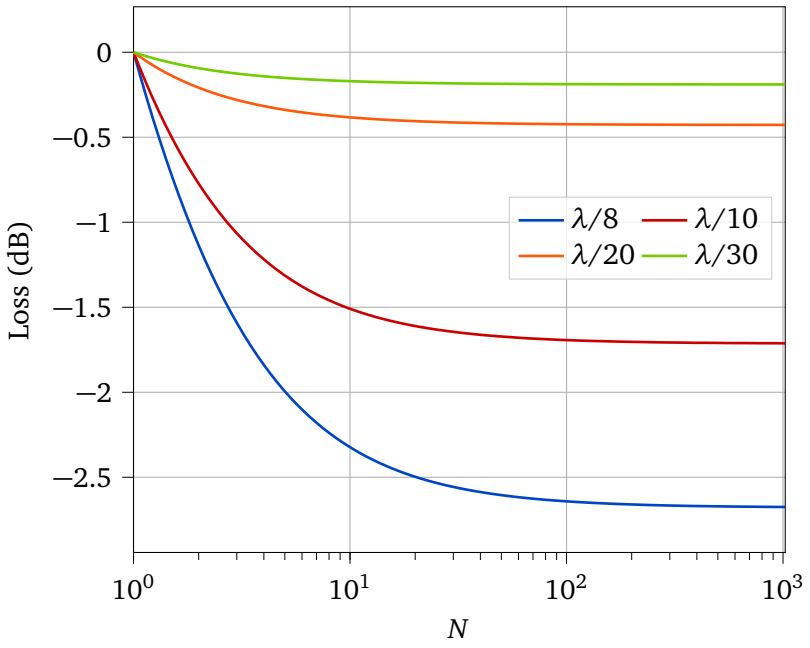

Figure 4.72: Array loss due to random surface errors over N elements for several values of σ_s.

the combining efficiency of the array with growing N. Even when the surface error is small, significant losses occur.

By combining (4.40) and (4.42), we can obtain the total directivity of the array:

$$D_{n,tot} = \frac{D_n}{L_s} = 2^n D \cdot \left(\frac{1-e^{-\sigma^2}}{N} + e^{-\sigma^2}\right) \tag{4.43}$$

In our model, every doubling of the number of antenna element requires another power divider and increases the length of the feeding lines. As we can see in Fig. 4.71, the feeding network forms a triangular shape. The feedline length leading to each individual element is approximated by:

$$l_n = \frac{(2^n - 1) \cdot d_y}{2 \sin\theta} \tag{4.44}$$

where d_y is the vertical spacing between the array antennas. Note that the shortest possible path between dividers is realized with $\theta = 45°$. The total length of all transmission lines in the array can be approximated by:

$$l_{tot} = l_2 \sum_{i=1}^{n} 2^i \cdot 2^{n-i} = l_n \cdot n2^n \tag{4.45}$$

The line- and divider losses are given as:

$$L_l = \alpha_{sspp} l_n \tag{4.46}$$

$$L_d = n l_{d,0} \tag{4.47}$$

The antenna gain is obtained from D_{tot} by also accounting for the losses occurring before the radiating elements, i.e., in the feeding network:

$$G_n = \frac{D_{n,tot}}{L_s L_l L_d} = \frac{2^n D}{\alpha_{sspp} l_n \cdot n L_{d,0}} \cdot \left(\frac{1-e^{-\sigma^2}}{N} + e^{-\sigma^2}\right) \tag{4.48}$$

We can see that the sensible physical size of an antenna array is limited by the losses of the feeding network and directivity of the individual antenna.

Table 4.6: Singular feedline length l_n, total line length l_{tot} and total sail size required to host the antenna A_{sail}, for different values of n, $\theta = 45°$.

2^n	l_n (m)	l_{tot} (m)	A_{sail} (m^2)
2	0.024	0.048	4.6×10^{-3}
4	0.072	0.19	0.019
8	0.17	0.58	0.074
16	0.36	1.5	0.3
32	0.75	3.9	1.2
64	1.5	9.2	4.8
128	3.1	21	19
256	6.1	49	76
512	12	1.1×10^2	3.0×10^2
1024	25	2.4×10^2	1.2×10^3

4.7.2 Array Size

The size of the array depends on the number of elements and θ. The size is limited by the sail's area and also by its shape. The sizes of the array for various n are given in Tab. 4.6. The line lengths for more than 128 elements become exceedingly long, with a single line becoming longer than 100λ for $n = 8$. The sail area required by 256 elements is 76 m^2, almost as much as the membranes of current solar sailing missions. Due to the unfavorable array geometry, the area required by even more antennas appears excessive.

4.7.3 Gain Estimate

We now move on to the estimation of the maximum gain achievable with this array. Despite previous efforts, several known unknowns remain in the system. Hence the following estimate will require some assumptions to be made.

First, the exact characteristics of the power divider are difficult to determine due to the issues discussed in Section 4.4 and 4.5.1 and the exact divider loss remained elusive. Therefore, the divider losses will be assumed to be within a most likely range. The gain difference between the simulated single antenna and double antenna array is about 3 dB, indicating low loss in the divider section. However, the simulated divider excess insertion loss was 1 dB, 1.8 dB and 2.3 dB (including amplitude imbalance), depending on the model. Therefore, we reason that a divider loss between 0.5 dB to 1.5 dB per division is a realistic range, where 1.5 dB is the worst case. Moreover, the following estimate will assume the amplitude imbalance issue solved.

Second, the directivity value used in the following is based on the gain value of the CST Microwave simulation of the 4x10 array, which was 16.3 dBi. To this end, we obtain the gain from a single antenna by accounting for the variable divider loss and maximum combination gain:

$$D = 16.3\,\text{dBi} - 3\,\text{dB} + l_{d,0} \tag{4.49}$$

Last, we assume $\sigma_s = 1$ mm, which means the likelyhood of the array elements having surface errors lower than 3.9 mm is 95 % and 98 % for errors lower than 4.6 mm. As we have seen in Section 2.1.4, the majority of the sail deformation is well below this magnitude, with creases forming an exception. However, the assumption in this analysis is that creases can be well defined, and therefore could be arranged such unavoidable deformations within the array fall within the given distribution.

The results of the gain estimation are presented in Fig. 4.73. The graphs in Fig. 4.73 (a) represent the results for variable line attenuation. The gain performance is insensitive to changes in line lengths for less than 64 elements, where the difference is ≤ 0.8 dB. Above 64 elements, the gain tapers off

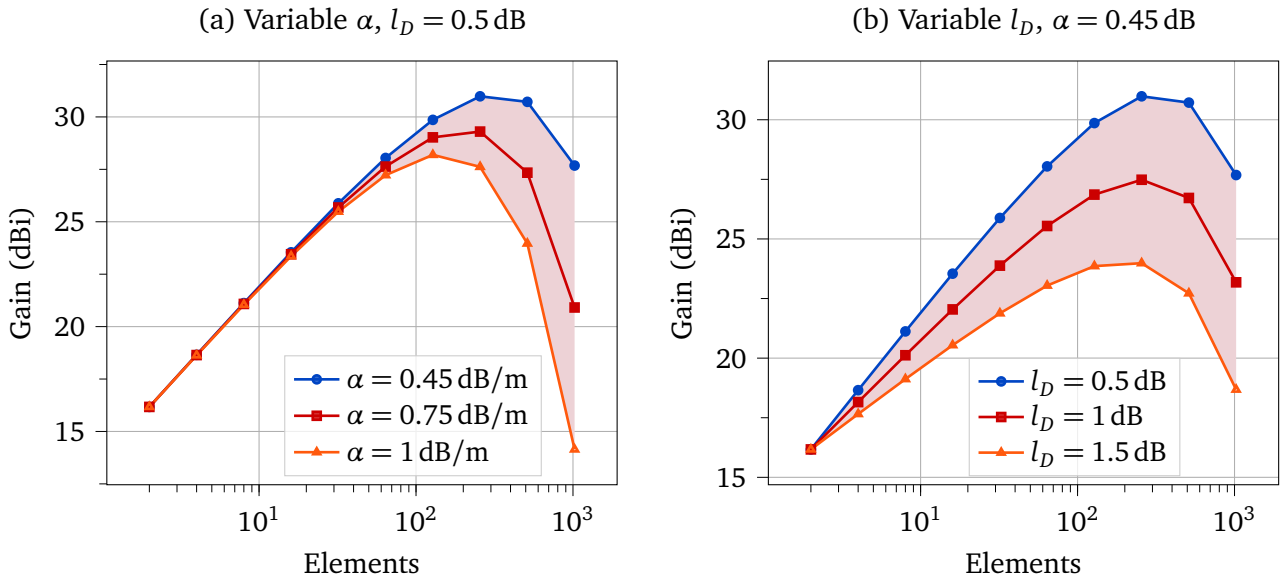

Figure 4.73: Estimated gain of the antenna array depending on element number, line attenuation α and divider loss l_D.

and reaches its peak value. The peak element number shifts with higher attenuation towards lower element numbers. The highest achievable gain is 31 dB ($\alpha = 0.45\,\mathrm{dB}$). After the peak, the losses exceed the gain added by additional elements and the total gain rapidly declines.

Fig. 4.73 (b) shows the results for different divider losses between 0.5 dB to 1.5 dB. Expectedly, a very strong impact of the divider loss can be observed. The lower peak, having $l_D = 1.5\,\mathrm{dB}$ is about 24 dBi at 256 elements, with only little difference to 128 elements. The middle peak $l_D = 1\,\mathrm{dB}$ is at about 26 dBi.

4.7.4 Antenna Mass

Earlier in this thesis, we supposed that integrating the antenna array into the solar sail could save a critical amount of mass in the entire solar sailing system. To substantiate this argument, we therefore need to develop a credible estimator for the antenna's mass impact on the sail system.

We will approach this problem by deriving a lower bound for the mass of the individual components of the antenna array. The additional mass coming from the antenna array can be separated into two categories: physical mass m_p, and virtual mass m_v. The source of physical mass is the additional metalization thickness, required by the antenna array. Virtual mass is added by the area around the array, which must be free of any metalization (see Fig. 4.74). Since these areas are, from a propulsion point of view, non-functional and add additional mass, they have to be considered as well.

For a microwave structure of a given length, we can conveniently derive these masses by defining a footprint A and a corresponding filling factor F, so that:

$$m_p = AF \cdot (k\delta - t_s) \cdot \rho_{Al} \tag{4.50}$$

$$m_v = A \cdot (1 - F) \cdot h \cdot \rho_D \tag{4.51}$$

where $k = 3$ is the metalization thickness in multiples of one skin depth ($\delta = 0.9\,\mu\mathrm{m}$ at 8.4 GHz), $t_s = 0.1\,\mu\mathrm{m}$ is the metalization thickness as required for propulsion, $\rho_{Al} = 2.7\,\mathrm{g\,cm^{-3}}$ is the density of Aluminium at 20 °C[125] and $\rho_D = 1.42\,\mathrm{g\,cm^{-3}}$ is the density of the membrane, $h = 3.5\,\mu\mathrm{m}$ is the membrane thickness. The total mass given by the sum $m_p + m_v$. At this point it must be noted that t_{sh} was chosen to resemble values found in recent solar sailing missions. Since missions closer to the sun

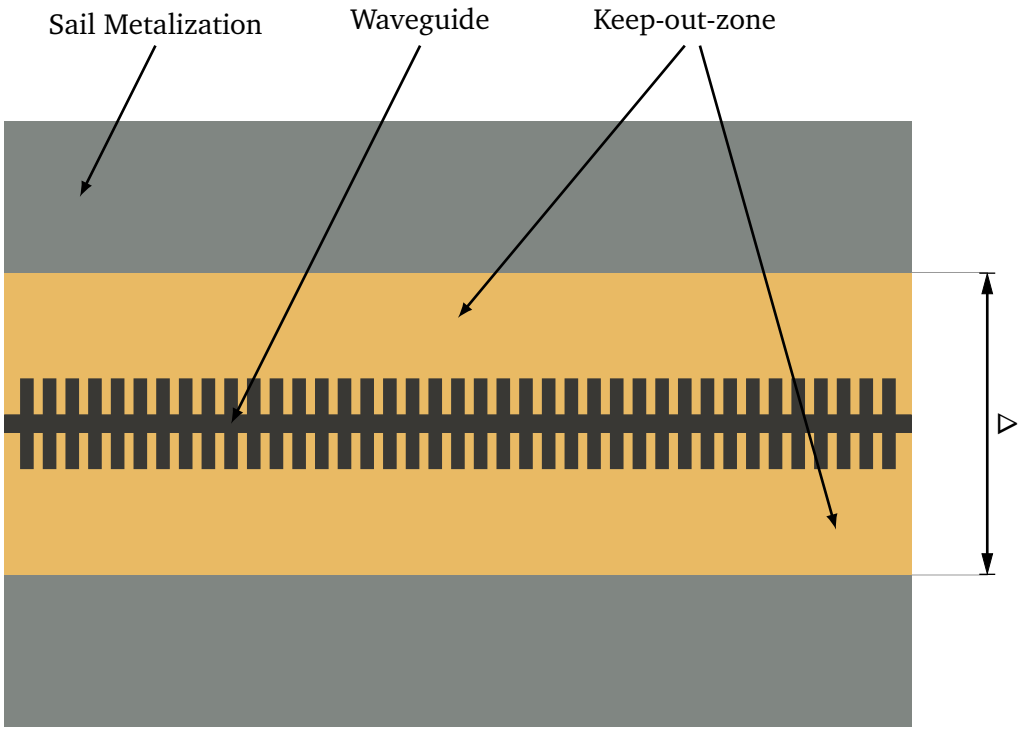

Figure 4.74: Schematic illustration of the areas comprising the filling factor of the mass calculation. The waveguide in the middle is a thick metal layer, surrounded by a *keep-out-zone* of total width Δ that separates the outer edge of the waveguide from the sail metalization.

Table 4.7: Summary of footprints and filling factors of SSPP unit cell, power divider and antenna.

Component	Footprint	Filling factor	Mass (g)	Linear Density (g/m)
Unit cell	106.5 mm^2	0.1262	-	0.26
Antenna	0.88 λ × 0.86 λ	0.3	2×10^{-3}	-

may require significantly thicker aluminium layers (cf. Section 2.1) to shield from UV light, this can be regarded as *worst-case* assumption.

As mentioned before, the filling factor differs between the individual array components. A summary of the filling factors and footprints is found in Tab. 4.7. The filling factor for the antenna array is simply determined via pixel counting from the production files. In addition, a keep-out-zone of 10 λ is placed around the antennas. The power divider is simply approximated by the waveguide. For the waveguide, the filling factor can simply be expressed as:

$$F = \frac{pw - 2gd}{p\Delta} \tag{4.52}$$

where Δ is the width of the *keep-out-zone* according to Fig. 4.74. The value of Δ should be chosen so that the interaction of the expanding electrical field with the metalization is negligible. Here, we benefit from the tight confinement of the E-field around the conductor. We remember back in Fig. 4.21, the E-field exhibited an exponential decrease from its peak value to −30 dB or less within 15 mm from the center. A decrease by 40 dB requires a significantly larger keep-out-zone of ±30 mm from the center. Laboratory tests with a showed no measureable impact of a metal plane placed at a distance >13 mm to a sample waveguide. According to a simulation with CST, this distance corresponds to a magnitude decrease of about −30 dB. To move on further with the analysis, we select $\Delta = 1\lambda$ as a conservative threshold.

We can now calculate the mass of all dividers and antenna elements depending on the total number of array elements. Using the results from the antenna gain calculation, we derive the aperture areal

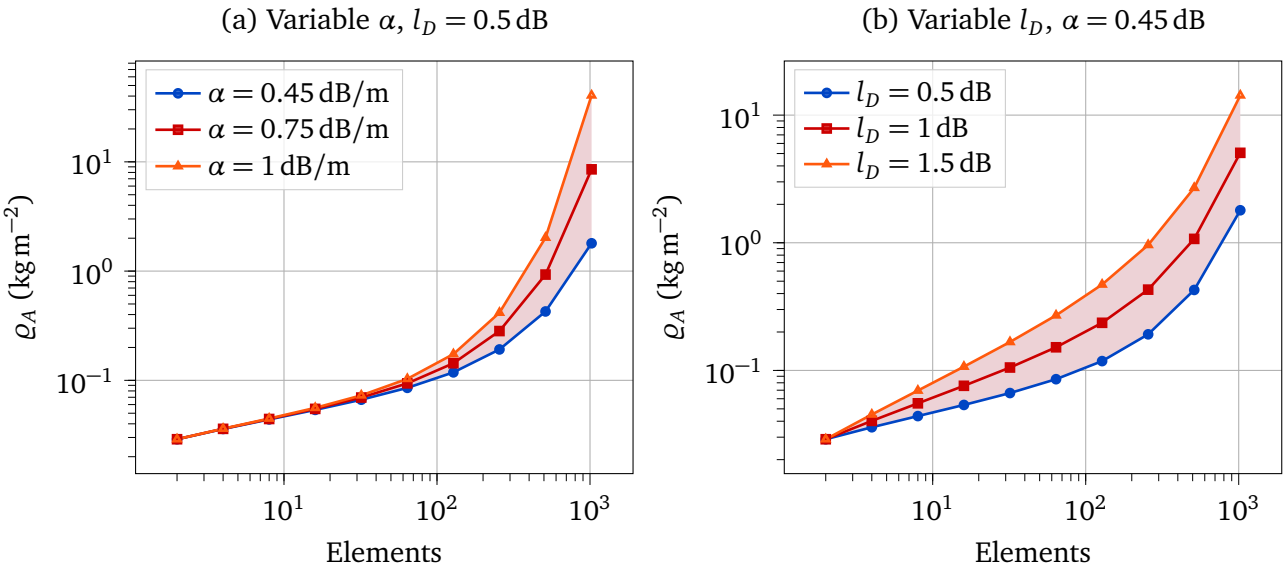

Figure 4.75: Total mass of the antenna array versus number of array elements for different metalization thicknesses δ and filling factors Δ.

density of the array. The results are shown in Figure 4.75. The results exhibit a pattern reminiscent of the antena gain results. In Figure 4.75 (a), until about 128 elements we can see little sensitivity to attenuation. Afterwards, ϱ_A diverges dramatically. For smaller element numbers, very low values of ϱ_A can be reached, with less than $0.1\,\mathrm{kg\,m^{-2}}$ for any of the attenuation values given. Even for 128 elements, any ϱ_A remains below $0.2\,\mathrm{kg\,m^{-2}}$.

Figure 4.75 (b) however gives a different perspective, as varying divider losses severely increase ϱ_A beyond the $0.1\,\mathrm{kg\,m^{-2}}$. Given a loss of 1 dB, this limit is exceeded at 32 elements. At 256 elements, the spread between $l_D = 0.5\,\mathrm{dB}$ and $l_D = 1.5\,\mathrm{dB}$ is almost 80 %, with the largest ϱ_A still just below $1\,\mathrm{kg\,m^{-2}}$.

4.7.5 Discussion

We return to the diagram first discussed in Chapter 3, aperture areal density and the effective aperture of several antennas used on spacecraft were compared. Now, including the results from this analysis, an updated diagram is shown in Fig. 4.76. As we can see, the membrane antenna array operates on the lower end of the effective aperture spectrum, while surpassing every existing antenna in terms of aperture areal density by more than one order of magnitude and at the same time, antennas of similar size by two orders of magnitude. This gives rise to the hope that this concept can improve solar sailing missions to closer targets, such as the inner planets or Mars.

Reaching the required number of elements may prove challenging from a manufacturing point of view. Therefore, smaller arrays, such as 32x10 may be much more feasible.

It is important to note that while the performance figures obtained in this section provide a solid starting point, the actual performance of larger arrays may be influenced by various factors, such as mutual coupling between elements, manufacturing tolerances and billowing. Therefore, further analysis and refinement are necessary to account for these factors and obtain accurate performance estimations.

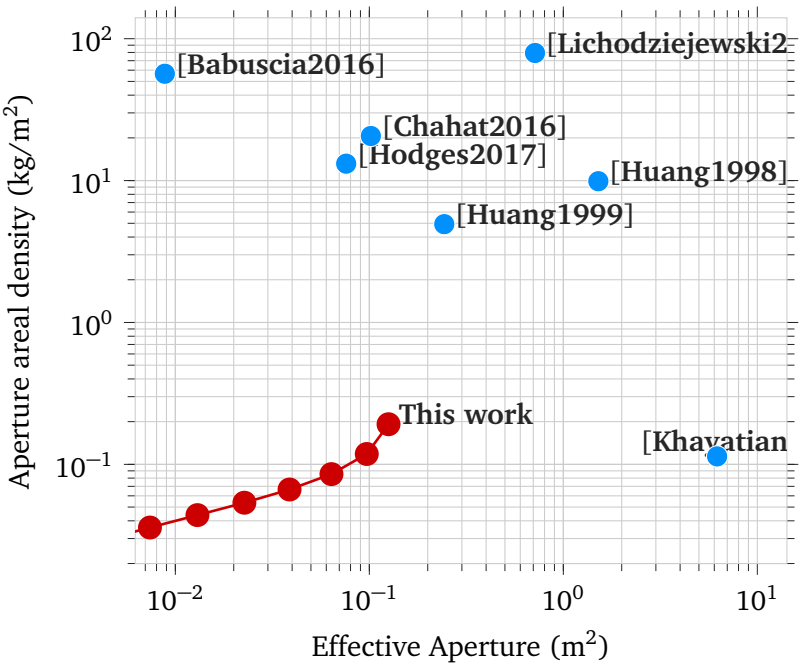

Figure 4.76: Comparison of the membrane antenna design of this thesis with the related works.

4.8 Future Work

In this chapter, many simulations were presented, showing the fundamental feasibility of the membrane array concept. However, this research is far from complete and in order to make strides to an actually usable antenna, several further steps need to be taken.

First of all, the IVD manufacturing process must be further improved to yield stable, usable results. Once this step is completed, prototypes of different waveguides can be produced and the losses depending on metal thickness and manufacturing tolerances can be studied. Of course, this would then also allow to manufacture an actual antenna array and study its properties after folding and under temperature influence and mechanical stress.

On the antenna side, further improvements with regard to excitation will bring positive results. The highest possible gain is achieved by uniform excitation, which is not currently the case. Likewise, non-uniform excitation may improve high side-lobe levels. Weighing these options is certainly needed in future work.

Further research is needed on the power divider side, in order to be able to produce larger arrays. Solving the amplitude imbalance problem is not expected to be a complicated problem, but of paramount importance. Moreover, as we have seen from the performance estimation, producing power dividers with low insertion loss is critical for larger arrays.

Larger arrays may be subject to destruction by micrometerites, which will cause reflections inside the array. Implementing isolating resistors can improve the issue to a certain degree, but may cause thermal issues, due to their low reflectivity. This may be solvable with reflective coating, but is out of scope here. Generally, manufacturing larger arrays is tightly bound to small tolerances. Given that nowadays, solar sail membranes are long swaths of membrane material combined together using adhesive tape, maintaining the electrical connections and tolerances may be difficult in the combining step.

The design of the membrane array so far evolves around the solar sail and the minimum amount of alterations needed. Other applications however, may have more relaxed requirements. A backside reflector will bring significant gains and may be feasible depending on the desired frequency.

4.9 Conclusion

This chapter presented the analysis of a planar antenna array integrated into the metal surface of the solar sail membrane. Due to the low dielectric thickness of the sail, the applicability of classical planar transmission line technology was uncertain. An analysis based on analytical formulas revealed that all of the investigated transmission lines failed either due to high attenuation or simply by geometric requirements beyond manufacturability. However, a suitable technology was found with single-conductor waveguides, namely the spoof surface plasmon polariton (SSPP). In contrast to other constituents of the planar transmission line (TL) family, the SSPP line can have low radiation and conductive losses. Through simulation, we found this type of waveguide to be able to carry microwaves in X-band with attenuation as low as $0.45\,\mathrm{dB\,m^{-1}}$.

A prototype circular polarized 1x7 non-uniform SSPP antenna array was manufactured on thin RO4350B dielectric and measured in an anechoic chamber. The measured results showed good agreement with the simulation. The antenna had a maximum gain of 11.1 dBi. A prototype three-port power divider was designed with moderate 1 dB excess insertion loss. However, issues with the coaxial adapter prevented further verification of the model. Further simulations of a four-way power divider showed that it cannot simply be scaled up and measures to prevent amplitude imbalance must be taken. Additionally, a combination of antenna and power divider was simulated in the form of a 2x10 antenna. The antenna showed good performance, with a maximum gain of 16.3 dBi and an axial ratio of 1.1 dB. By comparing the simulated array with the simulation of a uniform dipole array with the same configuration, we found that the array may be improved by about 1 dB by making the excitation more uniform.

Manufacturing the prototypes proved difficult, due to limited availability of manufacturing facilities and material. Therefore, we investigated a method for manufacturing prototypes on thin Kapton using copper electrodepsition. The method used an initial copper application through a shadow mask that projected the positive image of a waveguide structure onto a pre-treated Kapton membrane. The method showed very good geometric accuracy, but exhibited low surface adhesion. Hence, attaching the prototypes to measuring devices was exceedingly difficult and rendered this method unusable. Another manufacturing test was performed using the method of ion vapor deposition. Using this method, a stable $5\,\mu$m thick aluminium layer was deposited through a shadow mask on a thin Kapton membrane. The surface adhesion of the produced samples was excellent. The tests also showed that a more intricate method of pressing the shadow mask onto the membrane is needed, as regions with low pressure exhibited severe aluminium creep. Apart from these areas, the geometric accuracy of this method is excellent and also very thin gaps of 0.1 mm could be produced.

A theoretical analysis of the limits and potential of the membrane array was performed. To this end, we estimated the losses in a triangular feeding network, depending on the number of antenna elements. Using this data, the maximum gain achievable by combining the respective number of antenna elements was calculated. Afterwards, the results feeding network length and gain calculation were used to calculate the antenna areal effective aperture. The comparison of the results with existing antennas showed that the membrane antenna array could reach similar aperture sizes as present CubeSat antennas, but at siginifcantly lower mass. In our opinion, this renders this concept very attractive for future missions to closer targets, such as the inner planets or near-earth objects.

Chapter 5

Boom Antenna

In this chapter we investigate the concept of a slotted waveguide antenna (SWA) integrated in the solar sailing booms. From all of the different boom profiles previously discussed in section 2.1.3, CTM booms take a special place. As the name gives away, this type of boom forms an almost cylindrical shape when deployed, with empty space inside. This property makes the CTM booms interesting for an investigation as potential waveguide and ultimately, as a SWA. Waveguides are hollow structures typically with a circular or rectangular cross-section and conductive walls (see Figure 5.4). By introducing slots in the waveguides surface, the waveguide leaks radiation, forming a SWA.

In the first section of the chapter, we give a brief introduction of the concept of CTM booms. Afterwards we discuss the theoretical background of waveguides and SWAs in Section 5.1. Next, Section 5.2, we discuss the design options for a CTM boom waveguide. Afterwards in Section 5.3, we conduct a study of the CTM geometry with regard to its electromagnetic properties. In the subsequent Section 5.4, the radiation properties of a single slot and a SWA array are investigated. Section 5.5 discusses the manufacturing of the CTM booms used for waveguide attenuation measurements in Section 5.6 and mechanical testing in Section 5.7. Finally, we discuss future work on this topic in Section 5.8 and conclude the chapter in Section 5.9.

5.1 Introduction

The collapsible tubular mast boom was introduced into solar sailing by researchers of DLR[127]. The researchers recognized the advantages of the CTM structures manufactured from CFRP with regard to structural stability, volume and mass requirements. The booms were also considered as deployables for an L-Band SAR membrane antenna[63]. CTMs were the designated booms of the DLR Gossamer solar sailing mission[128, 129], due to their advantageous properties. The Gossamer booms consisted of two laminated half shells of one layer of plain-weave CFRP prepreg with a [0 90] fiber orientation and a thickness of only 0.12 mm. The linear density was approximately $30\,\mathrm{g\,m^{-1}}$.

More recently, Fernandez et al. investigated miniaturized CTM booms built with thin-ply CFRP as candidates for the NEA Scout mission[34, 126, 130]. The authors considered several different CFRP laminate configurations and geometric variations. The laminate stacking sequence used in manufacturing was [±45/0]. Three booms of different *flattened height* are shown in Figure 5.1. The authors reported that the CTM boom surpasses the more commonly utilized TRAC boom in terms of structural stability, particularly in terms of torsion stiffness, by orders of magnitude[130]. Event though NEA Scout did eventually use Elgiloy TRAC booms, the CTM is a very promising candidate for future solar sailing missions and thus, a worthwhile object of study in this thesis.

In its undeployed state, the CTM boom consists of two identical omega-shaped half-shells. As we can see in Fig. 5.2, the omega shape consists of two circular segments with radii R_1 and R_2 which subtend at angles α_1 and α_2. The contact area between the two half-shells, called *web*, has a width of w. The shell thickness is denoted as t_{sh}. In order to keep the design space limited, we adhere to the constraints

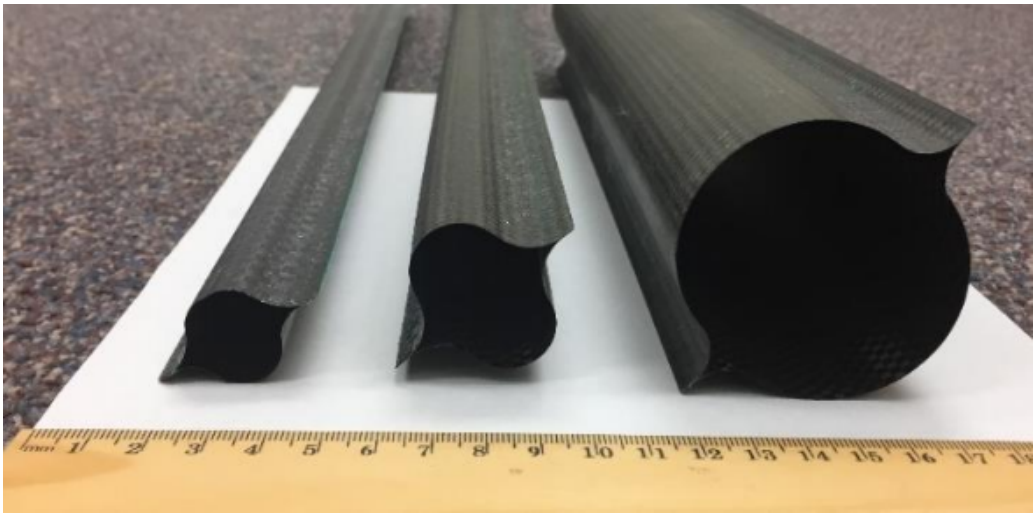

Figure 5.1: CTM booms manufactured by Fernandez[126] with flattened heights of 45 mm, 65 mm and 110 mm (left to right).

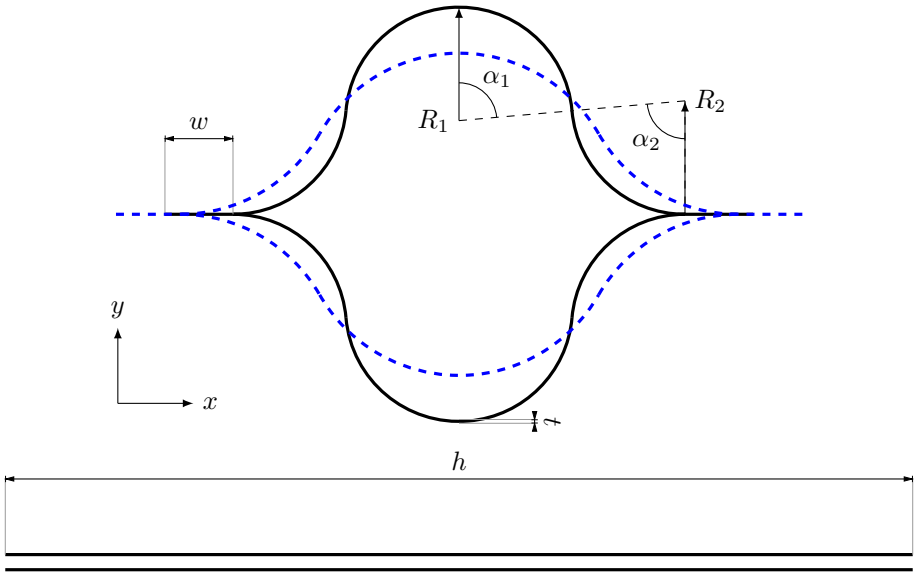

Figure 5.2: Shape definition of the CTM cross-section according to [126]. The two cross-section have the same h and $R_1 = R_2$ and with varying $\alpha = 85°$ (solid) and $\alpha = 60°$ (dashed). The x-axis normal to the sail plane. On the bottom we can see the flattened cross-section.

Figure 5.3: Electrically driven boom tip (left) and inflatable boom (right) from [128]. Reproduced with permission.

used by Fernandez[126], who designed the booms with $\alpha = \alpha_1 = \alpha_2$. When stored, the booms are flattend and rolled up. The flattened height h of the boom is calculated with the elegant formula[34]:

$$h = 2w + 2\alpha(R_1 + R_2) \tag{5.1}$$

For future reference, we will refer to a specific geometry by the shorthand CTM(R_1,R_2,α), where the radii are given in millimeters and the angle is given in degrees.

Unsurprisingly, the structural stability of the CTM boom is strongly affected by the geometry. Fernandez investigated miniaturized CTM booms with $t_{sh} = 0.115\,\text{mm}$ and a linear density of only $16.5\,\text{g}\,\text{m}^{-1}$[34]. Fernandez reports the x-moment of area to almost linearly decrease by 50 % with α increasing from 50° to 90° and the opposite effect for the moment of area in the y-direction[34]. In general, a increasing stiffness was observed for larger h. Moreover, they report higher flattening strains for larger values of w, reducing the feasible subtended angle α[130].

5.1.1 Deployment

Fernandez stored the completely flattened booms on centralized spools with thin inner diameter. To deploy the booms, the spools are simply rotated and the boom resumes its original configuration. However, Fernandez reports a reduction of α by 30° of the root section of the boom after prolonged storage[126]. A detailed study of this effect is missing and as we will see later, has a significant impact on its use as waveguide.

Block et al. studied the chaotic behavior of boom deployment[128]. They found that, while very light-weight, central deployment mechanisms place the structural loads at the transition zone between flattened and the unfurled cross-section, which may lead to chaotic behavior of the boom. The alternatives proposed by the authors are deployment via inflation and electrical tip drive (cf. Fig. 5.3).

The inflation method tested by Block et al. uses a $12\,\mu$m thick polymer bladder that loosely sits inside the boom and streches through its entire length. To deploy the boom, the bladder is pressurized, and the boom unfurls. On the other hand, the electrical tip drive uses a motor and battery assembly on the outer end of the boom. The boom is connected to the spacecraft via flanges and the tip drive slowly drives outwards until the boom is fully unfurled. Afterwards, the tip drive is jettisoned.

Both concepts are attractive for this thesis, because they allow the root of the boom to remain uncollapsed. A decisive advantage, as this makes the microwave adapter of a boom waveguide more convenient.

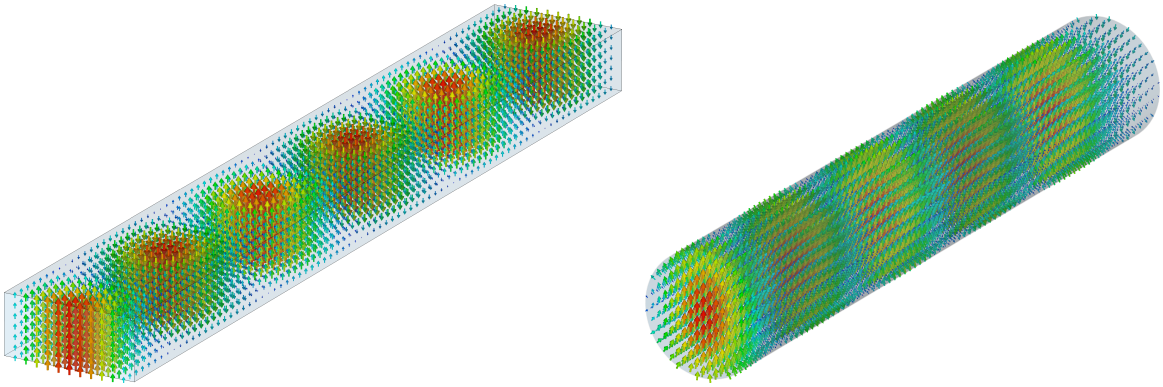

(a) Rectangular Waveguide (b) Circular Waveguide

Figure 5.4: E-fields of the fundamental TE mode of rectangular and circular waveguides.

5.1.2 Waveguides

The hollow geometry of the CTM boom may be used as a waveguide. Waveguides are hollow, tubular structures with metal walls, in which electromagnetic waves can propagate. Waveguides are popular in high power systems and at high frequencies due to their high power handling capabilities and very low loss[81].

The distribution of the electric and magnetic field inside the waveguide is determined by its shape. Most commonly, the waveguide is designed with a rectangular or circular cross-section, but other shapes are also possible[131]. Inside the waveguide, electromagnetic waves can propagate as a TE or a TM mode, whereas the TEM mode is not supported due to the missing center conductor[81]. The shape of the electrical field distribution of the fundamental TE mode in rectangular and circular waveguides is shown in Fig. 5.4. In absence of any attenuation, the propagation constant β is[81]:

$$\beta = \sqrt{k^2 - k_c^2} \tag{5.2}$$

where k is the free-space wavenumber and k_c is the wavenumber of the cutoff frequency f_c. f_c is the lowest frequency at which propagation occurs in a particular waveguide. f_c is determined by the geometric expansion of the waveguide walls; a smaller cross-section increases the cutoff frequency, whereas a larger cross-section decreases it. In a rectangular waveguide, k_c is[81]:

$$k_c = \sqrt{\left(\frac{m\pi}{a}\right)^2 + \left(\frac{n\pi}{b}\right)^2} \tag{5.3}$$

where m is the number of field variations along the long side of length a whereas n is the number of field variations along the short side of length b. Similarly a circular waveguide, m, n represent the number of radial and angular variations. A mode is identified by m, n and the transversal field component, e.g. TE_{10} identifies a mode with a transversal electric field having one horizontal and zero vertical variations.

As we see from (5.2), waveguides propagate fast waves, since $\beta < k$ and therefore the phase velocity v_p is faster than the medium speed of light. It follows that the guided wavelength λ_g is longer than the free-space wavelength.

Usually, waveguides are designed so that only the mode with the lowest f_c can propagate, as this mode has the lowest loss. This mode is called the *fundamental mode*. In most cases, the fundamental mode is TE. An exception to this is e.g. the TE_{01} mode of the circular waveguide, that is a higher-order mode but has lower loss[81]. If more than one mode can propagate at the desired operating band, the waveguide is *overmoded* and parasitic higher order modes may be excited.

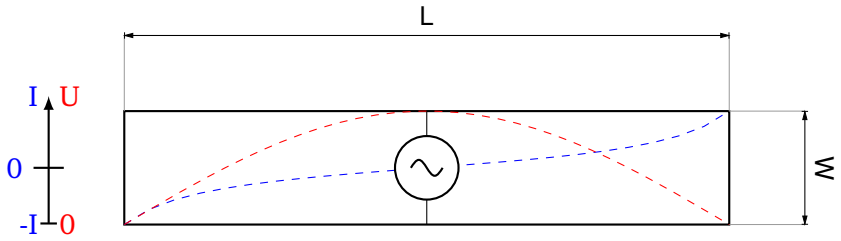

Figure 5.5: Slot antenna diagram with AC voltage source. The voltage in the slot is indicated in red. The current on the ground plane is shown in blue.

5.1.3 Slotted Waveguide Antenna

We now shift our focus towards the SWA. The SWA is a type of antenna that is formed by cutting slots into the surface of a waveguide. The slots act as radiating elements and the waveguide itself acts as a transmission line.

The theoretical slot is analyzed as an opening in infinite ground plane with a length $L \approx \lambda/2$ and a width $W \leq 0.1\lambda$ (see Fig. 5.5)[74]. The slot is excited via a voltage source in the center and a unidirectional electrical field forms between the two long sides[74]. The current flows around the slot, reaching its peak value at the center of the broad side. The center-fed slot theoretically has infinite impedance, because the current at the center is zero. However the source can also be moved off-center to lower impedance. By Babinet's principle, the slot antenna can be regarded as inverted dipole with the same radiation pattern but inverted polarization[74]. When the slot is backed by a cavity, such as a waveguide, the radiation pattern becomes unidirectional.

When we transfer the concept of the slot to the waveguide, any E-field gradient on the surface can act as voltage source. Multiple slots can be placed along the direction of travel to form a SWA array with higher gain. The array can be built as traveling wave array or resonant array[132]. The traveling-wave array is terminated in a matched load and in contrast, the resonant array is terminated in a short circuit. The short circuit forms a standing wave, in which the slots are placed with $\lambda_g/2$ separation[132]. The main beam of the resonant array radiates broadside, because all slots are excited with the same phase. The traveling-wave array excites each slot with a progressive phase.

An advantage of the travelling wave arrays is the greater frequency bandwidth for a given return loss compared to resonant arrays, at the expense of lower efficiency because of the power dissipated in the termination[133]. The maximum radiation efficiency of travelling wave antennas is limited. Therefore, as the traveling wave array grows in size, its return loss performance improves. Nevertheless, as the array size increases, the main beam's frequency scanning causes the gain bandwidth to decrease.[133].

5.1.4 CFRP Waveguides

CFRP structures are of great interest to the aerospace industry because of their high structural stability at very low mass. Very similarly to the goal of this thesis, the aerospace industry seeks to decrease mass by integrating microwave functionality into carbon aircraft structures[134]. Metallized CFRP waveguides have also been employed on European SAR spacecraft as early as 1981[135] and more recently on the Sentinel-1 SAR satellite[136]. However, this metalization process involves toxic and carcinogenic chemicals and is therefore not preferred[136]. Because carbon fibers are also conductive, pure CFRP waveguides are an attractive component of aerospace antennas.

Bojovschi et al. have investigated waveguides purely made from CFRP[137]. The authors studied several rectangular CFRP waveguides with $[0\ 90]_s$, $[90\ 0]_s$ and $[\pm 45]_s$ stacking sequences. The stack consisted of four layers with 125 μm thickness each. They found that fiber orientation significantly impacts the attenuation of the waveguide. Furthermore, they argue that this is because the current pen-

etrates the CFRP and interacts with the epoxy resin, thus causing large dielectric losses. The measured attenuation constants varied between 6.55 $\mathrm{dB\,m^{-1}}$ at 8 GHz with a $[90\ 0]_s$ stacking and 5.53 $\mathrm{dB\,m^{-1}}$ at 12 GHz with $[0\ 90]_s$. The $[\pm 45]_s$ sequence was found to have the highest attenuation of 7.12 $\mathrm{dB\,m^{-1}}$ and 5.6 $\mathrm{dB\,m^{-1}}$ at 8 GHz and 12 GHz, respectively. The authors note that comparable aluminium or carbon fiber waveguides would have an expected attenuation of 0.1 $\mathrm{dB\,m^{-1}}$ and 0.86 $\mathrm{dB\,m^{-1}}$, respectively.

Because of this high attenuation, Rudd et al. sought to improve the CFRP waveguides by coating the inside of the waveguide with a metalized carbon fiber veil[138]. In their paper, the authors report an improved attenuation of less than 1 $\mathrm{dB\,m^{-1}}$ between 8.2 GHz and 12 GHz for the carbon fiber veil. Recent investigatons by Rudd et al. regarding the attenuation of higher-order modes in rectangular CFRP waveguides indicate that TM modes can result in lower attenuation compared to TE modes[139].

Bojovschi et al. designed a 10 GHz CFRP SWA array with ten longitudinal slots based on a rectangular waveguide[134]. The antenna was designed as a linear polarized uniform resonant array and an CFRP as well as aluminum version with the same geometric specifications were manufactured and compared. Research by Coetzee shows that this method has an error, as both the slot resonant length and center offset vary between aluminium (PEC) and CFRP[140]. Bojovschi et al. report a 3 dB difference between the two versions, with only about 1.7 dB attributed to waveguide losses.

5.2 Waveguide Design

Having discussed the properties of CTM booms and waveguides, we will now move on to derive and discuss the fundamental antenna design options.

In the previous section we have seen that there are two promising deployment mechanisms that preserve the boom cross-section at the root. The first mechanism unfurls the waveguide through an inserted polymer bladder, the second uses a tip drive to unroll the boom. This is important, because it allows a flange or other type of feeding mechanism to be attached to the waveguide. Moreover, this remedies the reported flattening of the boom cross-section reported by Fernandez and we can assume a constant cross-section over the entire length of the boom. Furthermore, waveguides and SWA can be made from either metalized CFRP or using the CFRP structure directly, owing to the conductive property of carbon fibers.

With this insight, we can derive three fundamental options for the utilization of the boom:

1. unmetalized CFRP waveguide with CTM cross-section
2. metallized waveguide with CTM cross-section
3. filled with an inflated and metalized polymer bladder used as circular waveguide

The two antenna options, traveling wave antenna (TWA) and resonant antenna, depend on the type of termination possible with the respective waveguide configuration. Because of the unusual requirements connected to the application, some degree of mismatch will have to be tolerated. A short summary of the combination of termination and waveguide is presented in Tab. 5.1.

Potentially, we can create a matched termination using a sufficiently long waveguide section, such that the remaining power is dissipated via conductor losses. This option likely works best with the pure CFRP waveguide, because of its high expected attenuation. For the other two waveguide types, it is conceivable to reduce the metal thickness so that sufficient damping occurs via the skin effect.

The short-circuit termination is only viable with the polymer bladder. A punctured diaphragm at any point along the waveguide or at the end will support the gas flow during deployment and at the same time short-circuit the microwave. It's worth noting that a real open waveguide will typically radiate strongly and may not provide a well-defined open-circuit termination. However, in situations where

Table 5.1: Waveguide options and feasible terminations.

Waveguide	Termination		
	Match	Short	Open
Polymer Bladder	✓	✓	✗
CTM unmetalized	✓	✗	✗
CTM metalized	✓	✗	✗

the reflection is negligible and waveguide attenuation is high, an open waveguide could be used in place of a matched termination.

In the following, we will briefly discuss the advantages and disadvantages of the feasible options. Subsequently, we select the most promising candidates for further investigation.

5.2.1 CTM Waveguide

The most basic approach is the CFRP CTM waveguide. This option directly uses the CFRP as conductor and the waveguide geometry is given by the CTM parameters. Besides the slots cut into the surface, the root attachment point of the boom must be adjusted to also function as waveguide adapter. No further alterations of the boom itself are needed and the required production steps are kept to a minimum. Taking all of these factors into consideration, it's clear that this option stands out as the lightest of them all.

When considering the electrical properties of CFRP waveguides, the high attenuation has an important impact on antenna size. Specifically, due to the greater amount of power dissipated in the CFRP material, less power is available for radiation. This means that a CFRP waveguide typically allows for a smaller antenna compared to a metalized version. Depending on the incident power and mission profile, this may also have an impact on the thermal budget. Despite the potential issues with radiation and open-circuit termination, the high attenuation of a CFRP waveguide has a noteworthy advantage. Specifically, it means that the expected required length of the waveguide for a matched termination is typically only a few meters. Therefore, it is easier to realize in applications with smaller probes and shorter booms.

Using the CTM geometry directly results in strong coupling of structural and electrical design, which is generally discouraged. Specifically, we expect a degradation of the structural properties of the CTM boom through the introduction of the slots. A larger geometry will be required, which in return impacts the waveguide's properties and slot parameters. Even with smaller geometries, we expect the CTM waveguide to be overmoded, and parasitic modes may occur.

Metalized CTM Waveguide

The metalization improves the attenuation issue of a pure CFRP waveguide, resulting in a potentially larger antenna and higher radiation efficiency. However, this is associated with more production steps and higher mass. Due to the limitations of current vapor deposition techniques, the boom must likely be fabricated as two half-shells, which are subsequently metalized independently. It may prove labor intensive and difficult to deposit metal layers of different thicknesses in order to realize a matched termination.

A space-grade metalization of CFRP with good layer adhesion requires a pretreatment carried out with chromosulfuric acid, which is carcinogenic[136]. For this reason we abstain from building prototypes with this production step.

5.2.2 Polymer Bladder Circular Waveguide

The central point of this design option is a quasi-cylindrical polymer bladder that is situated within the CTM boom. If the bladder serves as a component of the deployment mechanism, it will span the entire length of the boom. Alternatively, if it is not necessary for deployment purposes, the bladder may terminate at any point along the boom, as needed. An advantage of this concept is that the dimensions of the polymer bladder can be adjusted by a certain degree, especially if it is not a component of the deployment mechanism.

In order to construct the SWA, both the boom and circular polymer waveguide require slots. However, the polymer balloon must remain air-tight in order to maintain its function during deployment. Instead, the slots should be created during the metalization process of the polymer. Once completed, both components' slots must be meticulously aligned and affixed in place using adhesive. This in return means that the boom can no longer be manufactured as a whole. Instead, the booms must be made from two-half shells, so that the adhesive can be properly aligned on one side.

While this option is attractive from an electric point of view, its has some drawbacks. The alignment of the slots in the polymer bladder with the slots in the adhesive foil and boom is difficult, especially if a large antenna with many slots is to be build. If the polymer is metalized on the inside, one potential issue to consider is the possibility of cold welding, causing the balloon not to assume its intended shape. Likewise, other effects like static electricity may also impede the formation of a regular shape.

5.2.3 Discussion

The CFRP CTM waveguide is the lightest option among all the waveguide concepts due to the direct use of CFRP as conductor. A drawback of the CFRP CTM waveguide are its strong coupling of structural and electrical design, which is generally discouraged. Due to the introduction of slots into the boom, there will be degradation of the structural properties of the boom, requiring a larger geometry that impacts the waveguide's properties and slot parameters. Additionally, the expected high attenuation of CFRP reduces potential antenna size and radiation efficiency. Finally, even with smaller geometries, the CTM waveguide is expected to be overmoded, and parasitic modes may occur.

The metalized CTM waveguide alleviates the attenuation associated with the CFRP conductor, at the expense of slightly increased mass and production complexity. Space-grade prototypes cannot be made within the scope of this thesis due to the health risks involved in the production.

The polymer bladder waveguide offers the advantage of adjustable dimensions if it is not part of the deployment mechanism. However, compared to the CFRP CTM waveguide, the manufacturing process is more complicated due to the need for slots in both the boom and the circular polymer waveguide, while ensuring the polymer balloon remains air-tight during deployment. Additionally, the alignment of the slots with the adhesive and boom can be difficult, especially for larger antennas.

For these reasons, we consider the CTM waveguide to be the best option for further investigation. The metalization may provide a critical advantage for larger antennas. However, the pure CFRP conductor is interesting for its potential simplicity and low mass. It will therefore be the focus of this work.

5.3 CTM Waveguide

In this section, we will discuss the electrical properties of CTM geometries at microwave frequencies. First, we will investigate the modes supported by the CTM geometry, their field and current distribution and attenuation. Afterwards, we study the effect of geometric variations on f_c.

5.3.1 Propagating Modes

We will now briefly investigate the propagation of waves in the CTM geometry. This is important for the later use as slotted waveguide antenna, as the field distribution of each mode determines optimal placement and size of the slots. These parameters in return affect antenna properties, e.g. maximum gain, main lobe direction and side lobe level. The attenuation due to conductor loss is a function of the geometry, frequency and conductor material.

To first illustrate the characteristics of the CTM waveguide, we begin the analysis with a CTM(15,10,85) geometry, by which we mean a geometry with R_1 =15 mm, R_2 =10 mm and α =85°. To determine the field distributions inside the CTM waveguide, we use a simulation model in CST Microwave Studio. CST has a built-in mode solver for arbitrary geometries with which we can determine the respective E- and H-fields. The frequency used in this analysis is 8.5 GHz.

Figure 5.6(a) qualitatively depicts the E-field and current distribution of the fundamental mode. The E-field lines perpendicular to the z-axis reveal this mode to be TE. The E-field is reminiscent of the $\mathrm{TE}_{01}^{\square}$ mode in a rectangular waveguide: The field strength is mostly uniform along the x-axis, while the main cosine-shaped variation is along the y-axis. The exception to this are distortions along the surface with strong curvature, where the geometry deviates most from a rectangular shape. Compared to the rectangular waveguide (cf. Fig. 5.4) this shifts the field maxima from the middle along the y-axis. Instead, the field is distorted, so that the maximum divides into two, close to where R_1 and R_2 subtend. We will refer to this mode as $\mathrm{TE}_{01}^{\square}$.

Figure 5.6(b), we find the second TE mode. This mode is more reminiscent of the $\mathrm{TE}_{11}^{\bigcirc}$ mode of a circular or elliptical waveguide. Again, the main deviation from this pattern is found where the two shells come close. Incidentally, this is also where most of the current is concentrated. We will refer to this mode as $\mathrm{TE}_{11}^{\bigcirc}$. As we will see later, this mode can also be the fundamental mode, depending on the subtended angle α.

Finally, the waveguide also supports a TM mode, which is the $\mathrm{TM}_{01}^{\bigcirc}$ mode shown in Fig. 5.6(c). The longitudinal E-field leads to an interesting current distribution, as seen on the right side of Fig. 5.6(c). In contrast to the current distributions of the other modes, the $\mathrm{TM}_{01}^{\bigcirc}$ current lines are all oriented in parallel to the z-axis. This could be an advantage in pure CFRP waveguides if the innermost fiber layer is unidirectional.

Figure 5.7 displays the attenuation constant of the discussed modes in a copper waveguide[1]. We can observe low attenuation, as is typical for waveguides, with a clear distinction between the individual modes. Note that the given values can be regarded as lower bound, as different material choice, manufacturing process and surface roughness will increase attenuation significantly.

In Figure 5.8, we can see the dispersion diagram of each mode. The propagating modes in the CTM waveguide are fast waves, i.e. $v_p > c_0$. The phase constant of the free-space TEM wave is given as the light line. We can observe the phase constant to decrease with increasing mode number.

5.3.2 Geometric Variation

Compared to conventional circular or rectangular waveguides, the CTM geometry offers a unique advantage in terms of flexibility. It possesses more degrees of freedom, allowing for a broader range of fundamental shapes. Depending on the specific parameters chosen, the shape of the CTM waveguide can manifest in various forms, such as lenticular, rectangular, oval, or even closely resembling a circular shape. The geometric parameters of CTM are variable and may be chosen either arbitrarily or with a certain goal. Hence it is important to assess the effect of a varying geometry on the function as waveguide. A full analysis of all parameter combinations is outside of the scope of this thesis. We study the parameters through their effect on f_c of the individual modes. The property f_c is ideal for this study, as it is directly derived from the geometry. Furthermore, f_c is also a good indicator of the

[1]The simulation of an anisotropic material was not performed due to limitations in the simulation capacity.

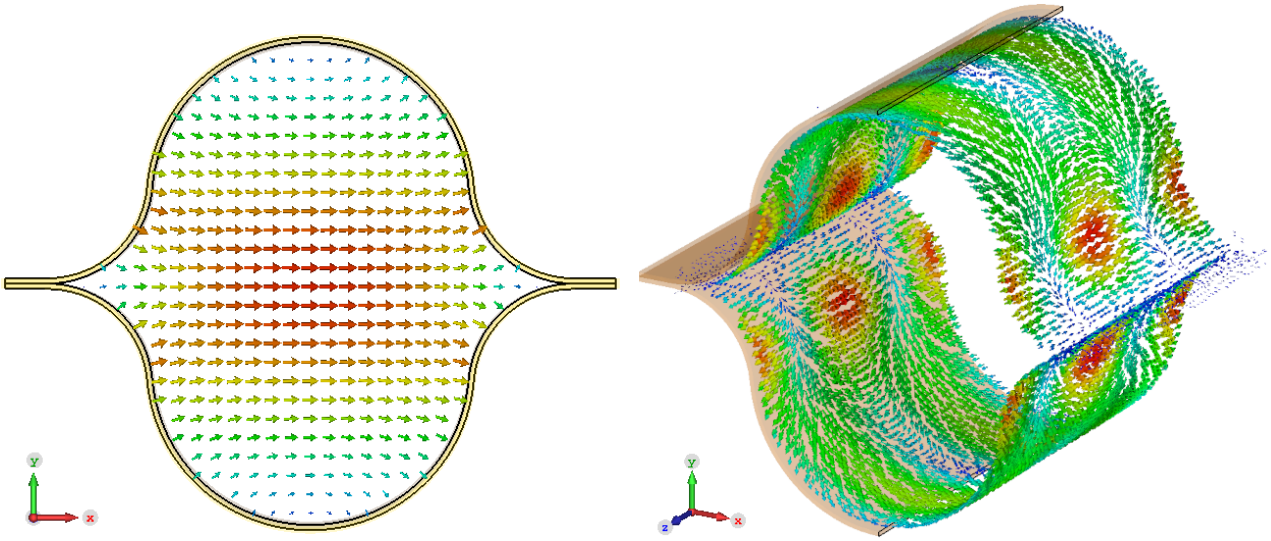

(a) E-field (left) and current distribution (right) of the fundamental $TE_{01}^{\square}$ mode.

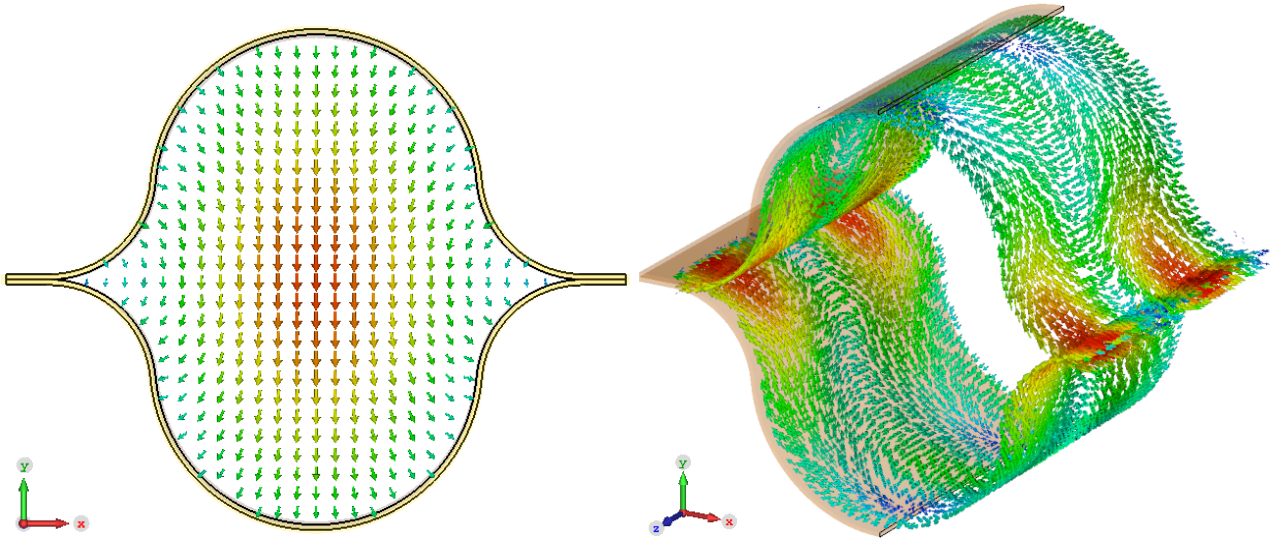

(b) E-field (left) and current distribution (right) of the $TE_{11}^{\bigcirc}$ mode.

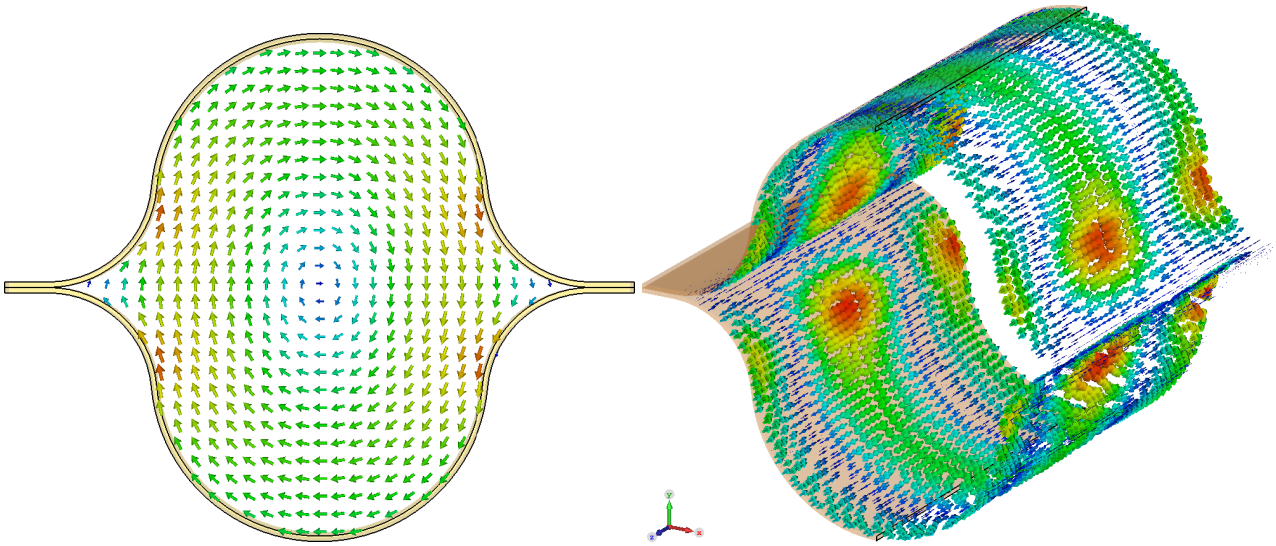

(c) H-field (left) and current distribution (right) of the $TM_{01}^{\bigcirc}$ mode.

Figure 5.6: Field and current distribution of the first three modes of the CTM(15,10,85) geometry.

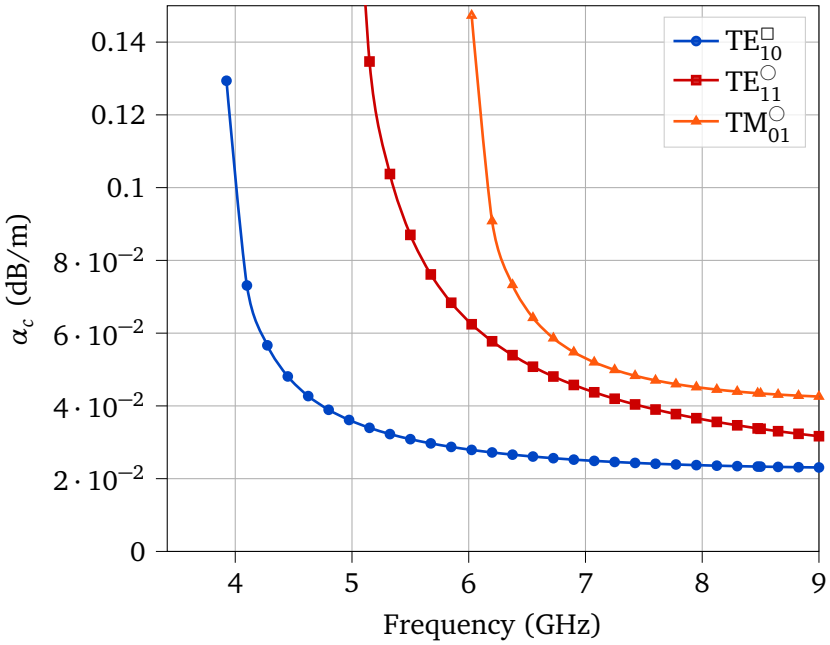

Figure 5.7: Attenuation of the first three modes in a CTM(15,10,85) copper waveguide.

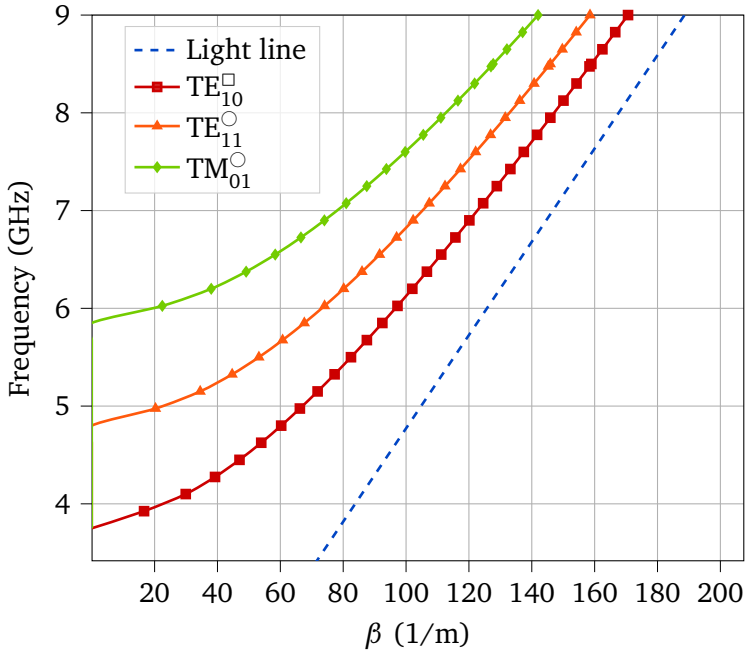

Figure 5.8: Phase constant β of the first three modes in a CTM(15,10,85) copper waveguide.

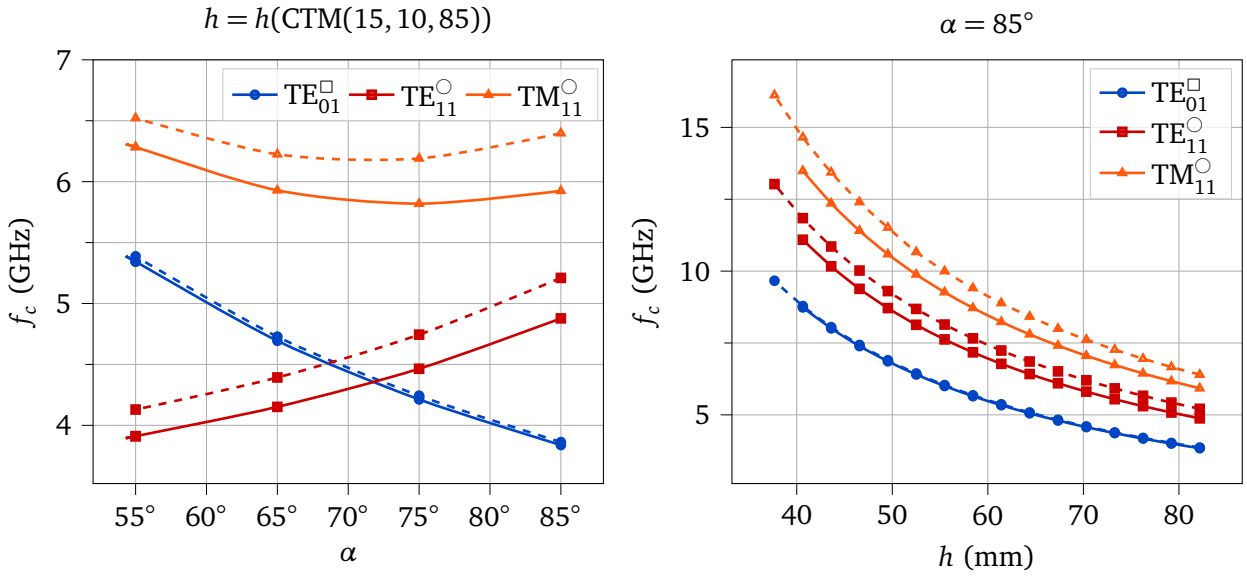

Figure 5.9: Variation of f_c of the CTM waveguide for $\mathrm{TE}_{01}^{\square}$, $\mathrm{TE}_{11}^{\bigcirc}$, and $\mathrm{TM}_{01}^{\bigcirc}$ modes as a function of geometric parameters. Left: Graphs for constant h and varying α. Right: Results for constant $\alpha = 85°$ and changing $R_1 + R_2$. Dashed lines represent $R_1 = R_2$, solid lines indicate $R_2 = \frac{2}{3}R_1$.

mode order, and also the usable frequency range.

An analysis of the effect of the geometric parameters on f_c is presented in Fig. 5.9. The left graph of this figure illustrates f_c for the first three modes, plotted as a function of the angle parameter α, while maintaining a constant flattened height. This height is specifically chosen to match the flattened height of the CTM(15,10,85) geometry. A notable observation is the behavior of the $\mathrm{TE}_{01}^{\square}$ mode. For values of α greater than 75°, this mode acts as the fundamental mode. However, as α decreases, it transitions to a higher-order mode. Interestingly, f_c of this mode shows an increasing trend with a decrease in α. Furthermore, this mode remains largely unaffected by variations in the R_1/R_2 ratio.

On the other hand, the $\mathrm{TE}_{11}^{\bigcirc}$ mode behaves differently. It serves as the fundamental mode when α is less than 75°, but transitions to a higher-order mode for larger α values. The f_c for this mode exhibits a decreasing trend with a decrease in α. Additionally, this mode is particularly sensitive to the R_1/R_2 ratio, with a noticeable 5.5 % to 6.8 % increase in f_c.

The $\mathrm{TM}_{01}^{\bigcirc}$ mode, in contrast, displays minimal variation across all angles, with f_c ranging between 5.9 GHz to 6.3 GHz. For α between 65° to 85°, f_c changes only slightly. However, for α below 65°, there's a noticeable increase. The influence of the R_1/R_2 ratio on this mode is similar to that on the $\mathrm{TE}_{11}^{\bigcirc}$ mode, but the offset grows with α, ranging from about 3.7 % to 8 %.

The right graph in Fig. 5.9 shifts the focus to f_c of the first three modes as a function of the flattened height h, while keeping α constant. A general trend observed across all modes is that f_c tends to increase as the flattened height decreases. The $\mathrm{TE}_{01}^{\square}$ mode, consistent with its behavior in the left graph, shows a remarkable insensitivity to changes in the R_1/R_2 ratio. However, both the $\mathrm{TE}_{11}^{\bigcirc}$ and $\mathrm{TM}_{01}^{\bigcirc}$ modes display a heightened sensitivity. Their cutoff frequencies increase by approximately 6 % and 8 %, respectively, when subjected to variations in the R_1/R_2 ratio.

We can further extract from the figure, that the practical lower limit of h for CTM waveguides is at about 50 mm. Below this value, the attenuation and λ_g of the fundamental mode rise significantly and render the waveguide impractical or unfeasible.

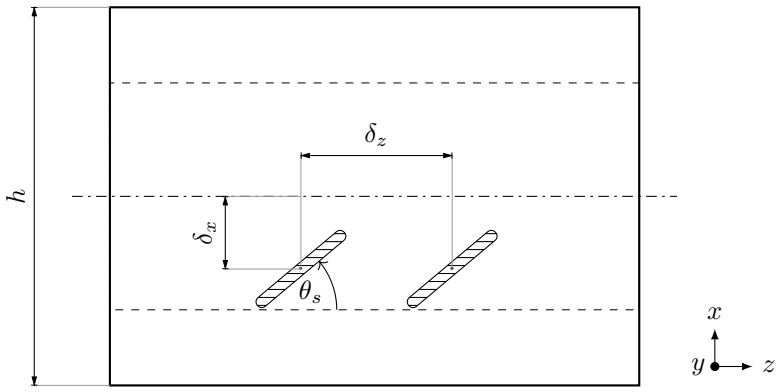

Figure 5.10: Coordinates of the slots on the flattened CTM boom with flattened height h. The dashed line marks the web area. The offset from the centerline δ_x and longitudinal slot offset δ_z are measured from the center of the slot area.

5.4 Slotted Waveguide Antenna

Having explored the potential of the CTM geometry as a waveguide, we now turn to the slotted CTM waveguide. As we recall from section 5.1, the theoretical slot is excited by a voltage source. In the practical case of the slotted waveguide, this voltage source is the E-field within the waveguide. Conveniently, any field gradient can serve as a voltage source. However, the slot's efficiency depends on the E-field magnitude, while its impedance varies with geometry and excitation location. To specify the slot's location, we introduce a coordinate system based on the flattened boom (cf. Fig. 5.10).

Using the single-slot antenna we determine the optimal slot geometry, location and rotation for each mode. Afterwards, we translate the results to a 10-slot SWA and investigate radiation pattern and slot spacing.

5.4.1 Slot Location

The most suitable slot location can be identified using the current maxima location on the waveguide's inner surface. We refer back to Fig. 5.6, where the maxima can be observed. For $\mathrm{TE}_{01}^{\square}$ the maximum current is roughly located where R_1 and R_2 subtend. In the maximum, the current is oriented along the direction of propagation, while between two maxima, it is rotated by 90°. This indicates a strong field gradient on the one hand, but since the we are discussing a travelling wave, this also limits efficiency, when the longitudinal component of the current on both sides of the slot reach zero. We can also observe a less pronounced gradient on the top. This location however, is unattractive as a slot located there would radiate into the sail plane.

In the case of $\mathrm{TE}_{11}^{\bigcirc}$, the current maximum located about were both half-shells meet and extends inwards from this point. At the maxima, the current flows perpendicular to the direction of propagation. Again, a less pronounced gradient is found on the top.

The surface current of the $\mathrm{TM}_{01}^{\bigcirc}$ flows parallel to the direction of propagation. The maxima which are located where R_1 and R_2 subtend.

5.4.2 Slot Resonant Length

As we have discussed before, the theoretical slot has a length l_s of about $\lambda/2$. The resonant length of a slot is a function of its offset in x-direction δ_x, and wall thickness t[141]. Additionally, this is different for every mode and inclination. A way to determine the resonant length is to maximize the radiation efficiency in a two-port model, which results in a slot with purely real admittance[141]. At the same time, this method gives an outlook on the achievable coupling and radiation efficiency of an array.

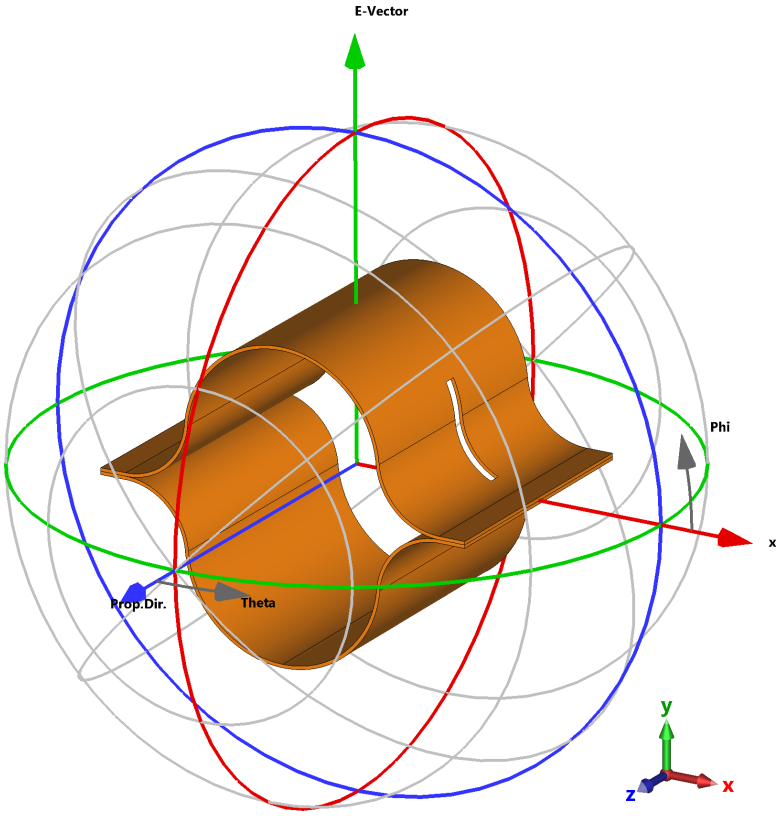

Figure 5.11: 2-port simulation model of a copper CTM TWA with one slot, angled at 90°.

In the following, we will perform a simulation parameter sweep over l_s, δ_x and θ_s in order to investigate the influence of these parameters. The following simulations are performed in CST Microwave Studio on a CTM(15,10,85) waveguide of pure copper. The wall thickness used for the simulations was fixed to 0.5 mm and the slot width was set to 2 mm. Figure 5.11 shows the model of a TWA with one slot.

First, we begin with a parameter sweep over the slot length in the range of 15 mm to $\lambda/2$ and δ_x between 21 mm to 25 mm in order to not cut into the web. The slot inclination θ_s is set constant to 90°, as this is the most promising configuration for the $\mathrm{TE}_{01}^{\square}$ and $\mathrm{TM}_{01}^{\bigcirc}$. The figure of interest in this study is the total radiation efficiency η_{tot}, which is defined as:

$$\eta_{tot} = \frac{\text{Power Radiated}}{\text{Total Power}}$$

Figure 5.12 shows the results of this sweep. We can observe that every graph shown in the figure exhibits a distinctive peak. The first observation we can make is the absolute values of η_{tot}. The $\mathrm{TM}_{01}^{\bigcirc}$ mode has the highest η_{tot}, with 32.5 %. This is more than twice as high as for the $\mathrm{TE}_{01}^{\square}$ mode, which peaks at 13.5 %. As expected, with this slot inclination, the $\mathrm{TE}_{11}^{\bigcirc}$ mode has low coupling and does not radiate well with a peak value just under 5 %.

For all modes we can observe an increase of the resonant slot length with increasing δ_x. The radiation efficiency decreases with decreasing δ_x, independent of l_s. However, in the observed range of this effect is only slight and gives some degree of freedom for designs.

Next, we will investigate the influence of θ_s on η_{tot}. For this study, we vary the slot inclination θ_s between 0° to 90° and we set the slot length to a constant value of 16 mm and δ_x to 24 mm, as these values are not extreme and exhibited good results across all modes. The results of this sweep are shown in Fig. 5.13. What can be seen in this figure is the dominance of the $\mathrm{TM}_{01}^{\bigcirc}$ mode, which has the highest η_{tot} at every slot angle $> 30°$. Note the better η_{tot} of the $\mathrm{TE}_{11}^{\bigcirc}$ mode around $\theta_s = 0°$. Moreover, the graphs of all modes have (local) maxima between 40° to 60°.

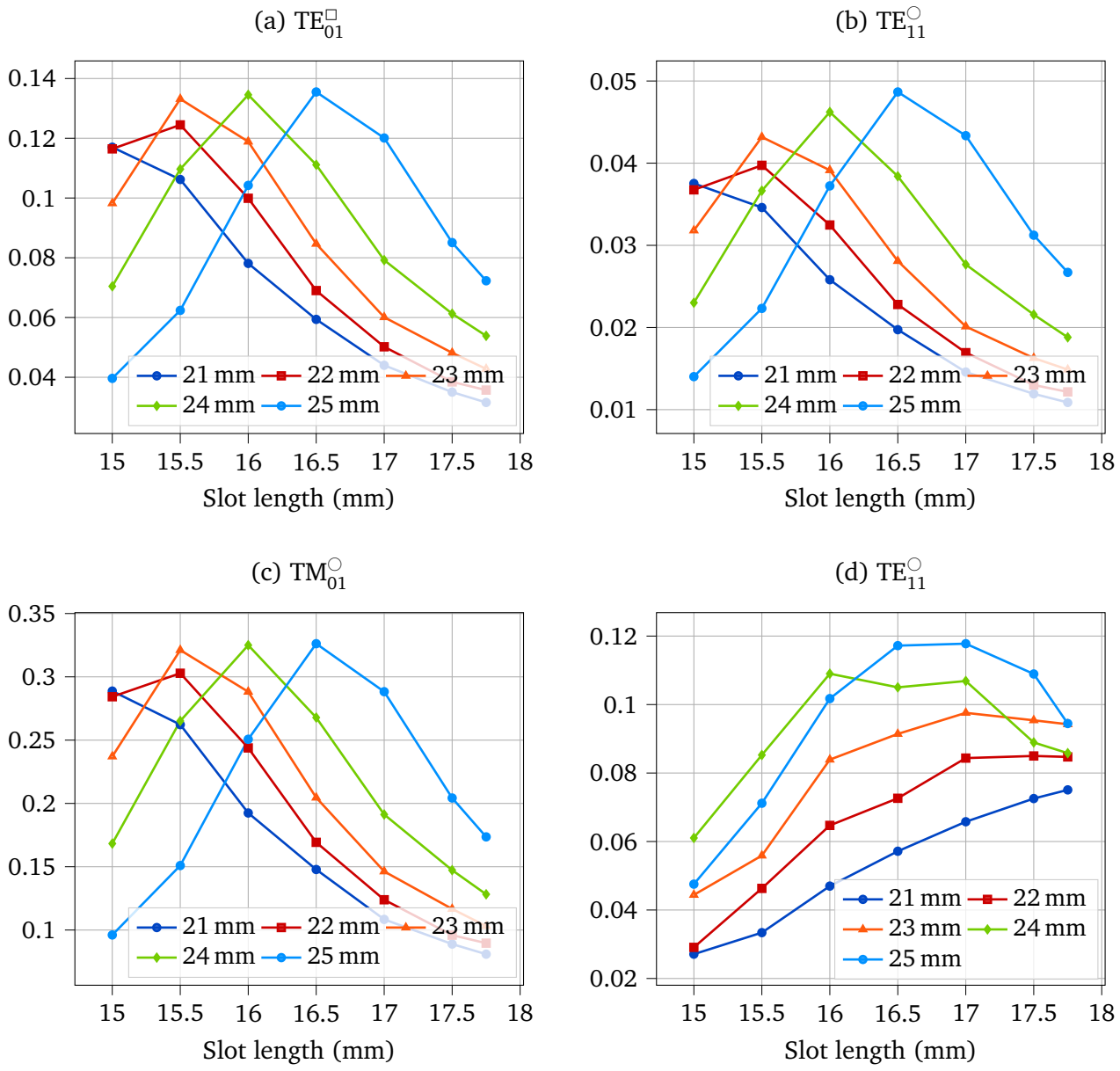

Figure 5.12: Total radiation efficiency of the 2-port model with a single slot inclined at 90° with a parameter sweep over slot length and δ_x for each mode. Diagram (d) also shows the results of the $TE_{11}^{\bigcirc}$ mode at a slot inclination of 40°.

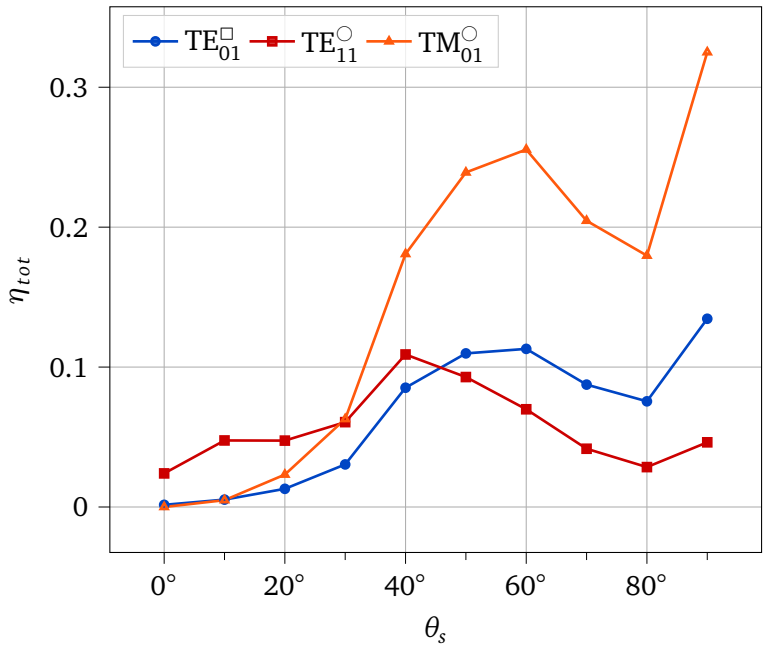

Figure 5.13: Total radiation efficiency of the single-slot 2-port model over θ_s with constant $l_s = 16\,\text{mm}$, $w_s = 2\,\text{mm}$ and $\delta_x = 24\,\text{mm}$.

5.4.3 Radiation Pattern

The slot radiates unidirectionally into the direction perpendicular to its surface, facing away from the waveguide. When the surface is planar, the main beam direction is therefore perpendicular to the surface as well. In the case of the slot antenna in a CTM waveguide, the curvature of the surface results in a spreading of the beam, decreasing directivity. The beam spreading is strongest, when the slot center is on a sharp bend, as this is the area that contributes most to the radiation. The effect is shown in Fig. 5.14. The figure shows the maximum directivity of the beam over a slot angle sweep from 0° to 90°. Interestingly, since we only observe directivity, this graph is virtually the same for all modes. From the graph we can see that the maximum directivity varies in a range of 5.4 dB to 8.5 dB, with a gradual decrease starting at 0° turning into a steep decline above about 30° and reaches its lowest point at 90°.

We can see that slot inclination has a strong influence on the directivity and also works in the opposing direction to η_{tot}. The expected maximum of this property in the middle range of the slot angle, where (local) maxima of the directivity were found (cf. Fig. 5.16). The product of directivity and η_{tot} is the realized gain. The realized gain is shown in Fig. 5.15. We can see in this figure a slight shift of the peaks towards smaller angles. The figure reveals that a slot inclination of 40° appears to be a good choice for any of the three modes. The best choice for $\text{TE}^{\square}_{01}$ and $\text{TM}^{\bigcirc}_{01}$ is 50°.

We further study the radiation pattern through φ and θ cuts of the directivity patterns of each mode and slot inclinations from 90° to 0°. Thereby, we can observe how curvature affects the entirety of the pattern. Again, the l_s is set to constant 16 mm, and the $\delta_x = 24\,\text{mm}$. The results are shown in Fig 5.16. The direction $(\varphi = 0°, \theta = 90°)$ is parallel to the x-axis, $(\varphi = 90°, \theta = 90°)$ is parallel to the y-axis (cf. Fig. 5.11). The figures reveal a wide main lobe for $\delta_s = 90°$, that gradually focuses towards $(\varphi = 40°, \theta = 90°)$. Moreover the graphs show a shift of the main lobe with decreasing θ_s, from about $\theta = 60°$ to 90°.

The figure further shows that a non-negligible part of the radiation pattern points in the direction of the sail membrane, $\varphi > 90°$ and $\varphi < -90°$. So far, we have not included this effect but will circle back to this topic later when we study the SWA array.

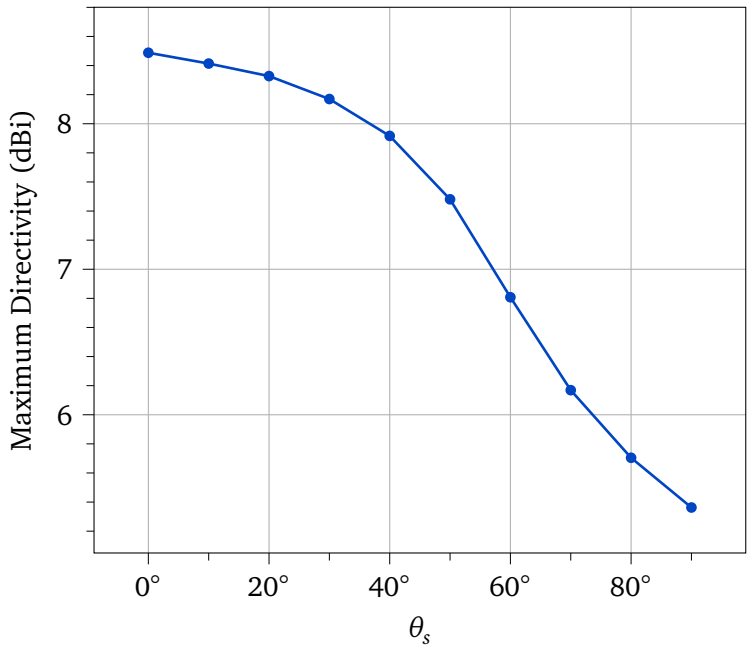

Figure 5.14: The maximum directivity of a slot with $l_s = 16\,\text{mm}$, $\delta_x = 24\,\text{mm}$. The maximum directivity is shown independent of the exciting mode.

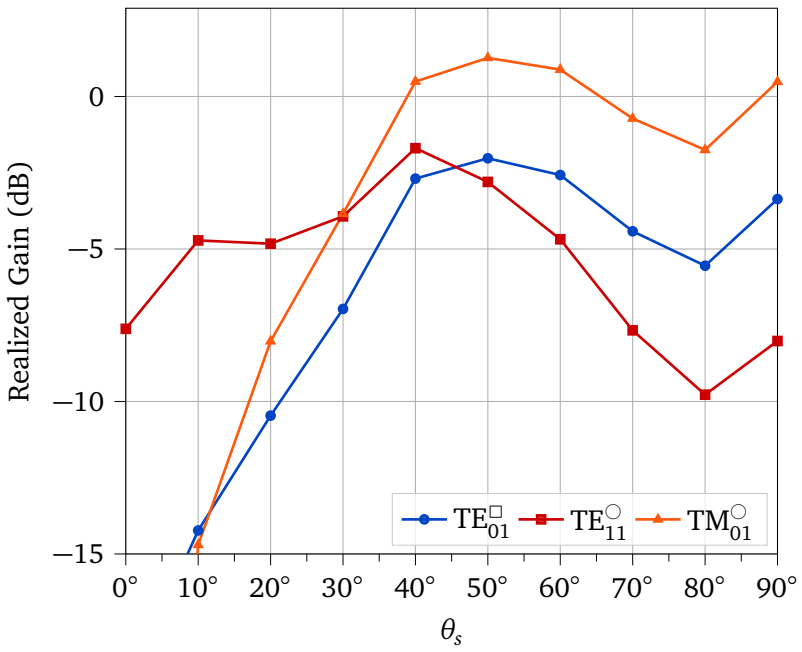

Figure 5.15: Maximum realized gain of the single-slot 2-port model over a parameter sweep of the slot inclination θ_s.

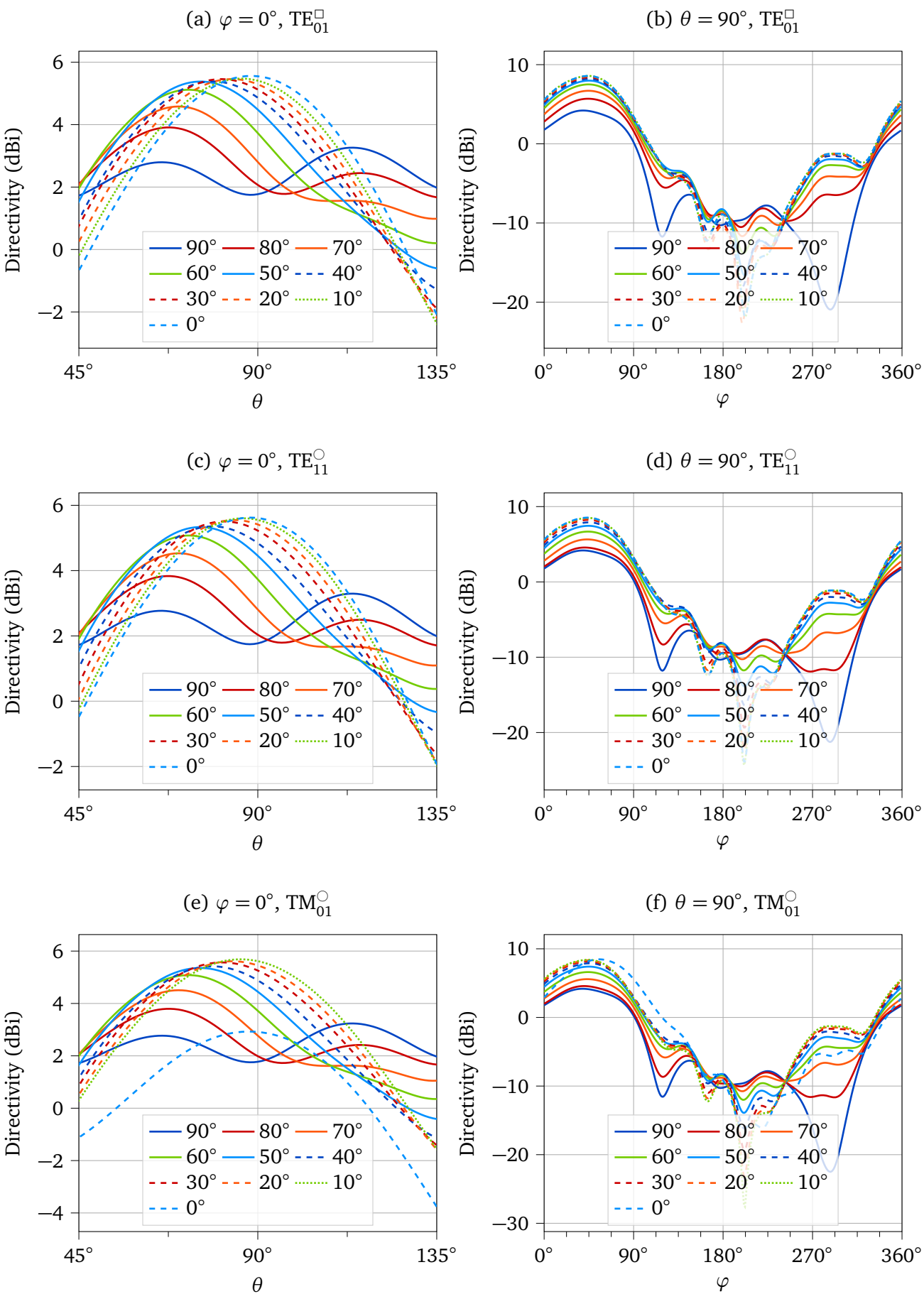

Figure 5.16: Directivity pattern of the slot antenna depending on θ_s.

5.4.4 10-Slot SWA

Previously, in Section 5.2, we determined the TWA to be the most promising approach towards a slotted CTM waveguide antenna. Having explored the properties of a singular slot, we now utilize the results to study a simulated TWA. Given the results of the previous section, we can reduce the studied modes in the following investigation to the $TM_{01}^{\bigcirc}$ since it provides the highest η_{tot}.

The SWA in the following study consists of 10 slots with a slot width of 2.24 mm, $\delta_x = 24$ mm and $l_s = 16$ mm. The used θ_s is, 45° and the simulation frequency is 8.4 GHz. The waveguide is simulated as PEC material with a wall thickness of 0.5 mm. The simulations were performed using the CST Microwave Studio Time Domain Solver. The figures of interest of the antenna array are maximum realized gain, beam squint angle and side lobe level. These properties will be studied by varying the z-slot separation δ_z and excitation frequency.

The simulation results of the $TM_{01}^{\bigcirc}$ excitation are presented in Fig. 5.17. The directivity patterns, depending on δ_z are presented in (a) and (b). Here we can observe a shift of the mainlobe towards $\theta = 90°$ for increasing δ_z. Interestingly, even as δ_z is approaching λ_g, the mainlobe reaches $\theta = 95°$, likely due to remaining reactances that accumulate along the waveguide. We can observe a strong sidelobe at 45° regardless of δ_z, with a SLL of −4 dB. The angular shift in the 8.4 GHz to 8.5 GHz range is 1° and the amplitude variation is less than 0.2 dB. Additionally, small sidelobe gains with increasing frequency. The maximum gain increases with δ_z and but flattens out above 39 mm. The maximum realized gain with 15.4 dBi is reached at $\delta_z = 44$ mm and $\theta_s = 45°$. The 3D radiation pattern is presented in Fig. 5.18.

Sail influence

The previous simulations of single slot and SWA revealed that a non-negligible part of the radiation pattern points in the direction of $\phi > 90°$. The solar sail is located in that direction and therefore, a partial reflection of the incoming signal can be expected. For a worst-case approximation, the solar sail is simulated as PEC surface, resulting in a total reflection of the incoming wave, instead of a partial reflection. In order to maintain reasonable simulation complexity, the surface is reduced to a rectangular plane with the dimensions 500 mm × 1000 mm. Note that this neglects any sail deformations. The simulation is performed with $\delta_z = 40$ mm, $\theta_s = 45°$.

The patterns of both modes are presented in Fig. 5.19. We can observe significant changes to the pattern compared to the previously obtained results (cf. Fig. 5.18). As we can see, the sail surface acts as reflector, resulting an a distortion and superelevation of the radiation pattern. Beyond $\phi = 90°$ the results show some degree of spillover, owing to the very limited expansion of the conductive plane.

5.4.5 Discussion

This section investigated the radiation properties of a single slot waveguide antenna, depending on the mode used. The single slot antenna was investigated with respect to the radiation efficiency and radiated pattern. The radiation efficiency affects the achievable efficiency of the entire array, and so, larger values are desirable. All modes are dependent on the slot angle, with maxima concentrating in the 40° to 60° range and again at 90°. In terms of radiation efficiency, the $TM_{01}^{\bigcirc}$ mode particularly stands out by a wide margin, compared to the other modes. The lower radiation efficiency of the TE modes necessitates either accepting significant losses or an exceedingly high number of slots in the final SWA. When examining the radiation pattern of the single slot, we find nonlinearly decreasing directivity with increasing slot angle, due to the curvature of the boom. The curvature spreads and shifts the radiated beam. Moreover this effect shifts the optimal slot angle towards lower values, but not enough to bridge the performance gap between the TM mode and the TE modes. This problem is expected to increase with smaller boom geometries.

This section furthermore investigated a non-uniform 10-slot TWA, excited by the $TM_{01}^{\bigcirc}$ mode. We

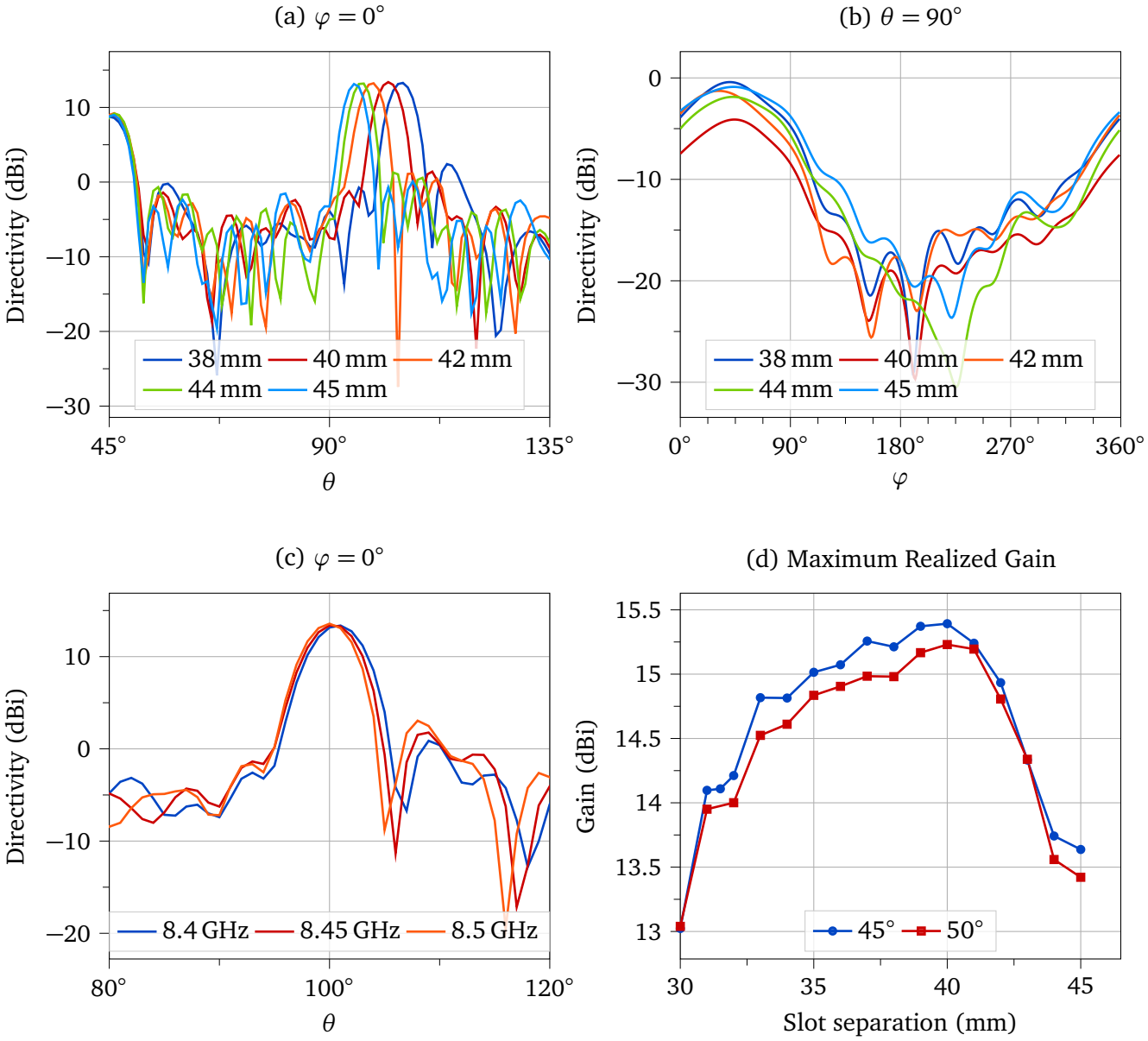

Figure 5.17: Simulated radiation pattern of the 10-slot SWA and $TM_{01}^{\bigcirc}$ excitation. Directivity patterns at 8.4 GHz with variable slot separation (a-b). Main lobe shift due to frequency and $\delta_z = 40$ mm (c). Maximum gain at inclination 45° and 50° and 8.4 GHz (d).

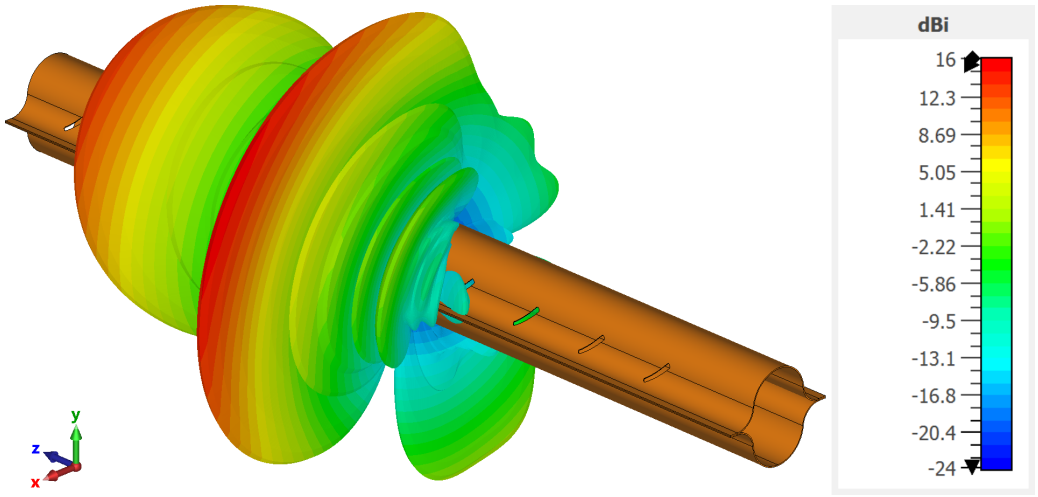

Figure 5.18: 3D copolar radiation gain pattern with $TM_{01}^{\circlearrowleft}$ excitation.

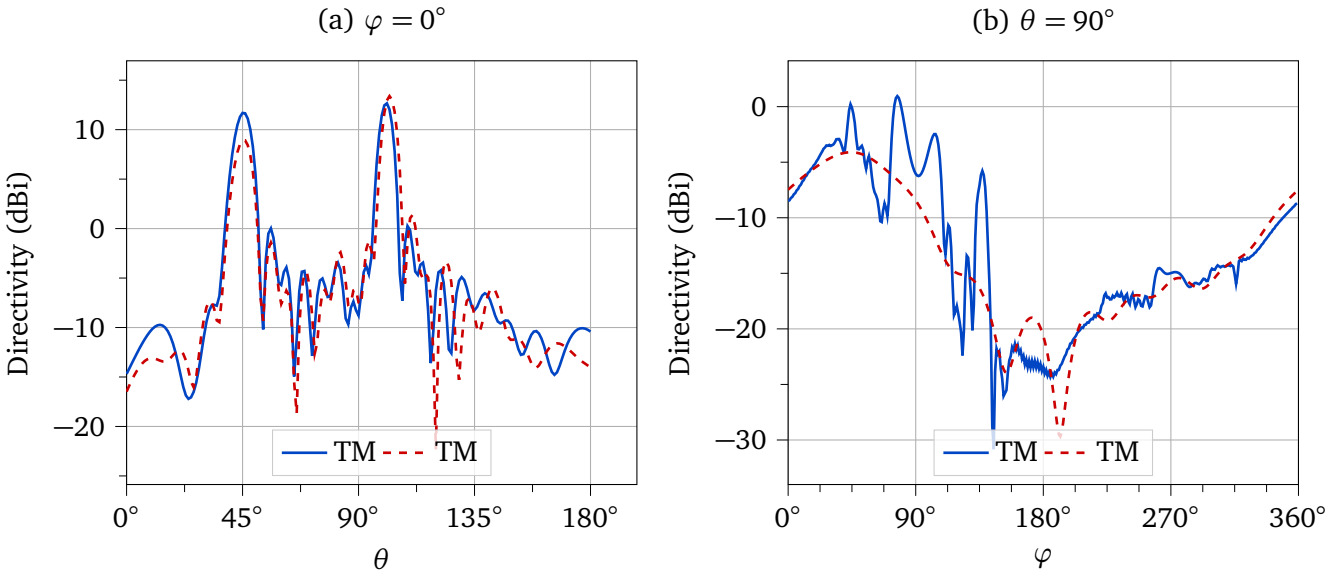

Figure 5.19: Simulated radiation pattern of the 10-slot SWA including the PEC sail, at 8.4 GHz. The corresponding result without the PEC plane is represented as dashed line.

found that the TM mode yields the highest realized gain of almost 15.4 dBi, at the cost of a significant SLL of −4 dB. The SLL is generally too high, which is partly due to the very basic design. By shaping the amplitude excitation of each slot, better results can be obtained. Finally, the simulation with a PEC plane attached to the antenna showed that a solar sail could severely impact the radiation pattern, shifting the direction of maximum of the mainlobe almost parallel to the sail plane. In the case of the perfectly planar surface, this can have a positive effect, but it is not reasonable to expect this behavior from a solar sail that is subject to wrinkles and billowing. The reflections are caused by the part of the radiation pattern that extends beyond the $\phi = 90^\circ$ limit. This is however a result of the curvature of the waveguide and cannot be remedied.

5.5 CFRP Manufacturing

In this section, we will briefly describe the manufacturing process of the CFRP CTM booms. The produced booms will later be used for mechanical and electrical testing. First, we will briefly introduce CFRP manufacturing with regard to this application. Afterwards, we select a process and material combination that meet the requirements. Finally, we present the results and issues encountered. The contents of this section were previously published in [142].

5.5.1 Overview

CFRP is a composite material consisting of two components: the carbon material and a polymer matrix. The carbon material consists of carbon fibers and is the primary load-bearing element. The polymer keeps the fibers in place, inhibits buckling and shields them from environmental impacts.

Carbon fiber material is available as woven fabric or as textile, with a range of patterns. Carbon fabrics and textiles are set apart by their handling and load carrying capabilities. Carbon fiber material available either dry, or preimpregnated with a polymeric matrix and called prepreg.

The manufacturing of CFRP can be summarized in the processing steps of preforming, matrix injection, curing and machining[2]. The choice of the manufacturing process ultimately depends on production volume and required mechanical stability. For low volumes and high stiffness, manually-laid prepregs or dry fiber mats are recommended.

In the preforming step, the 3D structure of the final part is created using the carbon material. The most common processes for this are automatic fiber placement in the case of prepregs, or dry fiber placement (DFP) when dry material is used. Processes that use automatic fiber placement typically also use autoclave curing, which involves high pressures and temperatures of up to 180°. This combination is a highly repeatable, yet associated with more complexity and even cost.

In the case of DFP the following step is resin injection via liquid composite molding (LCM). Two very common LCM techniques are (vacuum-assisted) resin transfer molding (RTM) and vacuum-assisted resin infusion process (VARI).

The RTM process uses two rigid molds that form a cavity in the middle. The dry preform is placed between the molds and compacted upon closing the mold. Resin is injected into the cavity with high pressures of 120 bar. Ambient pressure is maintained at the drain, which is why the resin spreads there and completely infiltrates the tissue. The RTM method was used by Ferndanez et al.[34].

VARI uses only one rigid mold and a flexible upper mold. The flexible upper mold is a foil that realizes an airtight seal around the preform. The resin is injected with ambient pressure, which means that the maximum pressure difference is 1 bar. As a result of the low pressure difference, the injection process is more lengthy. A flow promoter is introduced between vacuum foil and preform to enhance the spread.

[2]There are processes outside of this scheme which we will ignore in this context.

Table 5.2: Overview of material properties of TeXtreme 64 PW fabric and Tenax UTS50 carbon filament.

TeXtreme[143]		Tenax UTS50 F13[144, 145]	
Material Type	Dry Fabric	Filament Diameter	7 μm
Weaving Pattern	Plain Weave (PW)	Filaments per Roving	12 000
Fiber Weight	64 g m^{-2}	Density	1.78 g cm^{-3}
Aerial Weight	74 g m^{-2}	Tensile Strength	5100 MPa
Tow Width	25 mm	Tensile E-Modulus	245 GPa
Fabric Mat Width	100 cm	Elongation at Break	2.1 %

After the resin injection, the resin solidifies in the curing step. Depending on the type of resin used, this can take place at ambient temperatures or in an oven. In a final step, excess resin and fiber is trimmed and the part is finished.

5.5.2 Process and Material Selection

Due to the unavailability of an autoclave and the complexity of automated preforming for prototypes, the only option available is DFP. When considering the different LCM methods, we decided to proceed with VARI over RTM. The VARI process produces separate half-shells, which significantly improves the feasibility of a slot-cutting process later on. From a manufacturing perspective, the main factors we considered were complexity and cost of each method. RTM involves injecting the resin into the mold under pressure, which requires specialized equipment and a more complex mold design. This complexity also means that RTM is generally a more expensive process and requires more experience. The availability of the RTM equipment is lower, and so poses a significant resource risk.

In contrast, VARI is a simpler process. This method requires less specialized equipment and allows for more flexibility in the mold design, which can help to reduce costs. Furthermore, VARI is a more forgiving process in terms of temperature and viscosity control, which can reduce the risk of defects or other issues during the manufacturing process.

In addition to these factors, we also considered the scope and overall cost. While RTM may offer some advantages in terms of production speed, the higher complexity and cost of the process would have made it difficult to achieve the desired results within the scope of this thesis.

The goal of the prototype development is to create boom samples that closely resemble the final product in the mechanical properties and geometric dimensions. One consequence of this requirement is the requirement for thin-ply fabrics, as were used by Fernandez, to minimize the boom's thickness and achieve similar mechanical properties. Sourcing thin-ply materials is a difficult task, as was already noted by Ferndanez[34]. Therefore, from the available material, we chose the TeXtreme plain weave (PW) fabric from R&G Faserverbundwerkstoffe GmbH, which is made from Tenax UTS50 carbon filament. An overview of key properties of these materials can be found in Table 5.2.

To achieve quasi-isotropic properties in the material, a stacking sequence of [0 90/ $\pm$ 45] was selected (cf. Figure 5.20). This stacking sequence achieves quasi-isotropy by aligning fibers in both axial and off-axis directions, resulting in a material that exhibits similar stiffness and strength in all directions.

Furthermore, a lower layer count also reduces the risk associated with manual arrangement during layup. As each layer is added to the mold, there is a risk of misalignment or wrinkles, which can negatively impact the mechanical properties of the final product.

The designated resin is CR80, a cold-curing resin that has a high viscosity (cf. Tab 3) and is well-suited for use in VARI. The material properties of the cured CR80 with the selected CH80-10 solidifcation agent are given in Tab. 5.3. A drawback of this resin is that it requires a post-curing step in an oven to reach its full mechanical strength. This has an impact on the choice of the mold material.

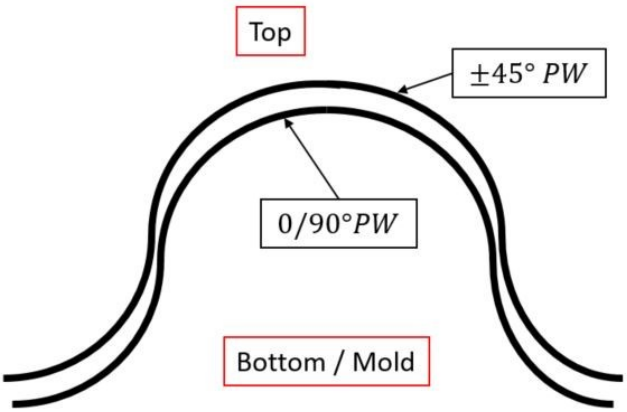

Figure 5.20: Laminate Configuration of the manufactured CTM booms[142]. Two Textreme carbon fiber mats are placed on top of the VARI mold.

Table 5.3: Overview of material properties of cured CR80 epoxy resin with CH80-10 solidifcation agent[146].

Property	Value
Tensile Strength	80 MPa
Tensile E-Modulus	3000 MPa
Flexural / Shear Modulus	2900 MPa
Flexural Strength	124 MPa
Density	1.17 g cm^{-3}
Heat Distortion Temperature	72 °C
Glass Transition Temperature	85 °C

polylactic acid (PLA) is a commonly used material for cold-curing resins. However, due to the post-curing step, PLA might deform, making it unsuitable for this project. Therefore, polyurethane is used for the form as it can withstand high temperatures without deforming. The mold has the shape of one half-shell, so that two production cycles are needed to manufacture one complete boom. With one mold, a half-shell with a length of about 0.5 m length can be manufactured.

The setup of the VARI process is shown in Fig. 5.21. After the infusion process and oven curing, the half-shells are removed from the mold (cf. Fig 5.22). The produced half-shells need to be cut, since the web is wider than required. The final step is bonding the two finished half-shells together. For bonding, a standard COTS acrylic adhesive is used.

5.5.3 Discussion

This section briefly discussed the manufacturing process for CFRP CTM booms. The thin-ply prepregs used in the literature proved difficult to obtain and therefore, a process based on DFP was without any alternative. The VARI process was chosen over the RTM process because it can provide a more accessible and cost-effective method to produce small booms. The process produces two half-shells that must to be bonded to produce a complete boom. This step requires precise alignment using additional tooling, which is a significant drawback compared to the RTM process. Additionally, the quality of the bond strongly depends on the used adhesive. Since the web is the region with the highest stresses when the boom is flattened, this is also a critical difference.

During production, several failure modes occurred. The most commonly encountered issues were due to faulty infiltration, i.e. resin buildup or air bubbles. Another issue was encountered during demolding, with half-shells stuck to the mold, requiring the treatment of the mold surface with an additional coating agent. After several production cycles, we noticed deformation of the polyurethane

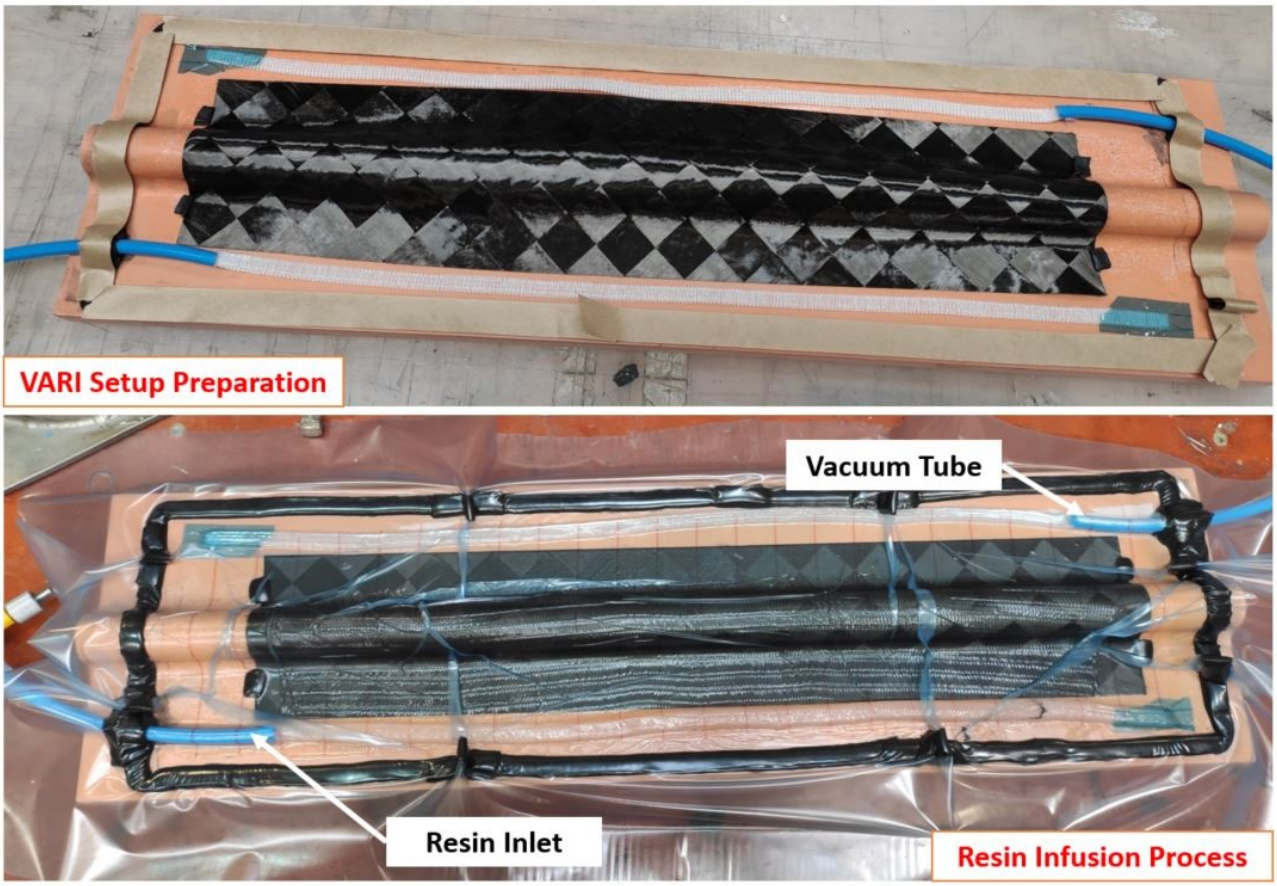

Figure 5.21: VARI setup preparation and resin infusion process[142].

Figure 5.22: Demolding of a boom half-shell and closeup pictures[142].

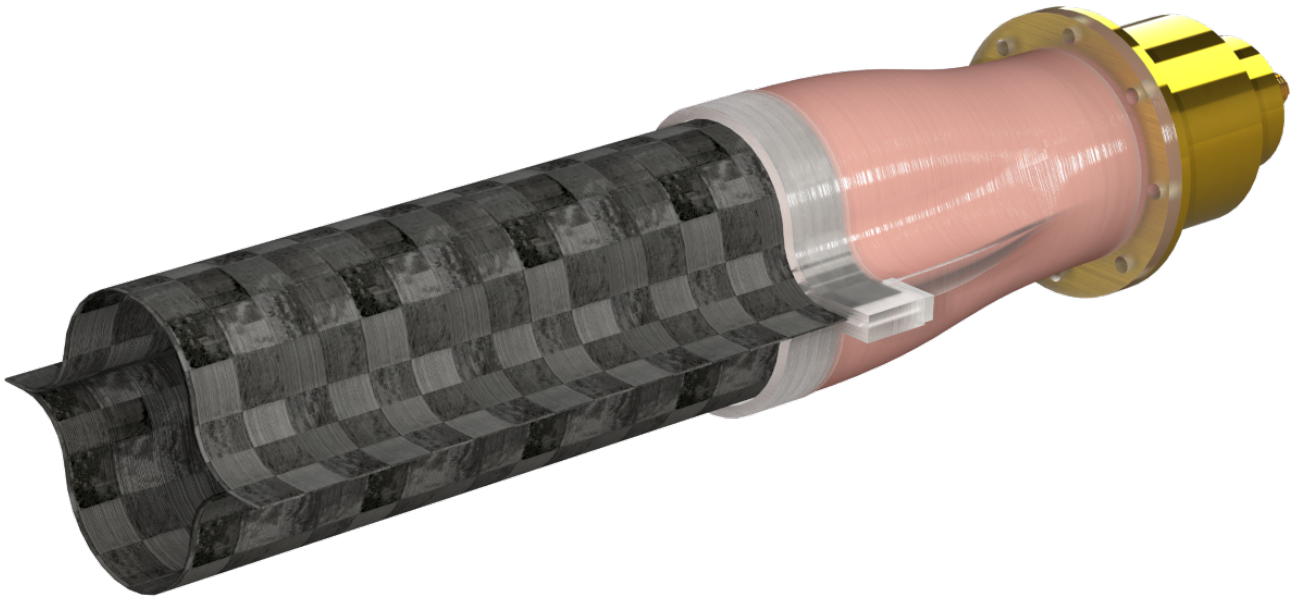

Figure 5.23: Rendering of the CTM adapter assembly with TM mode coaxial adapter.

mold. This could be remedied by weighting down the mold during the oven curing.

5.6 Waveguide Measurements

This section presents the measurement of the CFRP CTM structure as waveguide. For this purpose, first coaxial adapters for the TE and TM modes, and converters for the CTM mode are presented. Afterwards, the measurement setup is described and the results are presented.

5.6.1 Adapter Assembly

Previous simulations of the CTM geometry in CST utilized a perfectly matched port as excitation source, which is not feasible in a real-world scenario. In order to measure real prototypes, a converter of the coaxial mode of the measurement device, such as a VNA, as well as a fixture that will hold the waveguide in place, is needed. Previous experiments with a 3D-printed prototype revealed direct excitation in the waveguide via a coaxial probe to be feasible, but also very fragile and mechanically unstable. Therefore, the preferred path is an adapter that can connect the waveguide to the signal generator or network analyzer. In this section, we present adapter assemblies for TE and TM mode excitation.

The adapter is a modular assembly of two functional components (see Fig. 5.23). This choice ensures ease of manufacturing and testing and simlifies later adjustments (e.g. different boom geometry). The first component is a probe-fed circular waveguide that converts the TEM mode to either a TE or TM mode. In the subsequent transition, the circular waveguide is smoothly transformed into the CTM geometry. Coaxial adapter and converter are connected with flanges, so that the adapters can also be attached to each other. The connection is secured with screws. There are eight screw holes, allowing attachment in 45° steps. Together with the symmetry of the circular waveguide, this arrangement is able to provide different polarizations with the same components. At the end of the converter is a press-fit connector with a larger diameter, into which the boom is inserted and locked in place.

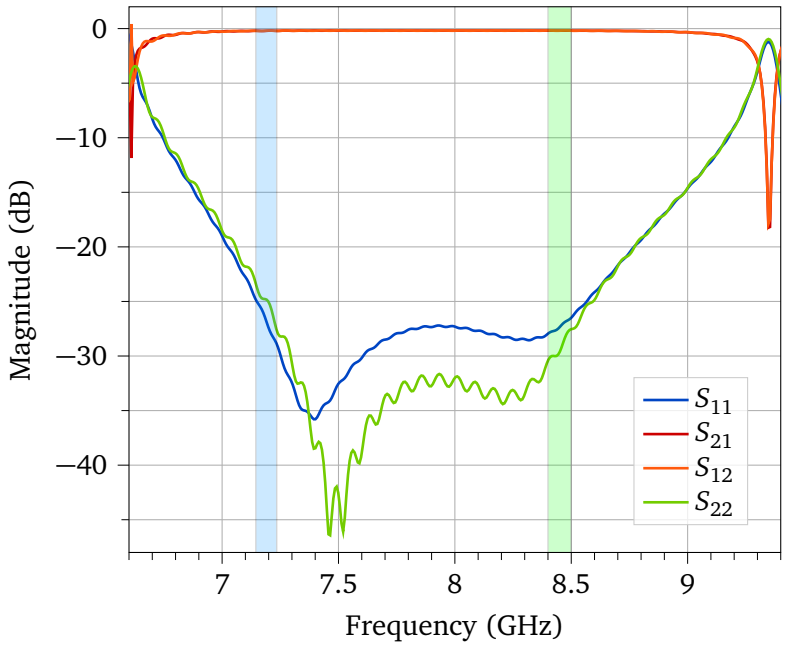

Figure 5.24: Simulated S-parameters of the waveguide adapter. Port 1 is the coaxial probe, port 2 marks the circular waveguide. The blue and green areas mark the lower and upper X-Band.

TE Mode Adapter

A circular waveguide makes a smooth transition to the CTM geometry simpler to design than a rectangular waveguide. The circular waveguide is designed for a f_c of 6.6 GHz, which corresponds to a diameter of 26.6 mm and a guided wavelength $\lambda_g = 56.0$ mm at 8.5 GHz. A low f_c raises the potential for testing in the lower 7 GHz X-band and also reduce the cross-section difference between the CTM geometry and the adapter. A more detailed drawing of the TE mode assembly with dimensions is presented in Fig. 5.26.

The circular waveguide adapter uses a probe-feed to convert from the coaxial TEM mode to a $\mathrm{TE}_{11}^{\bigcirc}$ mode. The optimal length of the probe was determined using CST's built-in optimizer with the goal to provide even results in the entire X-Band. The starting values for the optimization were $\lambda/4 = 8.75$ mm for the protruding length and a backshort distance of $\lambda_g/4 = 14$ mm. The optimization process resulted in a shortened protruding length of 8.2 mm, while the backshort distance remained constant.

The resulting S-Parameters of the simulated adapter are presented in Fig. 5.24. We can observe excellent performance parameters over the entire X-Band with a total bandwidth of nearly 2 GHz. Between 7 GHz to 8.78 GHz, the return loss is better than 20 dB. Within this passband, the insertion loss plateaus at about 0.19 dB. Note that the simulation assumes a surface made from pure, smooth copper ($\sigma = 5.8 \times 10^7\,\mathrm{S\,m^{-1}}$) and due to surface roughness and other imperfections, the measured insertion loss will be slightly higher.

Mode Converter

The mode converter creates a smooth transition between the incident $\mathrm{TE}_{11}^{\bigcirc}$ mode and the $\mathrm{TE}_{01}^{\square}$ or $\mathrm{TE}_{11}^{\bigcirc}$, depending on the polarization alignment. The cross-section of the transition is a non-linear shape, akin to a Klopfenstein taper[81], in order to provide smooth impedance tranformation. The transition length is 28 mm at 8.5 GHz, which is exactly $\lambda_g/2$ of the circular waveguide.

The simulated S-Parameters of this transition are presented in Fig. 5.25. Both polarization exhibit a gradual improvement of the reflection starting at the cutoff. There is a clear distinction between both polarizations above about 8 GHz. While the return loss of the $\mathrm{TE}_{11}^{\bigcirc}$ flattens out at about −25 dB,

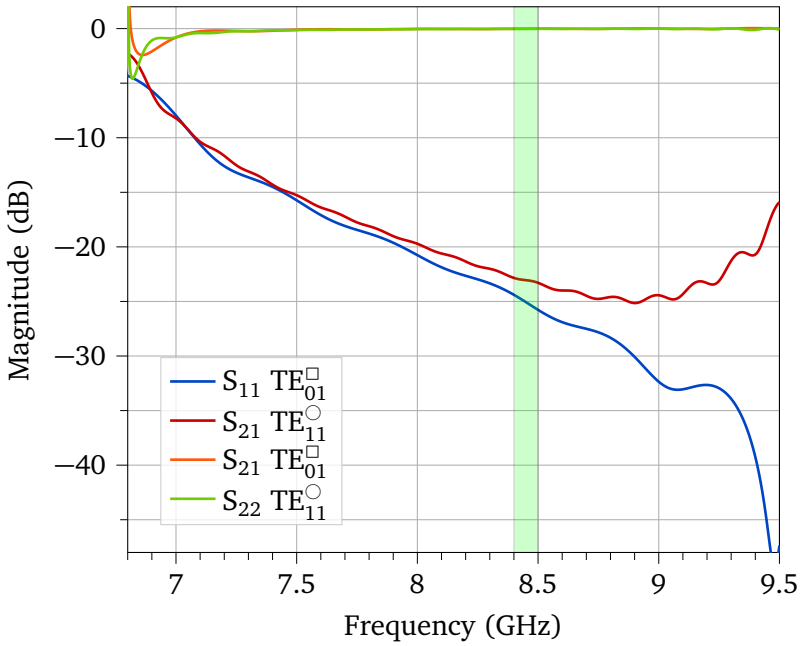

Figure 5.25: Simulated S_{11} parameters and S_{21} parameters of the TE modes of the converter . The upper X-band is highlighted in green.

the $TE_{01}^{\square}$ exhibits a steep decline to less than −40 dB. This shows that a longer transition might be beneficial for the upper X-Band, though the bandwidth of this design is not sufficient to feed both upper and lower X-Band efficiently at the same time. Due to the higher phase velocity of the widening waveguide, a longer converter could improve the design to a certain degree. A more sophisticated design might overcome this in the future.

The transition connects to the boom waveguide with a press-fit connector. The press-fit connector is an unmetalized section with 12 mm width and separated from the transition by a small ledge. The ledge increases the total cross-section by 0.5 mm, which is about twice the thickness of the CFRP boom. Later, the boom is pressed into the fitting and locked in place by the ledge. At the same time, the ledge minimizes the discontinuity between boom and transition. A drawback of this solution is the electrical connection, because the connecting surface is small and depends on manufacturing tolerances, the conductive surfaces may not align perfectly. This may then cause some degree of radiation leakage and reflection.

Manufacturing

The TE mode adapter and transition were 3D-printed with a stereolithography printer, as this allows the most flexibility in prototyping and reduces manufacturing cost. Stereolithography uses a laser to activate a photopolymer resin and works at room temperature. Therefore, inaccuracies due to thermal contraction do not exist. This method consistently achieves the best accuracy and precision of all additive manufacturing methods.

The so produced components were cured with UV light, which further solidifies the resin and facilitates the subsequent surface finish. Afterwards the contact areas on the flange and the backshort were smoothed and polished with sandpaper of increasing granulation (up to grit size 3000).

The adapter and converter were electropated, while the inside of the backshort cap was laid out with copper foil. Prior to electroplating, the components were rinsed with ethanol and distilled water. A subsequent application of adhesive primer to the inner surface improves adhesion between the polymer and subsequent copper varnish layer. Two layers of copper varnish were applied in total. The final electroplating was executed in six electropating steps with intermediate rinsing. This resulted in

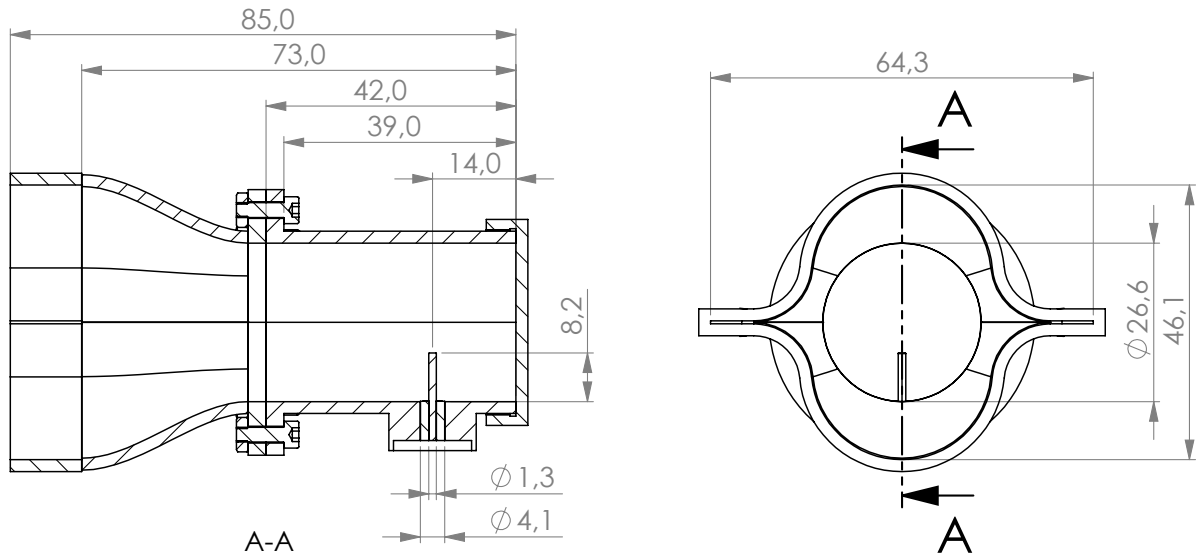

Figure 5.26: Drawing of the mode CTM converter and probe-fed adapter. Dimensions are given in mm.

a copper layer thickness of approximately 40 μm to 45 μm.

In the final step, excess dielectric was removed from the coaxial probes, and the center pins were shortened. In Fig. 5.27 we can see the circular waveguide adapters before this step.

Note that corrosion is inevitable with a pure copper surface. In this context however, the effect can be neglected due to the short time frame of this study.

Measurement

The producted prototypes were measured with a Rohde&Schwarz ZNB20 VNA. First, both adapters were measured in open configuration and afterwards, jointly in through configuration. The measured S-parameters presented in Fig. 5.28.

In the open configuration can see there is a small discrepancy between the resonance center of both adapters, consistent with the tolerance of the manual length adjustment. Considering this, the adapters are well-tuned to the desired frequency, with adapter 1 having a slightly lower frequency. As a result, the resonance in through configuration is also slightly shifted towards a lower frequency, and the return loss is the target band is higher, but remains acceptable with $< -19\,\mathrm{dB}$. The insertion loss is better than 0.6 dB in the target band.

TM Mode Adapter

As higher-order mode, the TM mode has a higher f_c and faster phase velocity. Hence, in addition to a different design of the coaxial transition, a wider diameter of the circular waveguide cross-section and a longer mode converter are needed.

As with the TE mode adapter, the assembly consists of two main components: the coaxial adapter and the mode converter. The dimensions of the coaxial adapter are given in Figure 5.29.

The conversion from TEM mode to TM mode is straightforward, as the magnetic fields of both modes are very similar. In the most basic fashion, the $\mathrm{TM}_{01}^{\bigcirc}$ excited via a longitudinally oriented coaxial probe, placed in the center of the waveguide[147, 148]. Yamamoto proposed a more sophisticated design with stepped impedance, which is also used in the following[149]. This design can significantly

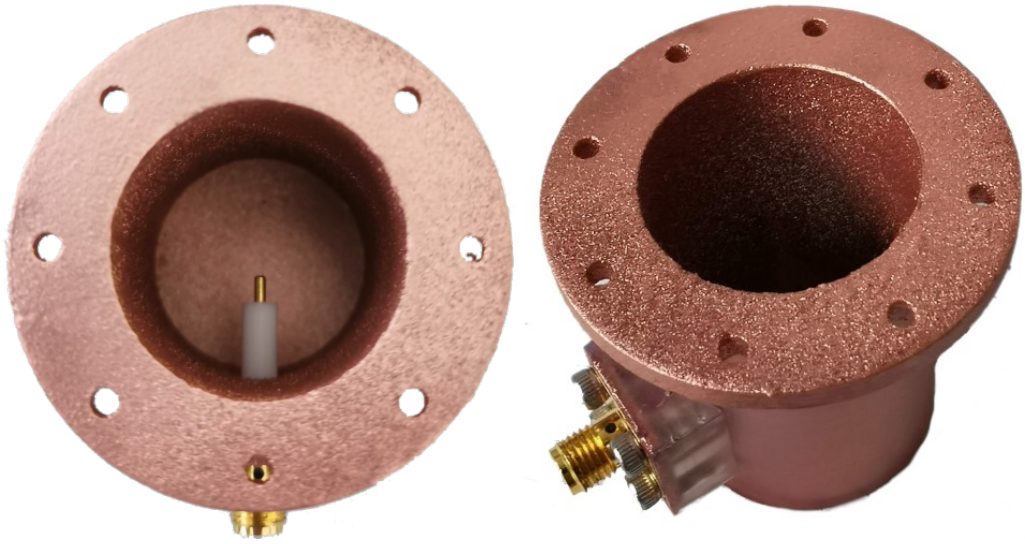

Figure 5.27: The galvanized 3D-printed circular waveguide feeds before the final steps of removing excess dielectric and shortening the probe.

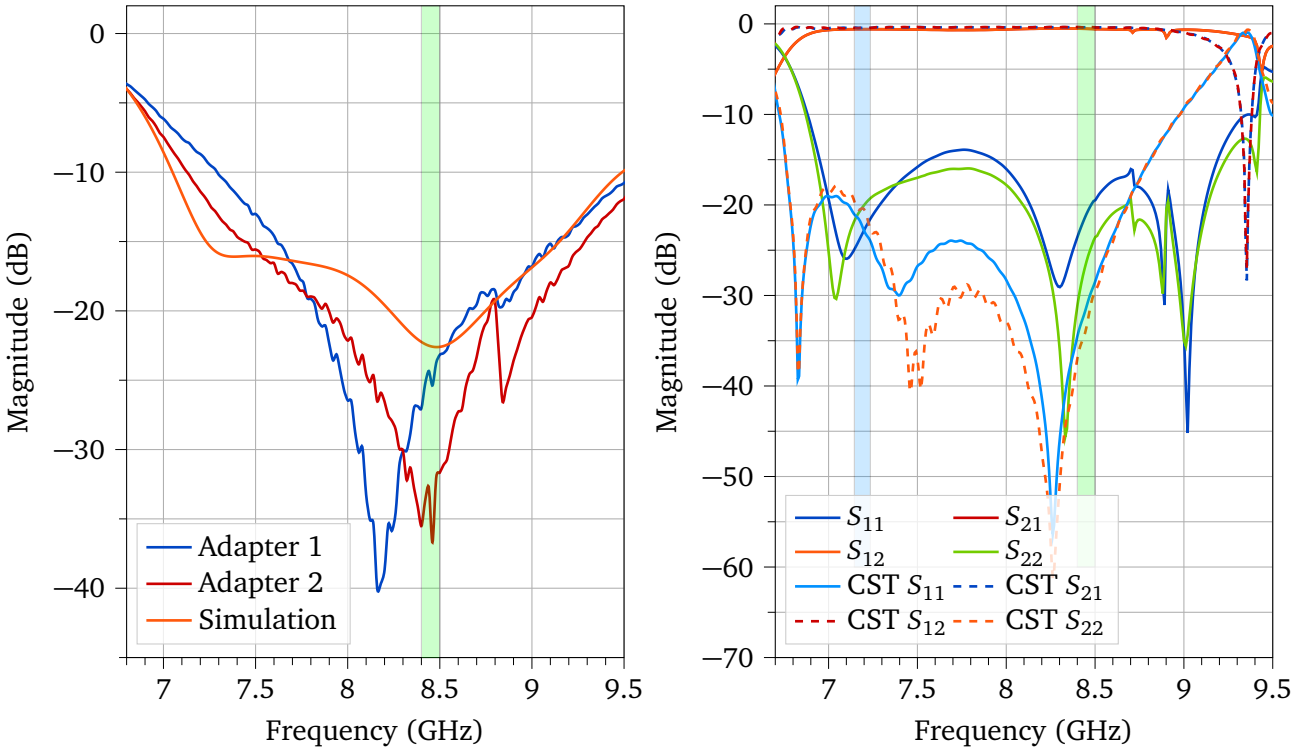

Figure 5.28: VNA measurements and CST simulation of two manufactured circular waveguide adapters in open (left) and through (right) configuration. The blue and green areas mark the lower and upper X-band.

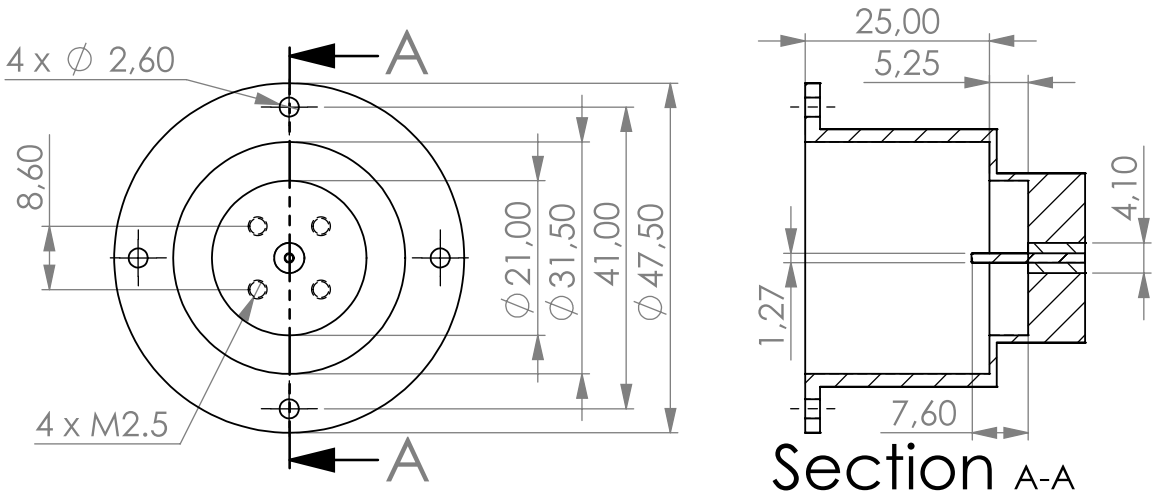

Figure 5.29: Drawing of the TM mode coaxial adapter. All dimensions are given in mm.

reduce return loss over a wide frequency range.

With the experience from the previous converter, the converter length was increased to 65mm. The simulated S-parameters of the converter are presented in Fig. 5.30. The converter offers low return loss of −20 dB for frequencies over 8 GHz. In the target band, the return loss is excellent, with less than −27 dB.

Manufacturing and Measurement

The converters were manufactured analog to the previous models. The electroplating process was shortened to only three steps, which saves time and does not affect the microwave conductivity of the copper significantly.

The symmetry of the coaxial adapter makes it perfect for manufacturing as turned part. Therefore, 3D-printing was not used here, and two adapters were turned from pure brass ($\sigma = 15.9 \times 10^6\,\mathrm{S\,m^{-1}}$). For best results, the coaxial probes were shortened to a length of 7.67(2) mm.

The adapters were measured using a Rohde&Schwarz ZNB20 VNA. The result of the through-configuration measurement is presented in Fig. 5.31. The input return loss of the adapters is excellent with less than −30 dB in the target frequency band. The adapters are well-matched over a wide range of 1 GHz or 12.5 %. Both adapters are in very close agreement, as result of the tight manufacturing tolerances. This is also reflected by the insertion loss, which is better than 0.3 dB between 8.2 GHz to 9.2 GHz and better than 0.25 dB in the target band.

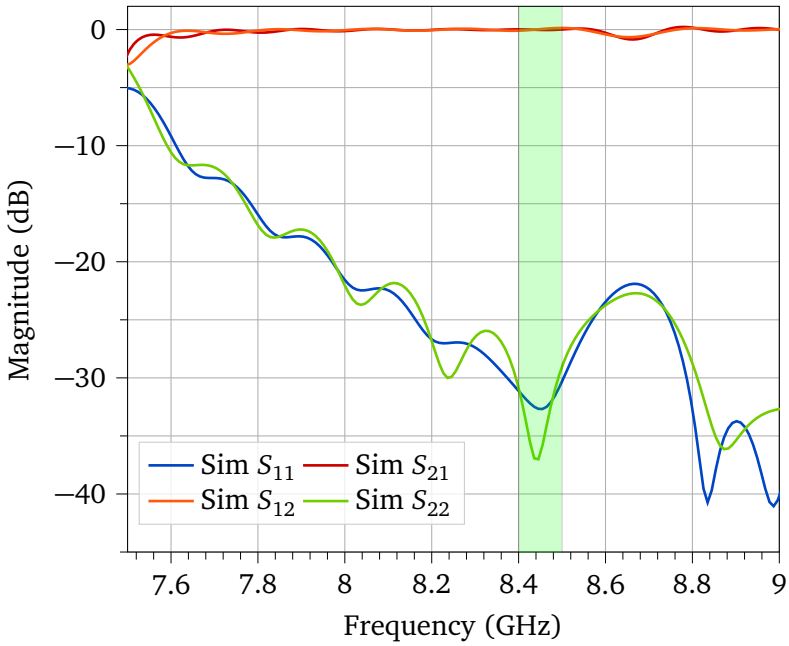

Figure 5.30: Simulation results of the TM-mode converter configuration. Port 1 represents the circular cross-section and port 2 represents the CTM cross-section. The upper X-band is highlighted in green.

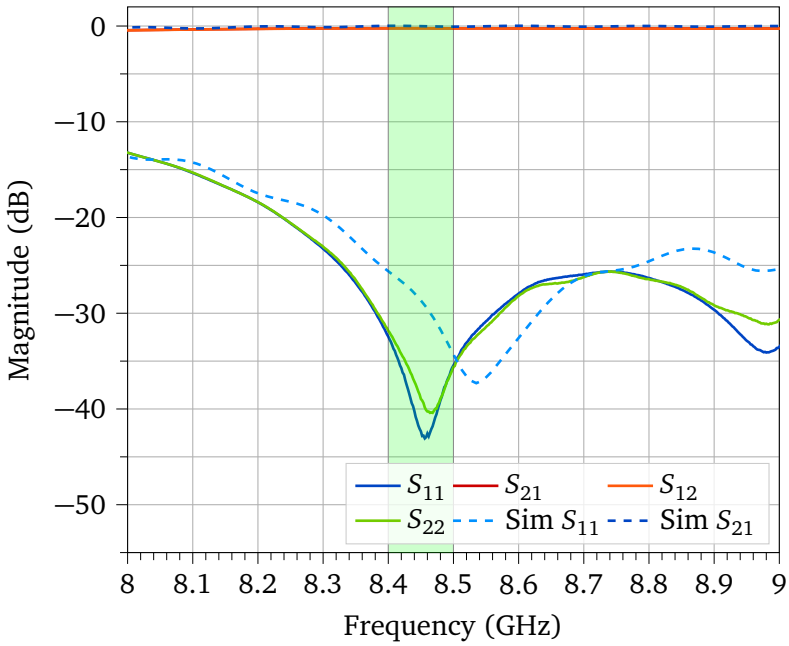

Figure 5.31: Measurement results and simulation of the TM-mode coaxial adapters in through configuration. The upper X-band is highlighted in green.

5.6.2 CFRP Waveguide Attenuation

We now turn to the measurement of the waveguide attenuation of CTM waveguides. Previously in Section 5.3 we provided simulated attenuation values of the fullmetal CTM(15,10,85) CTM geometry. In contrast to metal waveguides, the composite structure of CFRP is difficult to simulate as it strongly depends on the material properties and generally exceeds the available simulation capbabilities.

Setup

With the adapters presented above, we are able to perform measurements of pure carbon CTM waveguides. Using a Rohde&Schwarz ZNB20 VNA we determine the S-parameters of three different booms with the length of 3 cm, 39 cm and 53 cm. Using the previously discussed multiline-method (cf. Section 4.2.2), we derive the attenuation constant from these measurements. The measurement setup with the Rohde&Schwarz ZNB20 VNA is shown in Figure 5.32.

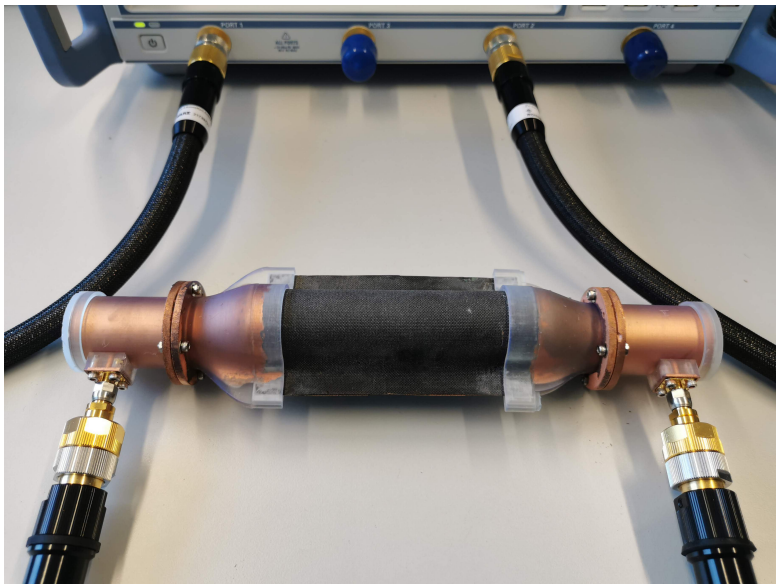

Figure 5.32: Measurement Setup of the CTM waveguide prototype with TE mode coaxial adapters.

Results

After the measurement, the S-parameters of the waveguide without the adapter and converter fixtures were deembedded using the 3 cm waveguide S-parameters. The resulting S_{21} parameters of the deembedded 50 cm waveguide are presented in Fig. 5.33. We can observe rapid frequency-dependend variation and spikes. In part these spikes are artifacts of the deembedding process, but also simply results of the material variation and internal reflections. Within the depicted range, there appears to be no frequency-dependend trend in the insertion loss that would indicate a frequency-dependent attenuation. Despite the spikes, there is an easily visible distinction between the insertion loss of the $\mathrm{TE}_{01}^{\square}$ mode and the other modes, indicating that this mode has the smallest attenuation. The $\mathrm{TE}_{01}^{\square}$ and $\mathrm{TM}_{01}^{\bigcirc}$ exhibit sudden spikes, most notably close to 8.3 GHz and 8.7 GHz, respectively. These are actually artifacts from the deembedding, due to mechanical imperfections, most likely the connection between the mode converter and CFRP waveguide.

Using the raw measured S-parameters, we calculate the attenuation constant of the waveguides using the multiline-method. Because of the aforementioned variation and sharp spikes in the magnitude of the S-parameters, this calculation is performed for each of the 668 measured frequency points between 8.0 GHz to 9.0 GHz. A combined statistic for α_c is then calculated over this frequency range,

Table 5.4: Mode-specific statistics of the calculated attenuation constant of the CTM CFRP waveguide in the range from 8.0 GHz to 9.0 GHz.

Mode	Length (m)	α_c (dB m^{-1})				
		Median	99%	1%	75%	25%
$TE_{01}^{\square}$	0.50	1.16	1.81	0.51	1.22	1.04
	0.36	1.12	3.79	0.50	1.40	0.94
$TE_{11}^{\bigcirc}$	0.50	2.59	3.09	2.16	2.67	2.32
	0.36	1.85	2.20	0.80	1.91	1.24
$TM_{01}^{\bigcirc}$	0.50	2.88	3.57	2.20	2.99	2.30
	0.36	2.85	3.81	2.02	3.23	2.34

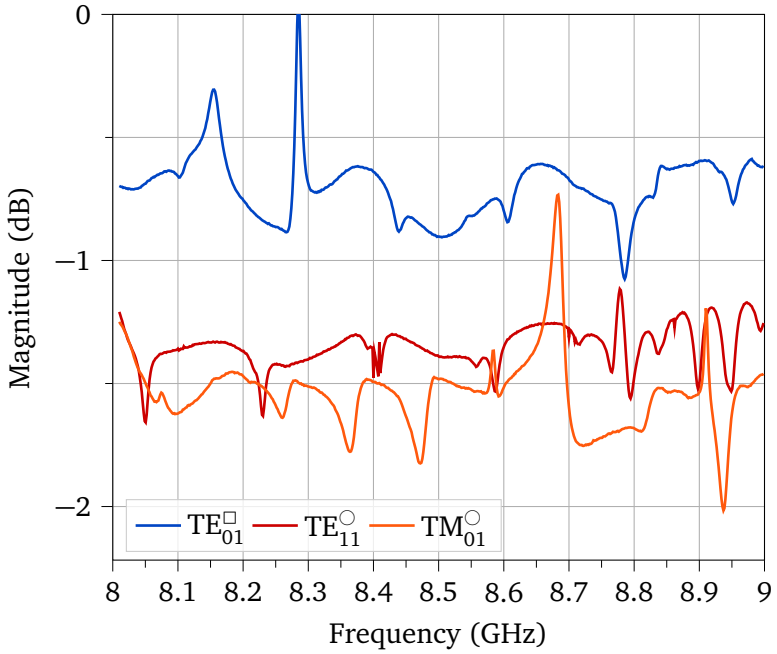

Figure 5.33: S-parameters of a deembedded 50 cm waveguide piece.

but separately for each deembedded waveguide. In this case, we assume the frequency-dependent portion of the losses to be negligible (cf. Fig 5.7).

The resulting statistics of α_c are presented in Table 5.4. The table shows the attenuation constant statistics for each mode and deembedded boom length. The obtained statistics for both waveguide lengths draw a consistent picture, especially for the $TE_{01}^{\square}$ and $TM_{01}^{\bigcirc}$ mode. The $TE_{01}^{\square}$ mode stands out with the lowest attenuation among the measured modes, with an median value between 1.12 dB m^{-1} to 1.16 dB m^{-1}. This result aligns well with the expectations for the fundamental mode of the waveguide, which usually exhibits the lowest attenuation. The $TE_{11}^{\bigcirc}$ mode exhibits a higher attenuation, and very high variation between the measured booms. We can observe significant disagreement of 0.74 dB m^{-1} difference in the median with the lower value being 1.85 dB m^{-1}. In fact, the distributions only overlap in the 99th/first percentile.

The $TM_{01}^{\bigcirc}$ mode draws a consistent picture of high attenuation with a median value between 2.85 dB m^{-1} to 2.88 dB m^{-1}. The statistical variation between the individual booms is very low.

The combined statistics of both measurements, separated by mode, are visualized in Fig. 5.34. The combined median value for $TE_{01}^{\square}$ is just below 1.16 dB m^{-1}, the $TE_{11}^{\bigcirc}$ mode exhibits a median of 2.18 dB m^{-1} and the $TM_{01}^{\bigcirc}$ mode has a median of 2.86 dB m^{-1}. The figure substantiates the previous observations of the individual measurements.

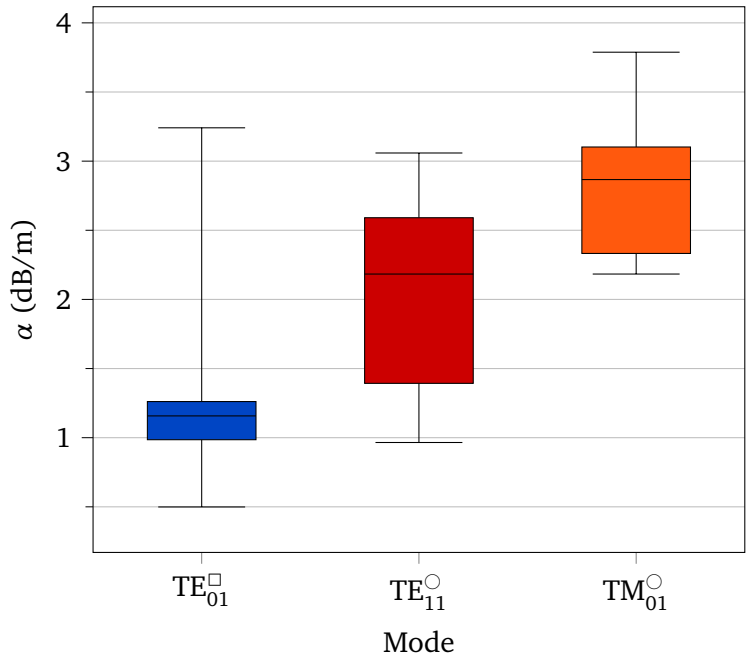

Figure 5.34: Distribution of the calculated attenuation constant of the carbon waveguide between 8.0 GHz to 9.0 GHz. The box represents the 25st/75th percentile and the 1st/99th percentile are represented by the whiskers.

5.6.3 Discussion

In this section, we discuss the results of the attenuation measurement of the CFRP CTM waveguide for the first three modes: $TE^{\square}_{01}$, $TE^{\bigcirc}_{11}$, and $TM^{\bigcirc}_{01}$.

To draw a comprehensive picture of the waveguide's performance, we calculated the attenuation statistics over a wide frequency range, between 8.0 GHz to 9.0 GHz, and separately for each deembedded waveguide. The frequency-dependent portion of the losses is assumed to be negligible in this analysis.

Regarding the confidence in the measurement results, the modes $TE^{\square}_{01}$ and $TM^{\bigcirc}_{01}$ exhibit relatively stable behavior, with regard to the obtained statistics. However, the presence of frequency-dependent variation and artifacts from deembedding highlights the importance of further investigation and improvements in the measurement setup. Better understanding of the sources of these variations and mitigating their impact would enhance the accuracy and reliability of the measured results.

The $TE^{\square}_{01}$ mode stands out with the lowest attenuation among the measured modes, with an median value of approximately 1.16 dB m^{-1}. This result aligns well with the expectations for the fundamental mode of the waveguide, which usually exhibits the lowest attenuation.

On the other hand, the $TE^{\bigcirc}_{11}$ mode appears to be very sensitive to mechanical tolerances or material differences, as indicated by the high variability in the measurements. The statistics obtained from the measurements exclude random measurement error as the source of this variability. Instead, it is more likely that differences in the measured booms cause the observed variation. Since this variation did not occur with the other two modes, it is helpful to reconsider Fig. 5.6. Here, we can observe that the current maxima of the $TE^{\bigcirc}_{11}$ mode, in contrast to the other modes, are located in close proximity to the web. This area is often subject to manufacturing imperfections, such as voids. Regrettably, with the available resources, this issue could not be conclusively resolved. Therefore, in future work this measurement should be repeated with a larger sample size and more controlled manufacturing process.

The results of the $TM^{\bigcirc}_{01}$ mode were very consistent over the two samples, but also rather sobering. With the highest attenuation measured, a median value of 2.88 dB m^{-1}, the $TM^{\bigcirc}_{01}$ mode is barely useful in larger antennas. The expected gain difference to the $TE^{\square}_{01}$ mode is likely diminished by the higher

attenuation. There might be some potential for improvement using higher-order TM modes[139], but this is beyond the scope of this work.

At this point, it is important to remember that the attenuation is strongly dependent on fiber orientation[137]. Given the findings by Bojovschi[137], the utilized [0 90/ ± 45] stacking is assumed beneficial for the $TE_{01}^{\square}$ in terms of attenuation. However, Fernandez et al. used a [±45/0] stacking sequence, which may cause different results due to the unfavorable 45° orientation. Therefore, it is recommended to investigate the effect of different stacking sequences on the attenuation of the CFRP CTM waveguide in future work. That said, there is a dependency between the mechanical requirements that dictate the optimal stacking sequence and electrical properties, which may be inconvenient in future designs.

In summary, the experimental results demonstrate that the CFRP waveguide has promising properties for guiding electromagnetic waves, with the $TE_{01}^{\square}$ mode showing the lowest attenuation and the $TM_{01}^{\bigcirc}$ mode having the highest measured attenuation. Further investigation and understanding of the $TE_{11}^{\bigcirc}$ mode's sensitivity to mechanical and material factors are required.

5.7 Mechanical Analysis

This section will discuss the effects of slotting the CTM boom on its structural properties. We can expect slotting to have a negative impact on the load bearing capabilities of the boom. Therefore, quantifying this impact, depending on the slot parameters, is essential for determining the usefulness of SWA CTM booms in solar sailing. The analysis was subject of the Master's thesis of Christoph Werner[150] which will be summarized in the following.

The analysis of the effect of slotting the CTM booms was carried out using both simulations and experimental testing. The experiments and simulations go hand in hand because the material parameters used in the simulations are determined through experiment.

5.7.1 Model Assumptions

We begin with the analysis of slotting effects on CFRP CTM boom. This analysis is carried out with simulations in COMSOL and not only includes the material properties of the CFRP but also the forces experienced in a model solar sailing probe. The simulations and experiments will only comprise static load cases, as dynamic cases strongly depend on the system setup and are potentially not representative of the entire spectrum of the technology.

The solar sail system model is based on the following assumptions:

1. The solar sail operates under microgravity conditions.
2. The sail assembly is nominally deployed.
3. The CTM booms have deployed with their nominal cross-section.
4. The only external force acting on the solar sail is solar radiation pressure due to light photons.
5. Thermal effects are neglected.

The assumed solar sail configuration in this analysis is that of a quadratic sail with four triangular petals. The petals are connected to CTM booms of 10 m length, and each petal has an area of 47.9 m^2. Using Eq. 2.2, we calculate the maximum force acting on the sail, given perfect reflectivity with $\eta = 1$ and $\beta = 0°$:

$$F = 2 \cdot P_0 A = 1.74\,\text{mN}$$

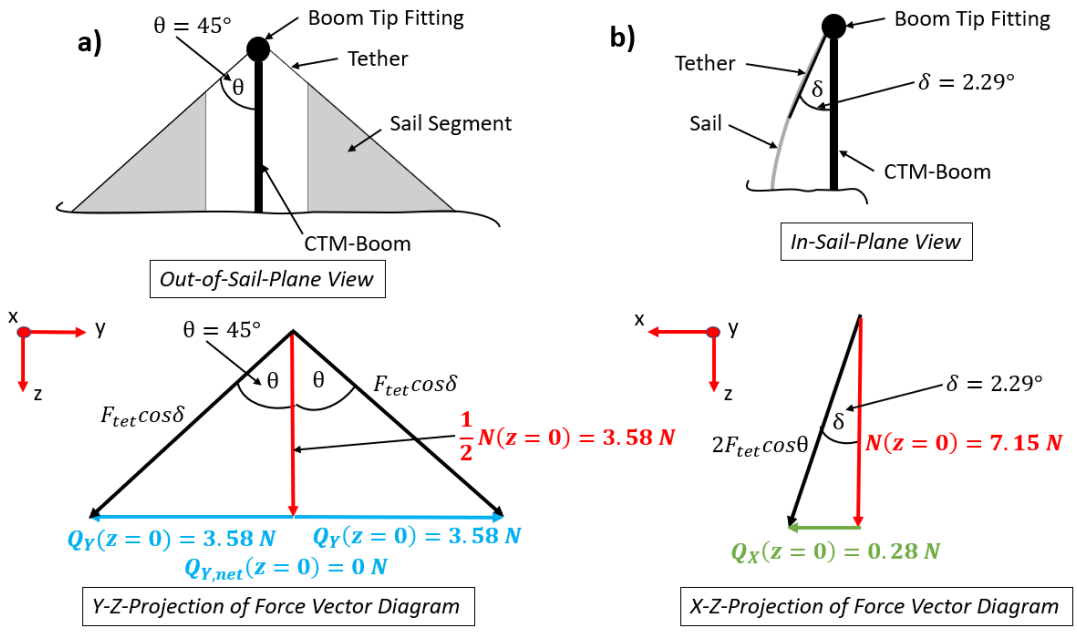

Figure 5.35: Force-vector diagrams and boom tip boundary conditions[150].

Table 5.5: Geometrical parameters of the investigated SWA.

l (mm)	l_s (mm)	N	$\delta_{z,0}$ (mm)	w_s (mm)	δ_z (mm)	δ_x (mm)	θ_s (°)
500	16	10	170	2	31.5	24	[0;90]

Figure 5.35 shows how the petals are attached to the booms via tethers. The solar radiation pressure results in billowing of the sail. The forces on the tethers are scaled from the known force of the ACS3 sailcraft[126] which has a sail area that is smaller by a factor of 2.25. Therefore, the maximum force acting on the tethers in this model are 2.25 times larger, or 5.06 N in absolute terms. The force at the boom tip is translated into a compressing force along the z-axis of 7.15 N. Assuming a symmetric distribution of the solar pressure, the lateral y-axis forces cancel each other out. There is a small bending force along the x-axis of 0.28 N, resulting in a bending torque at the boom mount around the y-axis of 2.8 N m.

5.7.2 Area Moments of Inertia

Compared to the unslotted boom, the slotted boom has a different cross-section in the slot, as material is removed from the shell. This reduces the area and torsional moments of inertia which is directly proportional to the stiffness of the structure. The area and torsional moments of inertia do not depend on material properties of the boom and therefore are perfect for an initial analysis and model creation.

From Figure 5.36, we can observe that the slot angle can be expected to have a critical impact on the moments of inertia. In order to quantify the effect of slotting, the area moments of inertia I_x and I_y as well as the torsional moment of inertia I_z was calculated using SolidWorks 2022. The caluculation assumed a shell thickness of 0.28 mm. The geometrical parameters of the slots are given below in Table 5.5. For the calculation, the cross-section cut was always placed in the center of the slot.

The calculated results are presented in Fig. 5.37. A first observation we can make from the graphs is an initial reduction of the moments of inertia at 0° between 0.5 % (I_x) and 1 % (I_y). This is followed by a shallow decline until about 60°. Afterwards there is a steep decline with the strongest rate of change between 75° to 80°, before flattening out between 80° to 90°. Relatively speaking, I_x is affected the least by the slot, with a difference of at most 3.3 %. I_y is affected the most, with 7.2 % difference

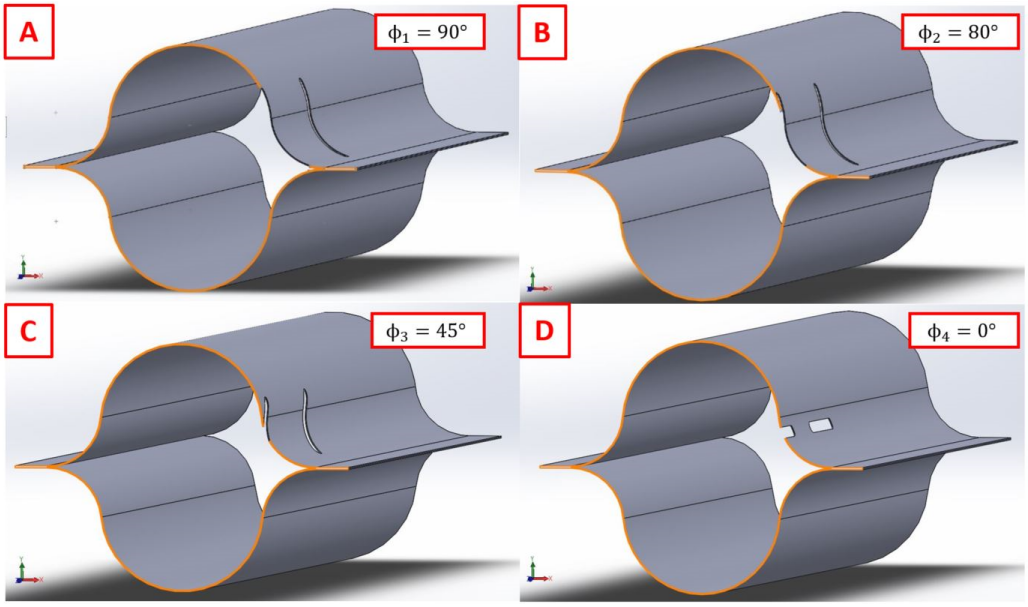

Figure 5.36: Cross-section of the CTM boom at different slot angles, cut through slot center[150].

Table 5.6: Statistics of the boom tip displacement experiments.

Bending Axis	Mean (mm)	Median (mm)	σ (mm)
X	8.51	8.47	0.120
Y	5.54	5.51	0.109

between the unslotted and 90° slotted boom.

As a result, we can expect a significant drop in stiffness for slot angles above 65°. For θ_s below this threshold, we can see an almost constant behavior with only little difference to the unslotted boom. This gives a wide band of angles to choose from in later designs and improves the trade-off space. The initial difference between the slotted and 0° slot stem from the slot width and so, thinner slots may improve the impact of the SWA on the overall load bearing capability.

5.7.3 Material Parameter Calibration

In the simulation, the CFRP is modeled as linear elastic material. The in the linear elastic regime, the properties of a composite material can be estimated using linear laminate theory (LLT)[151]. LLT calculates elasticity figures for a quasi-isotropic material the from the volume fractions of fiber material and matrix(cf. Eq. (3)). Initial values are calculated using the LLT from material properties obtained via literature research, datasheets and weighing. The resulting values are Young's modulus $E = 109.35\,\text{GPa}$ and poission ratio $\nu = 0.30$. The density calculated from the LLT is $1332\,\text{kg}\,\text{m}^{-3}$ and the density calculated from the weighed boom is $990\,\text{kg}\,\text{m}^{-3}$.

In order to verify the so obtained material properties, two bending experiments with a series of trials were carried out and compared with a simulation in COMSOL. In these experiments, a reference boom of 0.5 m length was loaded with a defined weight ($F = 31.27\,\text{N}$) and the displacement of the boom tip was measured (cf. Fig. 8). The weight was chosen to be much larger than the expected loads, in order to obtain measurable results. The experiments were carried out for both the X- and Y-axis with 10 measurements each. The resulting statistics are found in Table 5.6.

The subsequent simulation revealed that the initial parameters were overestimated and required adjustment, as they only resulted in a boom tip displacement of 1.52 mm in the y-axis bending case and 2.12 mm in the x-axis bending case. Further simulations were performed to establish refined parame-

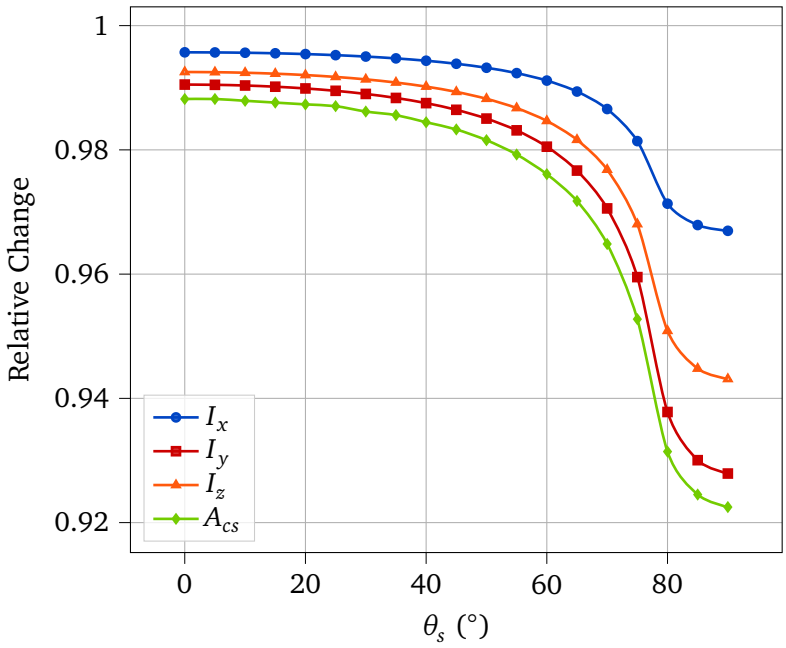

Figure 5.37: Area moment of inertia I_x and I_y, torsion moment of inertia I_z and cross-section area A_{cs} relative to the unslotted boom, depending on slot angle θ_s.

Table 5.7: Calibrated material properties used for the simulation of the SWA.

Bending Axis	E (GPa)	ν	ρ (kg m^{-3})
X	27.38	0.3	990.35
Y	30.15		

ters based on the sensitivity of the boom tip displacement on the LLT input parameters. To this end, each parameter was varied individually. When regarding the boom tip displacement as a function of the LLT input parameters, the effect of the E-module is found to be directly proportional, while a variation of ν of 100 % results in a change of 1.45 % and a variation of ρ of 55.56 % effected a change of 0.19 %.

The resulting refined material properties are given in Table 5.7. For both bending cases, two different E-modules provided the best results, indicating room for further study. It is worth noting that the simulation resulted in two possible values of ν, with one being 0.3 and the other being 0.15. While the influence of the density is low, it was decided to proceed with the lower density value obtained by weighing the reference boom.

5.7.4 Numerical Analysis

Using the calibrated material properties, we executed a numerical simulation of the three load cases in COMSOL. The influence of the boom stiffness was assessed, taking into consideration the geometrical parameters of the slots: length l_s, angle θ_s and width w_s. The results are presented in the following.

Bending Cases

We begin by considering the bending cases. We study the effect of the load application by comparing the boom tip displacement. The default parameters for the SWA from Table 5.5 are used for the simulation, unless stated otherwise. For illustration, Figure 5.38 depicts the stresses on the boom in the negative Y-axis bending case. The bending stress generally decreases longitudinally but is spread

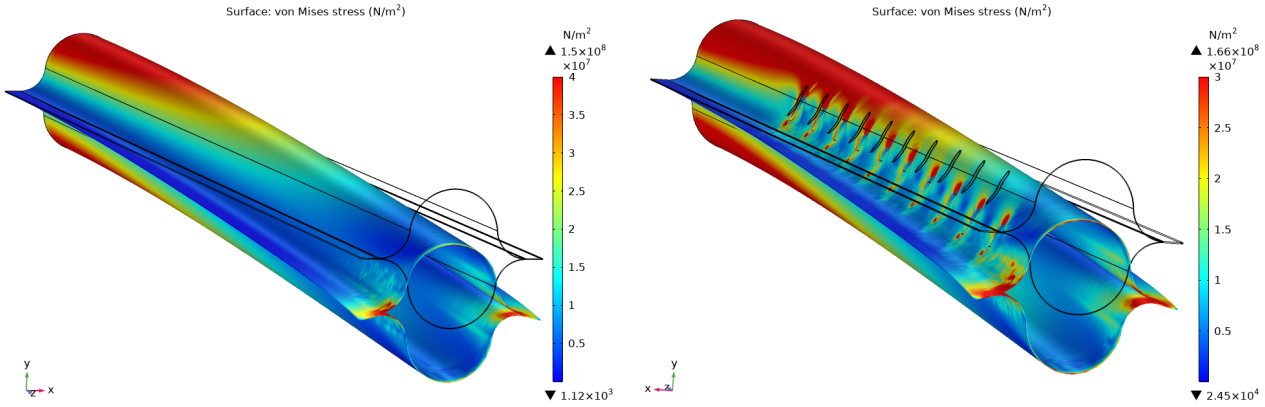

Figure 5.38: Comparison of the von Mises stress distribution in the reference boom (left) and the SWA (right) in the negative X-axis bending case with exaggerated displacement. The SWA in this picture has $\theta_s = 45°$. The slots exhibit strong stresses in the corners. The stresses visible on the boom tip are simulation boundary condition artifacts[150].

laterally by the slots. The bending results are presented in Fig. 5.39. The bending results for slot length and slot width use a default $\theta_s = 90°$.

The Y-axis bending case emerges as the pivotal bending scenario, given that loads are anticipated from this direction. The reference for boom tip displacement stands at 5.51 mm in the x-direction, and the reference maximum stress is found to be 391 MPa. Interestingly, for values of θ_s less than 20°, the influence on the bending seems minimal. However, for angles exceeding this threshold, there's an almost linear uptick. The deviation from the reference remains below 2% for $\theta_s < 45°$. When considering slot length, a notable 24% deviation from the reference is observed when the l_s reaches 22 mm. A deviation exceeding 10% from the reference is noted in boom tip displacement when w_s increases to 3 mm. It's worth highlighting that stress levels are significantly lower than those observed in the x-axis bending case, usually hovering within a range of a mere few percent. The maximum stress peaks, specifically at the slot's end and the web, occur at 85°, magnifying by a factor of 22 at the first slot and by a factor of 14 at the last slot, a clear manifestation of the compression loading of SWA.

The X-axis bending case, albeit not expecting any loads from static analysis, still warrants an examination for hypothetical scenarios where loads might be exerted. The reference displacement for the boom tip is 8.47 mm in the y-direction, with the maximum stress being 150 GPa. Deviations are relatively contained, with less than 3% from the reference for θ_s below 45 degrees. However, a more substantial deviation of 30% is noted for $l_s = 22$ mm. The influence of slot width variation is most pronounced in this case, registering deviations of up to 12% when the w_s is 3 mm. Among the bending cases, this one records the highest stresses, scaling to almost thrice the stress of the reference boom. Further dissection of the stress peaks at the slot end depicts a peak at 85°, with a staggering multiplication factor of 172 at the initial slot and a factor of 21 at the last slot, reaffirming the compression loading of SWA.

Across the bending cases, l_s emerges as the most defining parameter. This is particularly highlighted in the x-axis bending scenario where deviations from the reference shoot up to 30%, which is not entirely unexpected given that this comprises a significant fraction of the flattened height (h=37 mm). For l_s measuring 16 mm or less, deviations are contained below 10%. This gives rise to the hope that larger sail configurations, requiring wider CTM booms, will be affected less by the slots. Slot width comes up as the second most critical parameter influencing the bending outcomes. Notably, the lowest stress readings are recorded in the y-axis bending scenario, which aligns well with the anticipation that this is the predominant bending case.

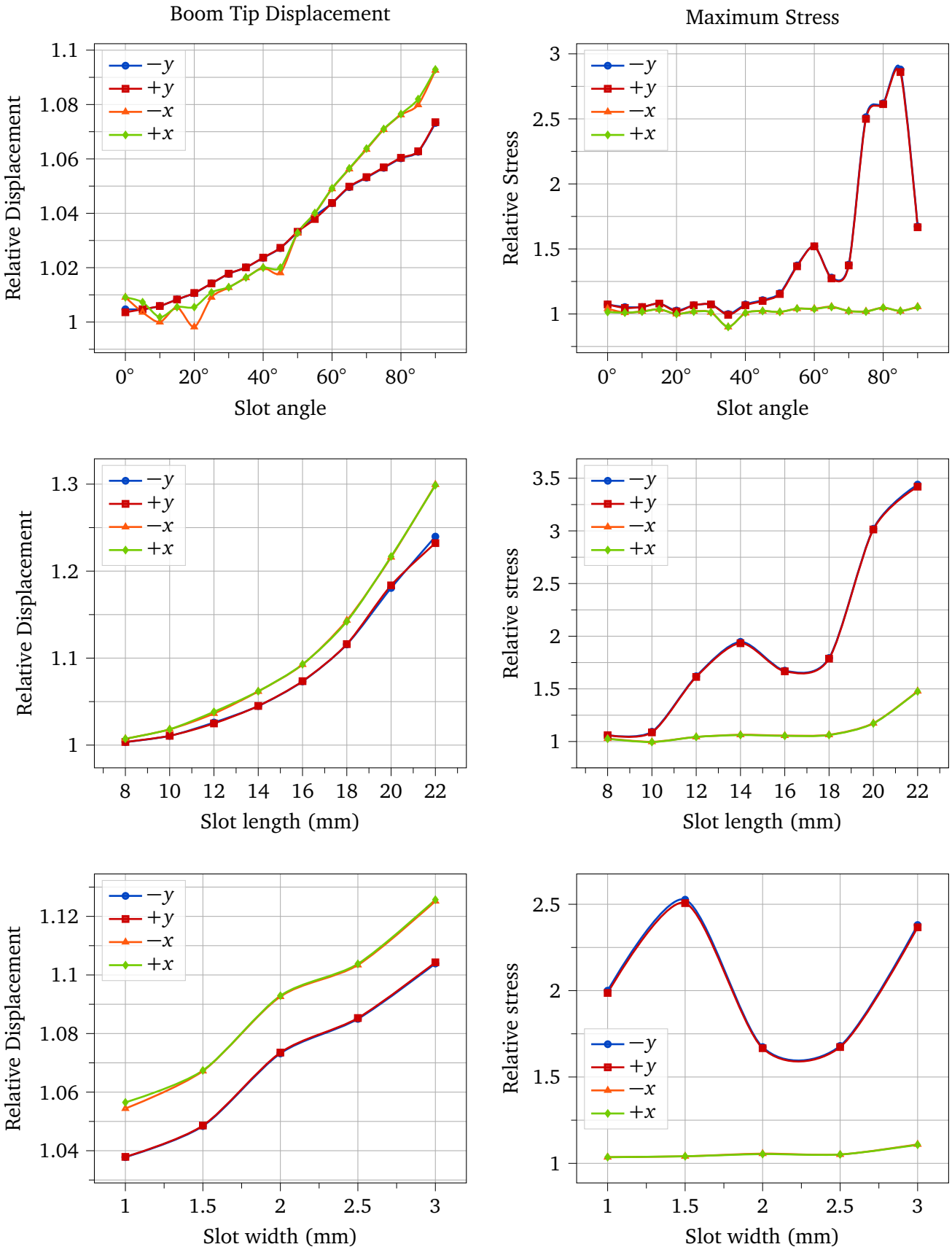

Figure 5.39: Bending cases: simulated boom tip displacement and equivalent van Mises stress of the SWA when loaded along a given axis.

Normal Load

The normal force is the dominant load acting on the boom in the static case. Carbon fibers are known to be very stiff in elongation cases but require further support when compressed. In CFRP this support is provided by the epoxy matrix, hence the load bearing capability of CFRP is dependent on the direction of the stress. Excessive compression ultimately results in kinking or local buckling of the boom.

For the normal load case simulation, a load of 31.7 N is applied in $-z$ direction at the boom tip. The reference boom tip displacement is 16.5 μm in the $-z$ direction, and the reference maximum stress is 1.73 MPa. The results for the slotted boom are presented in Fig. 5.40.

From the figure, we can observe an almost linear increase in the boom tip displacement with increasing slot angle. The maximum displacement is observed at $\theta_s = 90°$, where the boom tip displacement is 41.5 μm or about 2.5 times the reference value. There is a noticable difference to the 85° value, suggesting that the 90° configuration is to be avoided. The maximum stress occurs at 80° with a relative value of 7.3.

The slot length is the most critical parameter in this load case. The relative displacement for begins with a value of 1.2 at $l_s = 8$ mm and progresses almost linearly to a value of 3 at $l_s = 18$ mm. Further increasing the slot length results in significantly higher displacement, with a stark increase beyond $l_s = 20$ mm, where the slot covers a significant portion of the boom's flattened height. At this point, the boom tip displacement is 103 μm or about 6.2 times the reference value. The maximum stress illustrates a similar picture, with an almost linear increase up to $l_s = 20$ mm and a stark jump to the maximum of 13.2 times the reference value.

The slot width also makes an important contribution to the boom tip displacement, with relative values ranging between 1.8 to 2.5 times the reference value. Slot widths below 2 mm appear favorable in this regard, with the lowest displacement values observed at $w_s = 1$ mm. The maximum stress is also influenced by the slot width, with the maximum found at 1 mm and 8 times the reference value. This is explained by higher stress peaks at the slot ends when the slot becomes narrow.

Torsional Load

We now turn to the torsional load case. Even though the static load analysis yielded a zero torque around the z-axis, however, depending on the boom fittings and sail tether attachment, a torque may be generated. For the context of the subsequent analysis, we assume a torque of 1.75 N m directed at the web's center. The reference displacement and maximum stress, manifested at 20.4 and 3.12 MPa, respectively. The parametric results of the SWA are portrayed in Fig. 5.41.

Beginning with the slot angle, the relative displacement remains nearly constant within the range of 0° to 45°, fluctuating minutely between 1.01 to 1.03 times the reference. For larger angles, the displacement sharply increases. An observable peak in displacement is found between 80° to 85°, measuring at approximately 1.1 times the reference. The stress parameters show no such behavior, with the maximum stress oscillating between 1.025 t to 1.075 times the maximum of the reference. Interestingly, a potential outlier is discerned at 35° where the stress reduced to 0.9 of the reference.

The observation of the slot length yields that the relative displacement demonstrated a monotonic increase with slot length. The zenith of displacement is achieved at the highest simulated slot length of 22 mm, approximately 1.22 times the reference value. The maximum stress exhibited its pinnacle at the same length, with a staggering 80 times the reference. Between the lengths of 12 mm to 18 mm, the stress graph reaches a saddle point, but post this range, there is a pronounced escalation.

The relative displacement due to variation of the slot width appears to rise proportionally with an increase in slot width, with the exception of a saddle point at 1.5 mm to 2 mm. The apex of this rise was identified at 3 mm, which is roughly 1.12 times the reference value. The zenith of maximum stress for this parameter was at 1.5 mm, which was an astonishing 55 times the reference. Conversely, the

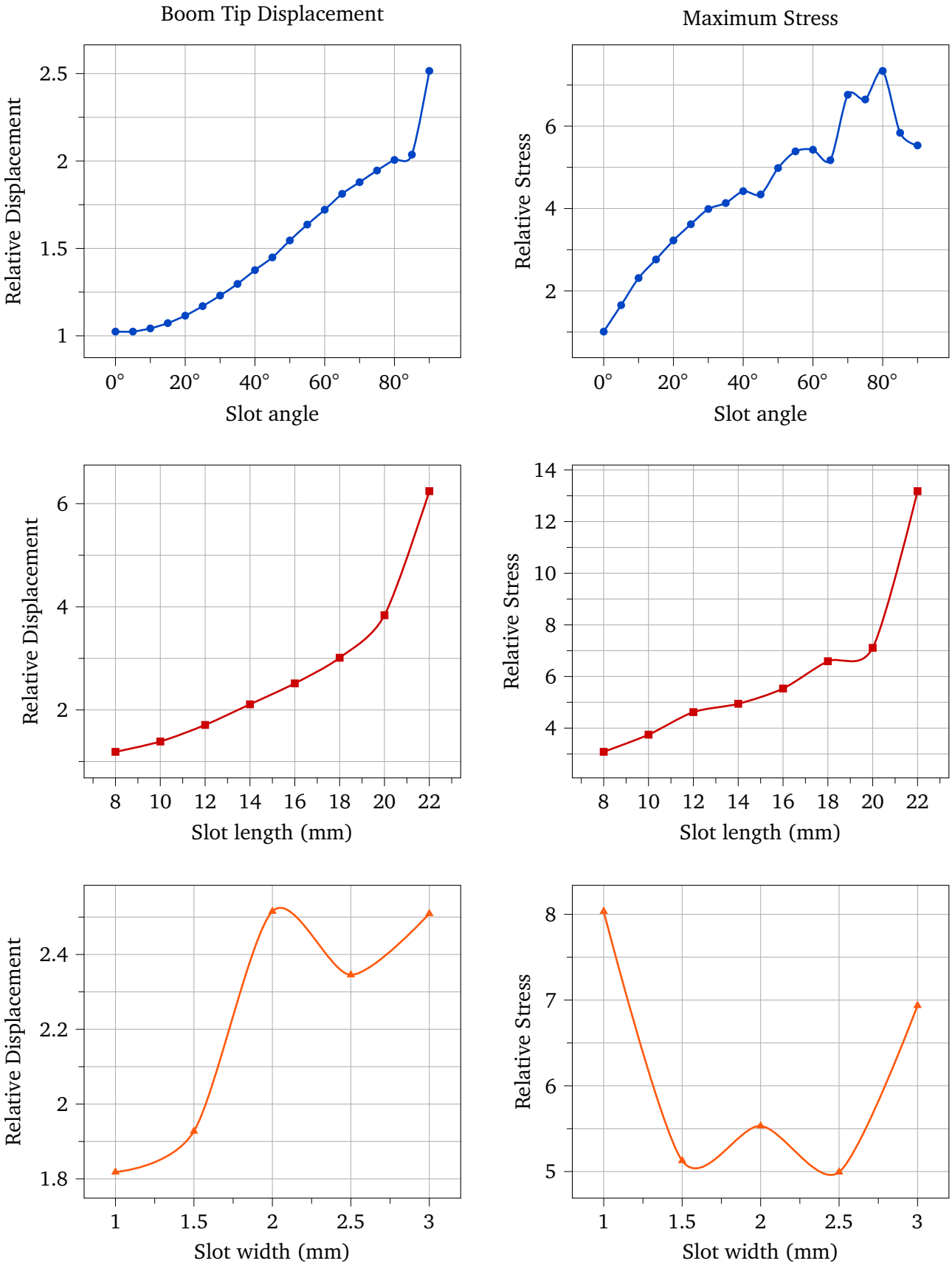

Figure 5.40: Normal load: simulated boom tip displacement and equivalent van Mises stress of the SWA.

Table 5.8: Mechanical parameters of the manufactured SWA.

l (mm)	l_s (mm)	N	$\delta_{z,0}$ (mm)	w_s (mm)	δ_z (mm)	δ_x (mm)	θ_s (°)
500	16	10	170	2	31.5	24	70

minimum was at 2.5 mm, which was still significantly high at 30 times the reference value.

5.7.5 Experimental Testing

At last, we turn to the experimental testing of the slotted CTM boom. For the experiment, three 10-slot SWA and three non-slotted booms were manufactured. Two experiment series were performend, first an elastic deformation experiment was carried out in order to compare the reference boom to its slotted pendant. Afterwards in the structural collapse experiment series, the booms are loaded until they fail.

The elastic deformation experiments focus on the negative x and y-axis bending load cases. The y-axis, which represents out-of-sail-plane deformation, is especially significant due to potential thrust loads, resulting in compression stresses on the slotted boom sample. Such stresses are considered more severe than tensional stresses because they can induce structural issues like buckling. The CTM boom's in-sail-plane deformation is less concerning because of the sail's symmetric design. The study also considered both potential stress scenarios on the integrated SWA array. Due to limited sample availability, measurements of the boom tip displacement were taken 20 times at a load of $Q_x = Q_y = 31.27\,\mathrm{N}$ for both non-slotted and slotted CTM samples. The experiment series didn't cover the normal load case due to measurement constraints in the micrometer range.

Subsequently, the structural collapse experiment series was performed on the same samples, covering the same bending load cases as the elastic deformation series, with the addition of the linear kinking analysis and normal compressive load case. The load on the samples was increased until they showed mechanical failure signs. Boom tip displacement values were measured, and the force applied was recorded for both bending cases. The slotted and non-slotted CTM samples' load-bearing capacities were compared, with failure modes documented for further discussions.

The geometrical parameters of the manufactured SWA are given in Tab. 5.8. The parameters used are the same as the default parameters used for the simulation, with one exception being the slot angle. Since the simulations revealed that a 90° angle is unfavorable, a lower value of 70° was chosen. This value can be regarded as tolerable worst-case, as lower angles are expected to perform better both structurally and electrically.

The SWA was manufactured by from a two regular CTM half-shells, one of which was slotted. The slots were produced using a CO_2 laser cutter with 2 kW of power at a 5 kHz cycling rate and 10%/90% pulse-to-pause ratio and a 3 mm nozzle. These settings are the result of previous test runs. During the laser cutting, the boom was flattened using a clamping plate. The resulting slots are depicted in Fig. 5.42.

The figure shows that the slots are look frayed and some carbon material was not removed perfectly. On the other hand, the laser evaporated some of the epoxy material surrounding the slots, exposing the bare carbon fibers on the front side, but not the backside. The manufacturing process should be improved for better results. A higher powered laser with shorter pulses could remedy this issue, but regrettably was not available. The results also indicate that an electrical test of the SWA would give only little benefit.

The experiment setup for the bending cases is depicted in Fig. 8. In order to provide a rigid restraint, the booms root were cast into concrete and screwed to a wall. The boom tip displacement measurement was done using a digital caliper. The weight was attached using a 3D-printed fixture that was special for each bending case. The fixture held a plate which provided the surface to hold the weights.

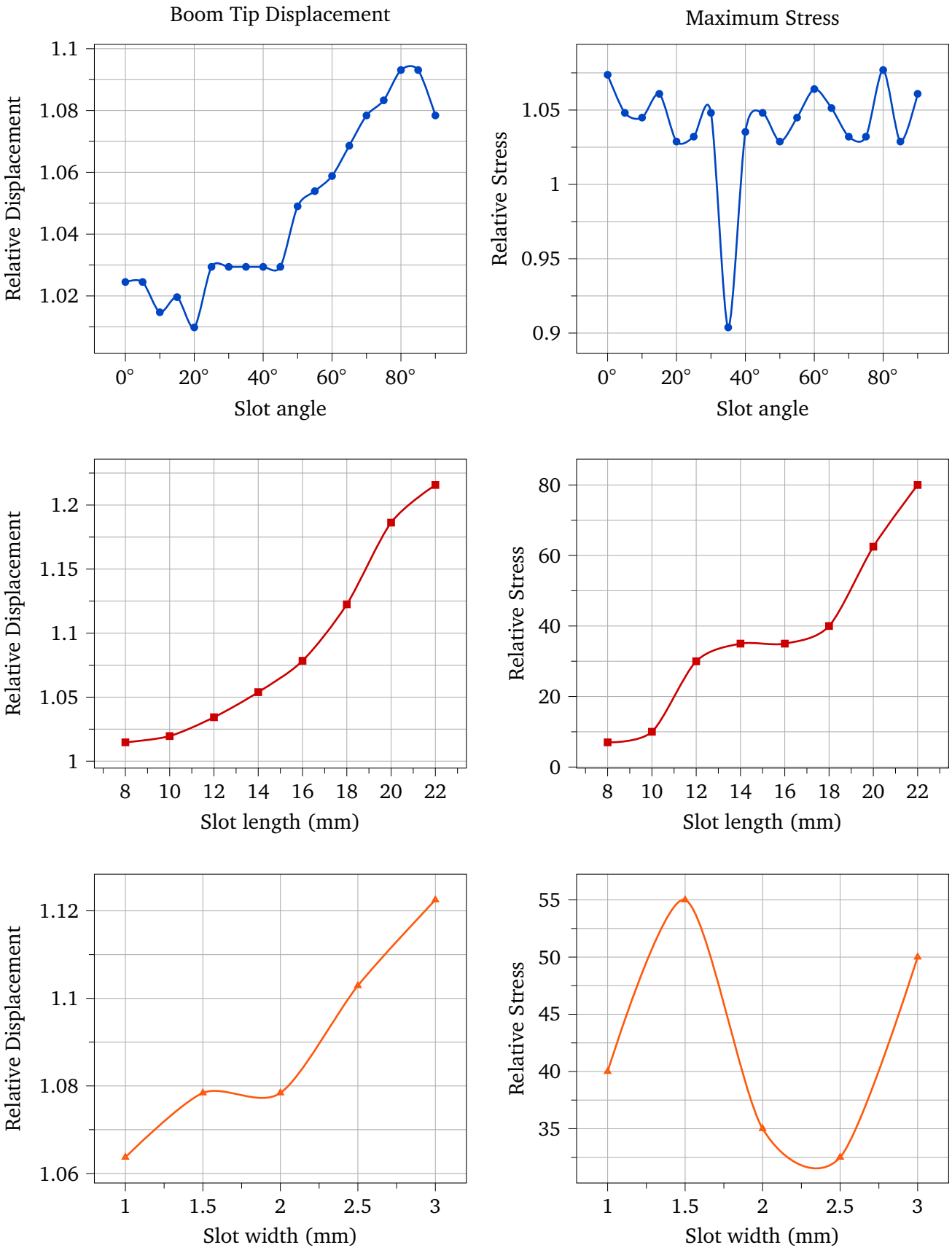

Figure 5.41: Torsional case: simulated boom tip displacement and equivalent van Mises stress of the SWA.

Figure 5.42: Macroscopic view of two lasercut slots after calibration.

Table 5.9: Statistics of the elastic deformation experiments.

Boom	Bending Axis	Mean (mm)	Median (mm)	σ (mm)
Ref	X	8.61	8.63	0.019
	Y	5.94	5.94	0.136
SWA	X	7.46	7.48	0.070
	Y	5.30	5.26	0.500

Elastic Deformation

The bending case elastic deformation cases were performed 20 times in total. In each cycle of the experiment, the digital caliper was initially set to its zero position when no load was applied. Following this, weights were meticulously placed onto the experimental setup. A waiting period of two minutes was observed to allow the system to settle. After this settling time, the deformation measurement was recorded. The cycle was then concluded by removing the weights.

The results of the experiment are presented in Tab 5.9, which provides statistics of the elastic deformation experiments. The table showcases the mean, median, and standard deviation σ of the deformations in millimeters (mm) for different bending axes and booms.

In the elastic deformation experiments, distinct differences were observed between the SWA and reference booms. For the x-bending case, the SWA boom showed a mean displacement of 7.46 mm, which is notably lower than the reference boom's mean displacement of 8.61 mm.

Conversely, in the y-bending case, the SWA boom's displacement was closely aligned with the reference. The SWA boom had a mean displacement of 5.3 mm, only slightly less than the reference's mean of 5.94 mm. One significant observation was the variability in the y-bending cases. The standard deviation for the SWA y-bending case was 0.500 mm, indicating a broader distribution of values compared to the reference's standard deviation of 0.136 mm. This variability was further highlighted when considering that the initial test for the SWA y-bending resulted in a notably higher displacement of 7.3 mm, while subsequent tests showed reduced values.

Interestingly, during testing, the y-bending SWA sample exhibited early signs of buckling, as can be observed in Fig. 5.43. This shows that the SWA is more susceptible to buckling than the reference boom. The buckling was not observed in the x-bending case. It is entirely possible that the early onset of buckling in this case has caused micro-damage that reduced the load-bearing capacity of the CTM boom in the subsequent destruction tests.

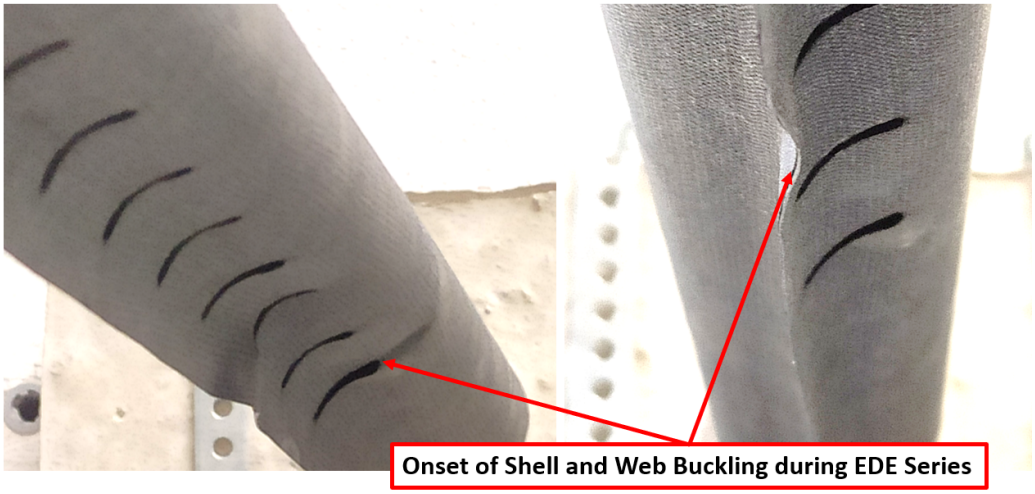

Figure 5.43: Early signs of buckling in the y-bending case [150].

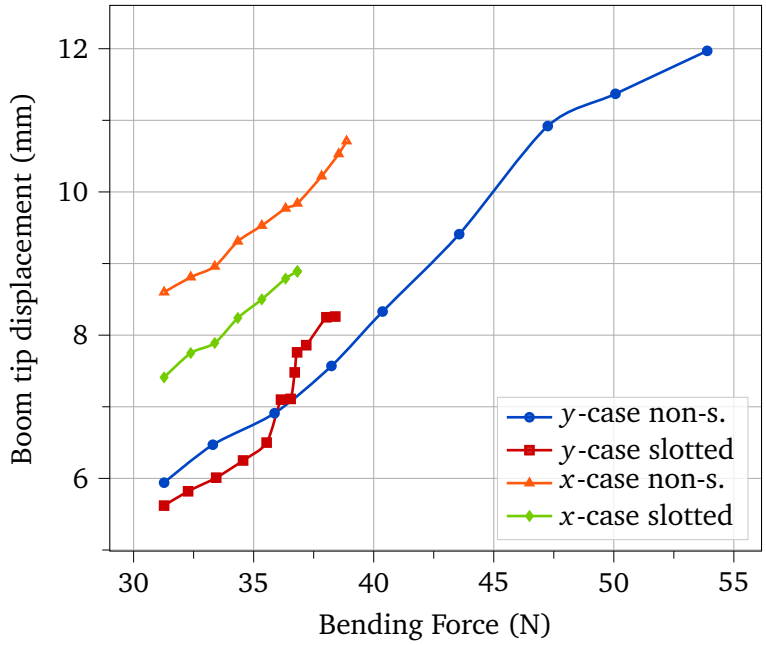

Figure 5.44: Results of the bending cases of the structural collapse experiments. Adapted from [150].

Structural Collapse

After the elastic deformation test, the structures were tested until failure by increasing the load in steps. The load was increased by adding weights to the fixture. The load was increased until the boom failed. The failure modes were documented and the load at failure was recorded. The results are presented in Fig 5.44 and will be discussed in the following.

As expected, the SWA consistently fails at lower loads than the reference boom. In the y-axis bending case, the SWA initially shows lower displacement than the non-slotted boom. A surprising result, given the criticality of this bending case. However, beyond approximately 36 N, the SWA is less stiff and quickly fails at 38.4 N. Meanwhile, the reference boom demonstrates a remarkable resistance to the bending force and only fails at about 53.9 N. This means a reduction of the load-bearing capability in this critical load case by 28.8 %. The failure modes of both booms is presented in Fig. 5.45. The figure show that both booms finally fail due to both buckling and web bond disintegration.

In the x-axis bending case, the slotted boom again shows lower displacement than the reference boom. However, the SWA fails earlier at 36.8 N, while the reference boom fails at 38.9 N. This means

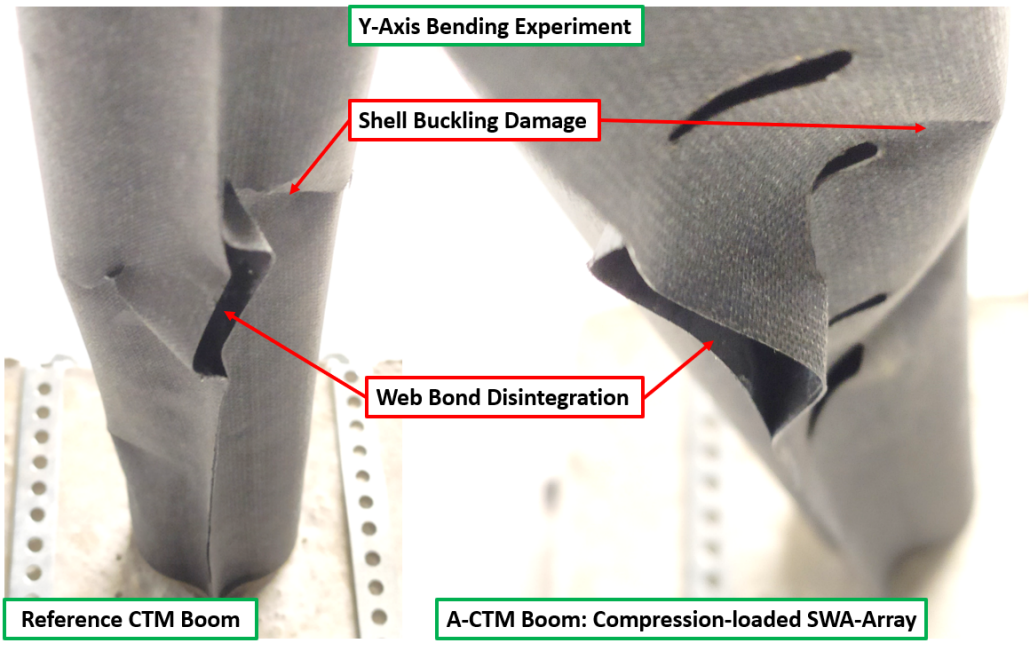

Figure 5.45: Failure mode of the SWA and non-slotted boom due to excessive compression stresses in the y-axis bending case[150].

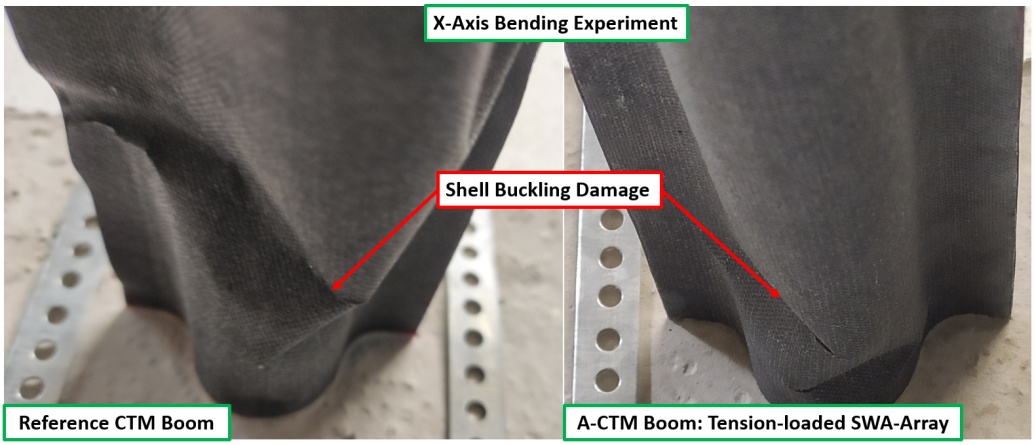

Figure 5.46: Failure mode of the SWA and non-slotted boom due to excessive compression stresses in the x-axis bending case[150].

a reduction of the load-bearing capability in this load case by only 5.4 % and the structure shows low sensitivity to slotting. Both the non-slotted and slotted booms fail due to buckling, as can be seen in Fig. 5.46. In both cases, the buckling damage appears in close proximity to the boom root.

In the case of z-axis compression loads, the reference boom could sustain weights of more than 23.95 kg without damage. The reference was loaded with up to 28 kg, where it failed. The SWA could sustain weights of more than 18.90 kg without damage. Next, the SWA was loaded with 23 kg, where it failed. A more fine-grained analysis is not possible due to the limited number of samples. The failure modes are presented in Figure 5.47. The figure shows that the non-slotted boom failed to shell-bond disintegration close to the boom root, whereas the slotted boom failed due to web bond disintegration and buckling in the slotted area.

5.7.6 Discussion

In the bending cases, the SWA initially exhibited lower displacement than the reference boom. This is a surprising result, given that the SWA is expected to have lower stiffness than the reference. However,

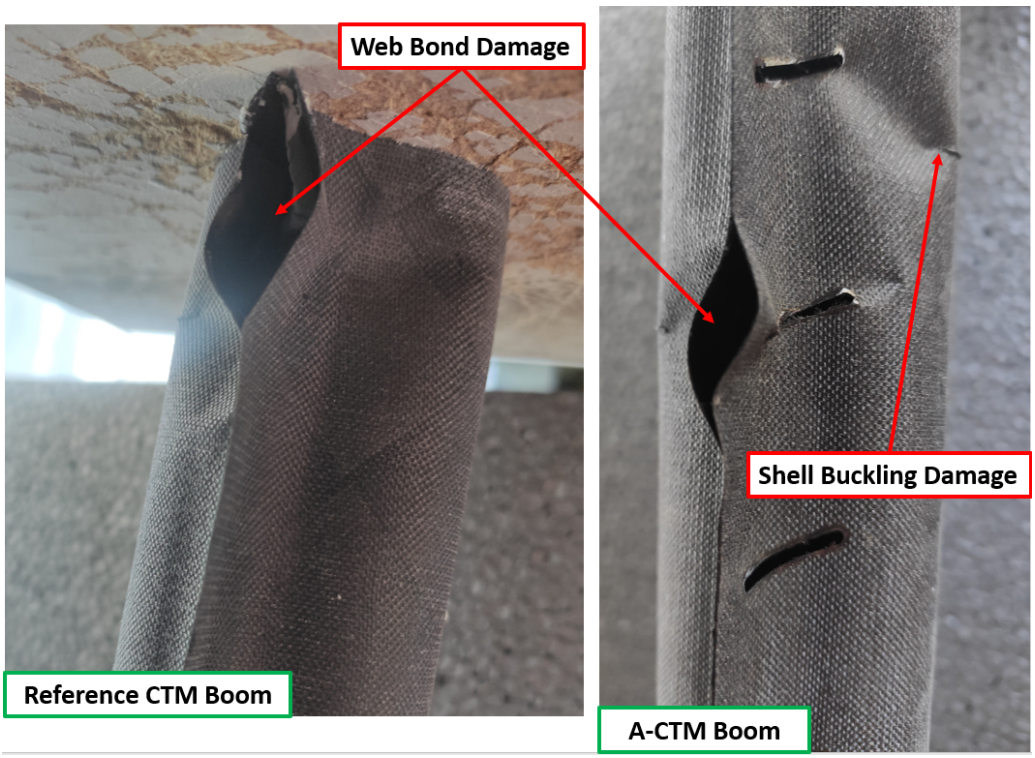

Figure 5.47: Failure mode of the SWA and non-slotted boom due to excessive compression force in the normal force case[150].

in all cases, the SWA fails earlier than the reference boom. Explaining this behavior by manufacturing tolerances alone is difficult, as the SWA shells were selected from the same pool of shells as the reference boom. However, concluding a higher stiffness based on the few experiments is not meaningful and more experiments are needed to confirm this behavior.

An interesting result from the x-axis bending case is the low sensitivity to slotting. The SWA fails only 5.4 % earlier than the reference boom. From the numerical prediction of I_x, a larger deviation between the reference and slotted boom was expected. The narrow difference between slotted and non-slotted boom could be explained by manufacturing tolerances and future work should revisit this experiment for confirmation. Both booms fail due to buckling, but not due to web bond disintegration, which in turn is expected from the simulation.

On the other hand, the y-axis bending case shows a significant reduction of the load-bearing capability of the SWA by 28.8 %. The failure mode is in line with the simulation, with the SWA failing due to web bond disintegration and buckling. Early buckling was observed in the high-stress y-axis bending case, which indicated that the boom stiffness was actually lowered and the SWA boom is more susceptible when high stresses occur. The large reduction of the load-bearing capability by 28.8 % is critical for a real application and indicates that a much larger boom would be required in a real application, resulting in a significant mass increase.

High stresses were also expected from the compression load case along the z-axis, which manifested in web bond disintegration and buckling in the experiements. Due to the limited number of samples, the load-bearing capability could not be accurately determined and falls within a wide range of 4 % to 47 %. Since the expected maximum stress was significantly lower in this case than in the other bending cases, the SWA was expected to perform similar to the reference. Hence, it is entirely possible that the real load-bearing capability of the SWA is close to the reference and want to motivate further investigations.

The experimental results show that the SWA is not a drop-in replacement for the reference boom. The SWA is more susceptible to buckling and web bond disintegration, which results in a significant reduction of the load-bearing capability. However, it must be noted that the chosen $\theta_s = 70°$ is a worst-

case scenario. A lower slot angle would result in a lower reduction of the load-bearing capability. An electrically more suitable $\theta_s = 40°$ to $50°$ (cf. Fig. 5.15) would certainly improve the load-bearing capability of the SWA.

5.8 Future Work

The findings reveal the modes $TE_{01}^{\square}$ and $TM_{01}^{\bigcirc}$ as having stable performances, though frequency-dependent variances and deembedding artifacts signal the need improved mode converters and attachment. Recognizing and minimizing these variances will heighten the measurement's precision and trustworthiness. Additionally, the $TE_{11}^{\bigcirc}$ mode's apparent vulnerability to mechanical or material discrepancies implies the necessity for meticulous design and fabrication processes.

To improve the conductivity of the boom, a conductive layer could be used. This could be achieved by using a conductive fabric[138] or metallic coating. However, since the coating must cover the entire inner boom, the coating must be applied post-curing which is challenging. Moreover, when rolled up, adhesive forces could cause the coating to peel off, and additional measures must be taken to prevent this.

The structural tests of the CTM booms have preliminary character, which showed in the structural collapse tests. Future work should focus on improving the manufacturing process so that the web bond is improved. This can be achieved by using a different adhesive or by using a single shell manufacturing process like RTM. Longer booms would require less load on the attachment points, which could also alter the results. Then, the structural collapse tests and elastic deformation experiments should be repeated to confirm the results. With the final results, the structural penalty of the SWA can be assessed.

The CO_2 laser cutting process showed promising results, albeit room for improvement. A higher powered laser with nanosecond pulses could remedy this issue. An improved laser cutting process is also of central importance for manufacturing a future SWA. Should a single shell manufacturing process be used, the slotting process must be revised, since the slots cannot be cut post-curing. Instead, cutting the dry fiber fabric before placement appears to be the most promising approach, connected with automated fiber placement to ensure the required degree of precision. An improved SWA design, ideally amplitude tapered, should then be manufactured and verified in an anechoic chamber.

5.9 Conclusion

In this chapter, we presented the concept of waveguides and slotted waveguide antenna (SWA) using carbon composite collapsible tubular mast (CTM) structures. These hollow structures are highly robust and can provide superior stability to the solar sail at much lower mass than conventional metal booms. Therefore, this class of boom is a promising candidate for future solar sail missions, such as ACS3.

In order to use this boom as SWA, several waveguide options were addressed, with the most straightforward approach being a pure-carbon composite waveguide, since it provides the least manufacturing complexity. Through simulation, it was shown that the CTM geometry could effectively support several waveguide modes. A subsequent analysis of the single slotted waveguide antenna showed great difference between the TE modes and TM mode in terms of radiation efficiency and achievable gain. The $TM_{01}^{\bigcirc}$ mode emerged as clearly superior in these cases. It was found that a slot rotation of $40°$ to $60°$ yielded optimal results, with a secondary maximum found at $90°$. Further research into a non-uniform 10-slot antenna excited by the $TM_{01}^{\bigcirc}$ mode showed gain nearing 15.4 dBi, albeit with a high SLL of -4 dB. Notably, the introduction of a solar sail dramatically shifted the radiation pattern, raising concerns about the sail's texture, such as wrinkles and billowing, affecting the pattern predictability. A more detailed analysis of the SWA is indictated.

In order to obtain experimental data of the CTM waveguide attenuation and structural impact of the

slot array, a manufacturing of CTM booms using the vacuum-assisted resin infusion process (VARI) process was carried out. The VARI process produces half-shells, which significantly simplify the slot cutting process. Moreover, it is a more accessible and cost-effective method to provide small quantities and boom lengths. The material used was a thin-ply spread-tow PW carbon fabric, with a tow of 25 mm. The fabric was placed with a $[0\ 90/\pm 45]$ stacking sequence for quasi-anisotropy. The process produces separate half-shells of 0.5 m length that must be bonded together post-curing.

The attenuation of the waveguide has a significant impact on its use in a SWA. Determining the attenuation constant of the individual modes was therefore a prime objective of this chapter. Due to the waveguides unusual shape, coaxial adapters for TE and TM modes, as well as mode converters and fixtures needed to be designed and manufactured. The adapters were characterized using a vector network analyzer and the scattering parameters were extracted. The TE mode adapters were found to be functional in the target frequency band, with a return loss of about −19 dB and an insertion loss of better than 0.6 dB. The TM coaxial adapter reached a return loss of less than −30 dB and an insertion loss of better than 0.3 dB in the target band.

To provide a detailed assessment, attenuation statistics were derived across a frequency range of 8.0 GHz to 9.0 GHz. The $\mathrm{TE}_{01}^{\square}$ mode displayed the lowest attenuation at about $1.16\,\mathrm{dB\,m^{-1}}$, in line with anticipations for the waveguide's fundamental mode. The $\mathrm{TE}_{11}^{\bigcirc}$ mode measurement showed inconsistent results across the measurements, most likely due to material inconsistencies. In any case, $\mathrm{TE}_{11}^{\bigcirc}$ had the second-highest attenuation, but a repetition of the measurement is indicated. The $\mathrm{TM}_{01}^{\bigcirc}$ mode exhibited the highest attenuation at $2.88\,\mathrm{dB\,m^{-1}}$ but displayed remarkable consistency. However, the attenuation is comparatively low for a CFRP waveguide. The CFRP waveguide exhibits potential for electromagnetic wave propagation, with the $\mathrm{TE}_{01}^{\square}$ mode leading in performance.

In a comprehensive numerical simulation study, the boom's response to varying loads was analyzed, especially concerning slot parameters such as length, width, and angle. The x-axis bending was deemed most crucial as loads are primarily expected from this direction. The x-axis bending case revealed considerable deviations from the reference, with slot length identified as a primary influencer. Overall, slot length was determined as the most defining parameter across all load cases, with large deviations observed particularly in the x-axis scenario. Generally, the y-axis bending case recording the lowest stress levels.

In an experimental study involving three 10-slot SWA and three non-slotted booms, the booms were loaded until they showed signs of failure. The slotted SWA consistently failed at lower loads compared to the non-slotted reference boom. For y-axis bending, the SWA failed at about 71 % of the maximum load of the reference. In x-axis bending, the difference was less pronounced, with the SWA failing at about 95 % of the reference's maximum load. In the important z-axis compression load case, the SWA failed at about 68 % to 95 % of the reference's maximum load. Better outcomes are expected from SWA with more electrically advantageous slot angles, which would also reduce the structural penalty. The most important failure modes were buckling and web bond disintegration, indicating that a better adhesive or manufacturing process is required. The manufacturing process of the SWA, involving a CO2 laser cutter, revealed that the slots in the CTM appeared frayed with some imperfect carbon removal.

In conclusion, the CTM geometry provides an intriguing combination of ultra-light weight and high structural stability and low stowage volume. The CTM SWA however, requires more attention regarding its impact on the space segment, as well as its suitability in a solar sailing in general. Nevertheless, having a rollable, lightweight, and robust medium-gain antenna can be of use in other applications, where the mechanical stresses are lower and the weight requirements are less stringent.

Chapter 6

Conclusion

This chapter concludes this thesis. The results and findings of this thesis are summarized in Section 6.1 and concluding thoughts are provided in Section 6.2. Finally, Section 6.3 provides an outlook on future work.

6.1 Summary

Solar sailing is one of the most promising technologies for future space missions. Solar sailing is a propellantless propulsion technology that uses the momentum of photons from the Sun to accelerate a spacecraft. The technology is currently being developed and has a variety of applications in space exploration. However, the solar sailing is still in its infacy and requires further research and development. One of the main challenges is increasing the specific acceleration, as this directly affects possible missions and mission duration. This can be achieved by building larger sails and lighter spacecraft components. This thesis investigated the feasibility of integrating antennas into the solar sail structures, as antennas are usually among the larger components of a spacecraft, especially when larger distances are to be overcome. In this thesis, we investigated novel concepts for antennas integrated into the sail membrane (cf. Chapter 4) or the sail boom (cf. Chapter 5) of a solar sail spacecraft.

The challenges faced when building the membrane antenna evolve around suitable microwave technology, the practical limits to the antenna size and the mass of the antenna. A theoretical analysis found that conventional microwave transmission lines are disadvantageous when combined with the thin solar sail membrane, as they are either unfeasible to manufacture, or suffer from high attenuation or require non-planar structures to operate properly. We found a solution to the problem in the class of single conductor transmission lines, also known as spoof surface plasmon polariton (SSPP) transmission lines. All structures required for an array, i.e. the transmission line, power dividers and antennas, can be made purely planar using the SSPP technology. Therefore, an array based on SSPP integrates better into the existing sail configuration. Using a combination of manufactured prototypes of power dividers and antennas, as well as numerical simulations of combined designs, we showed that the SSPP technology is a viable solution for solar sail antennas. Given the performance data of the prototypes, an analysis was carried out to estimate the performance of large arrays. The analysis revealed a potential peak gain of 31 dBi at 8.5 GHz and an aperture areal density of less than $0.2\,\mathrm{kg\,m^{-2}}$. This is a significant improvement over the state of the art, by about two orders of magnitude.

The second antenna concept involved booms of the solar sail assembly. A type of boom that has recently attracted attention is the collapsible tubular mast (CTM). The CTM is a deployable tubular structure, that can be coiled up for storage and deployed by a pulling force. The CTM made from carbon composites is a promising candidate for solar sail booms, as it is lightweight, compact and can be deployed in a controlled manner. The tubular form of the CTM boom sparked interest for its use as waveguide and antenna. In this thesis, the most direct approach, a slotted waveguide antenna

made from a pure carbon fiber reinforced plastic (CFRP) was investigated. The investigation involved analysis of the propagating electromagnetic modes, slot placement and sail effects using numerical simulations. Given the linear nature of the slotted waveguide antenna, this concept is restricted to medium gain applications. Several short boom pieces were manufactured and the waveguide attenuation was measured. The attenuation of the fundamental mode was measured to $1.2\,\mathrm{dB\,m^{-1}}$ in X-band, which is on the lower end given the frequency and conductor material. The higher-order TM_{11} mode was found to have the best properties for use as a slotted waveguide antenna, but exhibited higher attenuation with $2.9\,\mathrm{dB\,m^{-1}}$. Moreover, a structural analysis with the goal to reveal the structural impact of slotting the boom was carried out. Using numerical simulations, the expected stresses and deformations were calculated and compared to the original boom. The analysis revealed a significant reduction of the load-bearing capacity in the important y-axis bending case to 71 % of the original value. This is an important result as the main goal in the development of multifunctional structures is to avoid interferences between the different functions.

6.2 Conclusion

This thesis represents a substantial contribution to the advancement of solar sailing technology, with a particular emphasis on the innovative integration of antenna systems into solar sails and the exploration of carbon composite CTM as dual-purpose structures. This research serves as a practical guidepost for future developments in space exploration technologies, particularly for missions that require lightweight, efficient, and multifunctional spacecraft components.

The first part of the thesis successfully demonstrated the viability of integrating SSPP transmission lines into the solar sail membrane. This approach overcame the challenges associated with classical planar transmission lines, which were unsuitable due to the sail's low dielectric thickness. The research showed that SSPP waveguides could effectively transmit microwaves with minimal attenuation, making them a promising solution for space communications. The prototypes developed, including the circular polarized 1x7 SSPP antenna array and a power divider, validated the theoretical findings with practical results. These advancements not only enhance the communication capabilities of spacecraft but also contribute significantly to the overall goal of reducing the weight and complexity of space mission payloads.

In the second part of the thesis, the focus shifted to the potential of CTMs, specifically in CFRP, as multifunctional elements that serve both as structural supports and communication devices. The exploration of various waveguide modes using these CTM structures revealed the effectiveness of the $\mathrm{TM}_{11}^{\bigcirc}$ mode in terms of radiation efficiency and achievable gain. The vacuum-assisted resin infusion process used in manufacturing these CTMs proved to be a pivotal step in simplifying the manufacturing process and reducing costs, particularly for small quantities and custom designs.

Looking forward, the research conducted in this thesis opens numerous avenues for future exploration. The challenges and potential solutions identified in the integration of communication systems into solar sail structures, and the multifunctional use of CTMs, provide a foundation for continued innovation. Future research should focus on refining manufacturing processes, optimizing design for enhanced performance, and conducting extensive testing under space-like conditions.

This thesis not only addresses key challenges in the development of efficient and lightweight solar sails but also lays the groundwork for future innovations in space exploration technologies. The integration of communication systems into solar sail structures and the multifunctional use of CTMs represent significant steps toward more versatile, efficient, and capable space missions.

6.3 Outlook

The research conducted in this thesis on integrating antenna systems into solar sail structures opens several promising avenues for future exploration in space technology, particularly in enhancing communication capabilities of spacecraft. The development and refinement of the IVD process for creating effective antenna arrays are paramount. This process needs further optimization to ensure consistent and reliable results, which are crucial for the practical application of these antennas in space missions. Improving the stability and durability of these antenna systems, especially under the unique stresses of space conditions, remains a key area for future investigation. Addressing the challenge of adhering conductive layers to the solar sail membrane, while maintaining the membrane's flexibility and integrity, will be critical. This could involve exploring new materials or innovative application techniques.

Optimizing the design of waveguide systems, particularly for solar sails, is another critical research path. This includes improving mode converters and attachment methods to minimize performance variances and enhance measurement accuracy. Experimental validation of these systems in conditions that simulate the space environment will be vital in assessing their viability for long-duration space missions.

In parallel, the potential of carbon composite CTM as multifunctional elements, serving both structural and communication roles, should continue to be explored, albeit to a lesser extent. The suitability of CTM as waveguides and antennas, particularly in the context of their structural impact and potential for integration into solar sail designs, presents an intriguing opportunity for advancing space mission technology.

Overall, the advancements in solar sail antenna technology highlighted in this thesis not only improve the prospects for efficient, long-range space communication but also contribute significantly to the broader goal of developing lightweight, multifunctional components for space exploration. The continuation of this research will play a crucial role in enhancing the capabilities and scope of future space missions, pushing the boundaries of what is currently achievable in space technology.

Bibliography

[1] Dachwald, B. “Optimal solar-sail trajectories for missions to the outer solar system”. In: *Journal of Guidance Control and Dynamics* 28.August (2005), pp. 1187–1193. ISSN: 07315090. DOI: 10.2514/1.13301.

[2] Macdonald, M., Hughes, G. W., McInnes, C. R., Lyngvi, A., Falkner, P., and Atzei, A. “Solar Polar Orbiter: A Solar Sail Technology Reference Study”. In: *Journal of Spacecraft and Rockets* 43.5 (Sept. 2006), pp. 960–972. ISSN: 0022-4650. DOI: 10.2514/1.16408. URL: https://arc.aiaa.org/doi/10.2514/1.16408.

[3] Grundmann, J. T., Bauer, W., Biele, J., Boden, R., Ceriotti, M., Cordero, F., Dachwald, B., Dumont, E., Grimm, C. D., Herčík, D., Ho, T. M., Jahnke, R., Koch, A. D., Koncz, A., Krause, C., Lange, C., Lichtenheldt, R., Maiwald, V., Mikschl, T., Mikulz, E., Montenegro, S., Pelivan, I., Peloni, A., Quantius, D., Reershemius, S., Renger, T., Riemann, J., Ruffer, M., Sasaki, K., Schmitz, N., Seboldt, W., Seefeldt, P., Spietz, P., Spröwitz, T., Sznajder, M., Tardivel, S., Tóth, N., Wejmo, E., Wolff, F., and Ziach, C. “Capabilities of GOSSAMER-1 derived small spacecraft solar sails carrying MASCOT-derived nanolanders for in-situ surveying of NEAs”. In: *Acta Astronautica* 156.February 2018 (2019), pp. 330–362. ISSN: 00945765. DOI: 10.1016/j.actaastro.2018.03.019. URL: https://doi.org/10.1016/j.actaastro.2018.03.019.

[4] Vergaaij, M., McInnes, C. R., and Ceriotti, M. “Economic assessment of high-thrust and solar-sail propulsion for near-earth asteroid mining”. In: *Advances in Space Research* 67.9 (2021), pp. 3045–3058. ISSN: 18791948. DOI: 10.1016/j.asr.2020.06.012. URL: https://doi.org/10.1016/j.asr.2020.06.012.

[5] Mewaldt, R. A. and Liewer, P. C. “An interstellar probe mission to the boundaries of the heliosphere and nearby interstellar space”. In: *Space 2000 Conference and Exposition* September 2000 (Sept. 2000). DOI: 10.2514/6.2000-5173. URL: https://arc.aiaa.org/doi/10.2514/6.2000-5173.

[6] Tsuda, Y., Mori, O., Funase, R., Sawada, H., Yamamoto, T., Saiki, T., Endo, T., and Kawaguchi, J. “Flight status of IKAROS deep space solar sail demonstrator”. In: *Acta Astronautica* 69.9-10 (2011), pp. 833–840. ISSN: 00945765. DOI: 10.1016/j.actaastro.2011.06.005. URL: http://dx.doi.org/10.1016/j.actaastro.2011.06.005.

[7] Tsuda, Y., Mori, O., Funase, R., Sawada, H., Yamamoto, T., Saiki, T., Endo, T., Yonekura, K., Hoshino, H., and Kawaguchi, J. “Achievement of IKAROS-Japanese deep space solar sail demonstration mission”. In: *Acta Astronautica* 82.2 (2013), pp. 183–188. ISSN: 00945765. DOI: 10.1016/j.actaastro.2012.03.032. URL: http://dx.doi.org/10.1016/j.actaastro.2012.03.032.

[8] Khayatian, H. and Rahmat-Samil, Y. “A novel antenna concept for future solar sails missions”. In: *IEEE Aerospace Conference Proceedings*. Vol. 2. 2. IEEE, 2002, pp. 981–998. ISBN: 078037231X. DOI: 10.1109/AERO.2002.1035696. URL: http://ieeexplore.ieee.org/document/1035696/.

[9] Khayatian, B. and Rahmat-Samii, Y. “A novel antenna concept for future solar sails: application of fresnel antennas”. In: *IEEE Antennas and Propagation Magazine* 46.2 (Apr. 2004), pp. 50–63. ISSN: 1045-9243. DOI: 10.1109/MAP.2004.1305534. URL: http://ieeexplore.ieee.org/document/1305534/.

[10] Kepler, J. *Gesammelte Werke. Mysterium cosmographicum. De cometis hyperaspistes.* Ed. by Bialas, V. and Caspar, M. Vol. 8. Johannes Kepler Gesammelte Werke. München: Beck, 1963. URL: http://publikationen.badw.de/de/002334744.

[11] Rosen, E. *Kepler's Conversation with Galileo's Sidereal Messenger*. Ed. by Woolf, H. 5th ed. New York, New York, USA: The Johns Hopkins University, 1965, p. 39.

[12] McInnes, C. R. *Solar Sailing. Technology, Dynamics and Mission Applications*. London: Springer London, 1999. ISBN: 978-1-85233-102-3. DOI: 10.1007/978-1-4471-3992-8. URL: http://link.springer.com/10.1007/978-1-4471-3992-8.

[13] National Renewable Energy Laboratory. *Air Mass Zero: Extraterrestrial Solar Irradiance Spectra*. 2000. URL: https://www.nrel.gov/grid/solar-resource/spectra.html (visited on 11/01/2023).

[14] Spencer, D. A., Johnson, L., and Long, A. C. "Solar sailing technology challenges". In: *Aerospace Science and Technology* 93 (2019), pp. 1–12. ISSN: 12709638. DOI: 10.1016/j.ast.2019.07.009. URL: https://doi.org/10.1016/j.ast.2019.07.009.

[15] Mori, O., S, H., Funase, R., Morimoto, M., Endo, T., Yamamoto, T., Tsuda, Y., Kawakatsu, Y., Kawaguchi, J., Miyazaki, Y., and Shirasawa, Y. "First Solar Power Sail Demonstration by IKAROS". In: *Transactions of the Japan Society for Aeronautical and Space Sciences, Aerospace Technology Japan* 8.ists27 (2010), To_4_25–To_4_31. ISSN: 1884-0485. DOI: 10.2322/tastj.8.to_4_25.

[16] Jordaan, H. W. "Spinning Solar Sail: The Deployment and Control of a Spinning Solar Sail Satellite". Dissertation. Stellenbosch University, 2016, p. 179.

[17] NeXolve. *CP1 ™ Polyimide Characteristics Typical Properties of CP1 ™ Polyimide*. 2022. URL: https://nexolve.com/wp-content/uploads/2021/10/TDS_CP1_Clear.pdf (visited on 10/01/2022).

[18] ZHAO, P., WU, C., and LI, Y. "Design and application of solar sailing: A review on key technologies". In: *Chinese Journal of Aeronautics* (Nov. 2022). ISSN: 10009361. DOI: 10.1016/j.cja.2022.11.002. URL: https://linkinghub.elsevier.com/retrieve/pii/S1000936122002564.

[19] DuPont. *DuPont ™ Kapton ® EN*. 2022. URL: https://www.dupont.com/content/dam/dupont/amer/us/en/ei-transformation/public/documents/en/EI-10173-Kapton-EN-Data-Sheet.pdf.

[20] MatWeb. *DuPont™ Kapton® 50EN Polyimide Film, 13 Micron Thickness*. URL: https://www.matweb.com/search/DataSheet.aspx?MatGUID=6a1b3d24f63f4c1785059610581e3660 (visited on 01/18/2023).

[21] Matweb. *DuPont Teijin Films Mylar® C Polyester Film, 10 Gauge*. URL: https://www.matweb.com/search/DataSheet.aspx?MatGUID=9a5ab4af8d314d51a6020a94760041d4 (visited on 01/18/2023).

[22] MatWeb. *DuPont Teijin Films Teonex® Q72 Polyester Film, 14 Gauge*. Web Page. 2023. URL: https://www.matweb.com/search/datasheet.aspx?matguid=6cf22d021715415593838704e3efe234 (visited on 01/18/2023).

[23] Paquin, R. A. "Properties of Metals". In: *Handbook of Optics: Volume II - Design, Fabrication, and Testing; Sources and Detectors; Radiometry and Photometry*. Ed. by Bass, M. 2nd ed. McGraw-Hill Education, 1994, pp. 1198–1226. ISBN: 0-07-047974-7.

[24] Inagaki, T., Emerson, L. C., Arakawa, E. T., and Williams, M. W. "Optical properties of solid Na and Li between 0.6 and 3.8 eV". In: *Phys. Rev. B* 13.6 (1976), pp. 2305–2313. DOI: 10.1103/PhysRevB.13.2305. URL: https://link.aps.org/doi/10.1103/PhysRevB.13.2305.

[25] Spencer, D. A., Betts, B., Bellardo, J. M., Diaz, A., Plante, B., and Mansell, J. R. "The LightSail 2 solar sailing technology demonstration". In: *Advances in Space Research* 67.9 (May 2021), pp. 2878–2889. ISSN: 18791948. DOI: 10.1016/j.asr.2020.06.029. URL: https://doi.org/10.1016/j.asr.2020.06.029.

[26] Kezerashvili, R. Y. “Thickness requirement for solar sail foils”. In: *Acta Astronautica* 65.3-4 (Aug. 2009), pp. 507–518. ISSN: 00945765. DOI: 10.1016/j.actaastro.2009.01.062. URL: https://www.sciencedirect.com/science/article/pii/S0094576509000939.

[27] Kang, J. H., Gordon, K. L., Bryant, R. G., Stohlman, O. R., Wilkie, W. K., Stark, A. E., Barfield, R. S., Sindle, B. R., Finckenor, M. M., and Craven, P. D. “Durability characterization of mechanical interfaces in solar sail membrane structures”. In: *Advances in Space Research* 67.9 (May 2021), pp. 2643–2654. ISSN: 02731177. DOI: 10.1016/j.asr.2020.08.015. URL: https://linkinghub.elsevier.com/retrieve/pii/S0273117720305731.

[28] Seefeldt, P. “Development and Qualification of Deployable Membranes for Space Applications”. PhD Thesis. Bremen, 2018.

[29] Puig, L., Barton, A., and Rando, N. “A review on large deployable structures for astrophysics missions”. In: *Acta Astronautica* 67.1-2 (2010), pp. 12–26. ISSN: 00945765. DOI: 10.1016/j.actaastro.2010.02.021. URL: http://dx.doi.org/10.1016/j.actaastro.2010.02.021.

[30] Cadogan, D. and Scarborough, S. “Rigidizable materials for use in gossamer space inflatable structures”. In: *19th AIAA Applied Aerodynamics Conference*. Reston, Virigina: American Institute of Aeronautics and Astronautics, June 2001, p. 1417. DOI: 10.2514/6.2001-1417. URL: https://arc.aiaa.org/doi/10.2514/6.2001-1417.

[31] University of Surrey. *InflateSail CubeSat comes to a successful and fiery end*. 2017. URL: https://phys.org/news/2017-09-inflatesail-cubesat-successful-fiery.html (visited on 04/25/2022).

[32] Lichodziejewski, D., Derbès, B., West, J., Reinert, R., Belvin, K., and Pappa, R. “Bringing an effective solar sail design toward TRL 6”. In: *39th AIAA/ASME/SAE/ASEE Joint Propulsion Conference and Exhibit* February 2003 (2003). DOI: 10.2514/6.2003-4659.

[33] Seefeldt, P., Spietz, P., Sproewitz, T., Grundmann, J. T., Hillebrandt, M., Hobbie, C., Ruffer, M., Straubel, M., Tóth, N., and Zander, M. “Gossamer-1: Mission concept and technology for a controlled deployment of gossamer spacecraft”. In: *Advances in Space Research* 59.1 (Jan. 2017), pp. 434–456. ISSN: 18791948. DOI: 10.1016/j.asr.2016.09.022. URL: https://doi.org/10.1016/j.asr.2016.09.022.

[34] Fernandez, J. M., Rose, K., Younger, C. J., Dean, G. D., Warren, J. E., Stohlman, O. R., and Wilkie, W. K. “NASA’s advanced solar sail propulsion system for Low-cost deep space exploration and science missions that uses high performance rollable composite booms”. In: *International Symposium on Solar Sailing* (2017), p. 11.

[35] Papa, A. and Pellegrino, S. “Systematically Creased Thin-Film Membrane Structures”. In: *Journal of Spacecraft and Rockets* 45.1 (Jan. 2008), pp. 10–18. ISSN: 0022-4650. DOI: 10.2514/1.18285. URL: https://arc.aiaa.org/doi/10.2514/1.18285.

[36] Miura, K. “Method of packaging and deployment of large membranes in space”. In: *The Institute of Space and Astronautical Science report* 618 (1985), pp. 1–9.

[37] Zou, J., Li, D., Wang, J., and Yu, Y. “Experimental Study of Measuring the Wrinkle of Solar Sails”. In: *Aerospace* 9.6 (May 2022), p. 289. ISSN: 2226-4310. DOI: 10.3390/aerospace9060289. URL: https://www.mdpi.com/2226-4310/9/6/289.

[38] Whorton, M. S., Heaton, A., Pinson, R., Laue, G. P., and Adams, C. L. “NanoSail-D : The First Flight Demonstration of Solar Sails for Nanosatellites”. In: *22nd Annual AIAA/USU Conference on Small Satellites* (2008), pp. 1–6.

[39] Alhorn, D. C., Casas, J. P., Agasid, E. F., Adams, C. L., Laue, G., Kitts, C., and O’Brien, S. “NanoSail-D: The Small Satellite That Could!” In: *25th Annual AIAA/USU Conference on Small Satellites* (2011), pp. 1–15.

[40] Viquerat, A., Schenk, M., Lappas, V., and Sanders, B. “Functional and Qualification Testing of the InflateSail Technology Demonstrator”. In: *2nd AIAA Spacecraft Structures Conference*. Reston, Virginia: American Institute of Aeronautics and Astronautics, Jan. 2015. ISBN: 978-1-62410-345-2. DOI: 10.2514/6.2015-1627. URL: https://arc.aiaa.org/doi/10.2514/6.2015-1627.

[41] Betts, B., Spencer, D. A., Nye, B., Munakata, R., Bellardo, J. M., Wong, S. D., Diaz, A., Ridenoure, R. W., Plante, B. A., Foley, J. D., and Vaughn, J. "LightSail 2: Controlled Solar Sailing Using a CubeSat". In: *Fourth International Symposium on Solar Sailing 2017* (2017).

[42] Burton, R., Laystrom-Woodard, J., Benavides, G., Carroll, D., Coverstone, V., Swenson, G., Pukniel, A., Chosh, A., and Moctezuma, A. "Initial development of the cubesail/ultrasail spacecraft". In: *Joint Army Navy NASA Air Force (JANNAF) Spacecraft Propulsion Subcommittee Meeting*. 2010.

[43] Johnson, L., Castillo-Rogez, J., and Dervan, J. "IAC-17.B4.8.5: Near earth asteroid scout: NASA's solar sail mission to a NEA". In: *Proceedings of the International Astronautical Congress, IAC* 10 (2017), pp. 6359–6362. ISSN: 00741795.

[44] Wilkie, W. K. "Overview of the NASA Advanced Composite Solar Sail System (ACS3) Technology Demonstration Project". In: *AIAA Scitech 2021 Forum*. Vol. 1 PartF. January. Reston, Virginia: American Institute of Aeronautics and Astronautics, Jan. 2021, pp. 1–23. ISBN: 978-1-62410-609-5. DOI: 10.2514/6.2021-1260. URL: https://arc.aiaa.org/doi/10.2514/6.2021-1260.

[45] Eastwood, J., Kataria, D., McInnes, C., Barnes, N., and Mulligan, P. "Sunjammer - University of Glascow". In: *Weather* 70.February (2015), pp. 27–30.

[46] ESA. *IKAROS (Interplanetary Kite-craft Accelerated by Radiation Of the Sun)*. 2010. URL: https://earth.esa.int/web/eoportal/satellite-missions/i/ikaros (visited on 04/25/2022).

[47] NASA. *NEA Scout Status Update*. 2022. URL: https://www.nasa.gov/centers/marshall/news/2022/nea-scout-status-update.html (visited on 12/15/2022).

[48] Johnson, L. "Solar Sail Propulsion for Interplanetary Small Spacecraft". In: *Space Propulsion Conference*. Sevilla, 2018.

[49] McNutt, L., Johnson, L., Clardy, D., Castillo-Rogez, J., Frick, A., and Jones, L. "Near-earth asteroid scout". In: *AIAA SPACE 2014 Conference and Exposition* (2014), pp. 1–9.

[50] Wilkie, K. "The NASA Advanced Composite Solar Sail System (ACS3) Flight Demonstration: A Technology Pathfinder for Practical Smallsat Solar Sailing". In: *AIAA/USU Conference on Small Satellites*. Logan, UT, 2021. URL: https://digitalcommons.usu.edu/smallsat/2021/all2021/146/.

[51] Guo, Y. J. and Barton, S. K. *Fresnel Zone Antennas*. Boston: Kluwer Academic Publishers, 2002. ISBN: 978-1-4419-5294-3.

[52] Wood, R. W. " LIII. Phase-reversal zone-plates, and diffraction-telescopes ". In: *The London, Edinburgh, and Dublin Philosophical Magazine and Journal of Science* 45.277 (1898), pp. 511–522. ISSN: 1941-5982. DOI: 10.1080/14786449808621159.

[53] Malliot, H. A. "Zone plate reflector antennas for applications in space". In: *IEEE Aerospace Applications Conference Proceedings*. 1994, pp. 295–311. ISBN: 0780318315. DOI: 10.1109/aero.1994.291189.

[54] Khayatian, B., Rahmat-Samii, Y., and Pogorzelski, R. "An antenna concept integrated with future solar sails". In: *IEEE Antennas and Propagation Society, AP-S International Symposium (Digest)* 2 (2001), pp. 742–745. ISSN: 15223965. DOI: 10.1109/APS.2001.959830.

[55] Khayatian, B. and Rahmat-Samii, Y. "A dual-band dual-feed Fresnel zone antenna concept: application in solar sails missions". In: *IEEE Antennas and Propagation Society International Symposium (IEEE Cat. No.02CH37313)*. Vol. 1. 1. IEEE, 2002, pp. 638–641. ISBN: 0-7803-7330-8. DOI: 10.1109/APS.2002.1016425. URL: http://ieeexplore.ieee.org/document/1016425/.

[56] Sauder, J., Chahat, N., Thomson, M., Hodges, R., and Peral, E. "Ultra-Compact Ka-Band Parabolic Deployable Antenna for RADAR and Interplanetary CubeSats". In: *29th AIAA/USU Conference on Small Satellites* (2015), pp. 1–4. URL: http://hdl.handle.net/2014/45833.

[57] Chahat, N., Sauder, J., Hodges, R., Thomson, M., Samii, Y. R., and Peral, E. "Ka-band high-gain mesh deployable reflector antenna enabling the first radar in a CubeSat: RainCube". In: *2016 10th European Conference on Antennas and Propagation, EuCAP 2016*. IEEE, Apr. 2016, pp. 1–4. ISBN: 9788890701863. DOI: 10.1109/EuCAP.2016.7481692. URL: http://ieeexplore.ieee.org/document/7481692/.

[58] Peral, E., Statham, S., Taneli, S., Imken, T., Williams, A., Price, D., Sauder, J., and Chahat, N. "RainCube, a Ka-band Precipitation Radar in a 6U CubeSat". In: *AIAA/USU Conference on Small Satellites* 15.May (2017). URL: https://digitalcommons.usu.edu/smallsat/2017/all2017/80.

[59] Babuscia, A., Corbin, B., Knapp, M., Jensen-Clem, R., Van de Loo, M., and Seager, S. "Inflatable antenna for cubesats: Motivation for development and antenna design". In: *Acta Astronautica* 91 (Oct. 2013), pp. 322–332. ISSN: 00945765. DOI: 10.1016/j.actaastro.2013.06.005. URL: https://linkinghub.elsevier.com/retrieve/pii/S0094576513001951.

[60] Babuscia, A., Choi, T., and Cheung, K.-M. "Inflatable antenna for CubeSat: Extension of the previously developed S-Band design to the X-Band". In: *AIAA SPACE 2015 Conference and Exposition*. Reston, Virginia: American Institute of Aeronautics and Astronautics, Aug. 2015, p. 4654. ISBN: 978-1-62410-334-6. DOI: 10.2514/6.2015-4654. URL: https://arc.aiaa.org/doi/10.2514/6.2015-4654.

[61] Babuscia, A., Choi, T., Sauder, J., Chandra, A., and Thangavelautham, J. "Inflatable antenna for CubeSats: Development of the X-band prototype". In: *2016 IEEE Aerospace Conference*. IEEE, Mar. 2016, pp. 1–11. ISBN: 978-1-4673-7676-1. DOI: 10.1109/AERO.2016.7500679. URL: http://ieeexplore.ieee.org/document/7500679/.

[62] Hodges, R. E., Chahat, N., Hoppe, D. J., and Vacchione, J. D. "A Deployable High-Gain Antenna Bound for Mars: Developing a new folded-panel reflectarray for the first CubeSat mission to Mars." In: *IEEE Antennas and Propagation Magazine* 59.2 (Apr. 2017), pp. 39–49. ISSN: 1045-9243. DOI: 10.1109/MAP.2017.2655561. URL: http://ieeexplore.ieee.org/document/7859458/.

[63] Leipold, M., Sickinger, C., Runge, H., Sickinger, C., and Runge, H. "Large SAR membrane antennas with lightweight deployable booms". In: *28th ESA Antenna Workshop on Space Antenna Systems and Technologies, ESA/ESTEC* 1 (2005), p. 8. URL: http://www.dlr.de/fa/en/portaldata/17/resources/dokumente/publikationen/2005/11_leipold.pdf.

[64] Huang, J., Lou, M., Feria, A., and Kim, Y. "An inflatable L-band microstrip SAR array". In: *IEEE Antennas and Propagation Society International Symposium. 1998 Digest. Antennas: Gateways to the Global Network. Held in conjunction with: USNC/URSI National Radio Science Meeting (Cat. No.98CH36194)*. Vol. 4. IEEE, 1998, pp. 2100–2103. ISBN: 0-7803-4478-2. DOI: 10.1109/APS.1998.701623. URL: http://ieeexplore.ieee.org/document/701623/.

[65] Huang, J. and Feria, A. "A 1-m X-band inflatable reflectarray antenna". In: *Microwave and Optical Technology Letters* 20.2 (Jan. 1999), pp. 97–99. ISSN: 08952477. DOI: 10.1002/(SICI)1098-2760(19990120)20:2<97::AID-MOP4>3.0.CO;2-K.

[66] Huang, J. "The development of inflatable array antennas". In: *IEEE Antennas and Propagation Magazine* 43.4 (Aug. 2001), pp. 44–50. ISSN: 10459243. DOI: 10.1109/74.951558. URL: http://ieeexplore.ieee.org/document/951558/.

[67] Moussessian, A., Del Castillo, L., Edelstein, W. N., Hatake, T., Huang, J., Madsen, S., Paris, A., Sadowy, G., and Shapiro, A. "Transmit/Receive Membranes for Large Aperture Scanning Phase Arrays". In: *Earth Science Technology Conference (ESTC)* (2003).

[68] Huang, J. and Moussessian, A. "Thin-membrane aperture-coupled L-band patch antenna". In: *IEEE Antennas and Propagation Society Symposium, 2004.* Vol. 3. IEEE, 2004, 2388–2391 Vol.3. ISBN: 0-7803-8302-8. DOI: 10.1109/APS.2004.1331853. URL: http://ieeexplore.ieee.org/document/1331853/.

[69] Huang, J., Sadowy, G., Derksen, C., Del Castillo, L., Smith, P., Hoffman, J., Hatake, T., and Moussessian, A. “Aperture-coupled thin-membrane microstrip array antenna for beam scanning application”. In: *IEEE Antennas and Propagation Society, AP-S International Symposium (Digest)*. Vol. 1 A. IEEE, 2005, pp. 330–333. ISBN: 0780388836. DOI: 10.1109/APS.2005.1551317. URL: http://ieeexplore.ieee.org/document/1551317/.

[70] Lichodziejewski, D., Cravey, R., and Hopkins, G. “Inflatably deployed membrane waveguide array antenna for space”. In: *44th AIAA/ASME/ASCE/AHS/ASC Structures, Structural Dynamics, and Materials Conference*. 2003. ISBN: 9781624101007. DOI: 10.2514/6.2003-1649.

[71] Fralick, D. T., Lichodziejewski, D., Cravey, R. L., Bailey, M. C., and Hopkins, G. D. “Performance evaluation of a membrane waveguide array antenna”. In: *IEEE Aerospace Conference Proceedings* 2 (2003), pp. 1039–1044. ISSN: 1095323X. DOI: 10.1109/AERO.2003.1235517.

[72] Hopkins, G. D., Cravey, R. L., Fralick, D. T., Lichodziejewski, D., Redell, F., and Bailey, M. C. “Comparison of measured and modeled performance of a tensioned membrane waveguide array antenna”. In: *IEEE Antennas and Propagation Society, AP-S International Symposium (Digest)* 1 (2004), pp. 571–574. ISSN: 15223965. DOI: 10.1109/aps.2004.1329734.

[73] Shin, D. K. “Frequency and Channel Assignments”. In: *JPL DSN Deep Space Network Series* 810.005 (2014), p. 201.

[74] Balanis, C. A. *Antenna Theory: Analysis and Design, Fourth Edition*. John Wiley & Sons, Inc., 2016. ISBN: 978-1-118-642060-1.

[75] Appel, N. “Structure-Integrated Antennas for Solar Sails”. In: *2022 IEEE Aerospace Conference (AERO)*. IEEE, Mar. 2022, pp. 1–9. ISBN: 978-1-6654-3760-8. DOI: 10.1109/AERO53065.2022.9843275. URL: https://doi.org/10.1109/AERO53065.2022.9843275.

[76] Garg, R., Bahl, I., and Bozzi, M. *Microstrip Lines and Slotlines, Third Edition*. Microwave & RF. Artech House, 2013. ISBN: 9781608075355. URL: https://books.google.de/books?id=1PQfAgAAQBAJ.

[77] Holloway, C. L. and Kuester, E. F. “A Quasi-Closed Form Expression for the Conductor Loss of CPW Lines, with an Investigation of Edge Shape Effects”. In: *IEEE Transactions on Microwave Theory and Techniques* 43.12 (1995), pp. 2695–2701. ISSN: 15579670. DOI: 10.1109/22.477846.

[78] Frankel, M. Y., Gupta, S., Valdmanis, J. A., and Mourou, G. A. “Terahertz Attenuation and Dispersion Characteristics of Coplanar Transmission Lines”. In: *IEEE Transactions on Microwave Theory and Techniques* 39.6 (1991), pp. 910–916. ISSN: 15579670. DOI: 10.1109/22.81658.

[79] Cohn, S. “Slot Line on a Dielectric Substrate”. In: *IEEE Transactions on Microwave Theory and Techniques* 17.10 (Oct. 1969), pp. 768–778. ISSN: 0018-9480. DOI: 10.1109/TMTT.1969.1127058. URL: http://ieeexplore.ieee.org/document/1127058/.

[80] Janaswamy, R. and Schaubert, D. H. “Characteristic Impedance of a Wide Slotline on Low-Permittivity Substrates”. In: *IEEE Transactions on Microwave Theory and Techniques* 34.8 (1986), pp. 900–902. ISSN: 15579670. DOI: 10.1109/TMTT.1986.1133465.

[81] Pozar, D. M. *Microwave Engineering*. 4th Edition. John Wiley & Sons, 2011. ISBN: 978-0-470-63155-3.

[82] Ghione, G. and Naldi, C. “Parameters of coplanar waveguides with lower ground plane”. In: *Electronics Letters* 19.18 (1983), p. 734. ISSN: 00135194. DOI: 10.1049/el:19830500. URL: https://digital-library.theiet.org/content/journals/10.1049/el_19830500.

[83] Sommerfeld, A. “Ueber die Fortpflanzung elektrodynamischer Wellen längs eines Drahtes”. In: *Annalen der Physik* 303.2 (1899), pp. 233–290.

[84] Sievenpiper, D. F. “Artificial Impedance Surfaces for Antennas”. In: *Modern Antenna Handbook*. Wiley, Aug. 2008, pp. 737–777. DOI: 10.1002/9780470294154.ch15. URL: https://onlinelibrary.wiley.com/doi/10.1002/9780470294154.ch15.

[85] Goubau, G. “Surface Waves and Their Application to Transmission Lines”. In: *Journal of Applied Physics* 21.11 (Nov. 1950), pp. 1119–1128. ISSN: 0021-8979. DOI: 10.1063/1.1699553. URL: http://aip.scitation.org/doi/10.1063/1.1699553.

[86] Xu, Y. and Bosisio, R. G. “A study of planar goubau lines (PGLs) for millimeter- And submillimeter-wave integrated circuits (ICs)”. In: *Microwave and Optical Technology Letters* 43.4 (Nov. 2004), pp. 290–293. ISSN: 08952477. DOI: 10.1002/mop.20448. URL: https://onlinelibrary.wiley.com/doi/10.1002/mop.20448.

[87] Vaughn, B. and Peroulis, D. “An updated applied formulation for the Goubau transmission line”. In: *Journal of Applied Physics* 126.19 (2019). ISSN: 10897550. DOI: 10.1063/1.5125141.

[88] Barnes, W. L., Dereux, A., and Ebbesen, T. W. “Surface plasmon subwavelength optics”. In: *Nature* 424.6950 (Aug. 2003), pp. 824–830. ISSN: 0028-0836. DOI: 10.1038/nature01937. URL: https://www.nature.com/articles/nature01937.

[89] Cui, T. J. and Shen, X. “Spoof surface plasmons on ultrathin corrugated metal structures in microwave and terahertz frequencies”. In: *2013 7th International Congress on Advanced Electromagnetic Materials in Microwaves and Optics*. September. IEEE, Sept. 2013, pp. 537–539. ISBN: 978-1-4799-1232-2. DOI: 10.1109/MetaMaterials.2013.6809111. URL: http://ieeexplore.ieee.org/document/6809111/.

[90] Gao, X., Zhou, L., Yu, X. Y., Cao, W. P., Li, H. O., Ma, H. F., and Cui, T. J. “Ultra-wideband surface plasmonic Y-splitter”. In: *Optics Express* 23.18 (2015), p. 23270. ISSN: 1094-4087. DOI: 10.1364/oe.23.023270.

[91] Yin, J. Y., Ren, J., Zhang, H. C., Pan, B. C., and Cui, T. J. “Broadband Frequency-Selective Spoof Surface Plasmon Polaritons on Ultrathin Metallic Structure”. In: *Scientific Reports* 5 (2015), pp. 1–5. ISSN: 20452322. DOI: 10.1038/srep08165.

[92] Wu, Y., Li, M., Yan, G., Deng, L., Liu, Y., and Ghassemlooy, Z. “Single-conductor co-planar quasi-symmetry unequal power divider based on spoof surface plasmon polaritons of bow-tie cells”. In: *AIP Advances* 6.10 (Oct. 2016), p. 105110. ISSN: 2158-3226. DOI: 10.1063/1.4966051. URL: http://aip.scitation.org/doi/10.1063/1.4966051.

[93] Li, M., Wu, Y., Qu, M., Li, Q., and Liu, Y. “A novel power divider with ultra-wideband harmonics suppression based on double-sided parallel spoof surface plasmon polaritons transmission line”. In: *International Journal of RF and Microwave Computer-Aided Engineering* 28.4 (May 2018), e21231. ISSN: 10964290. DOI: 10.1002/mmce.21231. URL: http://doi.wiley.com/10.1002/mmce.21231.

[94] Zhou, S., Lin, J.-Y., Wong, S.-W., Deng, F., Zhu, L., Yang, Y., He, Y., and Tu, Z.-H. “Spoof Surface Plasmon Polaritons Power Divider with large Isolation”. In: *Scientific Reports* 8.1 (Dec. 2018), p. 5947. ISSN: 2045-2322. DOI: 10.1038/s41598-018-24404-0. URL: http://www.nature.com/articles/s41598-018-24404-0%20http://dx.doi.org/10.1038/s41598-018-24404-0.

[95] Zhou, S.-Y., Wong, S.-W., Lin, J.-Y., Zhu, L., He, Y., and Tu, Z.-H. “Four-Way Spoof Surface Plasmon Polaritons Splitter/Combiner”. In: *IEEE Microwave and Wireless Components Letters* 29.2 (Feb. 2019), pp. 98–100. ISSN: 1531-1309. DOI: 10.1109/LMWC.2018.2886318. URL: https://ieeexplore.ieee.org/document/8601390/.

[96] Zu, H., Wu, B., Wu, M., Chen, L., and Su, W. “Flexible Microwave Devices and Dual-frequency-scanning Antenna Based on Spoof Surface Plasmon Polaritons”. In: *2019 Photonics & Electromagnetics Research Symposium - Fall (PIERS - Fall)*. IEEE, Dec. 2019, pp. 514–520. ISBN: 978-1-7281-5304-9. DOI: 10.1109/PIERS-Fall48861.2019.9021331. URL: https://ieeexplore.ieee.org/document/9021331/.

[97] Xu, J. J., Zhang, H. C., Zhang, Q., and Cui, T. J. “Efficient conversion of surface-plasmon-like modes to spatial radiated modes”. In: *Applied Physics Letters* 106.2 (2015), pp. 1–6. ISSN: 00036951. DOI: 10.1063/1.4905580. URL: http://dx.doi.org/10.1063/1.4905580.

[98] Guan, D.-F., You, P., Zhang, Q., Lu, Z.-H., Yong, S.-W., and Xiao, K. "A Wide-Angle and Circularly Polarized Beam-Scanning Antenna Based on Microstrip Spoof Surface Plasmon Polariton Transmission Line". In: *IEEE Antennas and Wireless Propagation Letters* 16 (2017), pp. 2538–2541. ISSN: 1536-1225. DOI: 10.1109/LAWP.2017.2731877. URL: https://ieeexplore.ieee.org/document/7990495/.

[99] Zhang, Q., Zhang, Q., and Chen, Y. "High-efficiency circularly polarised leaky-wave antenna fed by spoof surface plasmon polaritons". In: *IET Microwaves, Antennas & Propagation* 12.10 (Aug. 2018), pp. 1639–1644. ISSN: 1751-8725. DOI: 10.1049/iet-map.2017.1054. URL: https://digital-library.theiet.org/content/journals/10.1049/iet-map.2017.1054.

[100] Zhang, H. C., Liu, S., Shen, X., Chen, L. H., Li, L., and Cui, T. J. "Broadband amplification of spoof surface plasmon polaritons at microwave frequencies". In: *Laser & Photonics Reviews* 9.1 (Jan. 2015), pp. 83–90. ISSN: 18638880. DOI: 10.1002/lpor.201400131. URL: https://onlinelibrary.wiley.com/doi/10.1002/lpor.201400131.

[101] Ma, H. F., Shen, X., Cheng, Q., Jiang, W. X., and Cui, T. J. "Broadband and high-efficiency conversion from guided waves to spoof surface plasmon polaritons". In: *Laser and Photonics Reviews* 8.1 (2014), pp. 146–151. ISSN: 18638880. DOI: 10.1002/lpor.201300118.

[102] Kianinejad, A., Chen, Z. N., and Qiu, C.-W. "Low-Loss Spoof Surface Plasmon Slow-Wave Transmission Lines With Compact Transition and High Isolation". In: *IEEE Transactions on Microwave Theory and Techniques* 64.10 (Oct. 2016), pp. 3078–3086. ISSN: 0018-9480. DOI: 10.1109/TMTT.2016.2604807. URL: http://ieeexplore.ieee.org/document/7567553/.

[103] Shen, F., Rong, S., Zhang, H., Peng, F., and Cui, N. "Correction and adjusting for the deformation on solar sail". In: *CEAS Space Journal* 8.4 (2016), pp. 315–322. ISSN: 18682510. DOI: 10.1007/s12567-016-0128-2.

[104] Zheng, Z., Tang, M., Mao, J., and Zhang, Y. "Transmission Loss Analysis of Grounded and Ungrounded SSPP Transmission Lines". In: *2020 International Conference on Microwave and Millimeter Wave Technology (ICMMT)*. 2. IEEE, Sept. 2020, pp. 1–3. ISBN: 978-1-7281-5733-7. DOI: 10.1109/ICMMT49418.2020.9386332. URL: https://ieeexplore.ieee.org/document/9386332/.

[105] Kianinejad, A. *Metamaterial Surface Plasmon-Based Transmission Lines and Antennas*. Springer Theses. Singapore: Springer Singapore, 2018, p. 120. ISBN: 978-981-10-8374-7. DOI: 10.1007/978-981-10-8375-4. URL: http://link.springer.com/10.1007/978-981-10-8375-4.

[106] Xu, Z., Li, S., Yin, X., Zhao, H., and Liu, L. "Radiation loss of planar surface plasmon polaritons transmission lines at microwave frequencies". In: *Scientific Reports* 7.1 (Dec. 2017), p. 6098. ISSN: 2045-2322. DOI: 10.1038/s41598-017-06454-y. URL: http://www.nature.com/articles/s41598-017-06454-y.

[107] Li, Z., Wang, J., Zhang, Z., and Chen, M. "Far field computation of the traveling wave structures and a new approach for suppressing the sidelobe levels". In: *IEEE Transactions on Antennas and Propagation* 61.4 (2013), pp. 2308–2312. ISSN: 0018926X. DOI: 10.1109/TAP.2013.2237738.

[108] Marks, R. B. "A Multiline Method of Network Analyzer Calibration". In: *IEEE Transactions on Microwave Theory and Techniques* 39.7 (1991), pp. 1205–1215. ISSN: 15579670. DOI: 10.1109/22.85388.

[109] Elsheikh, M. A. G. and Safwat, A. M. E. "Geometrical Modeling of Strip-Loaded CPW and Its Application to All CPW Air-Bridge Free Wilkinson Power Dividers". In: *IEEE Transactions on Microwave Theory and Techniques* 67.8 (Aug. 2019), pp. 3370–3376. ISSN: 0018-9480. DOI: 10.1109/TMTT.2019.2921328. URL: https://ieeexplore.ieee.org/document/8746623/.

[110] Nasr, A. M. and Safwat, A. M. "Multimode Coplanar Waveguide Cross-Junction: Equivalent Circuit Model and Air-Bridge Free Applications". In: *IEEE Transactions on Microwave Theory and Techniques* 65.10 (2017), pp. 3753–3760. ISSN: 00189480. DOI: 10.1109/TMTT.2017.2699646.

[111] Kong, G. S., Ma, H. F., Cai, B. G., and Cui, T. J. "Continuous leaky-wave scanning using periodically modulated spoof plasmonic waveguide". In: *Scientific Reports* 6.May (2016), pp. 1–9. ISSN: 20452322. DOI: 10.1038/srep29600.

[112] Hao, Z. C., Zhang, J., and Zhao, L. "A compact leaky-wave antenna using a planar spoof surface plasmon polariton structure". In: *International Journal of RF and Microwave Computer-Aided Engineering* 29.5 (2019), pp. 1–7. ISSN: 1099047X. DOI: 10.1002/mmce.21617.

[113] Sanchez-Escuderos, D., Ferrando-Bataller, M., Herranz, J. I., and Cabedo-Fabres, M. "Periodic Leaky-Wave Antenna on Planar Goubau Line at Millimeter-Wave Frequencies". In: *IEEE Antennas and Wireless Propagation Letters* 12 (2013), pp. 1006–1009. ISSN: 1536-1225. DOI: 10.1109/LAWP.2013.2278035. URL: http://ieeexplore.ieee.org/document/6578113/.

[114] Sanchez-Escuderos, D., Ferrando-Bataller, M., Herranz, J. I., and Rodrigo-Penarrocha, V. M. "Low-Loss Circularly Polarized Periodic Leaky-Wave Antenna". In: *IEEE Antennas and Wireless Propagation Letters* 15 (2016), pp. 614–617. ISSN: 1536-1225. DOI: 10.1109/LAWP.2015.2463672. URL: http://ieeexplore.ieee.org/document/7174955/.

[115] Wu, X., Cullen, D., Brist, G., and Ramahi, O. M. "Surface finish effects on high-speed signal degradation". In: *IEEE Transactions on Advanced Packaging* 31.1 (2008), pp. 182–189. ISSN: 15213323. DOI: 10.1109/TADVP.2007.914962.

[116] Shlepnev, Y. and McMorrow, S. "Nickel characterization for interconnect analysis". In: *IEEE International Symposium on Electromagnetic Compatibility* (2011), pp. 524–529. ISSN: 10774076. DOI: 10.1109/ISEMC.2011.6038368.

[117] Seiler, P. and Plettemeier, D. "Measurement of PCB Surface Finishes for Substrate Characterization up to 67 GHz". In: *2018 IEEE Antennas and Propagation Society International Symposium and USNC/URSI National Radio Science Meeting, APSURSI 2018 - Proceedings* (2018), pp. 1059–1060. DOI: 10.1109/APUSNCURSINRSM.2018.8608680.

[118] Farokhipour, E., Komjani, N., and Chaychizadeh, M. A. "An ultra-wideband three-way power divider based on spoof surface plasmon polaritons". In: *Journal of Applied Physics* 124.23 (2018). ISSN: 10897550. DOI: 10.1063/1.5050495. URL: http://dx.doi.org/10.1063/1.5050495.

[119] Yang, Z., Takacs, A., Charlot, S., and Dragomirescu, D. "Design of Kapton based passive circuits at microwave frequencies". In: *European Microwave Week 2015: "Freedom Through Microwaves", EuMW 2015 - Conference Proceedings; 2015 45th European Microwave Conference Proceedings, EuMC* (2015), pp. 873–876. DOI: 10.1109/EuMC.2015.7345903.

[120] Chauraya, A., Whittow, W. G., Vardaxoglou, J. C., Li, Y., Torah, R., Yang, K., Beeby, S., and Tudor, J. "Inkjet printed dipole antennas on textiles for wearable communications". In: *IET Microwaves, Antennas & Propagation* 7.9 (June 2013), pp. 760–767. ISSN: 1751-8733. DOI: 10.1049/iet-map.2013.0076. URL: https://onlinelibrary.wiley.com/doi/10.1049/iet-map.2013.0076.

[121] Goliya, Y., Rivadeneyra, A., Salmeron, J. F., Albrecht, A., Mock, J., Haider, M., Russer, J., Cruz, B., Eschlwech, P., Biebl, E., Becherer, M., and Bobinger, M. R. "Next Generation Antennas Based on Screen-Printed and Transparent Silver Nanowire Films". In: *Advanced Optical Materials* 7.21 (Nov. 2019), p. 1900995. ISSN: 2195-1071. DOI: 10.1002/adom.201900995. URL: https://onlinelibrary.wiley.com/doi/abs/10.1002/adom.201900995.

[122] Spietz, P., Spröwitz, T., Seefeldt, P., Grundmann, J. T., Jahnke, R., Mikschl, T., Mikulz, E., Montenegro, S., Reershemius, S., Renger, T., Ruffer, M., Sasaki, K., Sznajder, M., Tóth, N., Ceriotti, M., Dachwald, B., Macdonald, M., McInnes, C., Seboldt, W., Quantius, D., Bauer, W., Wiedemann, C., Grimm, C. D., Herčík, D., Ho, T. M., Lange, C., and Schmitz, N. "Paths not taken – The GOSSAMER roadmap's other options". In: *Advances in Space Research* 67.9 (May 2021), pp. 2912–2956. ISSN: 18791948. DOI: 10.1016/j.asr.2021.01.044.

[123] Hoppe, J. "Entwicklung eines Fertigungsverfahrens für Dünnschicht-Hochfrequenzschaltungen in der Raumfahrt". Bachelor's Thesis. Technical University of Munich, 2022, p. 128.

[124] D'Addario, L. R. "Combining loss of a transmitting array due to phase errors". In: *IPN Progress Report* (2008), pp. 42–175.

[125] Brislee, F. J. "The density of aluminium". In: *Transactions of the Faraday Society* 9 (1913), pp. 162–173.

[126] Fernandez, J. M., Rose, G., Stohlman, O. R., Younger, C. J., Dean, G. D., Warren, J. E., Kang, J. H., Bryant, R. G., and Wilkie, K. W. "An Advanced Composites-Based Solar Sail System for Interplanetary Small Satellite Missions". In: *2018 AIAA Spacecraft Structures Conference*. 210019. Reston, Virginia: American Institute of Aeronautics and Astronautics, Jan. 2018. ISBN: 978-1-62410-530-2. DOI: 10.2514/6.2018-1437. URL: https://arc.aiaa.org/doi/10.2514/6.2018-1437.

[127] Herbeck, L., Eiden, M., Leipold, M., Sickinger, C., and Unckenbold, W. "Development and test of deployable ultra-lightweight CFRP-booms for a Solar Sail". In: *European Space Agency, (Special Publication) ESA SP* 49.468 (2001), pp. 107–112. ISSN: 03796566.

[128] Block, J., Straubel, M., and Wiedemann, M. "Ultralight deployable booms for solar sails and other large gossamer structures in space". In: *Acta Astronautica* 68.7-8 (2011), pp. 984–992. ISSN: 00945765. DOI: 10.1016/j.actaastro.2010.09.005. URL: http://dx.doi.org/10.1016/j.actaastro.2010.09.005.

[129] Seefeldt, P., Spietz, P., and Christian, H. "The Design and Test of the GOSSAMER-1 Boom". In: January (2015), pp. 1–15.

[130] Fernandez, J. M. "Advanced Deployable Shell-Based Composite Booms for Small Satellite Structural Applications Including Solar Sails". In: *International Symposium on Solar Sailing 2017*. January. Kyoto, 2017.

[131] Goldberg, D. A., Laslett, L. J., and Rimmer, R. A. "Modes of elliptical waveguides: A correction". In: *IEEE transactions on microwave theory and techniques* 38.11 (1990), pp. 1603–1608.

[132] Granet, C., James, G. L., and Forsyth, A. R. "Aperture Antennas: Waveguides and Horns". In: *Modern Antenna Handbook*. John Wiley & Sons, Ltd, 2008. Chap. 3, pp. 97–156. ISBN: 9780470294154. DOI: https://doi.org/10.1002/9780470294154.ch3. URL: https://onlinelibrary.wiley.com/doi/abs/10.1002/9780470294154.ch3.

[133] Josefsson, L. and Sembiam, R., eds. *Slotted Waveguide Array Antennas - Theory, Analysis and Design*. Institution of Engineering and Technology (The IET), 2018. ISBN: 978-1-61353-190-7. URL: https://app.knovel.com/hotlink/toc/id:kpSWAATAD2/slotted-waveguide-array/slotted-waveguide-array.

[134] Bojovschi, A., Shariati, N., and Ghorbani, K. "Analysis of a carbon fibre reinforced polymer slotted waveguide array fed by a loop type end launcher". In: *2013 Asia-Pacific Microwave Conference Proceedings (APMC)*. IEEE, Nov. 2013, pp. 476–478. ISBN: 978-1-4799-1472-2. DOI: 10.1109/APMC.2013.6694836. URL: http://ieeexplore.ieee.org/document/6694836/.

[135] Wagner, R. and Braun, H. M. "A slotted waveguide array antenna from carbon fibre reinforced plastics for the European space SAR". In: *Acta Astronautica* 8.3 (Mar. 1981), pp. 273–282. ISSN: 00945765. DOI: 10.1016/0094-5765(81)90036-9.

[136] Bräuer, G., Brand, J., Britze, C., Dietz, A., Kondruweit, S., Thomas, M., and Vergöhl, M. "Für den weitesten Weg: Schichten im All". In: *Vakuum in Forschung und Praxis* 31.6 (2019), pp. 26–31. ISSN: 0947-076X. DOI: 10.1002/vipr.201900729.

[137] Bojovschi, A., Nicholson, K. J., Galehdar, A., Callus, P. J., and Ghorbani, K. "The role of fibre orientation on the electromagnetic performance of waveguides manufactured from carbon fibre reinforced plastic". In: *Progress In Electromagnetics Research B* 39 (2012), pp. 267–280. ISSN: 19376472. DOI: 10.2528/PIERB12011110.

[138] Rudd, M., Baum, T. C., Mapleback, B., Ghorbani, K., and Nicholson, K. J. "Reducing the attenuation in CFRP waveguide using carbon fiber veil". In: *IEEE Microwave and Wireless Components Letters* 27.12 (Dec. 2017), pp. 1089–1091. ISSN: 15311309. DOI: 10.1109/LMWC.2017.2762243. URL: http://ieeexplore.ieee.org/document/8093637/.

[139] Rudd, M., Thomas Baum, C., and Ghorbani, K. "Higher Order Modes Propagation in Rectangular Waveguides Made from Anisotropic Material". In: *Proceedings of the 2018 IEEE 7th Asia-Pacific Conference on Antennas and Propagation, APCAP 2018*. 2018, pp. 80–82. ISBN: 9781538656488. DOI: 10.1109/APCAP.2018.8538039.

[140] Coetzee, J. C. and Sheel, S. "Compensation for Waveguide Losses in the Design of Slot Arrays". In: *IEEE Transactions on Antennas and Propagation* 66.3 (Mar. 2018), pp. 1271–1279. ISSN: 0018-926X. DOI: 10.1109/TAP.2018.2790165. URL: http://ieeexplore.ieee.org/document/8247275/.

[141] Gray, D., Nicholson, K. J., Callus, P. J., and Ghorbani, K. *Methods of Designing and Feeding Carbon Fibre Reinforced Plastic Slotted Waveguide Antenna Arrays*. Tech. rep. Australian Department of Defence.

[142] Appel, N., Werner, C., Hoppe, J., and Stegmann, L. "Multi-Functional Radiating Structures for Solar Sailing Missions". In: *B2. IAF Space Communications and Navigation Symposium*. Paris: IAF, 2022.

[143] Lange+Ritter GmbH. *TEXTREME® – Gewebe aus gespreizten UD-Tapes*. 2021. URL: https://www.lange-ritter.de/fileadmin/user_upload/Downloads/Produkte/Kohlefaser/Kohlefaser_2021/Kohlefaser_Faserverstaerkungen_Textreme_44.pdf (visited on 09/04/2023).

[144] Sonoda, N., Ohki, T., and Hagihara, K. *RANDOM MAT, FIBER-REINFORCED COMPOSITE MATERIAL MOLDED ARTICLE, AND CARBON FIBER MAT*. 2016. URL: https://patents.google.com/patent/EP3015492B1.

[145] Teijin Carbon Europe GmbH. *Tenax Filament Yarn*. 2022. URL: https://www.teijincarbon.com/fileadmin/user_upload/Datenbl%C3%A4tter/Filament_Yarn/Product_Data_Sheet_TSG01en__EU_Filament_.pdf (visited on 11/01/2023).

[146] Sika Deutschland GmbH. *SikaBiresin CR80*. 2023. URL: https://industry.sika.com/en/home/advanced-resins/sports-and-leisure/composite-resin-systems/composite-systemsforvacuuminfusion/sikabiresin-cr80.html (visited on 11/01/2023).

[147] Ronde, F. C. de. "Idea W.G. to coax transitions using a F.B.M. monopole." In: *IEEE MTT-S International Microwave Symposium Digest*. Vol. 1988. IEEE, 1988, pp. 591–594. DOI: 10.1109/mwsym.1988.22104. URL: http://ieeexplore.ieee.org/document/22104/.

[148] MacPhie, R., Opie, M., and Ries, C. "Input impedance of a coaxial line probe feeding a circular waveguide in the TM/sub 01/ mode". In: *IEEE Transactions on Microwave Theory and Techniques* 38.3 (Mar. 1990), pp. 334–337. ISSN: 00189480. DOI: 10.1109/22.45357. URL: http://ieeexplore.ieee.org/document/45357/.

[149] Yamamoto, T., Urabe, K., and Tsuda, H. "Analysis of coaxial-to-circular waveguide transition". In: *IEEE Antennas and Propagation Society, AP-S International Symposium (Digest)* c (2014), pp. 1497–1498. ISSN: 15223965. DOI: 10.1109/APS.2014.6905074.

[150] Werner, C. "Structural Analysis of Multifunctional Radiating CTM-Boom Structures for Antenna Applications on Solar Sail Spacecraft". Master's Thesis. Technical University of Munich, 2022, p. 319.

[151] Schmeer, S., Magin, M., Meier, M., Mattern, S., and Schweizerhof, K. *Aktueller Stand und Trends in der CFK-Berechnung im Fahrzeugbau*. Schriftenr. Forschungsvereinigung Automobiltechnik e.V. (FAT), 2009.

[152] Chang, C. and Pham, T. *DSN Telecommunications Link Design Handbook*. Tech. rep. 810-006. Jet Propulsion Laboratory/California Institute of Technology, 2015, p. 832. URL: https://deepspace.jpl.nasa.gov/dsndocs/810-005/.

[153] Vassallo, E., Martin, R., Madde, R., Lanucara, M., Besso, P., Droll, P., Galtie, G., and De Vicente, J. "The European space agency's deep-space antennas". In: *Proceedings of the IEEE* 95.11 (2007), pp. 2111–2131. ISSN: 00189219. DOI: 10.1109/JPROC.2007.905189.

[154] Plemel, R., Warhaut, M., and Martin, R. “ESA Station Tracking Network (ESTRACK) Augmented by the Second Deep Space Antenna at Cebreros, Spain”. In: *SpaceOps 2006 Conference*. 2006. DOI: 10.2514/6.2006-5788. URL: https://arc.aiaa.org/doi/abs/10.2514/6.2006-5788.

[155] Orii, A., Suizu, M., Amakawa, S., Katayama, K., Takano, K., Motoyoshi, M., Yoshida, T., and Fujishima, M. “On the length of THRU standard for TRL de-embedding on Si substrate above 110 GHz”. In: *2013 IEEE International Conference on Microelectronic Test Structures (ICMTS)*. IEEE, Mar. 2013, pp. 81–86. ISBN: 978-1-4673-4848-5. DOI: 10.1109/ICMTS.2013.6528150. URL: http://ieeexplore.ieee.org/document/6528150/.

List of Publications

[1] Appel, N. “Structure-Integrated Antennas for Solar Sails”. In: *2022 IEEE Aerospace Conference (AERO)*. IEEE, Mar. 2022, pp. 1–9. ISBN: 978-1-6654-3760-8. DOI: 10.1109/AERO53065.2022.9843275. URL: https://doi.org/10.1109/AERO53065.2022.9843275.

[2] Appel, N., Werner, C., Hoppe, J., and Stegmann, L. “Multi-Functional Radiating Structures for Solar Sailing Missions”. In: *B2. IAF Space Communications and Navigation Symposium*. Paris: IAF, 2022.

[3] Langer, M., Trinitis, C., Appel, N., et al. “Dependable Computing for Miniturized Satellites”. In: *4th EIROforum School on Instrumentation*. 2015.

[4] Appel, N., Rückerl, S., and Langer, M. “Nanolink: A Robust and Efficient Protocol for Small Satellite Radio Links”. In: *Small Satellite Systems and Services Symposium – 4S*. European Space Agency, 2016.

[5] Günther, S. M., Appel, N., and Carle, G. “Galois Field Arithmetics for Linear Network Coding using AVX512 Instruction Set Extensions”. In: *arXiv* (Sept. 2019). arXiv: 1909.02871. URL: http://arxiv.org/abs/1909.02871.

[6] Langer, M., Appel, N., Günzel, P., Gutsmiedl, J., Janke, F., Klesbye, J., Losekamm, M., Perakis, N., and Pöschi, T. “The Evolution of the CubeSat Program MOVE”. In: (2015).

[7] Langer, M., Schummer, F., Weisgerber, M., Steinkirchner, K., Appel, N., Rueckerl, S., Hoehn, A., and Walter, U. *Methods for Developing Reliable Hard-and Software for the Next Generation of Small Satellites*. 2017.

[8] Rückerl, S., Appel, N., Klein, R. D., and Langer, M. “Software-Defined Communication on the Nanosatellite MOVE-II”. In: *Proceedings of the 69th International Astronautical Congress*. 2018.

[9] Langer, M., Schummer, F., Appel, N., Gruebler, T., Janzer, K., Kiesbye, J., Krempel, L., Lill, A., Messmann, D., Rueckerl, S., et al. “Move-ii-the munich orbital verification experiment ii”. In: *Proceedings of the 4th IAA Conference on University Satellite Missions & CubeSat Workshop, Rome, Italy*. 2017, pp. 4–7.

[10] Fuchs, C. M., Trinitis, C., Appel, N., and Langer, M. “A fault-tolerant radiation-robust mass storage concept for highly scaled flash memory”. In: *European Space Agency, (Special Publication) ESA SP*. Vol. SP-732. 2015. ISBN: 9789292212964.

[11] Schilling, K., Tzschichholz, T., Motroniuk, I., Aumann, A., Mammadov, I., Ruf, O., Schmidt, C., Appel, N., Kleinschrodt, A., Montenegro, S., et al. “Tom: A formation for photogrammetric earth observation by three cubesats”. In: *4th IAA Conference on University Satellite Missions and CubeSat Workshop, Rome, Italy*. 2017.

[12] Appel, N., Kimpe, A., Kraus, K., Langer, M., Losekamm, M. J., Milde, M., Pöschl, T., Rückerl, S., Schäfer, F., Stromsky, A., et al. “TDP-3 Vanguard: Verification of a New Communication System for Cubesats on BEXUS 22”. In: *23rd ESA Symposium on European Rocket and Balloon Programmes and Related Research, Visby, Sweden*. 2017.

[13] Appel, N., Rückerl, S., Langer, M., and Klein, R.-D. “Communications”. In: *Nanosatellites: Space and Ground Technologies, Operations and Economics*. John Wiley & Sons, Ltd Chichester, UK, 2020. Chap. I-2e, pp. 115–141. ISBN: 978-1-119-04203-7.

[14] Rückerl, S., Meßmann, D., Appel, N., Kiesbye, J., Schummer, F., Fähling, M., Krempel, L., Kale, T., Lill, A., Reina, G., et al. “First Flight Results of the MOVE-II CubeSat”. In: (2019).

[15] Schilling, K., Tzschichholz, T., Motroniuk, I., Aumann, A., Mammadov, I., Ruf, O., Schmidt, C., Appel, N., Kleinschrodt, A., Montenegro, S., and Nüchter, A. “Tom: A formation for photogrammetric earth observation by three CubeSats”. In: *Advances in the Astronautical Sciences*. Vol. 163. 2018, pp. 543–556. ISBN: 9780877036470.

List of Supervised Theses

[1] Hoppe, J. “Entwicklung eines Fertigungsverfahrens für Dünnschicht-Hochfrequenzschaltungen in der Raumfahrt”. Bachelor’s Thesis. Technical University of Munich, 2022, p. 128.

[2] Stegmann, L. “Lenticular Shaped Slotted Waveguide Antenna Design for Satellites”. Bachelor’s Thesis. Technical University of Munich, 2021, p. 45.

[3] Würl, S. *Implementierung einer verteilbaren Telemetriesoftware für die Satellitenmission MOVE II*. Interdisciplinary Project. Munich, Germany, 2019.

[4] Nardini, M. *Entwurf und Implementierung einer Software zur Steuerung und Überwachung einer Kleinsatellitenbodenstation*. Interdisciplinary Project. Munich, Germany, 2020.

[5] Mouterde, G. *Migation strategies for the evolving space debris situation*. Master Thesis. Munich, Germany, 2018.

[6] Patzwahl, L. *Scalable Operation Concepts for Swarm Satellites*. Master Thesis. Munich, Germany, 2019.

[7] Ellmann, S. *Implementation of the S3TP protocol on RODOS for the satellite MOVE-III*. Interdisciplinary Project. Munich, Germany, 2019.

[8] Singla Manau, A. *Comparative Study of different Antenna Concepts for Solar Sailing*. Master Thesis. Munich, Germany, 2020.

[9] Spögler, F. *Entwicklung einer Antennenfeed-Technologie für Sonnensegel*. Master Thesis. Munich, Germany, 2021.

[10] Maas, A. *The Legal Framework for Commercial Nanosatellite Developement in Germany*. Term Paper. Munich, Germany, 2020.

[11] Werner, C. *Characterization of CFRP Booms for Microwave Applications*. Semester Thesis. Munich, Germany, 2022.

[12] Werner, C. “Structural Analysis of Multifunctional Radiating CTM-Boom Structures for Antenna Applications on Solar Sail Spacecraft”. Master’s Thesis. Technical University of Munich, 2022, p. 319.

Appendices

A Auxiliary Material

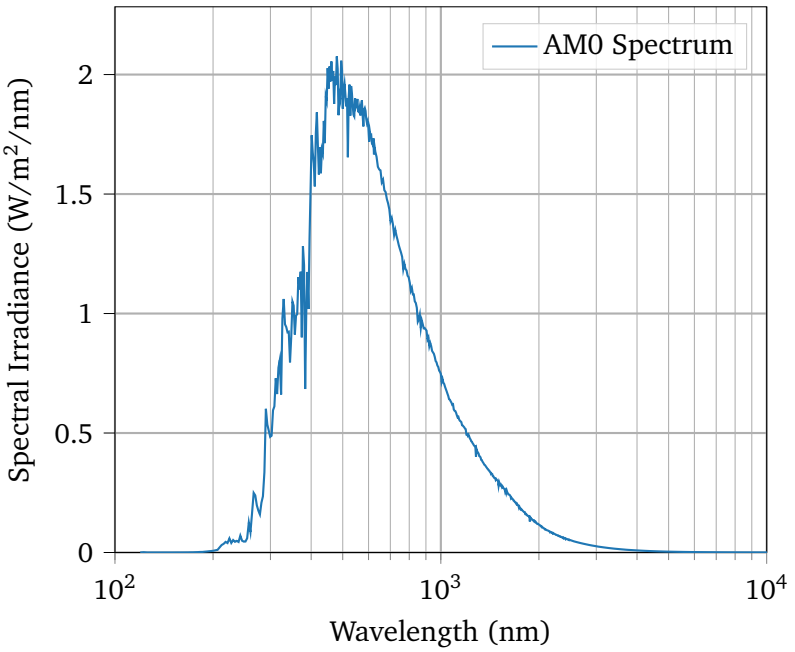

Figure 1: air mass zero solar irradiance spectrum[13].

Table 1: Properties of light-weight antennas.

Source	Mass (kg)	Gain (dBi)	Frequency (GHz)	Year
[64]	15	25.2	1.25	1998
[65]	1.2	33.7	8.3	1999
[8]	N/A	47.92	8.45	2002
[70]	56.7	23	1.413	2003
[61]	0.5	19.4	8.4	2016
[57]	2.1	42.6	35.75	2016
[62]	1	28.8	8.45	2017

Table 2: Excerpt of DSN/ESTRACK antenna characteristics.

Parameter	DSS-14 70m[152]	ESTRACK DSA2 35m[153, 154]
Receiving		
G/T		
S-Band	49.8 dB/K	>39.5 dB/K*
X-Band	61.5 dB/K	>51 dB/K†
Ka-Band	N/A	>55.8 dB/K
Polarization	LHCP/RHCP	
Ellipticity		
S-Band	<0.6 dB	N/A
X-Band	<0.8 dB	N/A
Transmitting		
EIRP		
S-Band	>105.6 dBW	>97 dBW
X-Band	115.8 dBW	>108 dBW
Ka-Band	N/A	>100.7 dBW
Polarization	LHCP/RHCP	
Ellipticity		
S-Band	<2.2 dB	N/A
X-Band	≤1.0 dB	N/A
(*) DSA1		
(†) DSA2, DSA3		

Table 3: Overview of material properties of CR80 epoxy Resin and CH80-10 solidifcation agent[146].

Material	Viscosity (at 25 °C)	Density (at 25 °C)
CR80 Epoxy Resin	900 mPa s	1.13 g mL^{-1}
CH80-10 Curing Agent	10 mPa s	0.95 g mL^{-1}

B Formulae

Slotline

Approximate form of the slotline's impedance for $0.0015 \leq 2a/\lambda_0 \leq 0.075$ and $2.22 \leq \epsilon_r \leq 3.8$[80]:

$$\begin{aligned} Z_{0s} = {} & 60 + 3.69\sin[\frac{(\epsilon_r - 2.22)\pi}{2.36}] + 133.5\ln(10\epsilon_r)\sqrt{2a/\lambda_0} \\ & + 2.81[1 - 0.011\epsilon_r(4.48 - \ln\epsilon_r)](2a/h)\ln(100h/\lambda_0) \\ & + 131.1(1.028 - ln\epsilon_r)\sqrt{h/\lambda_0} \\ & + 12.48(1_0.18\ln\epsilon_r)\frac{2a/h}{\sqrt{\epsilon_r - 2.06 + 0.85(2a/h)^2}} \end{aligned} \tag{1}$$

Microstrip

Microstrip dielectric attenuation[76]:

$$\alpha_d^{MS} = 8.69\frac{k_0\epsilon_r(\epsilon_e - 1)\tan\delta}{2\sqrt{\epsilon_e}(\epsilon_r - 1)} \qquad \text{dB/unit length} \tag{2}$$

$$\frac{w}{d} = \begin{cases} 8e^a/(e^{2a} - 2) & \text{for} \quad w/d < 2 \\ \frac{2}{\pi}\big[b - 1 - \ln(2b - 1) + (\epsilon_r - 1)/(2\epsilon_r)\cdot(\ln(b - 1) + 0.39 - (0.61)/\epsilon_r)\big] & \text{for} \quad w/d \geq 2 \end{cases}$$

Laminates

Linear laminate theory according to [151]:

$$E_\parallel = E_{f\parallel}\cdot\varphi + E_m\cdot(1 - \varphi)\cdot 0.9 \tag{3}$$

$$G_\perp = G_m\cdot((1 - \varphi) + \frac{G_m}{G_{f\parallel}\cdot\varphi})^{-1}\cdot 0.9 \tag{4}$$

$$E_\parallel = 2G_\perp(1 + \nu) \tag{5}$$

$$\rho = (\rho_{f\parallel}\cdot\varphi + \rho_m\cdot(1 - \varphi)) \tag{6}$$

where:

φ : Fiber volume fraction
Ψ : Matrix volume fraction

C Connector Tests

The connectors used for the SSPP PCB are Samtek SMA-J-P-X-ST-EM1, specified by the manufacturer up to 18 GHz. A test board was designed with RO4350B material with thickness 0.25 mm and width 8.3 mm. The CPW through length of $0.35\lambda_g$ was chosen with accordance to Orii et al. [155]. The taper has an initial width of 1.36 mm. The final CPW width is 1.7 mm. Two prototypes were tested.

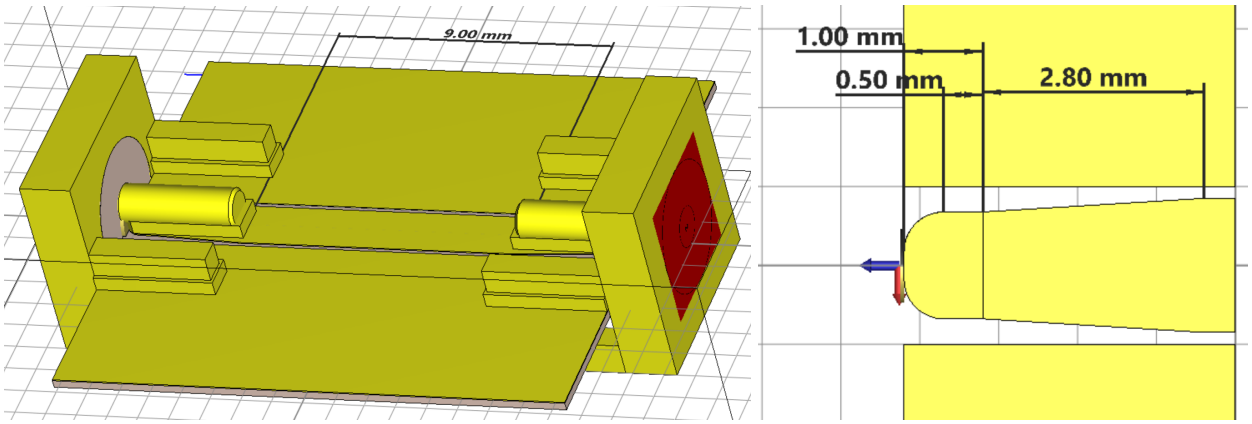

Figure 2: 3D model of the test PCB and geometry of the improved taper.

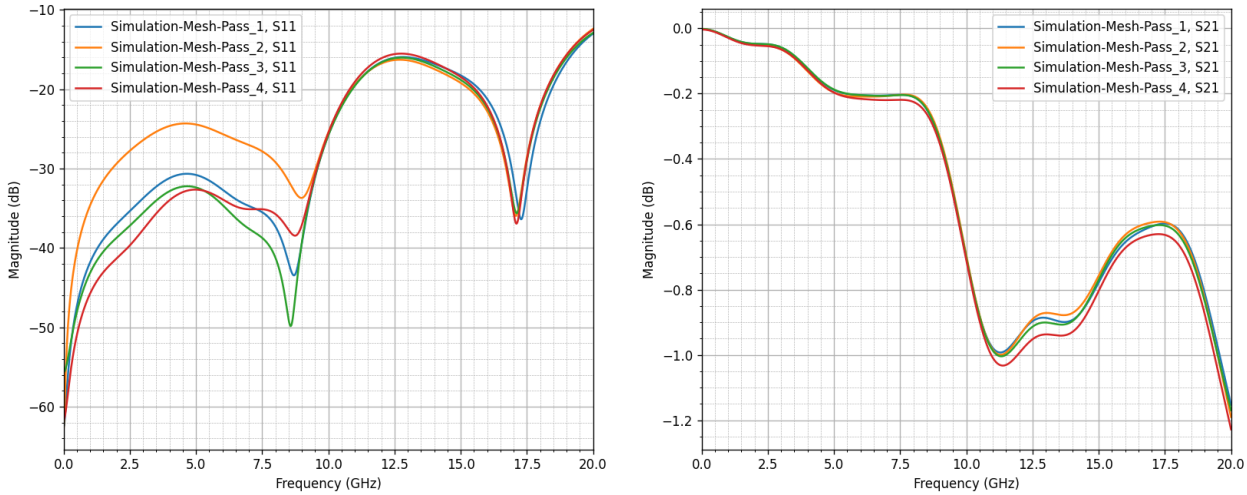

Figure 3: Simulated S-parameters of the test PCB.

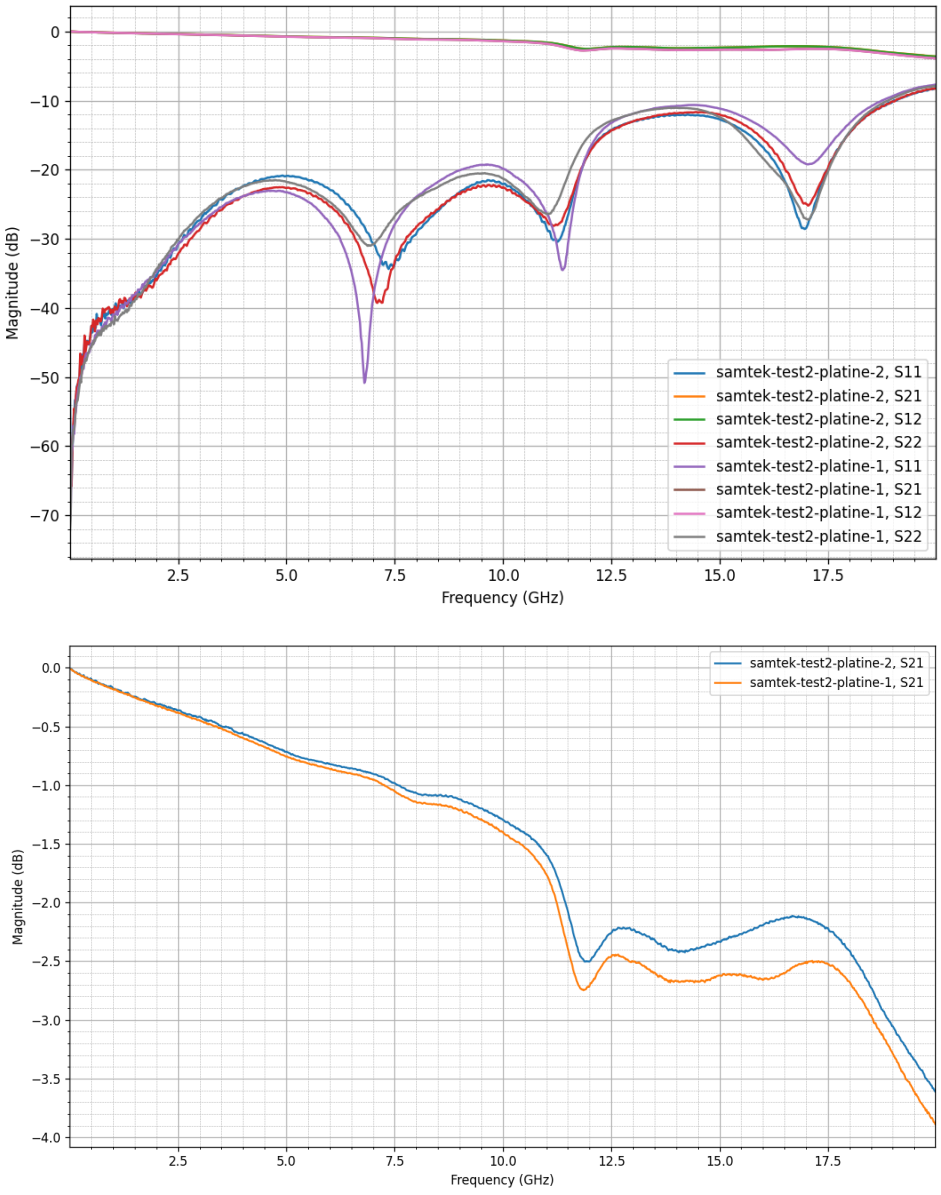

Figure 4: Measured S-parameters of the test PCB.

D Auxiliary Figures

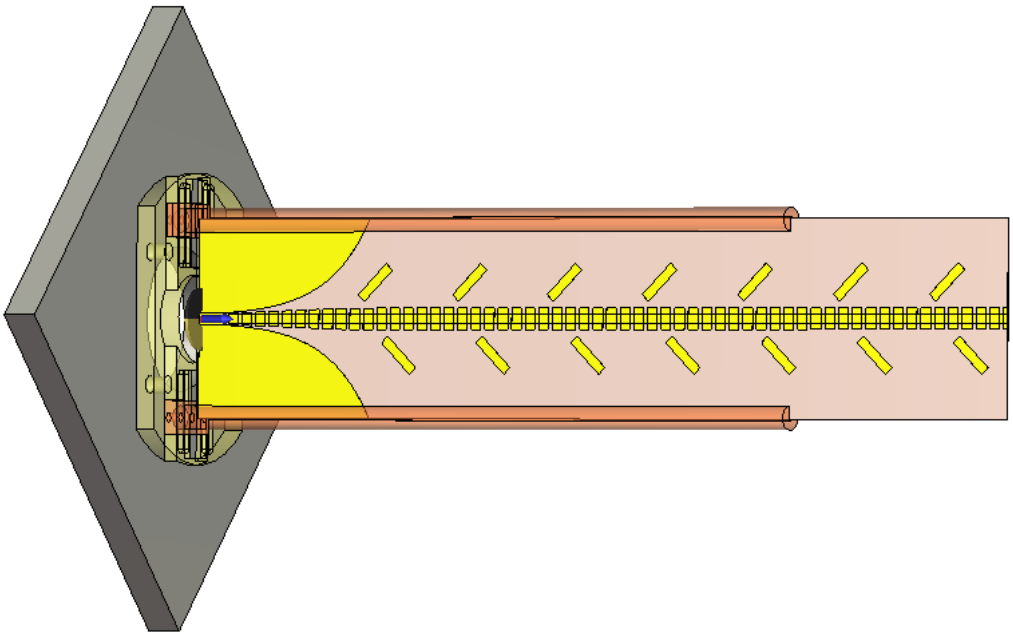

Figure 5: CST simulation model of the leaky wave antenna in the mounting bracket. The antenna is laterally stabilized by two arms, indicated in orange.

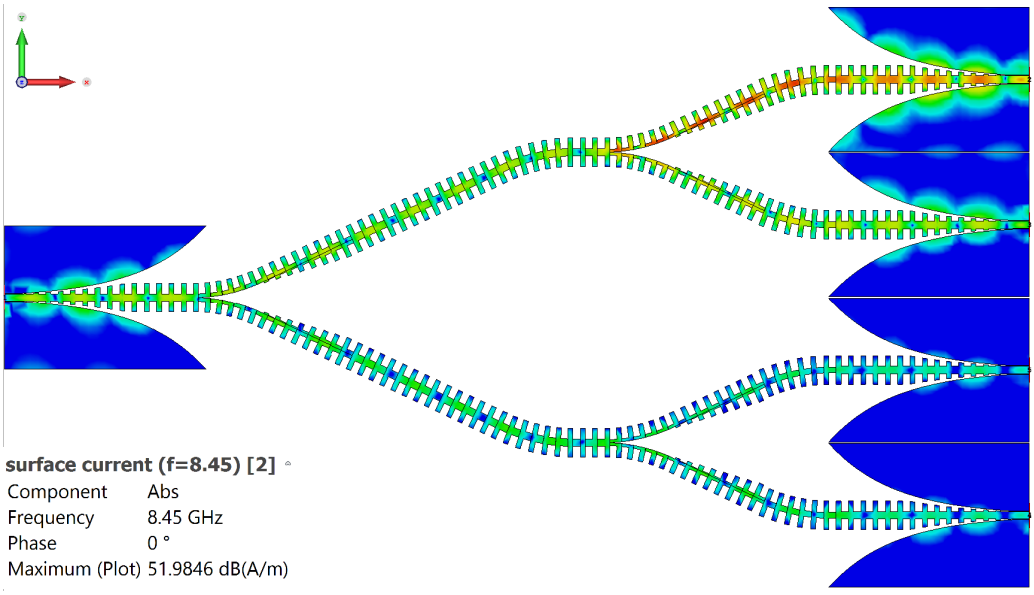

Figure 6: Surface current of the four-way divider with excitation from port 2.

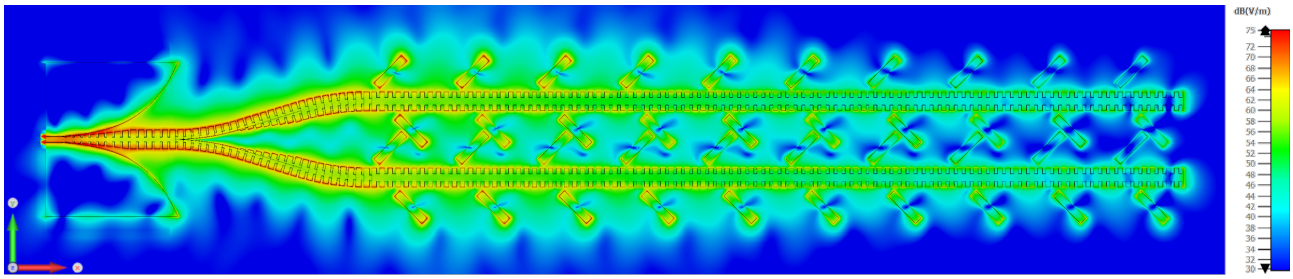

Figure 7: Average E-field of the antenna model with 40 radiating elements.

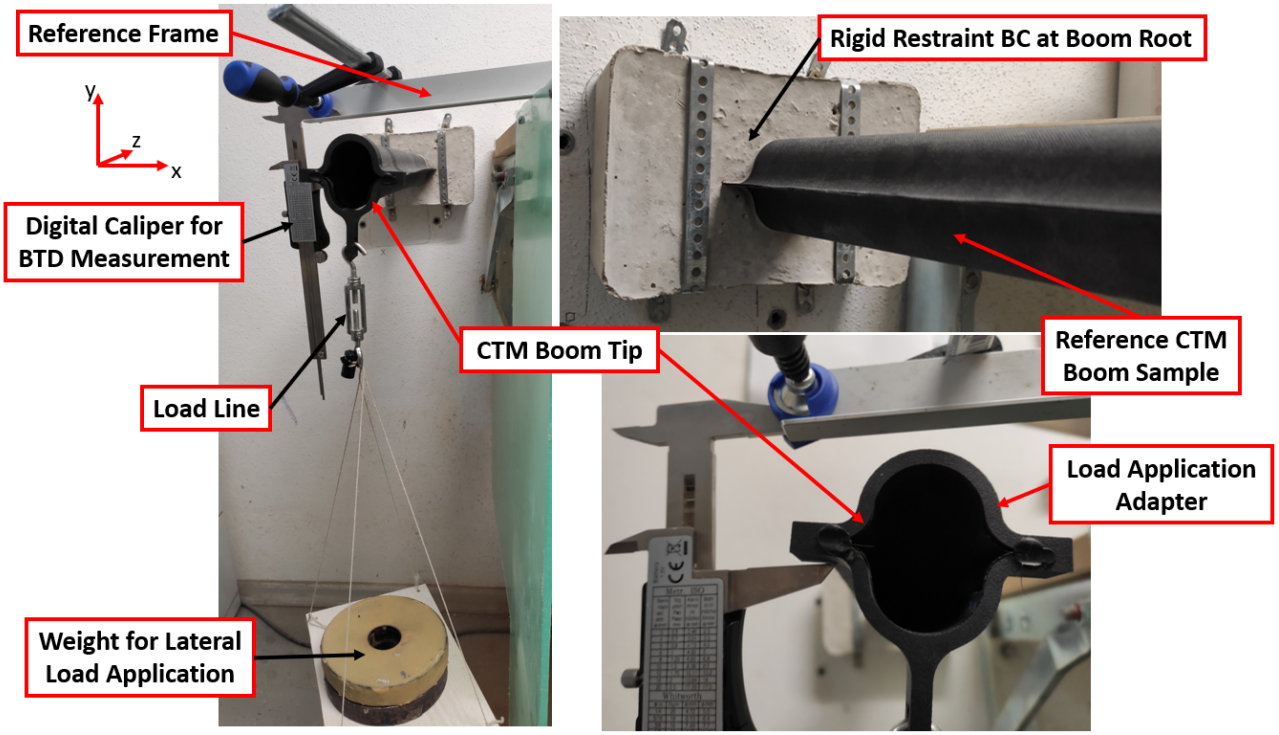

Figure 8: Measurement of the boom tip displacement (BTD) along the y-axis (x-axis bending). The other end of the boom is cast in concrete, ensuring a fixed suspension[150].

.

List of Figures

List of Tables

Acronyms

ACS3 Advanced Composite Solar Sail 3 13, 15, 17, 142

AM0 Air Mass Zero 6

AR Axial Ratio 54, 72

CFRP Carbon Fiber Reinforced Plastic ix, 11, 13–15, 26, 93, 97–101, 114, 116, 118, 120, 125, 127, 128, 130, 134, 143, 146

COTS Commercial Off-the-shelf 50, 76, 116

CP Circular Polarization 27, 51, 53

CPS Coplanar Strips 30, 32, 33, 50

CPW Coplanar Waveguide 30–33, 36, 43, 50, 51, 59, 70, 81, 83, 166

CTM Collapsible Tubular Mast ix, xi, 3, 10, 11, 13, 15, 24, 26, 93, 95, 96, 98–101, 104, 108, 111, 114, 116, 118, 119, 125, 127, 128, 132, 136, 142, 143, 145–147, 171

DFP Dry Fiber Placement 114–116

DL Downlink 20

DLR German Aerospace Center 11, 13, 15, 18, 93

DSN Deep Space Network 21, 25

ENIG Electroless Nickel Immersion Gold 54, 56, 64

ESA European Space Agency 13, 21

ESTRACK European Space Tracking 21, 25

GBL γ-Butyrolactone 77, 78

GCPW Grounded Coplanar Waveguide 31, 36, 37, 50

GEO Geostationary Orbit 8

IKAROS Interplanetary Kite-Craft Accelerated By Radiation Of The Sun 2, 13, 14, 17

IR Infrared Light 9

ITU International Telecommmunications Union 20

IVD Ion Vapor Deposition 3, 77, 80, 81, 83, 90, 147

JAXA Japan Aerospace Exploration Agency 13, 14

JPL Jet Propulsion Laboratory 11, 17, 18

LCM Liquid Composite Molding 114, 115

LEO Low-earth Orbit 15

LHCP Left Hand Circular Polarization 54, 164

LLT Linear Laminate Theory 130, 131

MarCO Mars Cube One 18

NASA National Aeronautics And Space Administration 11, 13–15, 18, 21

NEA Scout Near Earth Asteriod Scout 9, 11, 13–15, 17, 93

NMP N-methyl-2-pyrrolidone 77, 78

PCB Printed Circuit Board 3, 76, 166

PEC Perfect Electrical Conductor 41, 98, 111, 114

PEN Polyethylenenaphtalate 8, 14, 15

PET Polyethylene Terephthalate 8, 54

PGL Planar Goubau Line 40, 51

PLA Polylactic Acid 116

PMC Perfect Magnetic Conductor 41

PVD Physical Vapor Deposition 8, 76, 80

PW Plain Weave 115, 143

RF Radio Frequency 76

RHCP Right Hand Circular Polarization 164

RO4003C Rogers Corporation Laminate 4003C 59, 60, 64

RO4350B Rogers Corporation Laminate 4350B 51, 54, 60, 64, 66, 91, 166

RTM Resin Transfer Molding 114–116, 142

SAR Synthetic Aperture Radar 18, 19, 23, 93, 97

SIW Substrate-integrated Waveguide 30, 37, 39, 50

SLL Sidelobe Level 72, 111, 114, 142

SMA Subminiature Version A 51

SPP Surface Plasmon Polariton 40

SSPP Spoof Surface Plasmon Polariton ix, xi, 30, 40, 41, 43, 47, 50, 51, 53, 56, 58, 59, 62, 66, 67, 81, 83, 84, 91, 145, 146, 166

SWA Slotted Waveguide Antenna 26, 93, 97, 98, 100, 105, 108, 111, 128, 130–143, 175

TE Transversal Electric 33, 96, 98, 101, 118–121, 142, 143

TEM Transversal Eletromagnetic 30, 33, 35, 96, 101, 118, 119, 121

TL Transmission Line 28, 30, 31, 35, 39–41, 43, 47, 49–51, 58, 59, 66, 83, 91

TM Transversal Magnetic 40, 96, 98, 101, 118, 121, 128, 142, 143

TM/TC Telemetry And Telecommand 20

TRAC Triangular Rollable And Collapsible 10, 11, 13–15, 93, 171

TWA Traveling Wave Antenna 98, 106, 111

UL Uplink 20

UV Ultraviolet Light 7–9, 76, 120

VARI Vacuum-assisted Resin Infusion Process 114–116, 143, 146

VNA Vector Network Analyzer 54, 66, 118, 121, 123, 125